



HAL
open science

High-power laser system for Advanced Virgo gravitational wave detector: coherently combined master oscillator fiber power amplifiers

Li-Wei Wei

► **To cite this version:**

Li-Wei Wei. High-power laser system for Advanced Virgo gravitational wave detector: coherently combined master oscillator fiber power amplifiers. Other [cond-mat.other]. Université Nice Sophia Antipolis, 2015. English. NNT: 2015NICE4091 . tel-01284969

HAL Id: tel-01284969

<https://theses.hal.science/tel-01284969v1>

Submitted on 8 Mar 2016

HAL is a multi-disciplinary open access archive for the deposit and dissemination of scientific research documents, whether they are published or not. The documents may come from teaching and research institutions in France or abroad, or from public or private research centers.

L'archive ouverte pluridisciplinaire **HAL**, est destinée au dépôt et à la diffusion de documents scientifiques de niveau recherche, publiés ou non, émanant des établissements d'enseignement et de recherche français ou étrangers, des laboratoires publics ou privés.

UNIVERSITÉ NICE SOPHIA ANTIPOLIS
UFR Sciences
École Doctorale Sciences Fondamentales et Appliquées

THÈSE

pour obtenir le titre de

Docteur en Sciences

Discipline : Physique

présentée et soutenue par

Li-Wei WEI

**Système laser de haute-puissance pour
le projet Advanced Virgo :
les amplificateurs à fibre
combinés de façon cohérente**

◇ ◇ ◇

**High-Power Laser System for Advanced Virgo
Gravitational Wave Detector:
Coherently Combined
Master Oscillator Fiber Power Amplifiers**

Soutenue le 3 décembre 2015 à l'Observatoire de la Côte d'Azur,
devant le jury d'examen :

M.	Frédéric DU BURCK	Rapporteur
M.	Marc HANNA	Rapporteur
M.	Michel LINTZ	Examineur
Mme.	Catherine Nary MAN	Directeur de thèse
M.	Nicholas TRAYNOR	Examineur
M.	Benno WILLKE	Examineur

Abstract

Virgo is a cavity-enhanced Michelson interferometer built for the direct detection of gravitational waves whose existence was predicted by Albert Einstein in 1916 with the theory of general relativity. With its 3 km arm length, the differential strain sensitivity of Virgo reached the order of $10^{-22}\sqrt{\text{Hz}}^{-1}$. The Advanced Virgo project consists of major upgrades to the Virgo interferometer for even higher sensitivity, reaching the order of $10^{-23}\sqrt{\text{Hz}}^{-1}$ and thus leading to probable detections of gravitational waves.

To advance the quantum noise limit of precision interferometry, among other techniques, it is essential to increase the optical power of the laser beam injected to the Michelson interferometer. A low-noise single-frequency laser system delivering around 175 W of optical power in the fundamental Gaussian TEM₀₀ mode is called for, with relative power noise as low as $2.35 \times 10^{-9}\sqrt{\text{Hz}}^{-1}$ and frequency noise as low as $4.00 \times 10^{-7}\text{ Hz}\sqrt{\text{Hz}}^{-1}$.

This thesis discusses the realization of the aforementioned ultra-stable high-power laser system with the use of coherently combined master oscillator fiber power amplifiers. Commercially available fiber laser amplifiers are characterized in terms of beam quality, power noise, frequency noise, beam pointing stability, as well as long-term stability, and are coherently combined with Mach-Zehnder interferometry. The means for laser characterization are also developed in accordance with the stringent noise specifications.

The quasi-continuous operation of two low-noise fiber laser amplifiers delivering around 40 W of optical power over the course of a few thousand hours is demonstrated, providing for the first time a realistic measure of their robustness for laser interferometric gravitational wave detectors. Part of the laser beams from these fiber laser amplifiers, about 35 W each, are then combined in free-space with greater than 95% efficiency. Higher optical power may result from the combination of more units, while that from the rapid progress in the field of fiber laser amplifiers may also be considered. Despite the shortcoming of output power, the developed laser system complies with the noise requirements of Advanced Virgo.

Keywords: laser characterization, fiber laser amplifier, coherent beam combination, interferometry, gravitational wave detector

Résumé

Virgo est un interféromètre de Michelson dont les bras contiennent des cavités Fabry–Perot. Il a été construit pour détecter de manière directe les ondes gravitationnelles dont l’existence a été prévue par la théorie de la relativité générale d’Albert Einstein en 1916 selon la théorie de la relativité générale. Avec ses bras de 3 km, Virgo a été capable de mesurer des déformations relative différentielle au niveau de $10^{-22}\sqrt{\text{Hz}}^{-1}$. Le projet Advanced Virgo est une amélioration majeure de Virgo pour atteindre une sensibilité encore plus élevée, soit au niveau de $10^{-23}\sqrt{\text{Hz}}^{-1}$, avec laquelle la détection des ondes gravitationnelles deviendra probable.

Pour faire reculer la limite du bruit quantique dans l’interférométrie de précision, parmi d’autres techniques, il est nécessaire d’augmenter la puissance optique du faisceau laser injecté dans l’interféromètre de Michelson. On prévoit un système laser mono-fréquence de 175 W de puissance optique présentant des stabilités accrues pour le bruit relatif de puissance et pour le bruit de fréquence, soit $2.35 \times 10^{-9} \sqrt{\text{Hz}}^{-1}$ et $4.00 \times 10^{-7} \text{ Hz } \sqrt{\text{Hz}}^{-1}$, respectivement.

Ce travail de thèse a pour objet la réalisation de ce système laser de haute-puissance et de haute-stabilité basé sur l’utilisation d’amplificateurs à fibre combinés de façon cohérente. Des amplificateurs à fibre disponibles dans le commerce sont caractérisés en termes de qualité de faisceau, de bruit de puissance, de bruit de fréquence, de stabilité de pointé du faisceau, et également en terme de stabilité à long terme sur quelques milliers d’heures. On implémente l’interférométrie de Mach–Zehnder pour la combinaison cohérente de faisceaux. Les techniques de caractérisation de faisceaux laser sont aussi développées en considérant leurs limites ultimes.

Le fonctionnement quasi-continu des deux amplificateurs à fibre bas-bruits avec une puissance optique de 40 W est démontré comme une mesure de robustesse pour ses applications dans les détecteurs interférométriques d’ondes gravitationnelles. Une partie des faisceaux sortant de ces deux amplificateurs à fibre, 35 W chacun, sont combinés en espace libre avec une efficacité de plus de 95 %. On peut obtenir une puissance optique plus élevée en combinant un nombre plus grand d’unités. On pourra aussi considérer à moyen terme des unités plus puissantes compte tenu des rapides progrès dans le domaine des amplificateurs à fibre.

Hormis un déficit de puissance optique, le système laser développé dans ce travail sur la base de la combinaison cohérente de *Master Oscillator Fiber Power Amplifiers*, remplit les conditions posées par Advanced Virgo.

Mots-clés: caractérisation de laser, amplificateur à fibre, combinaison cohérente de faisceaux, interférométrie, détecteur des ondes gravitationnelles

Acronyms

AdV Advanced Virgo

AR Anti-Reflective

ASE Amplified Spontaneous Emission

AOM Acousto-Optic Modulator

CBC Coherent Beam Combination

EOM Electro-Optic Modulator

FSR Free Spectral Range

GWD Gravitational Wave Detector

IMC Input Mode Cleaner

INJ Injection Subsystem of Advanced Virgo

MOFPA Master Oscillator Fiber Power Amplifier

MOPA Master Oscillator Power Amplifier

NPRO Non-Planar Ring Oscillator

OMC Output Mode Cleaner

PMC Pre Mode Cleaner

PSD Power Spectral Density

PSL Pre-Stabilized Laser Subsystem of Advanced Virgo

RIN Relative Intensity Noise

SBS Stimulated Brillouin Scattering

SNL Shot Noise Limit

SQL Standard Quantum Limit

In general we look for a new law by the following process. First we guess it. Then we compute the consequences of the guess to see what would be implied if this law that we guessed is right. Then we compare the result of the computation to nature, with experiment or experience, compare it directly with observation, to see if it works. If it disagrees with experiment it is wrong. In that simple statement is the key to science. It does not make any difference how beautiful your guess is. It does not make any difference how smart you are, who made the guess, or what his name is if it disagrees with experiment it is wrong. That is all there is to it.

— Richard P. Feynman, *“Seeking New Laws”*

Contents

Abstract	iii
Résumé	v
Acronyms	vii
List of Figures	xv
1 Introduction	1
1.1 Gravity, General Relativity and Gravitational Waves	1
1.2 Gravitational Waves: Sources and Detectors	2
1.3 The Advanced Virgo Project	5
1.4 Motivation, Objective and Organization of the Thesis	6
2 Pre-Stabilized Laser System for Interferometric Gravitational Wave Detectors	9
2.1 Ultra Stable Laser Source: Non-Planar Ring Oscillator	11
2.2 Low-Noise High-Power Laser System	14
2.3 Single-Frequency Fiber Laser Amplifiers	15
2.4 Coherent Beam Combination	19
2.5 Laser Stabilization	19
2.6 Optical Cavity as Mode Cleaner	21
2.7 Pre-Stabilized Laser for Advanced Virgo: Specifications and a Conceptual Design	22
3 Laser Characterization	33
3.1 Optical Power Measurement	33
3.2 Advanced Virgo Frequency Band of Interest	34
3.3 Laser Power Noise Measurement	34
3.4 Beam Clipping Effect in Laser Power Noise Measurement	36
3.5 Spatial Inhomogeneity in Photodiode Responsivity	37
3.6 Laser Frequency/Phase Noise Measurement	43
3.7 Laser Beam Pointing Stability Measurement	51
3.8 Invariance of Gaussian Beam Pointing Stability	54
3.9 Beam Profile Measurement	56
3.10 Transverse Modes: LP_{01} in Fiber vs. Gaussian TEM_{00} in Free-Space	57
3.11 Power Spectral Density Measurement	58

3.12	Transfer Function Measurement	60
3.13	Automatized Data Acquisition	61
4	Master Oscillator Fiber Power Amplifier	63
4.1	Seed Lasers for Fiber Amplifiers	63
4.2	Fiber Coupling of the NPRO Laser	65
4.3	Fiber Coupling for General Beam Delivery	81
4.4	Nufern Fiber Amplifiers	84
4.5	Eolite Fiber Amplifiers	87
4.6	Azur Light Systems Fiber Amplifiers	89
4.7	Actuation Paths for Power Stabilization	109
5	Coherent Beam Combination	115
5.1	Dither-Locked Free-Space Mach–Zehnder Interferometry for Coherent Beam Combination	116
5.2	Phase Dynamic of Azur Light Systems Fiber Amplifiers	117
5.3	Combining Efficiency and Power Penalty	120
5.4	Power Noise	121
5.5	Frequency Noise and Beam Quality	125
5.6	Beam Pointing Stability	128
5.7	Long Term Monitoring Results	128
5.8	Laser Power Stabilization On Top of Coherent Beam Combination . .	129
5.9	Combining More Beams	136
6	Conclusions and Perspectives	139
6.1	High-Power Fiber Amplifiers	139
6.2	Coherent Beam Combination	140
6.3	Besides High-Power Laser	140
6.4	Beyond Advanced Gravitational Wave Detectors	141
	Bibliography	143
	Traduction partielle en français	159
	Appendices	171
A	Test Results of the 50 W Demo Fiber Amplifier from Nufern	173
B	Test Results of the 30 W Demo Fiber Amplifier from Azur Light Systems	185
C	Responsivity Maps of Excelitas C30665GH Photodiodes	195
D	Mapping Photodiode Responsivity	203
E	Numerical Calculation on Gaussian Beam Clipping Effects	221
F	MATLAB m-files for Gaussian Beam Waist Calculation	225

G GPIB Commands Wrapped with Perl	231
H NI-DAQmx Wrapped with Perl	245
I Calorimeter: Certificate of Calibration	251
Acknowledgements	259
Remerciements	261

List of Figures

1.1	Spacetime tells matter how to move; matter tells spacetime how to curve.	2
1.2	The orbital decay of PSR B1913+16.	3
1.3	Characteristic strain of commonly considered gravitational wave sources and the detection sensitivity of some of the related science projects.	4
1.4	The evolution of the sensitivity of Virgo, 2003–2011.	5
1.5	Advanced Virgo design sensitivity and noise budget.	6
1.6	Virgo interferometer aerial view.	7
2.1	Advanced Virgo Schematic Optical Layout.	10
2.2	The NPRO laser.	11
2.3	Typical power noise and frequency noise of the NPRO laser.	12
2.4	Power noise of the NPRO laser at high frequencies.	12
2.5	Schematic of the PW-ECL.	13
2.6	Power noise of various single-frequency laser sources.	13
2.7	Frequency noise of various single-frequency laser sources.	13
2.8	The electric field amplitudes of TEM modes. False color: red and blue are the maxima with opposite signs, and light green is the zero.	23
2.9	Cavity transmission vs. frequency.	24
2.10	The Advanced Virgo injection subsystem.	24
2.11	Advanced Virgo modulation sidebands overview.	25
2.12	Advanced Virgo reference specifications on the power noise in the gravitational wave detection band.	26
2.13	Advanced Virgo reference specifications on the frequency noise in the gravitational wave detection band.	27
2.14	Advanced Virgo reference specifications on beam pointing stability in the gravitational wave detection band at PSL output.	27
2.15	A conceptual design of the Advanced Virgo PSL subsystem.	28
2.16	Virgo PMC design parameters.	28
2.17	Free-running laser power noise specifications for Advanced Virgo.	30
2.18	Free-running laser frequency noise specifications for Advanced Virgo.	30
2.19	Free-running laser beam pointing stability specifications for Advanced Virgo.	31
3.1	The error function erf	38
3.2	Photodiode clipping effect: the κ factor, normalized with respect to ω	38
3.3	Photodiode clipping effect: the κ factor in unit m^{-1}	39

3.4	A projected case of lateral beam pointing stability from the Advanced Virgo specifications.	39
3.5	Schematic diagram of the photodiode responsivity mapping setup. . .	40
3.6	A photo of the optical setup for the mapping of photodiode responsivity.	41
3.7	κ induced by the beam clipping effect with $\omega = 35 \mu\text{m}$	42
3.8	Z-shaped and S-shaped scan patterns.	43
3.9	An example of the $\kappa_{x,y}(x, y)$ of the 3 mm diameter photodiodes of interest.	44
3.10	A Mach–Zehnder interferometer.	46
3.11	Phase noise measurement with a heterodyne Mach–Zehnder interferometer.	47
3.12	Dither Locking of a Mach–Zehnder Interferometer	47
3.13	Frontal Dither Locking of an Asymmetric Mach–Zehnder Interferometer	51
3.14	Quadrant Photodiode	51
3.15	Quadrant photodiode response S vs. relative movement x'	53
3.16	Comparison on the fields of the fundamental fiber LP and Gaussian TEM modes.	59
3.17	A control loop diagram with negative feedback amplifier.	61
4.1	Conceptual building blocks for coherently combined master oscillator fiber power amplifiers.	64
4.2	A possible configuration for the Advanced Virgo laser system.	66
4.3	An all-fiber configuration of the fibered seed lasers building block. . .	66
4.4	Specifications of PM980-XP polarization-maintaining single-mode fiber from various providers.	68
4.5	Setup for testing fiber coupling and beam delivery with up to $\sim 1 \text{ W}$ optical power.	68
4.6	Output power vs. input power of the 25 m long PM980-XP like fiber.	69
4.7	Power noise of a laser beam before and after fiber coupling ($\sim 1 \text{ W}$ coupled), and after a 25 m long PM980-XP alike fiber	69
4.8	κ due to fiber coupling.	71
4.9	Some commercially available fiber collimators designed for 1064 nm wavelength.	72
4.10	Beam propagation measurement of the PM980-XP fiber using a collimator with focal length $f \sim 6.34 \text{ mm}$	73
4.11	Fiber coupling of the NPRO laser.	73
4.12	Fiber coupling efficiency time series of NPRO-400.	74
4.13	Fiber coupling efficiency histogram of NPRO-400.	74
4.14	Output power vs. pumping current of NPRO-900.	75
4.15	Beam propagation measurement of NPRO-900. Pumping current $I = 2 \text{ A}$	75
4.16	Fiber coupling efficiency of NPRO-900.	76
4.17	Fiber coupling efficiency time series of NPRO-900.	77
4.18	Fiber coupling efficiency histogram of NPRO-900.	77
4.19	Beam propagation measurement of NPRO-800. Pumping current $I = 1.8 \text{ A}$	78

4.20	Fiber coupling of NPRO-800.	79
4.21	Fiber coupling efficiency time series of NPRO-800.	80
4.22	Fiber coupling efficiency histogram of NPRO-800.	81
4.23	Thermal lensing of neutral density filters.	82
4.24	A damaged facet and a normal facet of a PM980-XP fiber.	83
4.25	Input power, output power and temperature time series of the Nufern ~ 50 W fiber amplifier.	85
4.26	Power noise of the Nufern ~ 50 W fiber amplifier.	86
4.27	Beam pointing stability of the Nufern ~ 50 W fiber amplifier.	86
4.28	Output power time series of the Eolite ~ 27 W fiber amplifier.	87
4.29	Power noise spectrum of the Eolite ~ 27 W fiber amplifier.	88
4.30	Beam pointing stability of the Eolite ~ 27 W fiber amplifier.	88
4.31	Schematic diagram of the tested fiber amplifiers	89
4.32	Photos of ALS fiber amplifier.	90
4.33	The leakage beam from the optical isolator of ALS 2.	91
4.34	Acoustic noise of Rack A. Measured with ALS 2.	91
4.35	ALS fiber amplifiers: output power vs. laser diode pump current.	93
4.36	ALS fiber amplifiers: output power time series.	94
4.37	Fourier transform of ALS 2 output power time series.	94
4.38	Some exemplary excerpts of the output power time series after the restart of the ALS fiber amplifiers.	95
4.39	Some exemplary excerpts of the 24 h oscillations in the output power time series of the ALS fiber amplifiers.	96
4.40	Time series and ADEV of various signals associated with ALS 2 be- tween ~ 2 h and ~ 240 h.	98
4.41	Time series and ADEV of various signals associated with ALS 2 be- tween ~ 305 h and ~ 647 h.	99
4.42	Beam propagation measurement of ALS 2 after a lens.	100
4.43	Power noise at ALS 2 fiber amplifier input and output between 100 kHz and 100 MHz.	101
4.44	Power noise at ALS 2 fiber amplifier input and output between 10 Hz and 100 kHz.	101
4.45	Relative optical power noise vs. relative injection current noise, of the pumping laser diodes of the ALS 2 fiber amplifier.	102
4.46	Relative power noise of ALS 2 fiber amplifier output vs. relative optical power noise of the pumping laser diodes (1/4).	103
4.47	Relative power noise of ALS 2 fiber amplifier output vs. relative optical power noise of the pumping laser diodes (2/4).	103
4.48	Relative power noise of ALS 2 fiber amplifier output vs. relative optical power noise of the pumping laser diodes (3/4).	104
4.49	Relative power noise of ALS 2 fiber amplifier output vs. relative optical power noise of the pumping laser diodes (4/4).	104
4.50	Output power noise spectrogram of ALS 2 at low frequencies.	106
4.51	Output power noise spectrogram of ALS 2 at high frequencies.	107
4.52	Frequency noise of ALS 2.	109
4.53	Output beam pointing stability of ALS fiber amplifiers.	110

4.54	Current shunt for power stabilization.	111
4.55	Amplitude transfer function of the current shunt for laser power stabilization.	111
4.56	Voltage across the current shunt vs. pump current, ALS 2.	112
4.57	A quasi-three-level system for laser action.	113
4.58	Qualitative illustration on the amplitude modulation transfer of pump/input power to output power and the corner frequency ω_{eff} of a fiber amplifier.	113
4.59	Amplitude transfer function of the current shunt to the output power of ALS 2.	114
5.1	Schematic diagram of the setup for the CBC of two MOFPAs	116
5.2	Differential phase time series of an asymmetric Mach–Zehnder interferometer.	117
5.3	Time series of the differential phase evolution between the two ALS fiber amplifiers in the coherent beam combination setup.	119
5.4	Optical interference.	121
5.5	Coherent beam combination efficiency vs. optical power mismatch.	122
5.6	Loss analysis of mismatched Gaussian beams for coherent combination.	123
5.7	Bessel function of the first kind.	123
5.8	Power noise of the coherently combined beam.	124
5.9	Power noise of the individual fiber amplifier beams and the coherently combined beam.	126
5.10	Differential frequency noise between the two fiber amplifiers used for coherent beam combination.	127
5.11	Power noise of the combined beam when free-running and when phase-locked.	127
5.12	Beam pointing stability of the coherently combined beam vs Advanced Virgo free-running specifications.	129
5.13	Beam pointing stability of the individual beams and the combined beam.	130
5.14	Power noise measurement with an ADC card calibrated against the SR780 spectrum analyzer.	131
5.15	Spectrogram of the power noise of the ALS 1 fiber amplifier in the coherent beam combination experiment.	132
5.16	Spectrogram of the power noise of the ALS 2 fiber amplifier in the coherent beam combination experiment.	133
5.17	Spectrogram of the power noise of the combined beam in the coherent beam combination experiment.	134
5.18	Spectrogram of the differential phase noise in the coherent beam combination experiment.	135
5.19	A schematic diagram on the coherent beam combination with three fiber amplifiers.	137

Chapter 1

Introduction

1.1 Gravity, General Relativity and Gravitational Waves

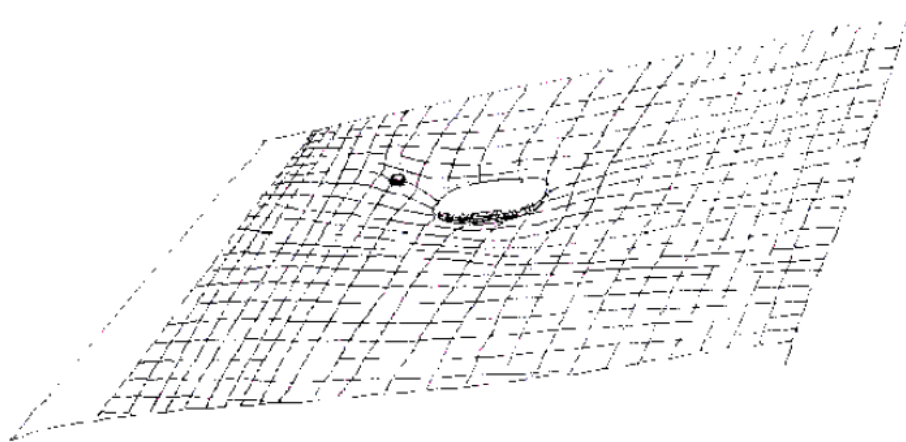
The Nobel Prize in Physics in 1993 was awarded to Russell A. Hulse and Joseph H. Taylor Jr. “for the discovery of a new type of pulsar, a discovery that has opened up new possibilities for the study of gravitation. [3–5]”

Modern study of gravitation dates back to Galileo Galilei’s finding during the 16–17th century that all objects accelerate equally when falling. The Apollo 15 mission demonstrated the famous “hammer and feather” drop test on the Moon [6].

In 1687, Isaac Newton published *Mathematical Principles of Natural Philosophy* (*Philosophiæ Naturalis Principia Mathematica*) in which the law of universal gravitation was presented; we all know the mystic apple story of Isaac Newton. The success of Newton’s law of universal gravitation may be highlighted by the discovery of Neptune, the first and only planet found by mathematical investigation instead of empirical observation. In 1846, calculations of Urbain Le Verrier led to the discovery of Neptune by Johann Gottfried Galle [7]. Newton’s theory of gravity, however, cannot fully account for the observed perihelion precession rate of Mercury. Albert Einstein’s general theory of relativity, published in 1915, on the other hand, provides an accurate correction to the Newtonian prediction.

In general relativity, space and time, which were considered absolute by Newton, are combined into a single continuum called spacetime. In Newtonian theory the presence of a mass particle creates a gravitational potential and matter-matter interaction is described by gravitational force. In general relativity gravity is regarded as curvature in spacetime caused by the presence of a mass particle, and instead of direct matter-matter interaction, gravitation is mediated by spacetime (Figure 1.1), as John Archibald Wheeler said: “Spacetime tells matter how to move; matter tells spacetime how to curve [8].”

Newton’s formulation of gravity requires that mass particles respond instantaneously to other mass particles irrespective of their distances, which infers that the speed of classical gravity is infinite and the motions of mass particles are correlated in real-time [9]. In general relativity, the motion of a mass particle creates ripples traveling in spacetime, that is, gravitational waves. Much as how special relativity extends the laws of motion to physical conditions with high velocities, general



Matter (the large stone) tells spacetime how to curve;
spacetime tells matter (the pebble) how to move.
(Drawing by John Wheeler.)

Figure 1.1: “Spacetime tells matter how to move; matter tells spacetime how to curve.” From [8].

relativity extends the laws of gravity to those with strong gravitational fields.

In 1974, Hulse and Taylor discovered PSR B1913+16, a pulsar in a binary star system. The orbital decay of PSR B1913+16 was found to match precisely the loss of energy and angular momentum due to the emission of gravitational waves predicted by general relativity (Figure 1.2) [10]. This is indirect but nevertheless strong evidence on the presence of gravitational waves, and a solid confirmation on the validity of general relativity in strong gravitational fields.

To date, in addition to the precise prediction of the perihelion precession rate of Mercury and the gravitational orbital decay of the Hulse-Taylor binary pulsar, Einstein’s theory of general relativity has provided accurate predictions for the other two “classical tests” [12]: the deflection of light by the Sun, and gravitational redshift — which is essential for the accuracy of the global positioning system (GPS) [13], as well as other modern tests [14].

The direct detection of gravitational waves will not only add another support to the theory of general relativity, but also open a new window to the better understanding of the Universe, as well as intriguing consequences in physics, astrophysics and cosmology [15].

1.2 Gravitational Waves: Sources and Detectors

Global efforts are underway towards the direct detection of gravitational waves¹. The detection of gravitational waves requires knowledge and models on possible sources and adapted detectors.

¹For the viewpoint of Joseph H. Taylor Jr. on indirect vs. direct detections, see “An Interview with Joseph Hooton Taylor, Jr.” in LIGO Magazine, Issue 7, September 2015. Online: <http://www.ligo.org/magazine/LIGO-magazine-issue-7.pdf#page=22>

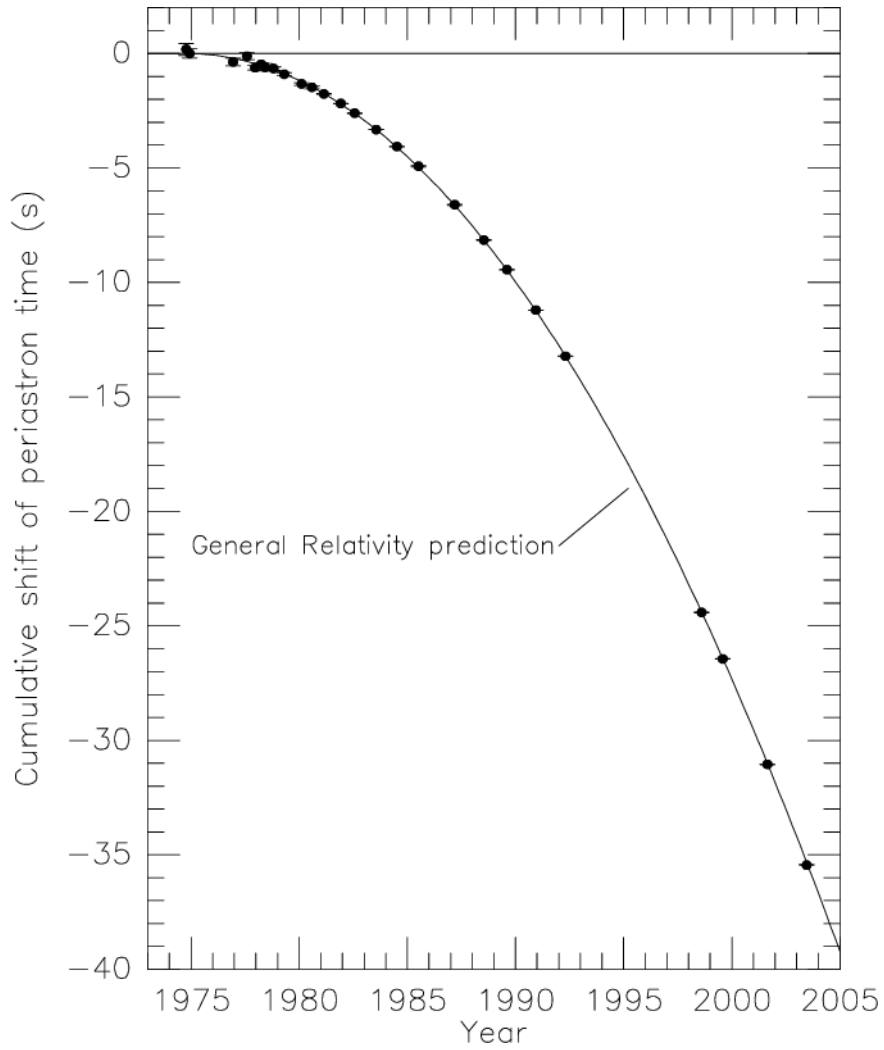


Figure 1.2: The orbital decay of PSR B1913+16 (a pulsar in a binary star system) was found to match precisely the loss of energy and angular momentum due to the emission of gravitational waves predicted by general relativity. From [11].

The passage of a gravitational wave induces a dimensionless strain amplitude, h , proportional to $\Delta L/L$ where ΔL is the change in separation of two masses a distance L apart [16]. Commonly considered sources of gravitational waves include supernovae, orbiting or coalescing binaries, and fast rotating non-axisymmetric stars [17]. Figure 1.3 shows the characteristic strain of commonly considered gravitational wave sources versus frequency and the sensitivity curves of some detectors [18].

To detect gravitational waves, Joseph Weber developed the first resonant-bar detectors in the 1960s [19]. If we think of acoustic waves, resonant-bars are like tuning forks in that they respond to a narrow frequency range.

Broadband detection can be achieved by laser interferometric gravitational wave detectors (GWDs) [20]. In the Michelson–Morley experiment [21], the Michelson interferometer showed its usefulness in bounding the anisotropy, and thus proving the constancy, of the speed of light. Similarly, the Michelson interferometer can also be deployed to measure the strain induced by the passage of gravitational waves, and is the basis of laser interferometric gravitational wave detectors. On top of the Michelson interferometer, modern advanced interferometric detectors have improved their sensitivity with many novel techniques based on the use of Fabry–Perot cavities.

Other known gravitational wave probing techniques include pulsar timing arrays [22] and polarization measurements of the cosmic microwave background [23].

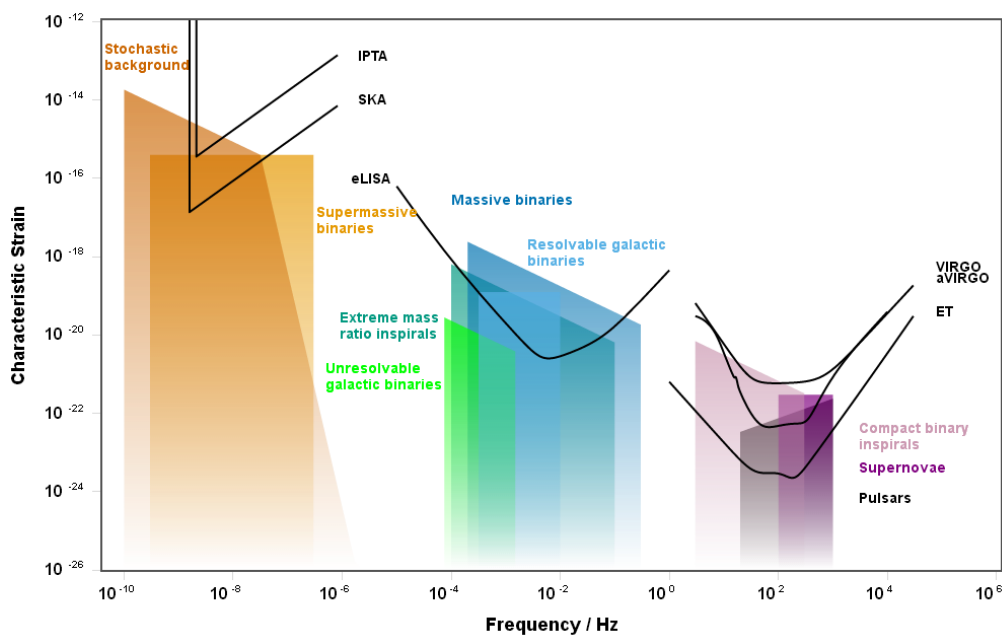


Figure 1.3: Characteristic strain of commonly considered gravitational wave sources and the detection sensitivity of some of the related science projects. From [18]. IPTA: International Pulsar Timing Array, SKA: Square Kilometer Array, eLISA: Evolved Laser Interferometer Space Antenna, aVIRGO: Advanced Virgo, ET: Einstein Telescope. Plotted with <http://rhcole.com/apps/GWplotter/>.

1.3 The Advanced Virgo Project

Virgo is a cavity-enhanced Michelson laser interferometer built for the detection of gravitational waves (Figure 1.6) [24]. With its 3 km arms, Virgo reached a differential strain sensitivity of the order of $10^{-22} \sqrt{\text{Hz}}^{-1}$ (Figure 1.4) [25], and correspondingly a binary neutron star inspiral range of 12 Mpc [26]. In comparison, the closest cluster of galaxies, Virgo, is 16.5 Mpc away [27].

In addition to the strain amplitude (which defines the minimum required sensitivity), the event rate, or population, of potential gravitational wave sources is equally important when it comes to the detection rate. Sources with large strain amplitudes are easier to measure, but may as well be very infrequent for detection. Taking these factors into account, with the LIGO²–Virgo detector network, the derived detection rate for binary neutron star coalescence was 0.02 yr^{-1} [28].

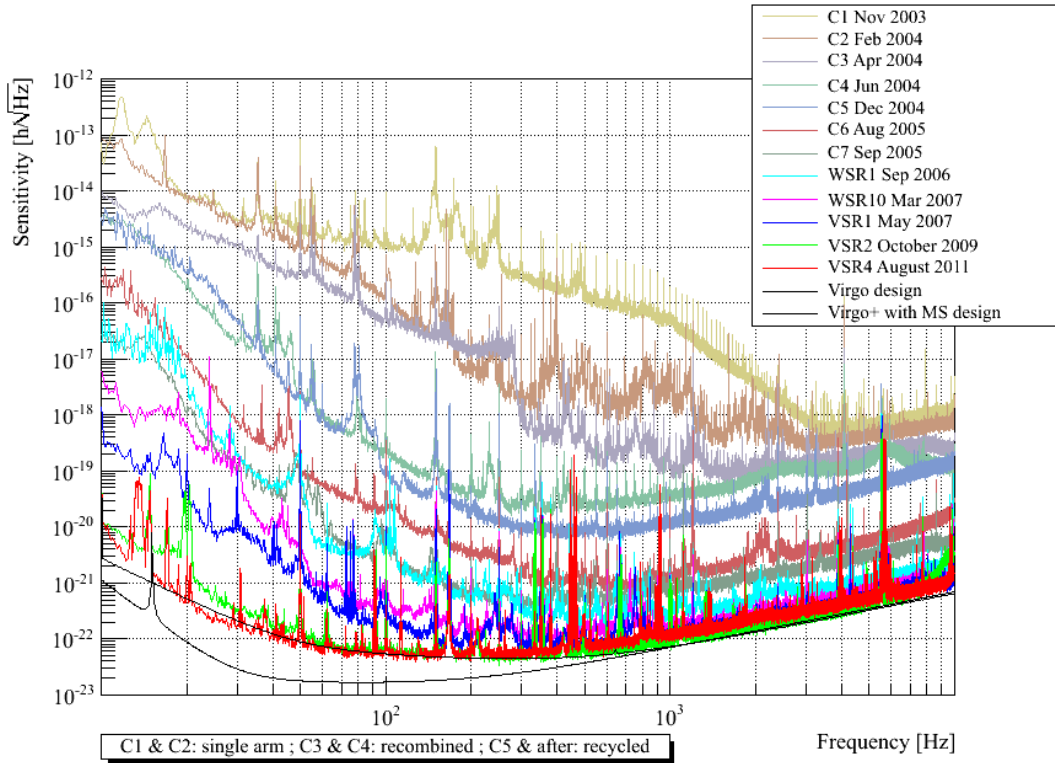


Figure 1.4: The evolution of the sensitivity of Virgo, 2003–2011. From [25].

Major upgrades of Virgo are underway for a better sensitivity and hence a higher detection rate of gravitational wave signals, resulting in the so-called Advanced Virgo (AdV) project. The differential strain sensitivity is expected to improve by tenfold, reaching the order of $10^{-23} \sqrt{\text{Hz}}^{-1}$ [29]. With the Advanced LIGO–Virgo detector network, the predicted detection rate for binary neutron star coalescence is 40 yr^{-1} [28].

²Laser Interferometer Gravitational-Wave Observatory, consists of two detectors similar to Virgo located in the Washington and Louisiana States of America.

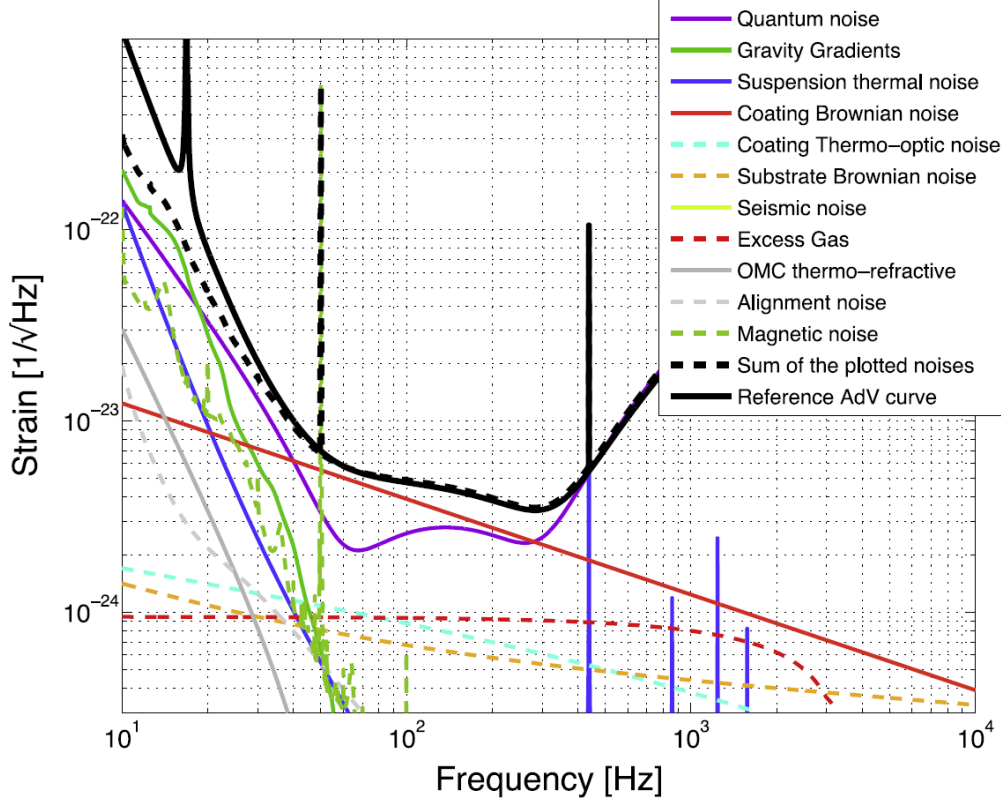


Figure 1.5: Advanced Virgo design sensitivity and noise budget. From [29].

1.4 Motivation, Objective and Organization of the Thesis

The quantum nature of light results in one fundamental limit in interferometric measurements, namely the shot noise. The coexistence of the shot noise and the radiation pressure noise defines the standard quantum limit of precision interferometry [30].

The shot noise limits the strain sensitivity of the interferometer at high frequencies. In order to reach the design differential strain sensitivity, the laser system in Advanced Virgo is foreseen to deliver 175 W single-frequency optical power in TEM₀₀ transverse mode.

Unlike the laser systems for Advanced LIGO [31], KAGRA [32] and initial Virgo [24] which are based on injection-locked laser oscillators and bulk solid-state laser amplifiers, Advanced Virgo foresees a stabilized laser system based on the coherent combination of master oscillator fiber power amplifiers.

Fiber laser amplifiers are an emerging technology that serves many interests for high-power applications [33]. Owing to the waveguide structure and the high surface-to-volume ratio, they offer good output beam quality even at high power levels. This, together with their compactness, alignment-free nature and high energy efficiency, make fiber laser amplifiers an appealing option for advanced gravitational wave detectors.

High power is not the only requirement for the laser system in Advanced Virgo.

There are also considerations on power and frequency noise performances, as well as beam pointing stability. It is therefore essential to gain knowledge and experience on fiber laser amplifiers from the viewpoint of interferometric gravitational wave detectors. Moreover, the power-scaling of a single-unit fiber laser amplifier may be challenging up to a certain limit. To overcome such limit, a straightforward workaround is the coherent combination of multiple fiber laser amplifiers. The objective of this thesis work is therefore to study the feasibility of the fiber laser amplifier technology and the coherent beam combination technique in the field of gravitational wave detection.

In Chapter 2, a brief review on related technologies in the field as well as a summary of the Advanced Virgo requirements are given. Chapter 3 is dedicated to a general coverage of laser characterization techniques. Then, based on the defined requirements and the developed characterization means, the test results of master oscillator fiber power amplifiers are given in Chapter 4, and those of their coherent combination in Chapter 5. Last, some conclusions and perspectives are given in Chapter 6.



Figure 1.6: Virgo interferometer aerial view. From: *Advanced Virgo — Listening to the cosmic whisper* <<http://public.virgo-gw.eu>>, in: *Galleries, Instruments, Observatory*.

Chapter 2

Pre-Stabilized Laser System for Interferometric Gravitational Wave Detectors

The passage of gravitational waves induces differential strain between the two arms of a Michelson interferometer and results in the change of fringe state at the output port. In principle, a perfectly symmetric Michelson interferometer with its output port locked to the dark fringe of the lowest order is virtually insensitive to frequency or phase departures of the light at its input port. The dark state of the interference fringe is also insensitive to power fluctuations at the input port. Any fringe deviation from the dark state could then be rendered as gravitational wave detection. This is the simplified picture of the detection principle of laser interferometers seeking gravitational waves. In practice, more delicate signal readout techniques are required to improve the responsivity to gravitational waves from quadratic to linear [34], and interferometric gravitational wave detectors are often asymmetric, both by design and due to imperfections by construction. The stability of the laser source is accordingly important in terms of power noise, frequency noise and beam pointing stability, as they couple to the readout of the gravitational wave strain signal.

It is then not surprising that advanced laser interferometric gravitational wave detectors [29, 35, 36] require ultra-stable laser sources given the mere strain magnitude at the order of $10^{-23} \sqrt{\text{Hz}}^{-1}$ of these latent waves (Figure 1.3).

Meanwhile, the quantum nature of light results in one fundamental limit in interferometric measurements, namely the shot noise. The co-existence of the shot noise and the radiation pressure noise defines the standard quantum limit of interferometric measurements [30, 37, 38].

Shot noise limits the strain sensitivity of the interferometer at high frequencies. Although it has been shown that the injection of squeezed light can lead to an increase as high as 3.7 dB in detector sensitivity [39], increasing the optical power in the interferometer is nevertheless an effective manner to overcome the limitations coming from the shot noise.

Figure 2.1 is a simplified optical layout of the Advanced Virgo gravitational wave detector, where the optical power inside the interferometer will be boosted by higher laser power and higher power recycling [40, 41].

When the output port of the Michelson interferometer is kept at a dark fringe, by energy conservation, the optical power is reflected back to the input port, and the interferometer acts like a mirror. By introducing the power-recycling mirror (PRM), we build a power-recycling cavity in which the intra-cavity optical power is significantly increased.

Like in all optical cavities, the higher the gain the finer the linewidth, which infers reduced detection bandwidth. The power recycling technique has a trade-off between optical power gain and the detection bandwidth.¹ Moreover, the power recycling gain is bounded by losses in the power recycling cavity, as well as other signal extraction considerations [44].

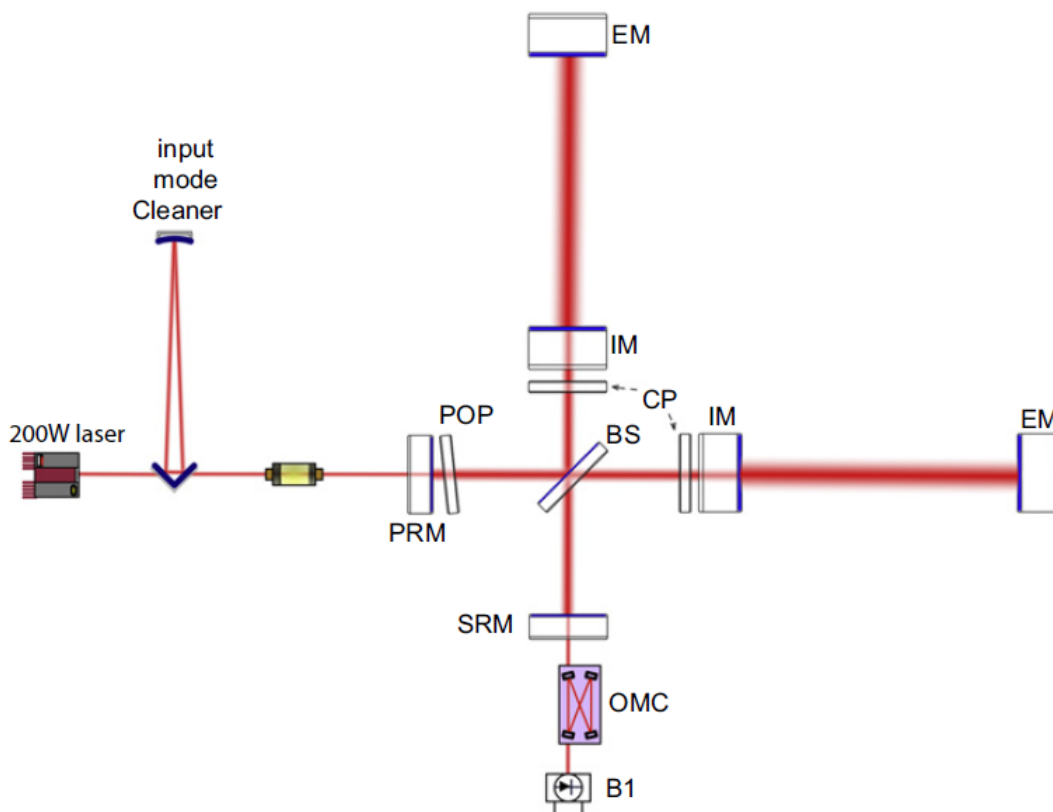


Figure 2.1: Advanced Virgo Schematic Optical Layout. PRM: power recycling mirror; POP: pickoff plate; BS: beam splitter; CP: compensation plate; IM: input mirror; EM: end mirror; SRM: signal recycling mirror; OMC: output mode cleaner; B1: photo-detection in transmission of the OMC. From [29].

In order to reach the design differential strain sensitivity, the laser source for Advanced Virgo is expected to deliver 175 W single-frequency optical power in TEM_{00} transverse mode. Studies on laser noise coupling to interferometer asymmetries require that the relative power noise of the laser beam at the input of the interfer-

¹For example, the *Quantum noise* curve in Figure 1.5 is shaped by radiation pressure noise at low frequencies, while at higher frequencies, it is shaped by the shot noise (which is white) and the transfer function of the Fabry–Perot arm cavities [42]. Likewise, the lump at intermediate frequencies is due to the signal recycling cavity [43].

ometer be as low as $2.35 \times 10^{-9} \sqrt{\text{Hz}}^{-1}$ (at 30 Hz) and the frequency noise be as low as $4.00 \times 10^{-7} \text{ Hz } \sqrt{\text{Hz}}^{-1}$ (at 55 Hz) [45].

This Chapter describes conceptually how an ultra-stable high-power single-frequency laser system may be achieved with available techniques and technologies. More general coverage related to this subject may be found in [46, 47].

2.1 Ultra Stable Laser Source: Non-Planar Ring Oscillator

Since its first appearance in 1985, the monolithic non-planar ring oscillator (NPRO) [48] has established its prominent role as an ultra-stable single-frequency laser source, and a key element for interferometric GWDs (all operational laser interferometric GWDs to date use the NPRO laser).

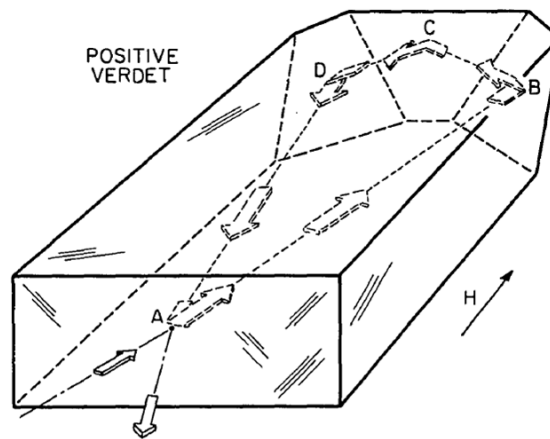


Fig. 1. The MISER laser design. Polarization selection takes place at the curved, partially transmitting face (point A). At points B, C, and D, total internal reflection occurs. A magnetic field H is applied to establish unidirectional oscillation. Magnetic rotation takes place along segments AB and DA . The focused pump laser beam enters the crystal at point A, and the output beam emerges at the same point.

Figure 2.2: The NPRO (originally known as MISER, monolithic isolated single-mode end-pumped ring) laser. From [48].

Figures 2.3 and 2.4 show typical power and frequency noise performances of the NPRO laser excerpted from [49], in which 8 commercially available NPRO lasers² were thoroughly characterized.

More recent developments have led to other ultra-stable single-frequency laser designs, notably the planar-waveguide external cavity diode laser (PW-ECL, Figure 2.5) [50] which has a noise performance comparable to the NPRO laser, but the NPRO laser is still unmatched when both the attainable output power and good noise performance are considered. The power noise (Figure 2.6) and frequency noise (Figure 2.7) of some single-frequency laser sources can be found in [51].

²Innolight (now Coherent), Mephisto 2000 NE LIGO

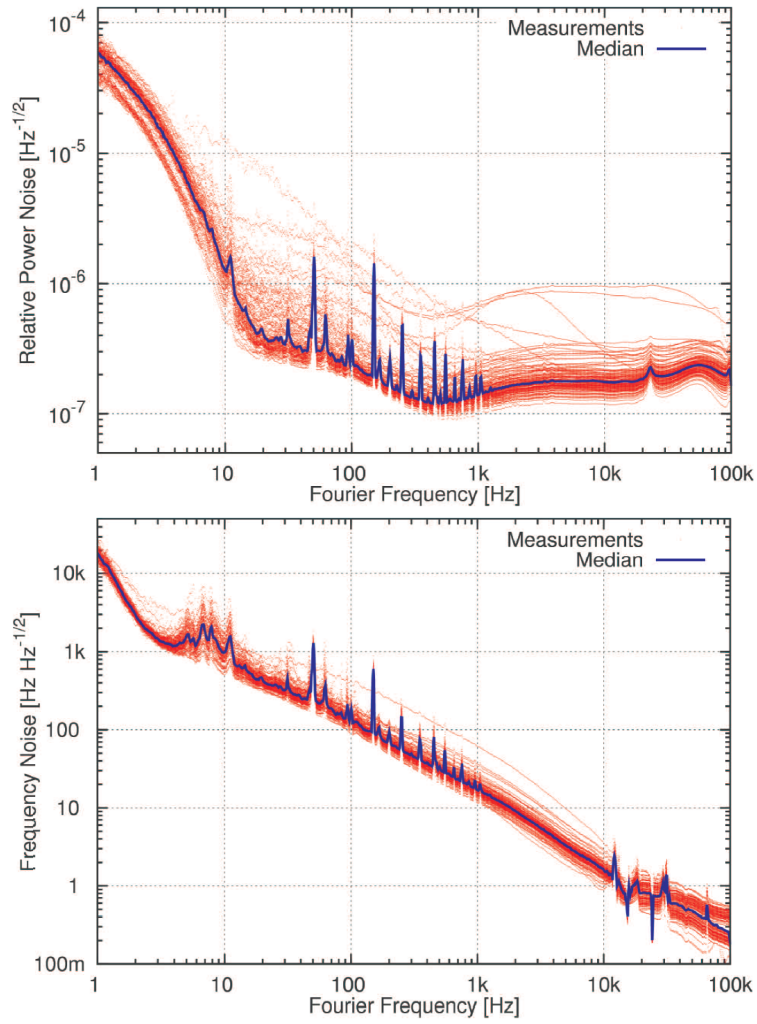


Figure 2.3: Typical power noise and frequency noise of the NPRO laser. From [49].

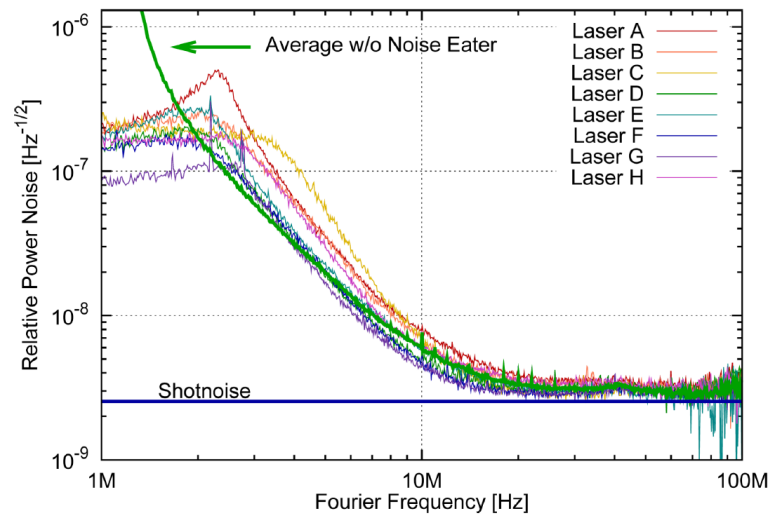


Figure 2.4: Power noise of the NPRO laser at high frequencies. From [49].

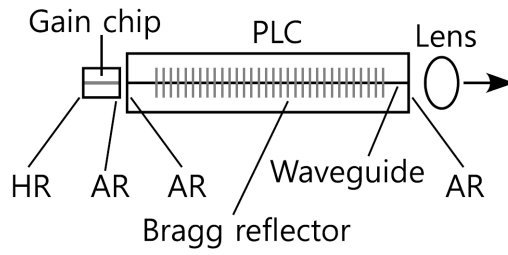


Figure 2.5: Schematic of the PW-ECL. HR: high reflection coating; AR: anti reflection coating; PLC: silica-on-silicon planar lightwave circuit. From [50].

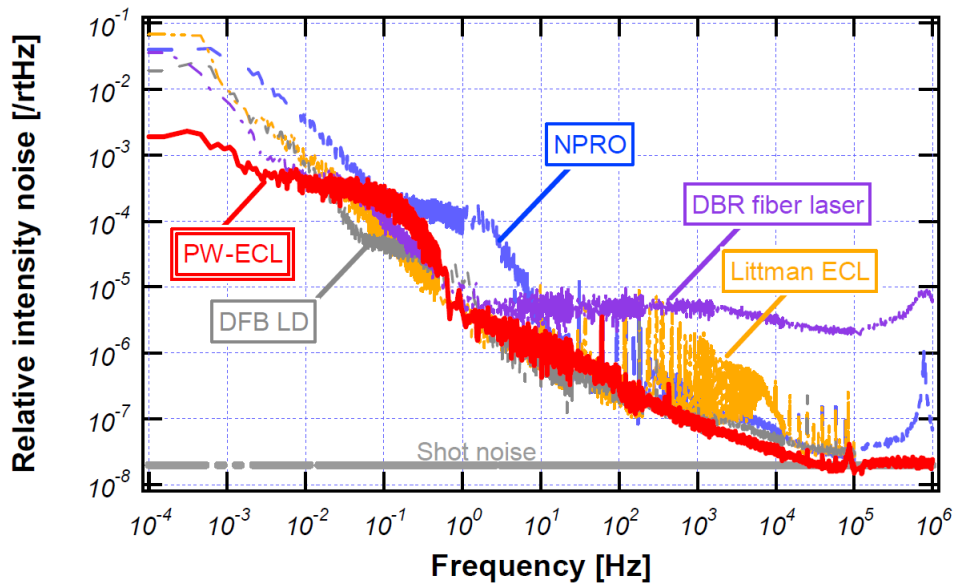


Figure 2.6: Power noise of various single-frequency laser sources. From [51].

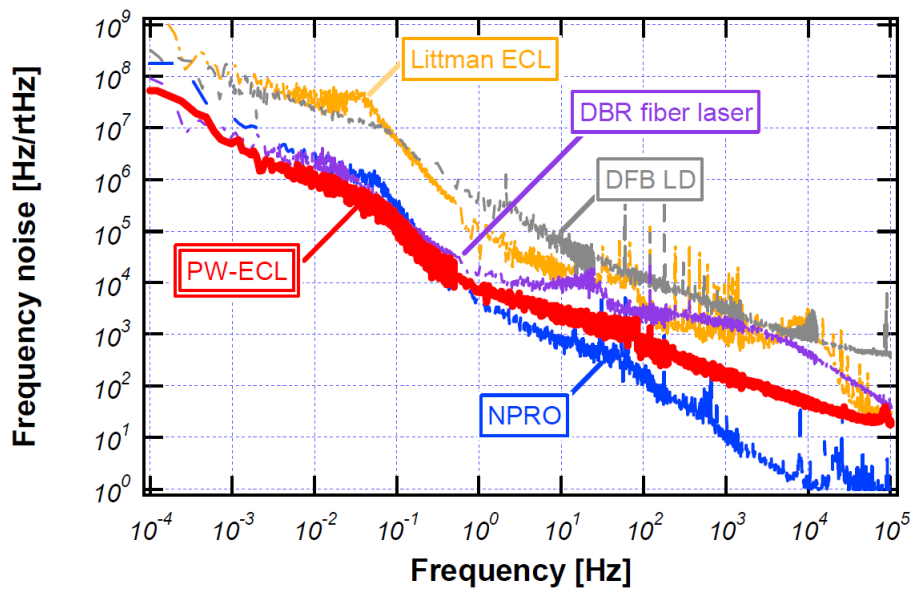


Figure 2.7: Frequency noise of various single-frequency laser sources. From [51].

Despite its exceptional stability, the NPRO still faces output power limits (up to few watts) due to thermo-optical effects as strong thermal-lensing associated with high pump power makes it difficult to maintain mode-selective pumping [52–54]. To reach higher laser power while maintaining low-noise performance for gravitational wave detection, further power-scaling is necessary.

2.2 Low-Noise High-Power Laser System

There are two major techniques in the power-scaling of a stable laser source: injection locking and master oscillator power amplifier. This Section discusses the respective advantages and disadvantages of these two techniques.

Injection-Locked Laser Oscillator

In high-power laser oscillators, it is often difficult, if not impossible, to achieve low-noise single-frequency operation because of issues related to high intra-cavity power. Injection locking [55, 56], is a technique known to synchronize, or *lock*, a slave laser oscillator to a master laser oscillator.

In laser interferometric GWDs, slave laser oscillators with desired output power and injection-locked to NPRO lasers have been used, for example, in Virgo, GEO 600 [57–59], Advanced LIGO [31] and KAGRA [60].

The required condition for injection locking is described by the Adler equation³

$$\Delta\nu < \Delta\nu_L = \Delta\nu_c \cdot \sqrt{\frac{P_m}{P_s}} \quad (2.1)$$

where $\Delta\nu$ is the frequency difference between the master and the slave laser oscillators, and $\Delta\nu_L$ is the locking range defined by $\Delta\nu_c$, the linewidth of the slave laser cavity, P_m , the power of the master laser, and P_s , the power of the slave laser oscillator [57]. Assuming a slave laser oscillator with 1 MHz cavity linewidth, 20 W output power, and seeded by a 500 mW master laser, the locking range is ~ 160 kHz. Since common laboratory environmental fluctuations can easily exceed such range and interrupt injection locking, active control electronics are necessary to maintain the frequency difference between the master and the slave laser oscillators within the locking range. There are many techniques for laser frequency stabilization, among which some will be briefly discussed in Section 3.6.

Injection-locked laser oscillator has its advantage in better noise performance due to the noise filtering properties of an optical cavity, but suffers from thermal issues due to high intra-cavity power.

Master Oscillator Power Amplifier

Master oscillator power amplifier (MOPA) is another configuration for low-noise laser power amplification in which a laser amplifier is used in the high-power stage

³“The Adler equation, with its various analytic solutions, comes from a classic paper by R. Adler, A study of locking phenomena in oscillators, Proc. IRE 34, 351–357 (1946), reprinted in Proc. IEEE 61, 1380 (October 1973) [56].”

instead of a laser oscillator. Consequently, MOPA possesses neither the inherent noise-filtering nor the power build-up properties associated with an optical cavity. The former signifies noise considerations, while the latter facilitates thermal management.

Commercially available single-frequency MOPA offers output power up to 55 W⁴. In Virgo, a laser amplifier with output power up to 65 W [61] was used during an intermediate operation phase known as Virgo+ [62].

2.3 Single-Frequency Fiber Laser Amplifiers

On top of the MOPA architecture, fiber laser amplifiers serve many interests for high-power applications [33]. Unlike their bulk solid-state counterparts that often require special geometrical designs [63, 64] and/or cryostats [65] to maintain good beam quality at high power levels, the intrinsically high surface-to-volume ratio of optical fibers further facilitates thermal management, while their wave-guiding property ensures good beam quality.

The active medium in fiber-optic laser amplifiers consists of silica glass doped with rare earth elements. For high-power applications at around 1 μm wavelength, ytterbium (Yb) is generally considered for its high wavelength conversion efficiency and its high permissible doping concentration. The former, together with the invention of double-cladding fibers [66, 67], and the advance of output power and brightness of diode laser pump sources and combiners, enables highly efficient operation and thus minimizes thermal impacts. The latter gives way to high gain per unit length, minimizes fiber length and consequently avoids undesired nonlinear effects.

With higher and higher demonstrated output power [54, 68–71], the master oscillator fiber power amplifier (MOFPA) architecture has become a viable, if not attractive, option for interferometric GWDs. There are, however, certain challenges that have to be handled with care to exploit the advantages of fiber laser amplifiers.

Stimulated Brillouin Scattering

The strong confinement of light in optical fibers leads to high optical intensity which appeals many studies and applications based on nonlinear optics [72], while in some applications such characteristics might just be undesirable.

Stimulated Brillouin scattering (SBS) [73, 74] is a nonlinear effect limiting the optical power that can be injected into a single-mode fiber [75–78]. A widely used approximate expression [74] for the SBS threshold of a fiber with length L is

$$P_{\text{threshold}} \approx 21 \cdot \frac{A_{\text{eff}}}{g_B \cdot L_{\text{eff}}}, \quad (2.2)$$

where A_{eff} is the effective area, g_B is the peak Brillouin gain for the dominant acoustic mode, and L_{eff} is the effective length of the fiber taking into account the

⁴Coherent, Mephisto MOPA, <https://www.coherent.com/products/?2067/Mephisto-MOPA>

optical loss α of the fiber given by

$$L_{eff} = \frac{1 - e^{-\alpha L}}{\alpha} \approx L \text{ for } \alpha L \ll 1. \quad (2.3)$$

The peak Brillouin gain g_B is almost independent of laser wavelength, and is in the range of $3 \times 10^{-11} \text{ m W}^{-1}$ to $5 \times 10^{-11} \text{ m W}^{-1}$ for typical silica fibers [74]. With a typical polarization-maintaining single-mode fiber for 1064 nm wavelength, the mode field diameter (MFD) is merely $7.2 \mu\text{m}^5$ and corresponds to a mode area of $4.07 \times 10^{-11} \text{ m}^2$. Since the fibers we use have rather short length ($L < 20 \text{ m}$) and low loss ($< 2.5 \text{ dB km}^{-1}$, i.e., $\alpha < 5.76 \times 10^{-4} \text{ m}^{-1}$), we approximate L_{eff} by L and obtain the SBS threshold as

$$P_{threshold} \approx 21 \cdot \frac{4.07 \times 10^{-11} \text{ m}^2}{5 \times 10^{-11} \text{ m W}^{-1} \cdot L} \simeq \frac{17 \text{ W}}{L(\text{m})}. \quad (2.4)$$

This infers that in order to sustain optical power of the order of 100 W, the fiber length must not exceed 0.17 m, which then loses largely the geometrical character of an optical fiber. To overcome the power limitation imposed by SBS in the single-frequency operation of fiber amplifiers, we have to reduce either the optical intensity or the Brillouin gain.

Large Mode Area Fibers

To achieve a target optical power level, the optical intensity may be reduced by using large mode area (LMA) fibers. A weakly guiding step-index fiber guides only the fundamental linearly polarized mode LP_{01} when the normalized frequency parameter V fulfills the following condition [79, 80]:

$$V = \frac{2\pi}{\lambda} \cdot a \cdot \sqrt{n_{core}^2 - n_{cladding}^2} = \frac{2\pi}{\lambda} \cdot a \cdot \text{NA} < 2.405, \quad (2.5)$$

where λ is the wavelength, a is the radius of the fiber core, NA stands for numerical aperture, n_{core} is the refractive index of the fiber core and $n_{cladding}$ is the refractive index of the fiber cladding [79]. The mode field radius w may be approximated by Marcuse's equation [81]:

$$\frac{w}{a} \approx 0.65 + \frac{1.619}{V^{1.5}} + \frac{2.879}{V^6}. \quad (2.6)$$

At a given V , the mode field radius is approximately proportional to fiber core radius. Accordingly, increased fiber core radius leads to larger mode area, and requires that the refractive index difference between the core and the cladding be reduced to ensure single-mode operation. This is one straightforward design for LMA fibers. More sophisticated designs may consist of photonic crystal structures [82].

At 1064 nm wavelength, commercially available passive fibers offer MFD up to $20.9 \mu\text{m}$ for single-mode operation⁶ and up to $12.6 \mu\text{m}$ for polarization-maintaining operation⁷, and ytterbium-doped photonic crystal fiber with MFD of $\sim 43 \mu\text{m}$ has been reported [83].

⁵Thorlabs, [P3-1064PM-FC-X](#); Nufern, [PM980-XP](#).

⁶NKT Photonics, [LMA-25](#).

⁷NKT Photonics, [LMA-PM-15](#)

Suppression of Brillouin Gain

In terms of fiber design, to reduce Brillouin gain, one common technique is to broaden the Brillouin gain bandwidth with varying Brillouin frequency shifts along the fiber. This can be done by:

- Varying the core dimensions: a reduction of 3.5 dB in the effective Brillouin gain was reported [84].
- Varying the dopant concentrations: a 7 dB improvement in SBS threshold was reported [85].
- Applying sinusoidal strain: a broadening of Brillouin gain from 50 MHz to 400 MHz was observed [86]. With a 40-step stair-ramp tensile-strain distribution, an 8 dB increase in SBS threshold was reported [87]. More recently, by applying longitudinally varying strains according to the signal power evolution and the temperature distribution, a 7 times increase of the SBS threshold was achieved [88].
- Applying temperature gradient, an increase of 3 to 4 times in SBS threshold was obtained with a $\sim 150^\circ\text{C}$ temperature gradient [89, 90].

It is also known that the counter-propagation pumping configuration creates larger intrinsic thermal gradient and thus helps mitigate SBS [71, 91]. Counter-propagation is also more gain efficient and therefore requires shorter active fiber length. However, counter-propagation pumping also tends to increase the level of amplified stimulated emission (ASE) in the direction of the signal beam [92].

Another option lies in the fiber design where the overlapping between the optical mode and the acoustic mode is minimized [93]. For example, by adjusting the relative doping level between the co-dopants in the fiber core, 6 dB higher SBS threshold was observed [94].

The Brillouin gain may also be suppressed by broadening the linewidth of the input beam. This technique, however, is not suitable when narrow linewidth is desired at the output of the fiber amplifier. A feasible amendment to this technique to recover the narrow linewidth, is to use sideband modulation/demodulation techniques. A 50% increase in SBS threshold has been demonstrated [95]. The inconvenience with this technique is that it requires high-power electro-optic modulators.

Power Scaling of Single-Frequency Fiber Amplifiers

The first single-frequency MOFPA, seeded with an NPRO laser, delivering 5.5 W output power with M^2 value of ~ 1.1 , was reported in 1999 [68]. A 30 m double-clad neodymium-doped fiber supporting 4 to 5 higher-order modes was used in this demonstration. The MFD was $\sim 8.5\ \mu\text{m}$ and the maximum output power was limited by the onset of SBS. The preservation of the narrow linewidth of the NPRO laser by the fiber amplifier was demonstrated later in 2001 [69], and in 2003 a 100 W MOFPA with 1.1 M^2 value was reported [54], reaching the power level required for advanced laser interferometric GWDs.

To date, single-frequency MOFPAs delivering several hundreds of watts of output power have been reported by various groups [70, 71, 88, 96], and a physical limit of 2 kW is suggested taking into account the effects of SBS, thermal lensing and pump power, given arbitrary choices of MFD [97].

Transverse Mode Instability

One minor inconvenience of LMA fibers is that they are more prone to bending losses and therefore do not inherit the full flexibility of fibers, while the more difficult issue limiting the use of LMA fibers is the potential transverse mode instability at high power levels which significantly degrades beam quality and may lead to temporal fluctuations of the profile of the output beam [98].

Transverse mode instability is considered as the reason for the recent stagnation of the output power of fiber amplifiers [99]. The study of its origin, and eventually its mitigation, has attracted much attention in the community [98–102]. A commonly accepted origin of this phenomenon is the thermally induced change in the refractive index profile of the fiber [99, 102]. An intrinsic heat source is the quantum defect, while other heat sources may also play a role, among which photo-darkening has been strongly suggested in a recent experiment [99].

Photo-Darkening

Interferometric GWDs require laser sources that are not only high-power and low-noise, but also stable in the long run to ensure uninterrupted operation and maximize detection rate. Previous Virgo Science Runs lasted 3 to 5 months each.

Beside the aging of pumping laser diodes and the degradation of optics, which are the common factors determining the lifetime of laser systems, fiber amplifiers suffer an additional aging process known as photo-darkening. Photo-darkening is the photo-induced temporal increase in the transmission loss of the doped glass [103–105]. The increase in transmission loss is broadband, with higher rates at shorter wavelengths [104, 106].

The physical origin of photo-darkening is still under discussion but often attributed to the formation of color centers. The initial rate of photo-darkening has been shown to scale with the excited-state Yb population, and consequently depends strongly on the configuration of the fiber amplifier [107].

Amplified Stimulated Emission

Laser gain medium has finite lifetime in the excited state before it decays via spontaneous emission or non-radiative process. In a laser amplifier, spontaneously emitted photons are equally amplified as the signal photons, resulting in amplified spontaneous emission (ASE).

In principle, ASE is omni-directional and often negligible compared to the signal beam. In a fiber amplifier, however, owing to the waveguide structure, directional ASE can be an issue. The most direct impact is the increase in noise.

Moreover, Yb-doped fiber amplifiers are quasi-three-level laser systems, in which the lower laser energy level is not fully depleted in thermal equilibrium. Accordingly,

at a given gain, Yb-doped fiber amplifiers require high pumping to compensate for re-absorption and are often subject to ASE.

Pump Brightness and Signal/Pump Beam Combiner

As discussed in [33, 97], the brightness of the pumping laser diodes plays an important role in the increase of output power of fiber amplifiers. Tandem-pumping is often required, and may be realized with a fiber coupler such as a tapered fused fiber bundle [108] in an all-fiber setup. Fiber couplers have finite efficiency, and loss-induced heating can lead to destructive consequences. Associated with high power, the combiner for the signal beam and pumping beams also plays a key role in fiber amplifiers, especially when the counter-propagation pumping configuration is taken where the core of the tapered fused fiber bundle has to handle high power [71].

2.4 Coherent Beam Combination

As discussed in the previous section, the power-scaling of single-frequency fiber amplifiers has stagnated at the level of few hundreds of Watts, with an estimated physical limit of ~ 2 kW [97].

Further power-scaling can be done by extending the line of thought to the system level by combining multiple high-power fiber amplifiers. There have been numerous schemes proposed for laser beam combining [109], notably those focused on Yb-doped fiber amplifiers [110]. The single-frequency and single-mode requirements imposed by laser interferometric systems are concurrently favorable for coherent beam combination (CBC). For example, a recent report on the CBC of two 10 W single-frequency fiber amplifiers showed $> 95\%$ combining efficiency with 97% of the combined beam in TEM₀₀ mode, and observed no significant increase in noise due to CBC [111].

2.5 Laser Stabilization

To reach the required low noise level, laser stabilization techniques in terms of power [112] and frequency [113] are crucial in interferometric GWDs.

Power Stabilization

As discussed in the beginning of this chapter, Advanced Virgo requires that the relative power noise of the laser beam at the input of the interferometer be of the order of $10^{-9} \sqrt{\text{Hz}}^{-1}$ in the gravitational wave detection band between 10 Hz and 10 kHz, reaching $2.35 \times 10^{-9} \sqrt{\text{Hz}}^{-1}$ at 30 Hz.

Although in optics, or radiometry, strictly speaking, *power* and *intensity* are not equivalent, conventionally the term *relative intensity noise*, abbreviated as *RIN* and expressed in amplitude power spectral density (PSD), is used to describe the relative power noise of a laser system.

The main challenge in laser power stabilization to the order of $10^{-9} \sqrt{\text{Hz}}^{-1}$ lies in the measurement floor of photo-detection, or *RIN* detection. The classical limit is defined by three noise processes, thermal (Johnson) noise, shot noise and technical (flicker) noise. The first two are white noises, while the latter is often *pink*, whose power spectral density is inversely proportional to the Fourier frequency. Shot noise often appears to be the dominating limit after carefully handling the others, resulting in the so-called shot noise limit (SNL) *RIN* level, which, in terms of PSD, is:

$$RIN_{SNL} = \frac{\sigma_I}{I} = \sqrt{\frac{2 \cdot e}{I}} \cdot \sqrt{\Delta f} \quad (2.7)$$

in which

$$\sigma_I = \sqrt{2 \cdot e \cdot I \cdot \Delta f} \quad (2.8)$$

is the shot noise current associated with an average current I , the elementary charge $e \sim 1.602 \times 10^{-19} \text{ C}$ and the frequency bandwidth Δf . In general, *RIN* measurements are normalized with respect to 1 Hz bandwidth and bear the unit $\sqrt{\text{Hz}}^{-1}$.

To reach *RIN* level of $2.35 \times 10^{-9} \sqrt{\text{Hz}}^{-1}$, a photo-current of $\sim 58 \text{ mA}$ is needed. Very few commercially available photodiodes meet this requirement, and accordingly non-standard and optimized operating conditions, such as increased bias (to extend linearity range and to reduce capacitance), large beam/photodiode diameter and efficient heat sink, may be required.

There exists a non-classical *RIN* detection technique called optical AC coupling which surpasses the SNL [114]. Optical AC coupling exploits the spectral selectivity of Fabry–Perot cavities: the DC content is transmitted while the AC content is reflected. However, this technique is not only complicated and hardware costly, but also limited by the finite spectral resolution of optical cavities. Optical AC coupling can only be applied to *RIN* detection for Fourier frequencies higher than the spectral resolution of the optical cavity.

A more convenient alternative is to use photodiode arrays, as is foreseen for both Advanced LIGO [115] and Advanced Virgo [116].

Another important consideration of *RIN* detection lies in the coupling between the spatially inhomogeneous responsivity and/or the finite surface area of photodiodes, and the finite pointing stability of the laser beam. Last, apart from *RIN* detection, the actuator for *RIN* suppression should not be overlooked. These two aspects will be discussed with more details in Sections 3.3 and 4.7, respectively.

Frequency Stabilization

Laser frequency stabilization serves many interests in a broad range of applications. The general idea is to stabilize, or *lock*, the laser frequency, usually via an external electro-optic modulator owing to the need for fast actuation, with respect to an ultra-stable optical cavity.

The most commonly used technique in this subject is the Pound-Drever-Hall (PDH) locking [113, 117] scheme which uses modulation sidebands.

In Advanced Virgo, the laser frequency will be pre-stabilized with respect to the input mode-cleaner (IMC), followed by a second-stage frequency stabilization loop

that directly takes reference from the ~ 3 km long arm cavity in the Michelson interferometer and acts simultaneously on the IMC cavity length and the laser frequency [118, 119]. The Michelson interferometer will then be locked to the Reference Cavity [120] in the low frequency range to avoid unbounded drifts, as illustrated in Figure 2.15.

2.6 Optical Cavity as Mode Cleaner

In addition to active stabilization, optical cavities were also found useful as the so-called mode cleaners for their selectivity in terms of both longitudinal and transverse modes [121, 122]. Optical cavities can be approximated as first-order low-pass filters with amplitude transfer function

$$|H(s)| = \left| \frac{1}{1 + s/\omega_c} \right|, \quad (2.9)$$

where $\omega_c = 2\pi f_c$ denotes the angular cutoff frequency of the optical cavity, and $s = i\omega$ is the complex frequency in the Laplace s -domain of the signal beam. The cutoff frequency f_c is half the spectral resolution⁸ of an optical cavity. This means that noises whose frequencies lie outside the spectral resolution of an optical cavity will be attenuated.

The exact transmission T vs. frequency departure of an ideal Fabry–Perot cavity may be derived as [124]:

$$T(\Delta\nu) = \left[1 + \frac{4\mathcal{F}^2}{\pi^2} \cdot \sin^2 \left(\pi \cdot \frac{\Delta\nu}{\nu_0} \right) \right]^{-\frac{1}{2}}, \quad (2.10)$$

where $\Delta\nu$ is the frequency departure from optical cavity resonance, ν_0 is the the free spectral range (FSR), and \mathcal{F} is the finesse of the optical cavity.

A ring cavity design is favored to avoid optical feedback and hence the need for optical isolation. In an optical cavity, in general the TEM_{mn} ⁹ modes with the same order $m+n$ are degenerate, meaning that they have the same cavity resonance frequency. The ring geometry breaks the axial symmetry of the circulating beam, and if the number of the reflections in the cavity is odd, non-degeneracies will be observed between transverse modes that are symmetric with respect to the normal vector, of the plane of, and which intersects the axis of, the circulating beam, and those which are not. This may be explained by the geometrical mirroring of the electric field upon mirror reflection. For each reflection a phase difference of π occurs between these two sets of transverse modes defined by symmetry.

⁸Throughout the context of the thesis the terms *spectral resolution* and *cavity linewidth* are used interchangeably and arbitrarily to refer to the *full-width at half-maximum* (FWHM), the *half-intensity* width, or *half-width* [123] of the interference fringes in a Fabry–Perot cavity. We note that in contrary to the width definition of a Gaussian beam, which is at $1/e^2$ intensity, the cavity *spectral resolution* or linewidth is defined at the half maximum, or the 3 dB width, which complies with the conventions in electronics, as illustrated in Figure 2.9.

⁹Unless otherwise mentioned, throughout the text of the thesis TEM_{mn} refers to Hermite–Gaussian transverse modes.

In the case of a triangular cavity with a horizontal beam propagation plane, the frequency departure of higher-order TEM_{mn} modes from the fundamental TEM₀₀ mode can be generalized as [124]:

$$\Delta\nu_{mn} = \frac{\nu_0}{\pi} (m + n) \cos^{-1}(\sqrt{g}) + \frac{\nu_0}{2} \cdot \frac{1 - (-1)^m}{2}, \quad (2.11)$$

where g accounts for the geometry of the triangular cavity. In the case of the Virgo PMC for which the cavity round-trip length is $2L$, input/output mirrors are flat and the end mirror has a radius of curvature (RoC) of R , the corresponding g is:

$$g = 1 - \frac{L}{R}. \quad (2.12)$$

When the optical cavity is locked to resonant with the fundamental TEM₀₀ mode, the higher-order transverse modes whose electric field amplitudes (Figure 2.8) are asymmetric in the above-mentioned manner (i.e., whose m is odd) will experience an additional phase of π , and therefore an additional frequency departure of one-half the free spectral range (Figure 2.9). Another way of thinking is that these modes will have to circulate another cavity round-trip to make up the 2π modulus, thus halving their free spectral range.

Taking into account the stability criterion ($0 \leq g \leq 1$) of an optical cavity, a triangular cavity provides the additional degree of freedom on introducing a large frequency departure, and hence large attenuation, to the first higher-order modes, either TEM₀₁ or TEM₁₀, without exotic optical cavity configurations.

Figure 2.9 shows the cavity transmission vs. frequency, first-order filter approximation, and the frequency departures of higher-order modes with a triangular cavity.

2.7 Pre-Stabilized Laser for Advanced Virgo: Specifications and a Conceptual Design

In Advanced Virgo, the high-power laser beam passes through the injection subsystem, where the laser beam is modulated, isolated, steered and analyzed, before being sent to the interferometer. Figure 2.10 is a schematic diagram of the injection subsystem in Advanced Virgo [125]. Requirements related to the pre-stabilized laser system are therefore discussed at two levels, at the output of the pre-stabilized laser system, and at the input of the interferometer.

In addition to the noise requirements coming from the asymmetry in the Michelson interferometer [45, 127], for sensing, control and readout purposes, a few modulation sidebands at radio frequencies are introduced in the injection subsystem, as shown in Figure 2.11. The noise requirements of these sidebands [45, 128] are also to be respected by the pre-stabilized laser system.

Advanced Virgo Input Mode Cleaner

The Advanced Virgo Input Mode Cleaner (IMC) has a mode waist radius of 5.17 mm, a finesse of 1200 and a half round trip length of 143.424 m [125]. Accordingly,

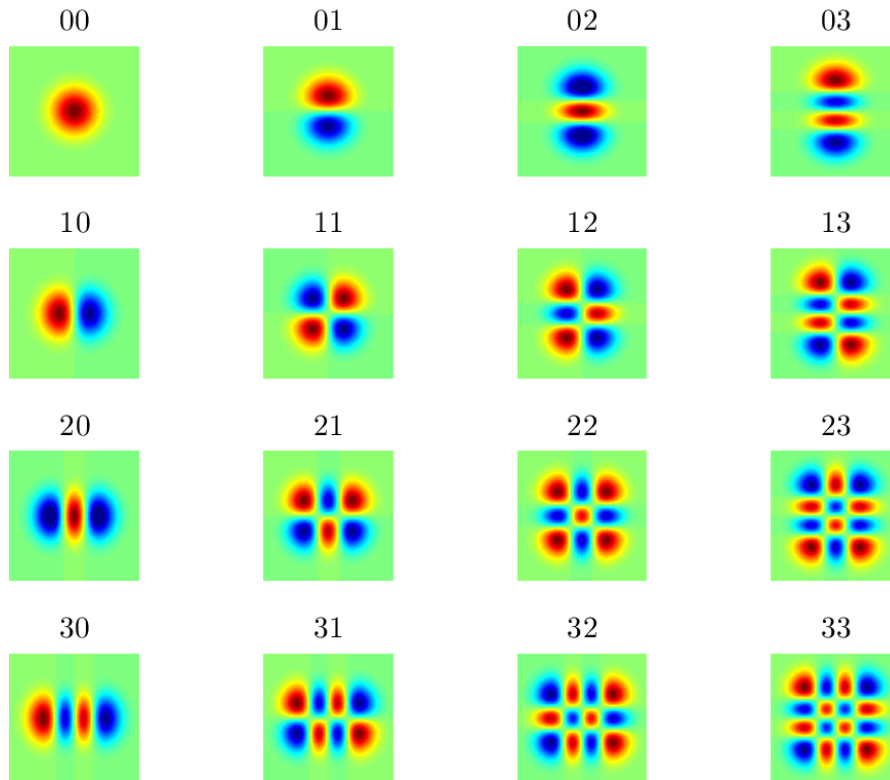


Figure 2.8: The electric field amplitudes of TEM modes. False color: red and blue are the maxima with opposite signs, and light green is the zero.

the IMC has a free-spectral range (FSR) of ~ 1.045 MHz, a spectral resolution of ~ 871 Hz and hence a low-pass filtering pole at ~ 436 Hz.

Laser Specifications at Interferometer Input

At the input of the Advanced Virgo interferometer, the laser specifications are given as following.

- Optical Power: > 125 W in TEM₀₀ [26].
- Power Noise:
 - $< 2.35 \times 10^{-9} \sqrt{\text{Hz}}^{-1}$ at 30 Hz; see Figure 2.12 for 10 Hz to 6 kHz [45, 127].
 - $< 8 \times 10^{-9} \sqrt{\text{Hz}}^{-1}$ at 6.27 MHz [128].
 - $< 1.5 \times 10^{-8} \sqrt{\text{Hz}}^{-1}$ at 56.44 MHz [128].
 - The requirements from [45] at 6.27 MHz, 8.36 MHz and 56.44 MHz are relatively less stringent and therefore omitted, as well as those for 22.38 MHz and 131.69 MHz [125].
- Frequency Noise:

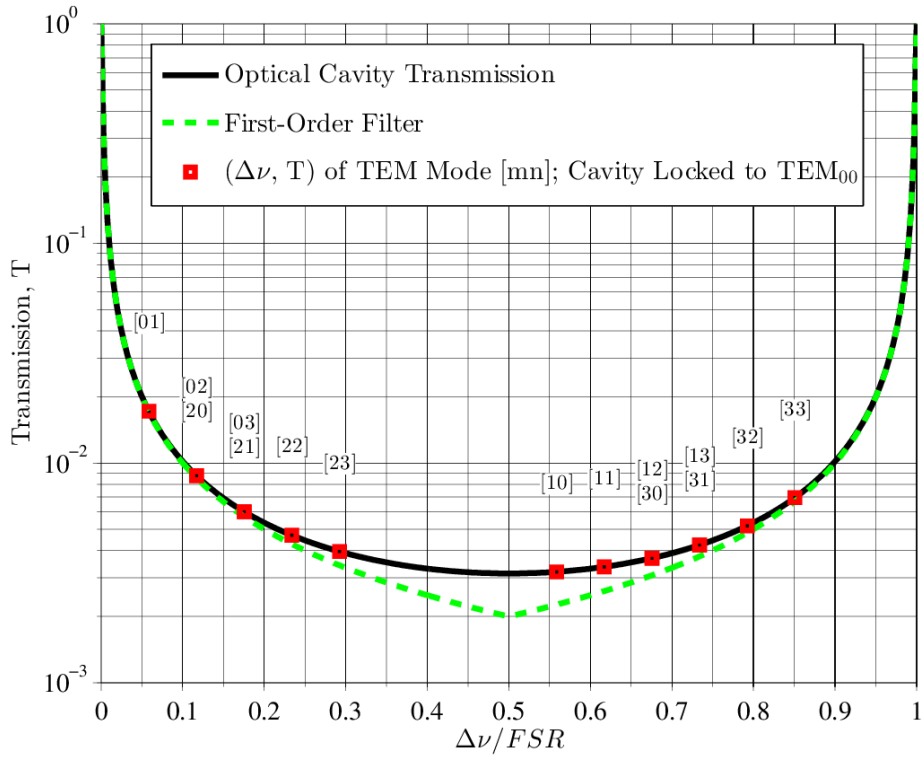


Figure 2.9: Cavity transmission vs. frequency, first-order low-pass filter approximation, and the frequency departures of higher-order modes with a triangular cavity consisted of two flat mirror plates and one curved R-max mirror. FSR: Free spectral range. Cavity round-trip length: 0.28 m, mirror radius of curvature: 4.2 m; finesse: 500. (Parameters of the actual pre mode cleaner of Virgo.)

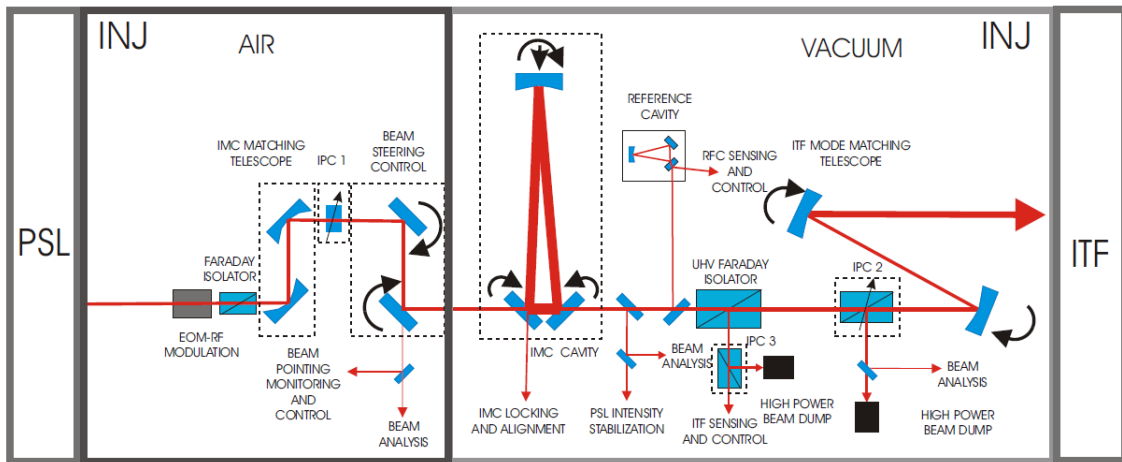


Figure 2.10: The Advanced Virgo injection (INJ) subsystem. PSL: pre-stabilized laser subsystem; ITF: Michelson interferometer; EOM: electro-optic modulator; RF: radio frequency; IMC: input mode cleaner; IPC: input power control; RFC: reference cavity; UHV: ultra-high vacuum. From [125].

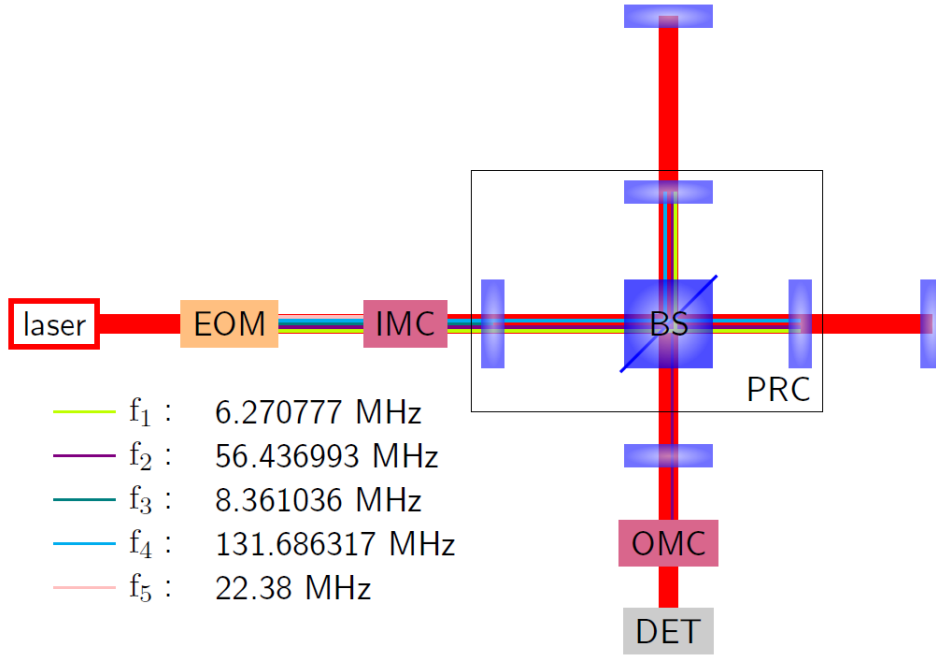


Figure 2.11: Advanced Virgo modulation sidebands overview. BS: beam-splitter; PRC: power-recycling cavity; DET: Advanced Virgo detection subsystem. From [126]. Note that the frequencies f_1 , f_2 , f_3 , f_4 are set to be resonant with the IMC, and are therefore integer multiples of the FSR of the IMC.

- $< 4.00 \times 10^{-7} \text{ Hz } \sqrt{\text{Hz}}^{-1}$ at 55 Hz; see Figure 2.13 for 10 Hz to 6 kHz [45, 127].
 - $< 1 \text{ Hz rms}$ [125].
 - The requirements from [45] at 6.27 MHz, 8.36 MHz and 56.44 MHz are relatively less stringent and therefore omitted, as well as those for 22.38 MHz and 131.69 MHz [125].
- Beam Pointing Stability: $< 10^{-12} \text{ rad } \sqrt{\text{Hz}}^{-1}$ ($f > 10 \text{ Hz}$) [125].

Laser Specifications at PSL/INJ Interface

There are also specifications given at the interface between the pre-stabilized laser subsystem and the injection subsystem.

- Optical Power: $> 175 \text{ W}$ in TEM_{00} [125].
- Beam Pointing Stability: See Figure 2.14 for 10 Hz to 10 kHz [129]. The specifications shown here are defined with respect to the parameters of the Pre Mode Cleaner (PMC), which has a mode waist radius ω_0 of $500 \mu\text{m}$ and correspondingly a half divergence angle θ of $677 \mu\text{rad}$. It should be noted that due to the interchangeability of angular and lateral beam pointing stability (cf. Section 3.8), the 4 specifications curves may be reduced to 2 via quadratic sum, as is shown in Figure 2.19.

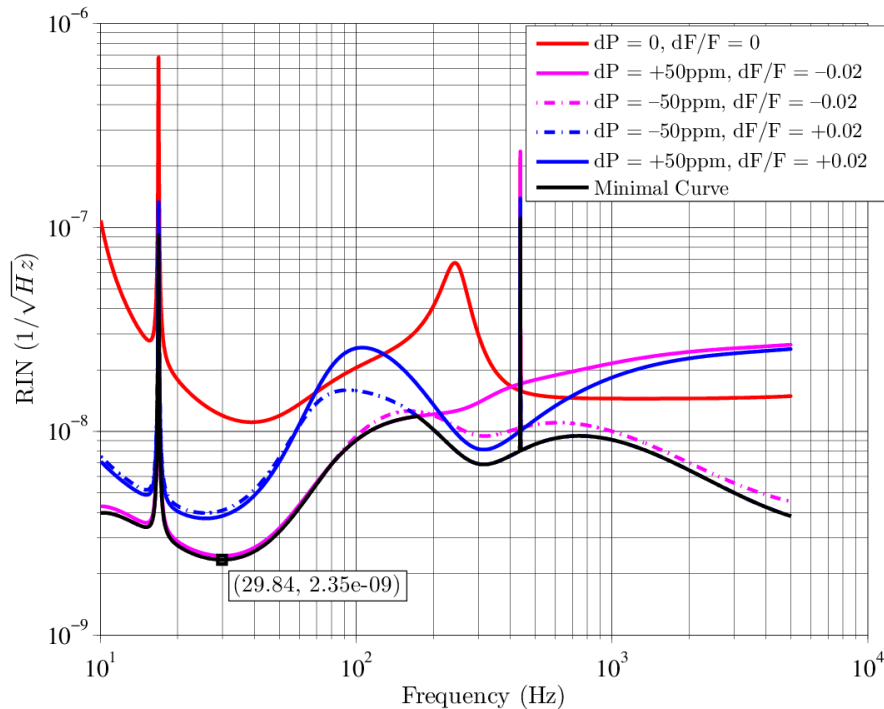


Figure 2.12: Advanced Virgo reference specifications on the power noise in the gravitational wave detection band [45, 127]. dP: loss difference between the two arms of the interferometer (assuming 75 ppm average loss); dF: Finesse difference between the two arms of the interferometer (assuming 450 average Finesse, F).

A Conceptual Design of the Advanced Virgo PSL subsystem

Taking into account the various considerations, Figure 2.15 shows a conceptual reference design of the PSL subsystem for Advanced Virgo and its relation with the interferometer. In this reference design, two fiber amplifiers seeded by the NPRO laser are coherently combined using the phase-dithering technique with the EOM 2, and filtered by the PMC before being sent to the injection subsystem (Figure 2.10). For laser power stabilization, a high-power photodiode array [116] after the IMC is used for feedback control. In terms of laser frequency stabilization, the EOM 1 following the NPRO ensures fast actuation. Sequentially [118, 119],

- The PMC is locked with respect to the NPRO laser.
- Then, the NPRO laser is locked onto the IMC.
- Finally, the IMC and the NPRO laser are simultaneously locked onto the Michelson interferometer, which is the best frequency reference available, since noise motions at the end mirror level are absolute and factored out by the long baseline such that the resulting relative noise is minimized.
- To avoid unbounded slow drifts, which may complicate the lock acquisition and/or exceed the actuation range of the output mode cleaner (OMC, Figure 2.1) as well as other actuators, the interferometer is servoed to the RFC [120] with a very low bandwidth.

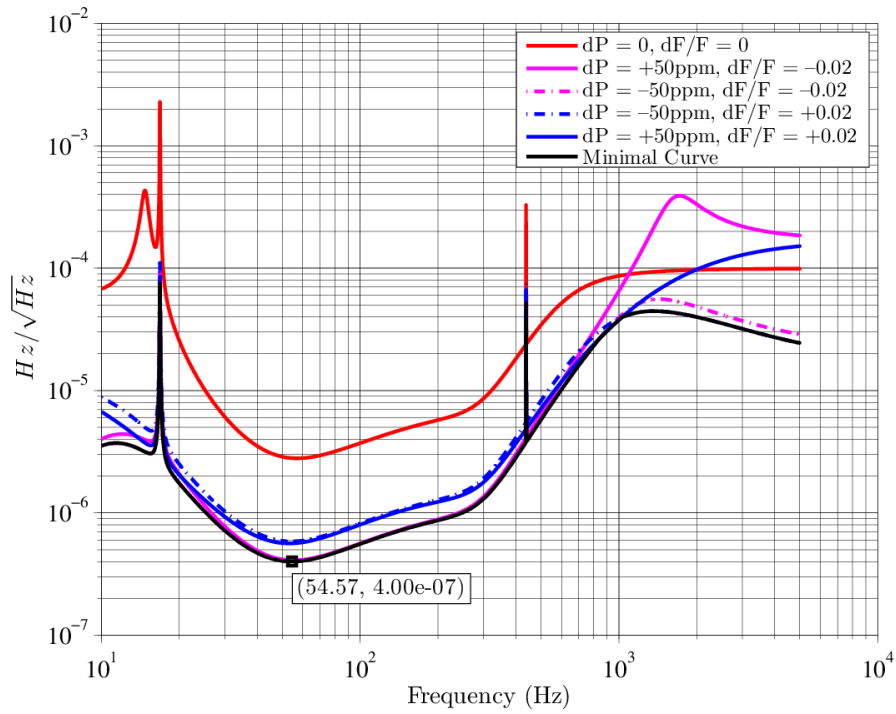


Figure 2.13: Advanced Virgo reference specifications on the frequency noise in the gravitational wave detection band [45, 127]. dP: loss difference between the two arms of the interferometer (assuming 75 ppm average loss); dF: Finesse difference between the two arms of the interferometer (assuming 450 average Finesse, F).

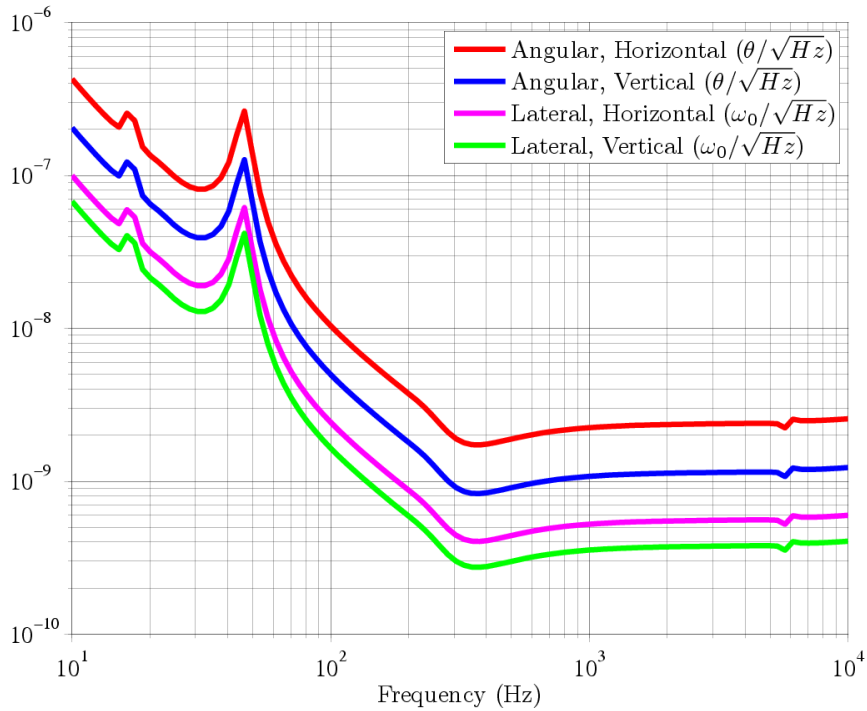
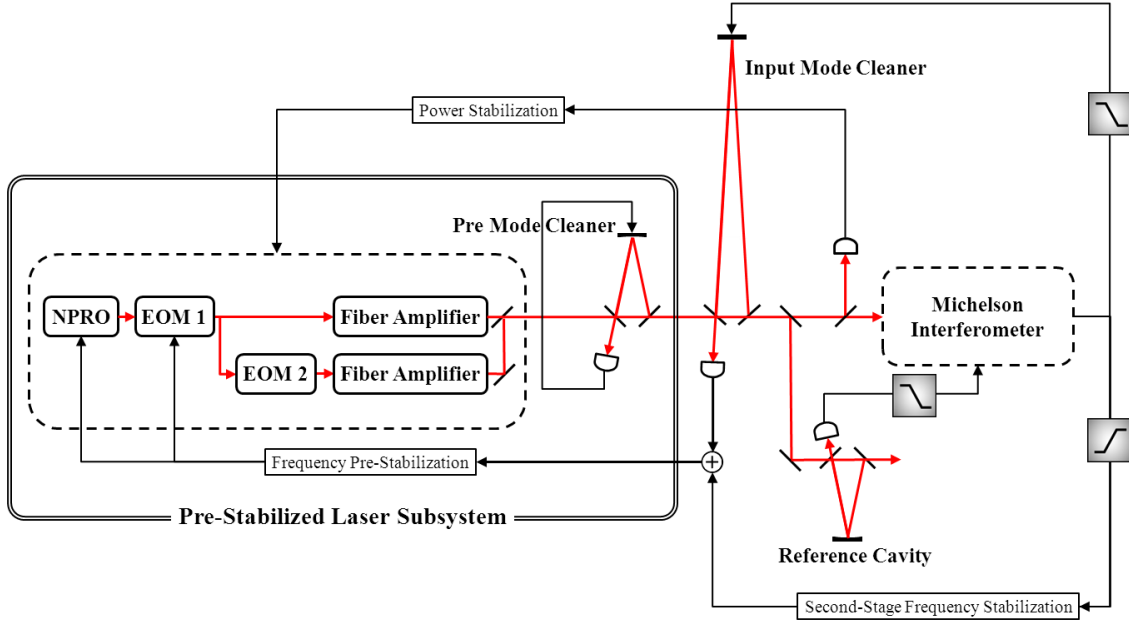


Figure 2.14: Advanced Virgo reference specifications on beam pointing stability in the gravitational wave detection band at PSL output [129].



NPRO: Non-Planar Ring Oscillator EOM: Electro-Optic Modulator

Figure 2.15: A conceptual design of the Advanced Virgo PSL subsystem [129].

Advanced Virgo Pre Mode Cleaner

Advanced Virgo foresees to re-use the design of the Virgo PMC, a triangular cavity with design parameters shown in Figure 2.16. Figure 2.9 is plotted according to these parameters.

The Virgo PMC has been tested up to 65 W [130]. Although further studies are required to verify the compatibility with higher power, the noise attenuation performances of the Virgo PMC, placed horizontally, are taken for reference [129]:

- TEM_{10} transmission: 0.0032 [129].
- TEM_{01} transmission: 0.017 [129].
- Noise transmission (Equation 2.10 with $FSR = 1.07$ GHz):
 - 0.168 at 6.27 MHz.
 - 0.0191 at 56.44 MHz.

Mode waist	Mode divergence	Finesse	Length	End mirror curvature	Triangular cavity	Pole Pole
500 μm	675 μrad	500	0.14 m	4.2 m		1.07 MHz

Figure 2.16: Virgo PMC design parameters. From [129]. We note that the free spectral range (FSR) is 1.07 GHz.

Advanced Virgo Laser Stabilization

The reference open-loop transfer function (OLTF) (cf. Section 3.12) of the laser power stabilization loop [131] is shown as curve © in Figure 2.17, and that of the laser frequency stabilization loop [118, 119] is shown as curve Ⓓ in Figure 2.18. The PMC and the IMC also contribute to noise attenuation.

Free-Running Laser Specifications of Advanced Virgo

Finally, with the conceptual reference design shown in Figure 2.15, taking into account the performance of the laser stabilization loops and the mode cleaners, we define the free-running laser specifications for Advanced Virgo.

Defining the specifications of the laser system while free-running, i.e., without active stabilization nor passive noise filtering of optical cavities, is essential because we are not always able to perform full-scale experiments with the whole Michelson interferometer setup of the gravitational wave detector.

Readily, by comparing these free-running laser specifications to Figures 2.3, 2.4, 2.6 and 2.7, it is clear why the NPRO laser has always been used to light up the interferometric GWDs. Also, following the advance of related technologies, the migration to fiber oriented laser sources has appeared to be an option.

- Optical Power: ~ 200 W, considering the loss of the PMC.
- Power Noise: See Figure 2.17. We note that at high frequencies, a curve is drawn with respect to the specifications at 6.27 MHz for reference. The specifications are in power spectral density (PSD) with the unit $\sqrt{\text{Hz}}^{-1}$.
- Frequency Noise: See Figure 2.18. The specifications are in power spectral density (PSD) with the unit $\text{Hz} \sqrt{\text{Hz}}^{-1}$.
- Beam Pointing Stability: See Figure 2.19. We note that the specifications here are simply the curves shown in Figure 2.14 multiplied by the attenuation factor of the PMC. The quadratic sum of the curves in the horizontal and the vertical planes are shown for reference following the invariance discussed in Section 3.8.

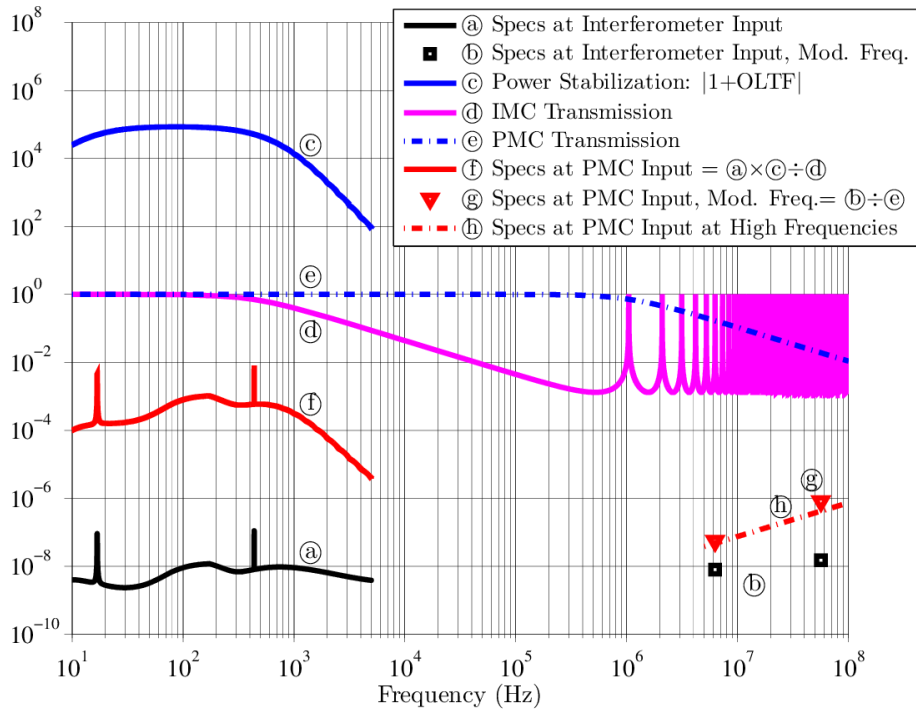


Figure 2.17: Free-running laser power noise specifications for Advanced Virgo. The specifications are in power spectral density (PSD) with the unit $\sqrt{\text{Hz}}^{-1}$.

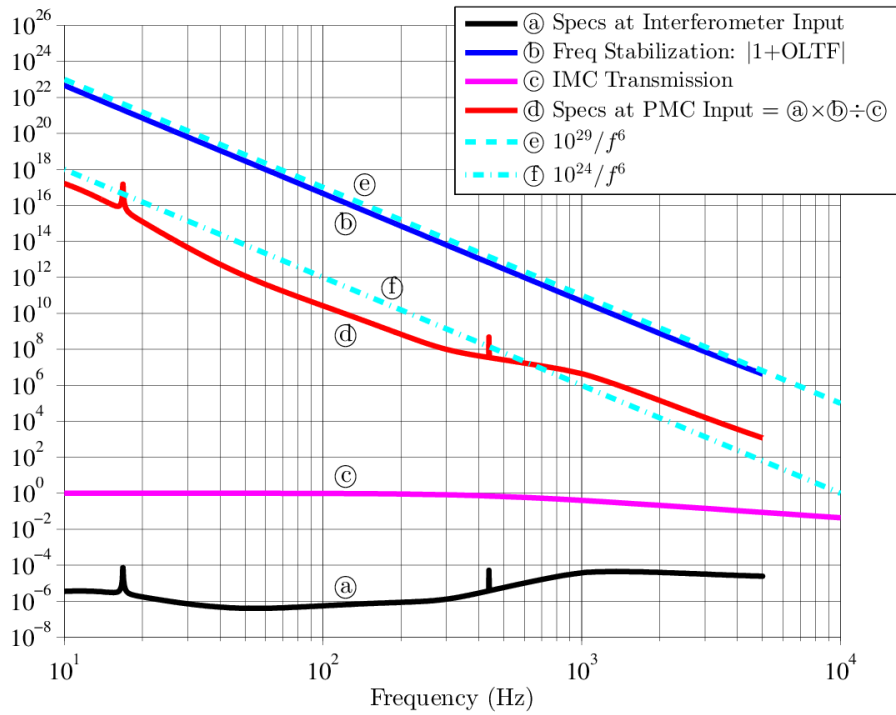


Figure 2.18: Free-running laser frequency noise specifications for Advanced Virgo. The specifications are in power spectral density (PSD) with the unit $\text{Hz} \sqrt{\text{Hz}}^{-1}$.

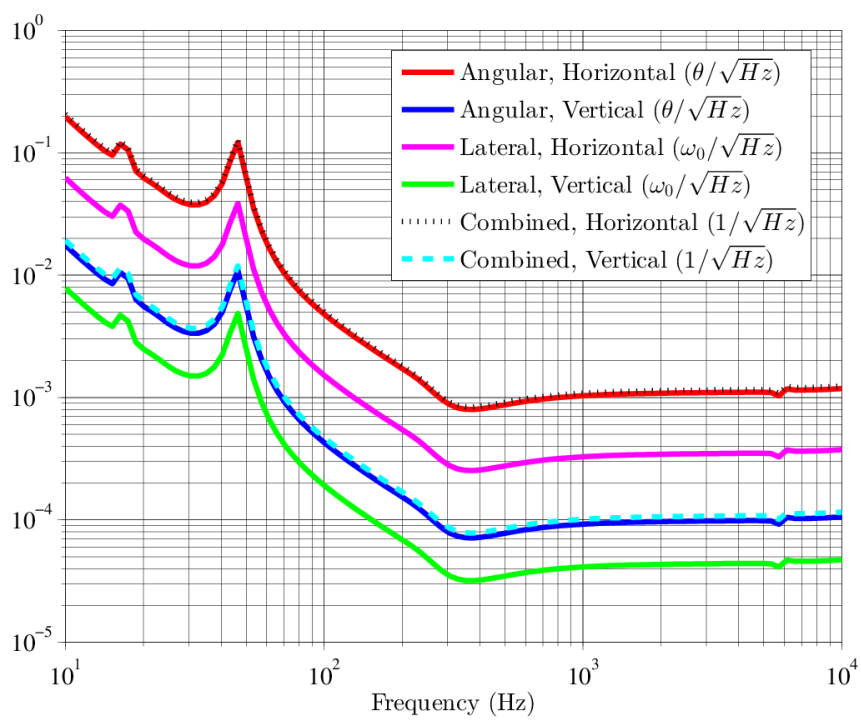


Figure 2.19: Free-running laser beam pointing stability specifications for Advanced Virgo.

Chapter 3

Laser Characterization

The specifications of a design are not complete without well-defined means for characterization. This section discusses how important characteristics of a laser system may be measured.

I will first present our means for absolute optical power measurement, the calibrated calorimeters. This is the most important DC-type measurement in this thesis work.

Then, before going toward AC-type measurements, I will first define the frequency band of interest given the requirements of Advanced Virgo. Subsequently, I will talk about how care should be taken in laser power noise measurements by taking into account the effects of finite aperture and inhomogeneity of the photodiodes. Some results on the study of photodiode inhomogeneity are presented.

In terms of laser frequency/phase noise, I will present the measurements based on Mach–Zehnder interferometry with various locking schemes. In terms of laser beam pointing stability, quadrant photodiodes are used and the formulae are given, followed by a discussion on the invariance of Gaussian beam pointing stability through an optical system. The laser beam profile is assessed with the use of single-mode fibers; I will present the comparison on the fundamental transverse modes in free-space and in fiber.

Last, some discussions are given on the acquisition of electric signals and the measurement of open-loop transfer function (OLTF).

3.1 Optical Power Measurement

Two types of photo-detectors [132] are used in the thesis work, calorimeters and photodiodes. They both give information on the optical power of an impinging laser beam.

Calibrated calorimeters¹ are used to give absolute values on optical power, and photodiodes are used to accurately measure relative fluctuations. Calorimeters with

¹NIST-traceable, $\pm 2.5\%$ uncertainty (95 % level of confidence)

power ratings up to 2 W², 3 W³, 30 W⁴ and 300 W⁵ are used in the experiments. The 30 W and 300 W calorimeters were re-calibrated during the course of the study (Appendix I). The 2 W and 3 W calorimeters show consistent readings to within 4 %.

In our optical power monitoring experiments, fused-silica plates are generally used as beam samplers where the sampled beam is injected to a photodiode, while the calorimeters are used both as a beam dump and as an optical power meter. It should be noted that, depending on how the calibration of the beam-sampling setup is made, the uncertainty can be up to $\sim 3\%$, in addition to the calibration uncertainty of the calorimeters. Correspondingly, unless otherwise mentioned, the worst-case estimate on the uncertainty of our optical power measurements is $\sim 5.6\%$, while care is generally taken to reduce the uncertainty to that of the calibration of the calorimeters, which is $\sim 2.5\%$.

3.2 Advanced Virgo Frequency Band of Interest

The gravitational wave detection band of terrestrial laser interferometric GWDs is generally between ~ 10 Hz and ~ 10 kHz (Figure 1.3). Additionally, in Advanced Virgo, five modulation frequencies will be implemented: three for the control of the interferometer (~ 6 MHz, ~ 8 MHz and ~ 56 MHz), one for the lock acquisition of the interferometer (~ 131 MHz), and one for the control of the input mode cleaner (~ 22 MHz) [133].

Accordingly, the laser system has to be characterized in the frequency bands from 10 Hz to 10 kHz, and from ~ 1 MHz to ~ 100 MHz, in terms of the quantities discussed in Section 2.7.

3.3 Laser Power Noise Measurement

As briefly mentioned in Section 2.5, laser power noise is described by its relative intensity noise (RIN) [134], generally defined as $P(f)/P_0$ in terms of power spectral density (PSD), where P_0 denotes the average DC power and $P(f)$ denotes power fluctuation at frequency f :

$$RIN(f) = \frac{P(f)}{P_0}. \quad (3.1)$$

Indium-gallium-arsenide (InGaAs) photodiodes are used for their good responsivity at 1064 nm. A photodiode converts the optical power of an impinging beam into photo-current with a responsivity in unit A W^{-1} . The responsivity S of a photodiode is given by:

$$S = \eta \cdot \frac{e}{h \cdot c} \cdot \lambda \quad (3.2)$$

where η , e , h , c , and λ denote quantum efficiency, elementary charge, Planck constant, speed of light, and wavelength, respectively.

²Melles-Griot, Model 13 PEM 001/J

³Gentec-EO, Model XLP-12-3S-H2. Date of Calibration: Feb. 16, 2012

⁴Gentec-EO, Model PS330-WB. Date of Calibration: Nov. 25, 2014

⁵Gentec-EO, Model UP55N-300F-H9-D0, Date of Calibration: Nov. 18, 2014.

The photo-current is then converted into voltage reading by using low-noise transimpedance amplifiers (TIA) with frequency dependent transimpedances (expressed in Ω) to improve RIN detection sensitivity. The frequency dependent gain $G_{TIA}(f)$ may then be defined as

$$G_{TIA}(f) = \frac{R_{AC}(f)}{R_{DC}}, \quad (3.3)$$

where $R_{AC}(f)$ is the AC transimpedance at frequency f and R_{DC} is the DC transimpedance.

The voltage reading $V(f)$ can then be written as

$$V(f) = G_{TIA}(f) \cdot R_{DC} \cdot S \cdot P(f) \quad (3.4)$$

such that

$$RIN(f) = \frac{P(f)}{P_0} \equiv \frac{1}{G_{TIA}(f)} \cdot \frac{V(f)}{V_{DC}}. \quad (3.5)$$

Clearly, to achieve better RIN detection sensitivity, a high DC voltage reading (i.e., a large photo-current, or a high DC transimpedance) and a large TIA gain are favored while the measurement noise of $V(f)$, often determined by the input noise of amplifier circuits, should be kept low. This equation also illustrates the common gain-bandwidth product limit, as a high DC transimpedance impairs bandwidth.

To reach RIN detection sensitivity of the order of $10^{-9} \sqrt{\text{Hz}}^{-1}$, the choice of the diameter of photodiodes is often a trade-off between capacitance and saturation threshold. Capacitance limits speed, while saturation threshold limits RIN sensitivity. Photodiodes with larger active area have higher capacitance which results in RC filtering when combined with the load resistance, while photodiodes with smaller active area have lower saturation threshold, provide lower photo-current, and consequently are prone to the detection limit coming from the shot noise (Equation 2.7).

Also, the finite pointing stability of a laser beam has to be considered when it comes to RIN detection as it may result in spurious results due to its coupling with the finite size of the photodiode and/or the spatially inhomogeneous responsivity of the photodiode.

For convenience, a coupling factor, κ , in unit m^{-1} , is introduced for quantitative discussion of these effects:

$$\sigma_{RIN,\Delta} = \frac{P_{\Delta}(f)}{P_0} = \kappa \cdot \Delta_{\text{photodiode}}(f), \quad (3.6)$$

where $\sigma_{RIN,\Delta}$ is the induced error in RIN measurement and P_{Δ} is the fluctuation in the power read, or *seen*, by the photodiode accompanied with beam displacement $\Delta_{\text{photodiode}}$.

3.4 Beam Clipping Effect in Laser Power Noise Measurement

The optical power P_0 of a Gaussian beam with peak intensity I_0 and beam radius ω can be derived by the double integral

$$\begin{aligned}
 P_0 &= I_0 \int_{-\infty}^{\infty} \int_{-\infty}^{\infty} \exp\left[\frac{-2(x^2 + y^2)}{\omega^2}\right] dx dy \\
 &= I_0 \int_0^{2\pi} \int_0^{\infty} \exp\left[\frac{-2r^2}{\omega^2}\right] r dr d\theta \\
 &= I_0 \cdot 2\pi \cdot \frac{-\omega^2}{4} \exp\left(\frac{-2r^2}{\omega^2}\right) \Big|_{r=0}^{r=\infty} \\
 &= I_0 \cdot \frac{\pi}{2} \cdot \omega^2.
 \end{aligned} \tag{3.7}$$

Since the integrals over the x- and y- axes are equivalent and may be separated, we rewrite the double integral into

$$P_0 = I_0 \cdot \sqrt{\frac{\pi}{2}} \cdot \omega \cdot \int_{-\infty}^{\infty} \exp\left(\frac{-2x^2}{\omega^2}\right) dx, \tag{3.8}$$

where the integral over the y-axis is evaluated to yield a constant. We then calculate the integral over the x-axis with a finite aperture to demonstrate the beam clipping effect in laser power noise measurement. It should be noted that the analytical derivation below assumes infinite aperture along the y-axis. Given the radius r and the center x' of the photodiode and let

$$t = \frac{\sqrt{2}}{\omega} \cdot x, \tag{3.9}$$

from Equation 3.8 we have

$$\begin{aligned}
 P(x', r) &= I_0 \cdot \sqrt{\frac{\pi}{2}} \cdot \omega \cdot \int_{x'-r}^{x'+r} \exp\left(\frac{-2x^2}{\omega^2}\right) dx \\
 &= I_0 \cdot \sqrt{\frac{\pi}{2}} \cdot \omega \cdot \frac{\omega}{\sqrt{2}} \cdot \left[\int_0^{\frac{\sqrt{2}}{\omega}(x'+r)} \exp(-t^2) dt - \int_0^{\frac{\sqrt{2}}{\omega}(x'-r)} \exp(-t^2) dt \right] \\
 &= I_0 \cdot \sqrt{\frac{\pi}{2}} \cdot \omega \cdot \frac{\omega}{\sqrt{2}} \cdot \frac{\sqrt{\pi}}{2} \cdot \left[\operatorname{erf}\left(\frac{\sqrt{2}}{\omega}(x'+r)\right) - \operatorname{erf}\left(\frac{\sqrt{2}}{\omega}(x'-r)\right) \right], \\
 &= \frac{P_0}{2} \cdot \left[\operatorname{erf}\left(\frac{\sqrt{2}}{\omega}(x'+r)\right) - \operatorname{erf}\left(\frac{\sqrt{2}}{\omega}(x'-r)\right) \right],
 \end{aligned} \tag{3.10}$$

where erf is the Gauss error function⁶ (Figure 3.1)

$$\operatorname{erf}(x) = \frac{2}{\sqrt{\pi}} \int_0^x e^{-t^2} dt \tag{3.11}$$

⁶See, e.g., <http://mathworld.wolfram.com/Erf.html>

that can be readily computed with software packages like MATLAB⁷. The κ factor associated with the beam clipping effect is then the spatial derivative of $P(x', r)$ in the x-direction divided by $P(x', r)$:

$$\kappa_x = \frac{1}{P(x', r)} \cdot \frac{\partial}{\partial x} P(x', r), \quad (3.12)$$

which can be easily computed with the property by definition:

$$\frac{\delta}{\delta z} \text{erf}(z) = \frac{2}{\sqrt{\pi}} e^{-z^2}. \quad (3.13)$$

The resulting equation for κ_x is then:

$$\kappa_x = \frac{1}{P(x', r)} \cdot \sqrt{\frac{2}{\pi}} \cdot \frac{P_0}{\omega} \cdot \left\{ e^{-\left[\frac{\sqrt{2}}{\omega} \cdot (x'+r)\right]^2} - e^{-\left[\frac{\sqrt{2}}{\omega} \cdot (x'-r)\right]^2} \right\} \quad (3.14)$$

To account for photodiode geometry and spatial inhomogeneities, numerical calculations may also be implemented to derive the κ factor (Appendix E), while calculations based on the above equations are shown in Figure 3.2, and in Figure 3.3 where a beam radius of 0.5 mm is assumed on the photodiode.

To get some numbers on how the clipping effect may affect laser power noise measurements, by taking the combined beam pointing stability specifications shown in Figure 2.19 and assuming only lateral movements with a beam waist located at the photodiode with 500 μm radius, which is that of the PMC, we arrive at Figure 3.4, which gives realistic values for reference, among which we take arbitrarily the free-running specs in the vertical plane for discussion. If the photodiode has a diameter $2r$ of 1 mm and a centering error x' of 10 μm , the resulting $|\kappa|$ of about 40 m^{-1} according to Figure 3.3. Combining these two observations we see that the measurement floor for RIN detection can only be as low as $\sim 1.6 \times 10^{-6} \sqrt{\text{Hz}}^{-1}$ (at $\sim 400 \text{ Hz}$).

3.5 Spatial Inhomogeneity in Photodiode Responsivity

In addition to finite active area, the spatial inhomogeneity in photodiode responsivity also introduces errors in RIN measurement. A scanning setup driven by stepper motors was developed to systematically assess the spatial inhomogeneity in photodiode responsivity.

The design goal is to measure κ down to about 1 m^{-1} , which may be suggested from the power noise specifications shown in Figure 2.12 and the projected lateral beam pointing stability specifications shown in Figure 3.4. Figure 3.5 is a schematic drawing of the measurement setup, and Figure 3.6 is a photo of the optical setup. The light source is a 100 mW 1064 nm wavelength continuous-wave NPRO laser⁸.

⁷Definition of the error function in MATLAB: erf(x) = 2/sqrt(pi) * integral from 0 to x of exp(-t^2) dt

⁸Lightwave, now LUMENTUM

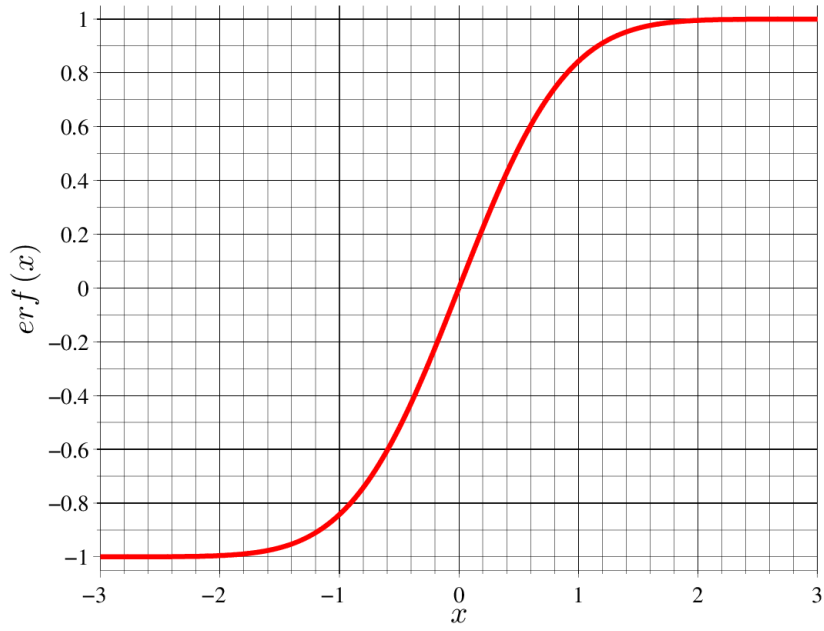


Figure 3.1: The error function erf .

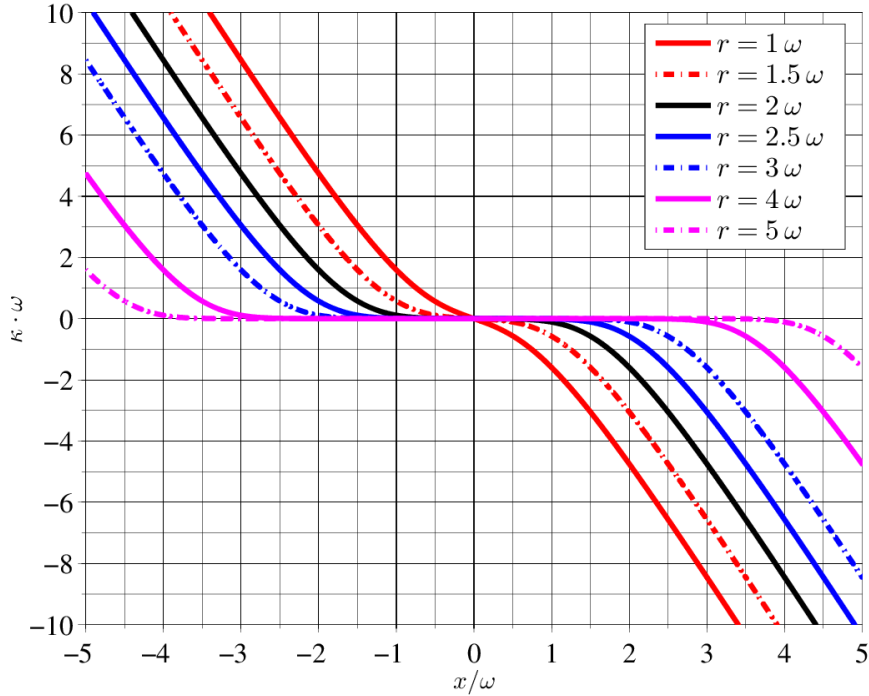


Figure 3.2: Photodiode clipping effect: the κ factor with respect to misalignment x' and photodiode radius r , all normalized with respect to the radius ω of the impinging beam.

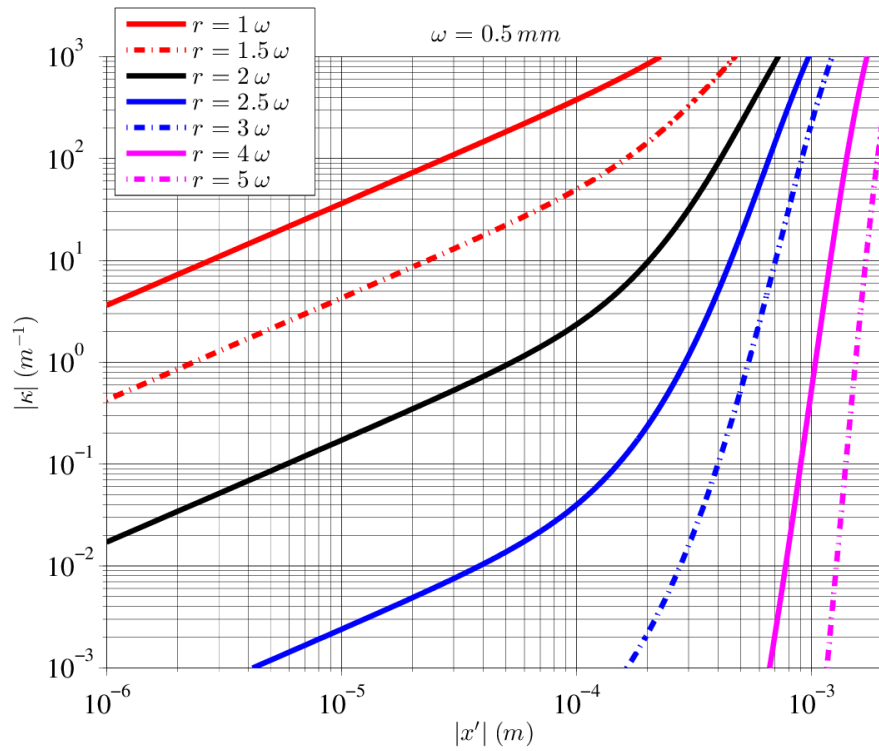


Figure 3.3: Photodiode clipping effect: the κ factor in unit m^{-1} with respect to misalignment x' and photodiode radius r , assuming 0.5 mm impinging beam radius.

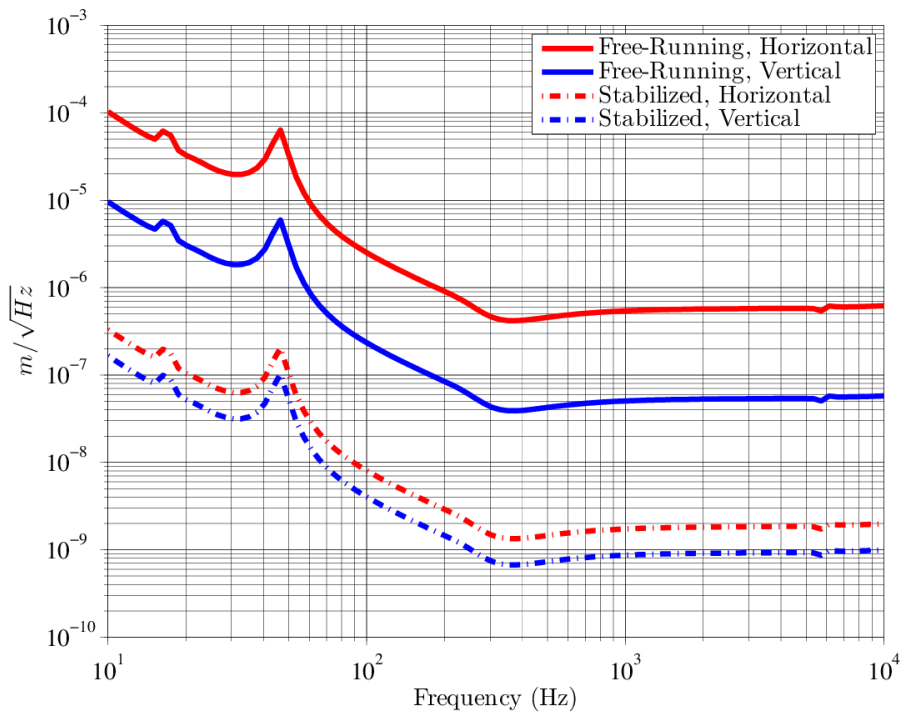


Figure 3.4: A projected case of lateral beam pointing stability from the Advanced Virgo specifications.

Linear polarization is ensured by two dielectric polarizers at Brewster angle each with 20 dB polarization extinction ratio (PER). Two uncoated fused-silica plates are inserted, and their angles of incidence tuned, to direct about 5% (5 mW) of the incident beam to the monitor and the sample photodiodes.

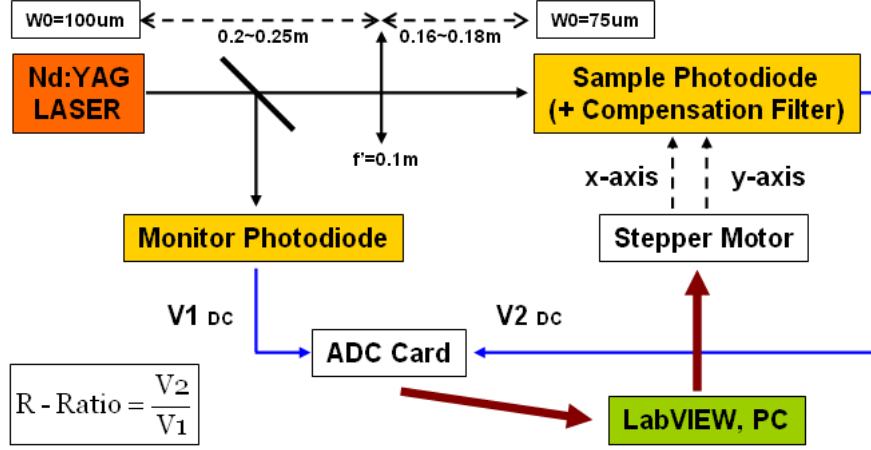


Figure 3.5: Schematic diagram of the photodiode responsivity mapping setup. We note that the beam radius on the sample photodiode was subsequently reduced from 75 μm to 35 μm .

The beam radius is 100 μm at the surface of the monitor photodiode, and 35 μm at that of the sample photodiode. Both photodiodes are 3 mm in diameter. Following Equation 3.14, the κ induced by the beam clipping effect is shown in Figure 3.7, giving the maximum measurement range with a target κ resolution. For the 3 mm diameter photodiodes we are interested in, with 35 μm beam radius, the available range for $\kappa < 1 \text{ m}^{-1}$ is up to $\sim 1.4 \text{ mm}$.

We check also the linearity of the photodiodes for a beam radius down to 50 μm . The sample photodiode is mounted on a motorized stage with x - and y - translational displacements, where xy is the surface plane of the photodiode. Displacements are propelled by two stepper motors⁹ with 5 μm absolute precision and 12 mm actuation range, and controlled by a computer with a customized LabVIEW Virtual Instrument (VI).

The step of the scan is set to 50 μm . Taking into account the design goal of $\kappa = 1 \text{ m}^{-1}$ sensitivity, this infers a relative power change of 50×10^{-6} , or 50 ppm. The photocurrents given by the monitor and the sample photodiodes are converted to voltage signals by 1 $\text{k}\Omega$ transimpedance amplifiers, hereinafter referred to as V_{monitor} and V_{sample} , respectively. At each step, an analog-to-digital-converter (ADC)¹⁰ with 12-bit resolution acquires the voltage signals. To minimize operational point dependent drifts which ultimately limit measurement accuracy, the power of the laser is stabilized by comparing V_{monitor} to a voltage reference¹¹.

Assuming a carrier signal with non-offset¹² DC voltage well-sized to the input

⁹Newport SMC100PP

¹⁰Measurement Computing, PCI-DAS1000 (12-bit, 250 kHz)

¹¹LM336 circuit

¹²Subtracting a voltage reference from the signal.

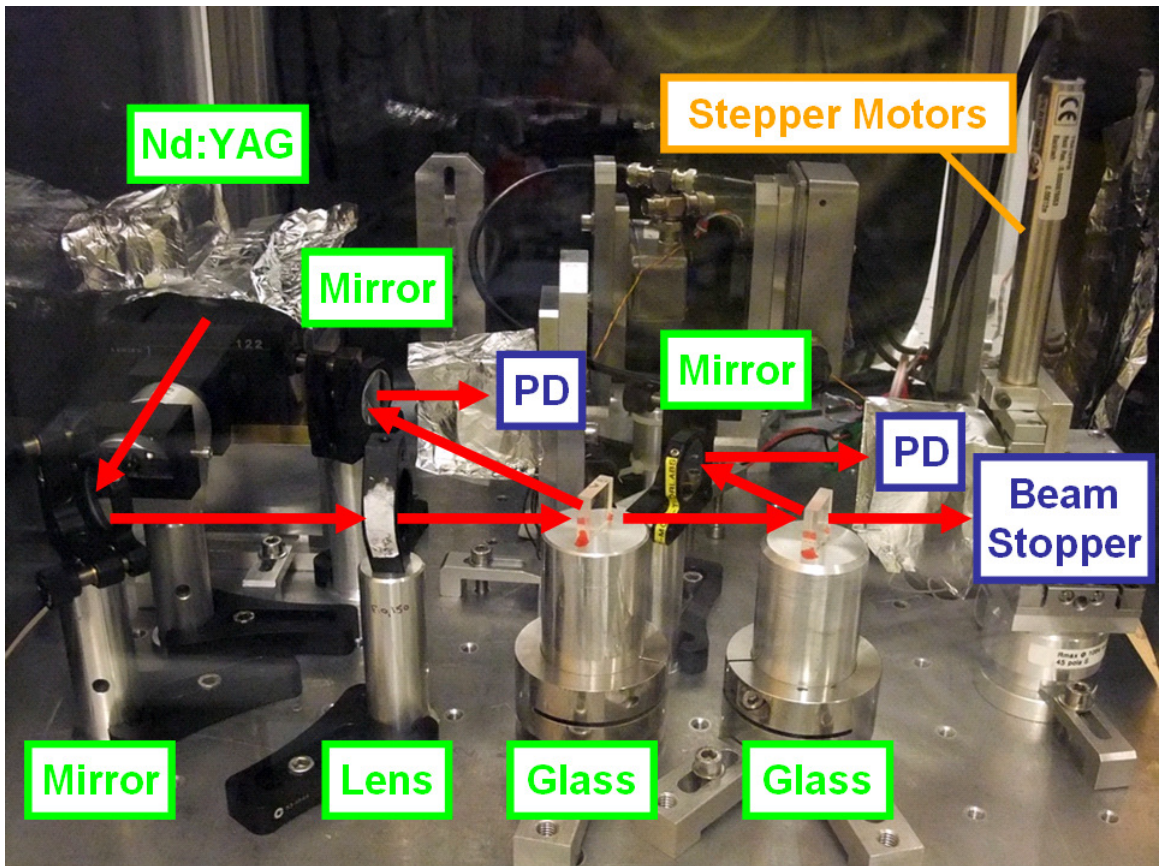


Figure 3.6: A photo of the optical setup for the mapping of photodiode responsivity. We note the pair of Brewster polarizers between the Nd:YAG laser and the first mirror.

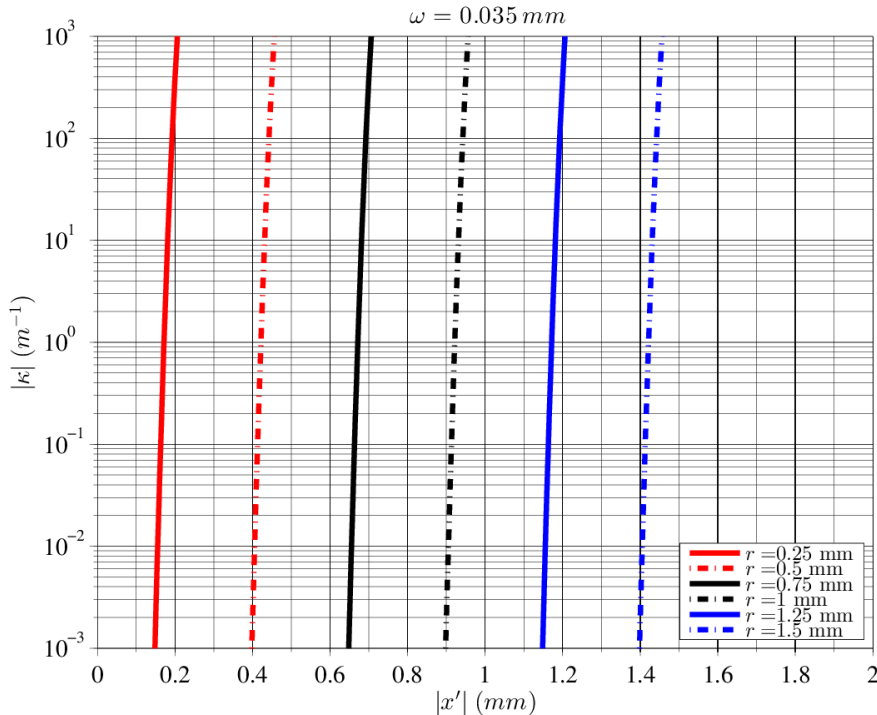


Figure 3.7: κ induced by the beam clipping effect with $\omega = 35 \mu\text{m}$.

range of the ADC, with 12-bit resolution the minimum detectable AC fluctuation per acquisition is 244 ppm (2^{-12}). With $50 \mu\text{m}$ step-size, this corresponds to minimum detectable κ of about 5 m^{-1} , which is insufficient for our design goal. To overcome this issue, hardware-wise, one can use either an ADC with more bits (e.g., 16 bits, which is rather common, lead to $\kappa \sim 0.3 \text{ m}^{-1}$), or subtract the DC voltage with a stable voltage reference. For the sake of convenience, we opted for a statistical technique encompassing oversampling¹³ and averaging to improve κ sensitivity at the cost of slightly longer measurement time. The ADC is set to take 50 000 acquisitions with 250 kHz sampling frequency, followed by the averaging of the acquisitions in the VI.

By averaging over 50 000 samples, the standard error of the mean is reduced by a factor of 224 ($\approx \sqrt{50000}$). Ideally, this factor also corresponds to the boost of ADC resolution and leads to κ sensitivity of $\sim 0.02 \text{ m}^{-1}$.

In the above-mentioned case, the data acquisition time is 0.02s, which corresponds to the period of the 50 Hz AC signal in the power grid, and accordingly any coupling from the power grid is rejected. There were no other spurious peaks observed in the noise spectrum. This way, we make sure that the κ sensitivity of our measurements was not limited by the ADC.

Both the Z-shaped scan and the S-shaped scan are implemented in the VI (Figure 3.8). To reduce scan time, S-shaped scans were used in the measurements presented. A typical scan takes about 2 h for $50 \mu\text{m}$ step-size over $3 \text{ mm} \times 3 \text{ mm}$ area.

The temporal stability of the setup was assessed by keeping both photodiodes

¹³See, for example, “Enhancing ADC resolution by oversampling”, <http://www.atmel.com/Images/doc8003.pdf>.

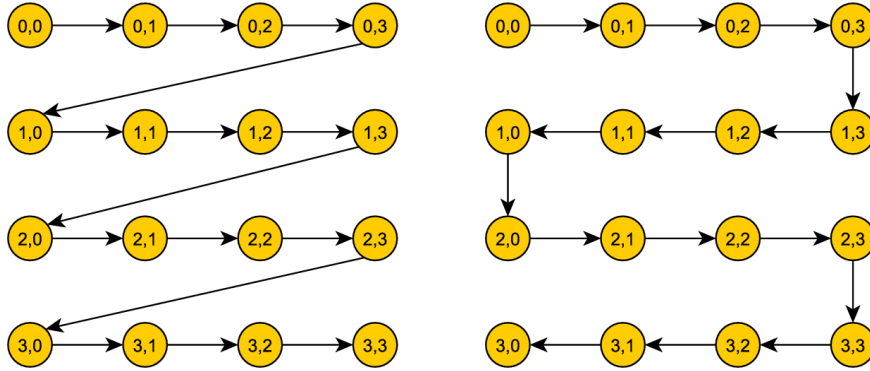


Figure 3.8: Z-shaped (left) and S-shaped (right) scan patterns.

fixed and registering the ratio between V_{sample} and $V_{monitor}$. Typical short-term standard deviation of the ratio is about 7×10^{-6} , corresponding to κ sensitivity of 0.14 m^{-1} . The standard deviation for 5 h is about 1×10^{-4} . The stability of the scanning process is accessed by comparing successive scans of the same photodiode.

Once the responsivity map is obtained, the associated $\kappa_x(x, y)$ and $\kappa_y(x, y)$ are deduced from its gradients along the x - and the y - axes. Figure 3.9 shows an example of the results of the 3 mm photodiodes¹⁴ of interest. The results of more photodiodes of the same model can be found in Appendix C. The measured value of κ for this photodiode model is typically few m^{-1} .

InGaAs photodiodes with 1 mm and 3 mm diameter are used in our experiments to convert optical power to photo-current. The former is used to ensure high-speed operation, while the latter is used to minimize the coupling of beam pointing instability to RIN detection.

3.6 Laser Frequency/Phase Noise Measurement

There is no perfect reference in frequency measurements [135]. Lasers are optical oscillators whose frequencies also have finite stability.

An optical field may be represented in the form of a phasor:

$$A \cdot e^{i[\omega t + \phi]} \quad (3.15)$$

where A is the amplitude, ω is the angular frequency, and ϕ is the phase. Equation 3.15 describes an ideal oscillator, while temporal fluctuations can take place in the form of $A(t)$, the amplitude noise, $\omega(t)$, the frequency noise, and $\phi(t)$, the phase noise:

$$A(t) \cdot e^{i[\omega(t) \cdot t + \phi(t)]}. \quad (3.16)$$

From Equation 3.15 we see that frequency and phase noises are not that different, the only difference being the factor t , time.

In the time and frequency community, the instantaneous, normalized frequency departure $y(t)$ from the nominal frequency ν_0 is related to the instantaneous phase

¹⁴Excelitas C30665GH

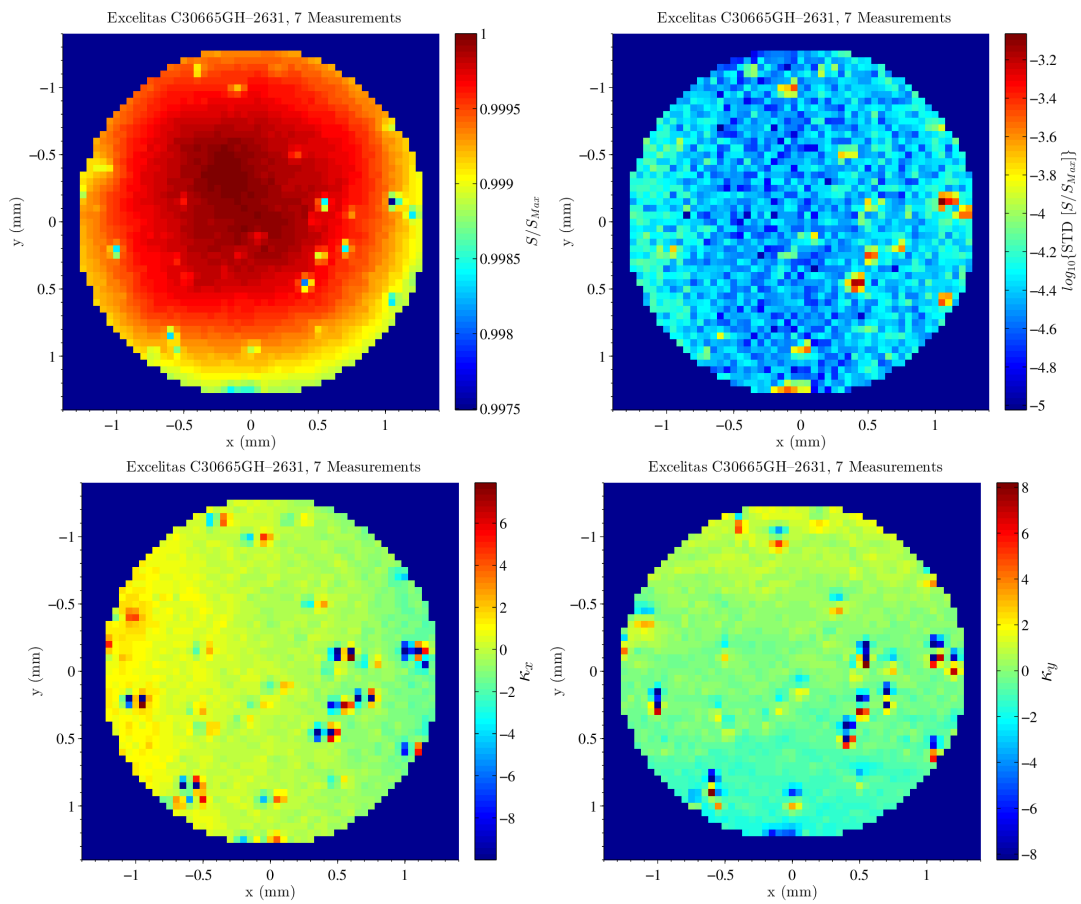


Figure 3.9: An example of the $\kappa_{x,y}(x, y)$ of the 3 mm diameter photodiodes of interest.

fluctuation $\phi(t)$ about the nominal phase $2\pi\nu_0 t$ by [136]:

$$y(t) = \frac{1}{2\pi\nu_0} \frac{d\phi(t)}{dt}. \quad (3.17)$$

In the Fourier frequency domain, the power spectral densities $S_y(f)$ and $S_\phi(f)$ are related by [136]:

$$S_y(f) = \frac{f^2}{\nu_0^2} S_\phi(f), \quad (3.18)$$

or

$$\text{Amplitude PSD}\{\nu\}(f) = f \cdot \text{Amplitude PSD}\{\phi\}(f) \quad (3.19)$$

when frequency and amplitude PSD are considered. This may be derived from the definition of the instantaneous frequency [137]:

$$\nu(t) = \frac{1}{2\pi} \frac{d\phi(t)}{dt} \quad (3.20)$$

and the functional relationship of Fourier transform (F. T.):

$$\begin{aligned} F.T.\{f(x)\} &= \int_{-\infty}^{\infty} f(x) \cdot e^{-2\pi i x \xi} dx = \hat{f}(\xi) \\ F.T.\left\{\frac{d^n}{dx^n} f(x)\right\} &= (-2\pi i \xi)^n \cdot \hat{f}(\xi). \end{aligned} \quad (3.21)$$

Laser Frequency Noise Measurement Using Optical Cavities

An optical cavity may serve as a frequency discriminator for a laser beam, or vice versa. Once the optical cavity and the laser beam are in resonance, i.e., mutually locked, the control signal to remain the lock gives information on the frequency departure. If the optical cavity is passive (i.e. the feedback actuates on the laser beam) and relatively stable, we can then render the departure as the frequency noise of the laser beam.

The Pound-Drever-Hall method [113, 117] is a typical technique in locking the frequency of a laser to an optical cavity, or vice versa. Other techniques are Hänsch-Couillaud [138], which utilizes polarization, and tilt-locking [139, 140], which utilizes higher-order cavity modes. An unorthodox technique using a higher-order Laguerre-Gaussian mode of order 2 has also been reported [141]. Once the laser beam and the optical cavity are locked, the control signal then bears the information on frequency noise.

Mach-Zehnder Interferometry

In a homodyne Mach-Zehnder interferometer, the laser beam is split into two arms and then recombined (Figure 3.10). The optical power of the interference fringe of two collinear plane waves $n = 1, 2$ with optical power P_n and phase ϕ_n is in the form [142]

$$P = P_1 + P_2 + 2 \cdot \sqrt{P_1 \cdot P_2} \cdot \cos(\phi_1 - \phi_2). \quad (3.22)$$

The fringe state depends on the phase difference, $\phi_\Delta \equiv \phi_1 - \phi_2$. If we can trace P fast enough (faster than the time it takes for ϕ_Δ to change by 2π), then in principle by calculating (and carefully manipulating) the inverse cosine of P , we can recover ϕ_Δ .

An alternative method is to lock P to a constant value by a phase actuator in the Mach–Zehnder interferometer. The phase correction ϕ_c introduced by the actuator to maintain the lock then reflects ϕ_Δ to within the measurement noise ϕ'_c :

$$\phi_c = \phi_\Delta + \phi'_c. \quad (3.23)$$

ϕ'_c can come from both the phase actuator and the coupling between the finite laser frequency stability and the finite symmetry of the interferometer.

A simple side-of-the-slope technique will do the job for the locking of the interferometer, while locking at the extrema requires modulation techniques, among which we discuss three possible schemes, *heterodyning*, *phase dithering* and *frontal phase modulation*, in the following.

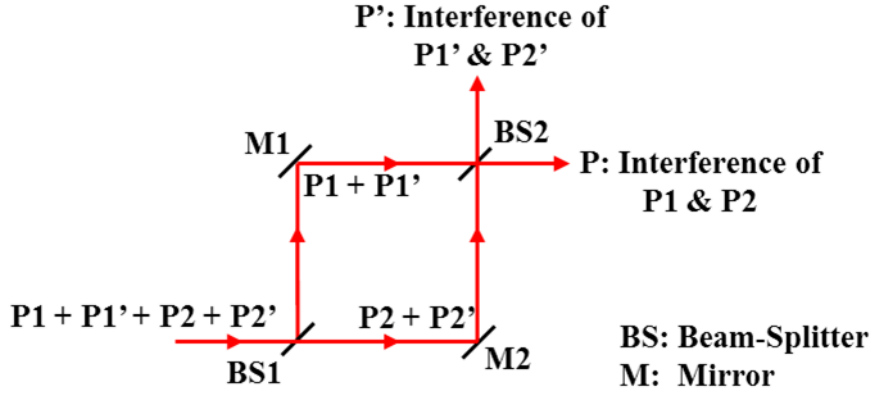


Figure 3.10: A Mach–Zehnder interferometer. Here the T/R ratio of BS2 = $P1/P1' = P2'/P2$; and the T/R ratio of BS1 = $(P2 + P2')/(P1 + P1')$. T: intensity transmission; R: intensity reflection.

A Heterodyne Mach–Zehnder Interferometer

Let us first consider a heterodyne Mach–Zehnder interferometer where the optical frequency of one beam is shifted by an acousto-optic modulator (AOM) (Figure 3.11), and write the electric field complex amplitudes of the two beams ($n = 1, 2$) with optical power P_n in terms of phasors:

$$\begin{aligned} \tilde{E}_1 &= E_1 \cdot e^{i\omega_1 t} \cdot e^{i\phi_1} \\ \tilde{E}_2 &= E_2 \cdot e^{i\omega_2 t} \cdot e^{i\phi_2}, \end{aligned} \quad (3.24)$$

where E is the scalar amplitude, ω is the angular frequency of the optical field, and ϕ is the phase. For mathematical convenience, we also define:

$$\begin{aligned} \omega_m &= \omega_2 - \omega_1 \\ \Delta\phi &= \phi_2 - \phi_1. \end{aligned} \quad (3.25)$$

The optical power of the heterodyne interference, P , is:

$$\begin{aligned}
 P &= \left(\tilde{E}_1 + \tilde{E}_2 \right) \cdot \overline{\left(\tilde{E}_1 + \tilde{E}_2 \right)} \\
 &= E_1^2 + E_2^2 + E_1 \cdot E_2 \cdot e^{-i\Delta\phi} \cdot e^{-i\omega_m t} + E_1 \cdot E_2 \cdot e^{i\Delta\phi} \cdot e^{i\omega_m t} \\
 &= P_1 + P_2 + 2 \cdot \sqrt{P_1 \cdot P_2} \cdot [\cos(\omega_m t) \cdot \cos(\Delta\phi) - \sin(\omega_m t) \cdot \sin(\Delta\phi)] \quad (3.26)
 \end{aligned}$$

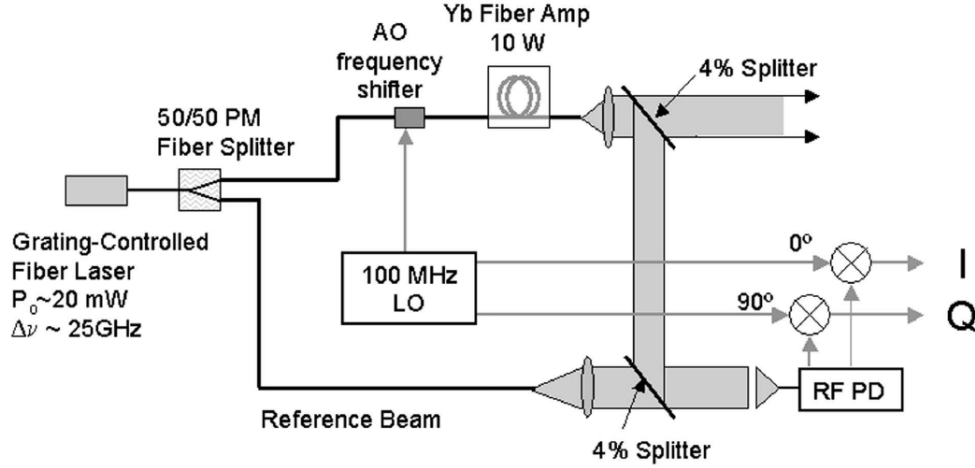


Figure 3.11: Phase noise measurement with a heterodyne Mach-Zehnder interferometer. From [143].

Based on the product-to-sum identities in trigonometry as shown in Equation 3.31, by homodyning the interference signal with a local oscillator with a proper phase, we can either extract the sine term or the cosine term in which the phase information is encoded. By extracting both terms, it is possible to track phase deviations larger than 2π without ambiguity [143].

Dither Locking of a Mach-Zehnder Interferometer

Figure 3.12 shows another possible configuration to lock a fiber Mach-Zehnder interferometer at its extremum based on phase dithering.

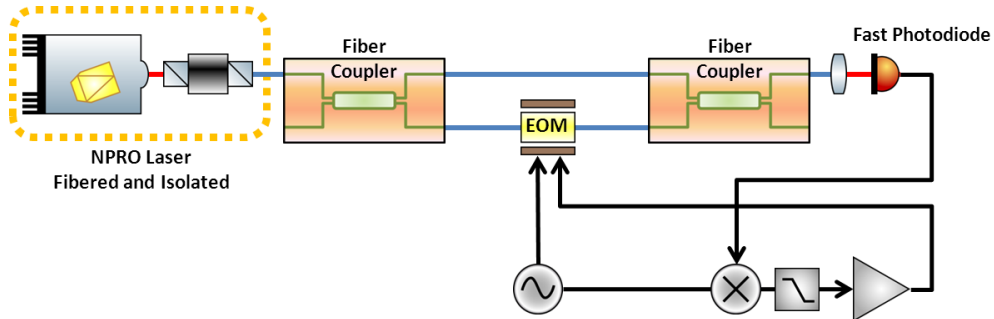


Figure 3.12: Dither Locking of a Mach-Zehnder Interferometer

To lock the fringe state ($\phi_\Delta - \phi_o \rightarrow 0$, where ϕ_o is the locking point), a dithering phase signal $\phi_m = \beta_m \cdot \sin(\Omega_m t)$, $\Omega_m = 2\pi f_m$ is applied to one of the two waves with

an electro-optic modulator (EOM), resulting in

$$P = P_1 + P_2 + 2 \cdot \sqrt{P_1 \cdot P_2} \cdot \cos(\phi_\Delta + \phi_m). \quad (3.27)$$

Applying the trigonometric identity

$$\begin{aligned} \cos(\phi_\Delta + \phi_m) &= \cos(\phi_\Delta) \cdot \cos(\phi_m) - \sin(\phi_\Delta) \cdot \sin(\phi_m) \\ &= \cos(\phi_\Delta) \cdot \cos[\beta_m \cdot \sin(\Omega_m t)] - \sin(\phi_\Delta) \cdot \sin[\beta_m \cdot \sin(\Omega_m t)] \end{aligned} \quad (3.28)$$

and Jacobi-Anger expansions

$$\begin{aligned} \cos[\beta_m \cdot \sin(\Omega_m t)] &= J_0(\beta_m) + 2 \sum_{k=1}^{\infty} J_{2k}(\beta_m) \cos(2k\Omega_m t) \\ \sin[\beta_m \cdot \sin(\Omega_m t)] &= 2 \sum_{k=1}^{\infty} J_{2k-1}(\beta_m) \sin[(2k-1)\Omega_m t] \end{aligned} \quad (3.29)$$

where J_α denotes Bessel functions of the first kind and $k \in \mathbb{N}$, the cosine term may be rewritten as

$$\begin{aligned} \rho &\equiv \cos(\phi_\Delta + \phi_m) \\ &= \cos(\phi_\Delta) \cdot \{J_0(\beta_m) + 2J_2(\beta_m)\cos(2\Omega_m t) + 2J_4(\beta_m)\cos(4\Omega_m t) + \dots\} \\ &\quad - \sin(\phi_\Delta) \cdot \{2J_1(\beta_m)\sin(\Omega_m t) + 2J_3(\beta_m)\sin(3\Omega_m t) + 2J_5(\beta_m)\sin(5\Omega_m t) + \dots\}. \end{aligned} \quad (3.30)$$

The interference fringe is then registered with a photodiode with responsivity S (Equation 3.2) and a transimpedance amplifier (TIA) with frequency-dependent gain $G_{TIA}(f)$, resulting in the voltage signal $\xi = G_{TIA}(f) \cdot S \cdot P$. By homodyning ξ with a local oscillator signal $\xi_{LO} = V_{LO} \cdot \sin(k\Omega_m t + \Phi_{LO})$, and low-pass filtering, based on the trigonometric identities

$$\begin{aligned} \sin(k\Omega_m t + \Phi_{LO}) \cdot \sin(k\Omega_m t) &= \frac{1}{2} \cdot \{\cos(\Phi_{LO}) - \cos(2k\Omega_m t + \Phi_{LO})\} \\ \sin(k\Omega_m t + \Phi_{LO}) \cdot \cos(k\Omega_m t) &= \frac{1}{2} \cdot \{\sin(\Phi_{LO}) + \sin(2k\Omega_m t + \Phi_{LO})\}, \end{aligned} \quad (3.31)$$

we extract the amplitude $A(k\Omega_m)$ of the frequency component at $k\Omega_m$ in ξ as

$$\begin{aligned} A(k\Omega_m) &= G_{TIA}(k\Omega_m) \cdot S \cdot \{-V_{LO} \cdot J_k(\beta_m) \cdot \cos(\Phi_{LO}) \cdot \sin(\phi_\Delta)\} \quad \text{for } k = 1, 3, 5 \dots \\ &= G_{TIA}(k\Omega_m) \cdot S \cdot \{V_{LO} \cdot J_k(\beta_m) \cdot \sin(\Phi_{LO}) \cdot \cos(\phi_\Delta)\} \quad \text{for } k = 2, 4, 6 \dots \end{aligned} \quad (3.32)$$

To lock the fringe at the bright state ($\phi_\Delta \rightarrow 0$) and maximize the amplitude of the error signal, we set $k = 1$ and $\Phi_{LO} = 0$ or π to obtain the error signal:

$$\epsilon(\phi_\Delta) = \pm G_{TIA}(f_m) \cdot S \cdot J_k(\beta_m) \cdot \sin(\phi_\Delta). \quad (3.33)$$

The error signal can then be used to lock the interference at its extrema (or, in principle any arbitrary locking point, while in practice there may be limits coming

from the saturation of the electronics) with a phase actuator (e.g. the EOM, as it is readily there), whose phase correction signal reflects ϕ_Δ .

The error signal derivation so far is based on plane waves, while in practice, TEM₀₀ Gaussian beams (in free-space) and LP₀₁ linearly polarized beams (in single-mode fiber), likely with imperfect, nonidentical, and/or even non-stationary mode profiles, are to be combined. These imperfections will affect the accuracy and uncertainty of the phase lock ($\phi_\Delta(t) - \phi_o \rightarrow \phi_\epsilon(t)$), and it can be even more complicated when power fluctuations in the two beams are considered, but we limit ourselves to the simple derivation shown here which should suffice a general understanding.

It may be worthy noting that ϕ_Δ can also be measured even without the phase lock using phase dithering. From Equation 3.30, we see that the information of the cosine term can be obtained by mixing the interference signal with the second harmonic frequency — or, simply by observing the DC term in the interference. With both the sine term and the cosine term, ϕ_Δ can then be extracted without the 2π ambiguity, as discussed previously in the heterodyne Mach–Zehnder interferometer setup.

Phase Noise Measurement Floor with a Mach–Zehnder Interferometer

The coupling of the laser frequency noise $\delta\nu$ to the phase noise ϕ_Δ at the output of the interferometer due to the optical path length difference ΔL between the two arms of a Mach–Zehnder interferometer may be derived by assuming lock condition such that:

$$\Delta L = (n + \Delta_n) \cdot \lambda = (n + \Delta_n) \cdot \frac{c}{\nu}, \quad (3.34)$$

where $n \in \mathbb{N}$, Δ_n is the offset of the locking point, λ is the laser wavelength, c is the speed of light, and ν is the laser frequency. Then, the change in ΔL with respect to the change in ν is:

$$\frac{\delta}{\delta\nu}(\Delta L) = -n \cdot \frac{c}{\nu^2}, \quad (3.35)$$

and the change in phase, $\delta\phi_{\Delta L}$, is:

$$\delta\phi_{\Delta L} = \frac{\delta(\Delta L)}{\lambda} \cdot 2\pi = 2\pi \cdot \frac{\Delta L}{c} \cdot \delta\nu. \quad (3.36)$$

The coupling may be minimized with reduced asymmetry, while in some cases may be amplified for phase actuation, or for a different locking configuration.

Frontal Phase Modulation for the Locking of an Asymmetric Mach–Zehnder Interferometer

When the Mach-Zehnder interferometer is asymmetric, it may also be locked by frontal phase dithering (Figure 3.13), provided that the system is carefully tuned. If we write the electric field complex amplitudes of the two interfering beams similar

to those in Equation 3.24 as

$$\begin{aligned}\tilde{E}_1 &= E_1 \cdot e^{i\omega t} \cdot e^{i\phi_m(t)} \cdot e^{i\phi_1} \\ \tilde{E}_2 &= E_2 \cdot e^{i\omega t} \cdot e^{i\phi_m(t)} \cdot e^{i\phi_2},\end{aligned}\quad (3.37)$$

where ω is the optical frequency, $\phi_m(t)$ is the phase modulation, and ϕ is the phase, after some algebra, we will only converge to Equation 3.22. In fact, the phase modulation from frontal dithering only has effect when the difference in the time of arrival of the two beams at the interference is significant when compared to the period of the modulation signal.

To account for the time delay, we write the electric field complex amplitudes as

$$\begin{aligned}\tilde{E}_1 &= E_1 \cdot e^{i\omega t} \cdot e^{i\phi_m(t)} \\ \tilde{E}_2 &= E_2 \cdot e^{i\omega(t-\Delta t)} \cdot e^{i\phi_m(t-\Delta t)} \cdot e^{i\Delta\phi},\end{aligned}\quad (3.38)$$

where $\Delta t = \Delta L/c$ is the time delay due to the asymmetry ΔL , $\phi_m(t) = \beta_m \cdot \sin(\Omega_m t)$ is the phase modulation, and $\Delta\phi$ is the phase difference accumulated between the beam-splitter and the beam-combiner. Accordingly, the optical power of the interference, P , is:

$$\begin{aligned}P &= (\tilde{E}_1 + \tilde{E}_2) \cdot \overline{(\tilde{E}_1 + \tilde{E}_2)} \\ &= E_1^2 + E_2^2 \\ &\quad + E_1 \cdot E_2 \cdot e^{i[\phi_m(t) + \omega\Delta t - \phi_m(t-\Delta t) - \Delta\phi]} \\ &\quad + E_2 \cdot E_1 \cdot e^{-i[\phi_m(t) + \omega\Delta t - \phi_m(t-\Delta t) + \Delta\phi]} \\ &= P_1 + P_2 \\ &\quad + 2 \cdot \sqrt{P_1 \cdot P_2} \cdot \cos[-\phi_m(t) - \omega\Delta t + \phi_m(t-\Delta t) - \Delta\phi] \\ &= P_1 + P_2 \\ &\quad + 2 \cdot \sqrt{P_1 \cdot P_2} \cdot \cos\left[\omega\Delta t - \Delta\phi + \beta_m \cdot \sin(\Omega_m t) \right. \\ &\quad \quad \quad \left. - \beta_m \cdot \sin(\Omega_m t) \cdot \cos(\Omega_m \Delta t) \right. \\ &\quad \quad \quad \left. + \beta_m \cdot \cos(\Omega_m t) \cdot \sin(\Omega_m \Delta t) \right].\end{aligned}\quad (3.39)$$

Then, if we choose a proper modulation frequency Ω_m and a proper time delay Δt such that

$$\Omega_m \cdot \Delta t = \left(\frac{1}{2} + n\right) \cdot \pi \quad (n \in \mathbb{N}), \quad (3.40)$$

we obtain

$$\begin{aligned}P &= P_1 + P_2 + 2 \cdot \sqrt{P_1 \cdot P_2} \cdot \cos[\omega\Delta t - \Delta\phi + \beta_m \cdot \sin(\Omega_m t) + \beta_m \cdot \cos(\Omega_m t)] \\ &= P_1 + P_2 + 2 \cdot \sqrt{P_1 \cdot P_2} \cdot \cos\left[\omega\Delta t - \Delta\phi + \sqrt{2} \cdot \beta_m \cdot \cos\left(\Omega_m t - \frac{\pi}{4}\right)\right],\end{aligned}\quad (3.41)$$

which has a form that is similar to Equation 3.27. The information on the differential phase between the two arms, $\Delta\phi$, can then be extracted using the same technique

as in dither locking. We also see that any frequency departure of the laser source from ω affects the accuracy of the measurement.

This technique is often attributed to Lise Schnupp¹⁵ in the field of laser interferometric gravitational wave detectors. The derivations shown here are rather sketchy. More rigorous derivations and analyses may be found in [34, 144].

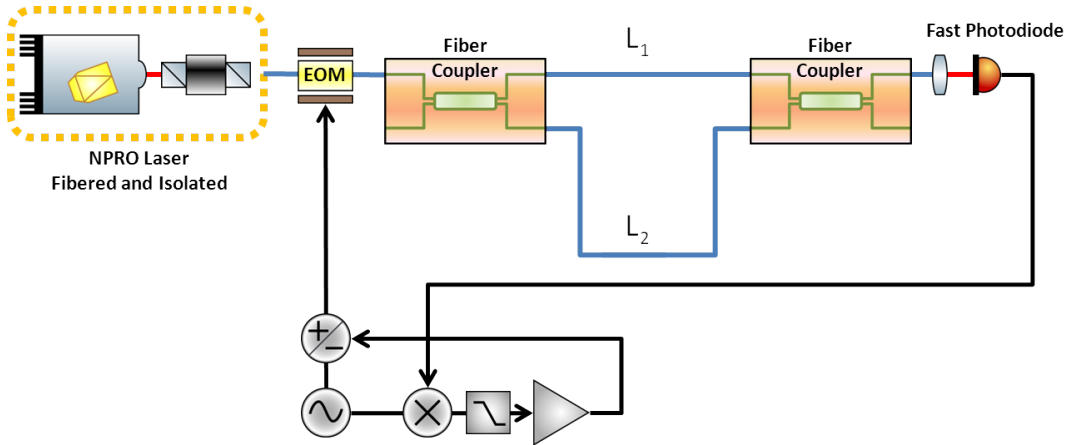


Figure 3.13: Frontal Dither Locking of an Asymmetric Mach-Zehnder Interferometer

3.7 Laser Beam Pointing Stability Measurement

InGaAs quadrant photodiodes are used to measure laser beam movements. With a Gaussian beam, the derivation of the measurement principle is more or the less the same as the beam clipping effect in RIN measurements described in Section 3.4. Likewise, the analytical derivations below assumes infinite aperture along the y-axis.

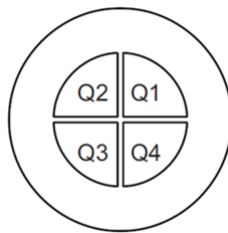


Figure 3.14: Quadrant Photodiode

Assuming a quadrant photodiode with the four quadrants numbered as Figure 3.14, the horizontal beam movement can be measured by comparing the optical power collected by quadrants Q1 and Q4, P_R , to the optical power collected by Q2

¹⁵For a presentation at a European Collaboration Meeting on Interferometric Detection of Gravitational Waves (Sorrento, Italy, October 1988). See, e.g., Chapter 8 of [2] and [34].

and Q3, P_L [145]:

$$\begin{aligned} P_R(x') &= \sqrt{\frac{2}{\pi}} \cdot \frac{P_0}{\omega} \cdot \int_{x'}^{\infty} \exp\left(\frac{-2x^2}{\omega^2}\right) dx \\ P_L(x') &= \sqrt{\frac{2}{\pi}} \cdot \frac{P_0}{\omega} \cdot \int_{-\infty}^{x'} \exp\left(\frac{-2x^2}{\omega^2}\right) dx \end{aligned} \quad (3.42)$$

where a change of variable as in Equation 3.9 is performed, x' is the x-coordinate of the center of the quadrant photodiode with respect to the laser beam, and P_0 is the total optical power of the laser beam. We can define a dimensionless factor S by

$$\begin{aligned} S(x') &= \frac{P_R(x') - P_L(x')}{P_0} \\ &= \sqrt{\frac{2}{\pi}} \cdot \frac{1}{\omega} \cdot \left[\int_{x'}^{\infty} \exp\left(\frac{-2x^2}{\omega^2}\right) dx - \int_{-\infty}^{x'} \exp\left(\frac{-2x^2}{\omega^2}\right) dx \right] \end{aligned} \quad (3.43)$$

When the laser beam is centered on the quadrant photodiode, $x' = 0$,

$$\begin{aligned} \left. \frac{\partial P_R(x)}{\partial x} \frac{1}{P_0} \right|_{x'=0} &= -\sqrt{\frac{2}{\pi}} \cdot \frac{1}{\omega} \\ \left. \frac{\partial P_L(x)}{\partial x} \frac{1}{P_0} \right|_{x'=0} &= \sqrt{\frac{2}{\pi}} \cdot \frac{1}{\omega} \end{aligned} \quad (3.44)$$

and therefore

$$\left. \frac{\partial S(x)}{\partial x} \right|_{x'=0} = -2 \cdot \sqrt{\frac{2}{\pi}} \cdot \frac{1}{\omega}. \quad (3.45)$$

Any relative movement between the laser beam and the quadrant photodiode, x' , about the origin is then

$$x' = -\sqrt{\frac{\pi}{8}} \cdot S \cdot \omega \approx -0.627 \cdot S \cdot \omega, \quad (3.46)$$

which is a commonly known equation. It should be noted, however, that S is not linear with respect to x' , especially when S is large. By introducing the function *erfc*¹⁶:

$$\operatorname{erfc}(x) = 1 - \operatorname{erf}(x) = \frac{2}{\sqrt{\pi}} \int_x^{\infty} e^{-t^2} dt \quad (3.47)$$

and Equation 3.9, Equation 3.43 may be recast as:

$$\begin{aligned} S(x') &= \sqrt{\frac{2}{\pi}} \cdot \frac{1}{\omega} \cdot \left[2 \cdot \int_{x'}^{\infty} \exp\left(\frac{-2x^2}{\omega^2}\right) dx - \int_{-\infty}^{\infty} \exp\left(\frac{-2x^2}{\omega^2}\right) dx \right] \\ &= \sqrt{\frac{2}{\pi}} \cdot \frac{1}{\omega} \cdot \left[2 \cdot \frac{\omega}{\sqrt{2}} \frac{\sqrt{\pi}}{2} \cdot \operatorname{erfc}\left(\frac{\sqrt{2}}{\omega} \cdot x'\right) - \sqrt{\frac{\pi}{2}} \cdot \omega \right] \\ &= -\operatorname{erf}\left(\frac{\sqrt{2}}{\omega} \cdot x'\right). \end{aligned} \quad (3.48)$$

¹⁶<http://mathworld.wolfram.com/Erfc.html>

To extend the derivation to a quadrant photodiode with finite radius r , it can be shown that

$$S(x') = \operatorname{erfc}\left(\frac{\sqrt{2}}{\omega} \cdot x'\right) - \frac{1}{2} \cdot \operatorname{erfc}\left(\frac{\sqrt{2}}{\omega} \cdot (x' + r)\right) - \frac{1}{2} \cdot \operatorname{erfc}\left(\frac{\sqrt{2}}{\omega} \cdot (x' - r)\right). \quad (3.49)$$

To further consider geometrical effects, numerical calculations may be considered, as in Section 3.4.

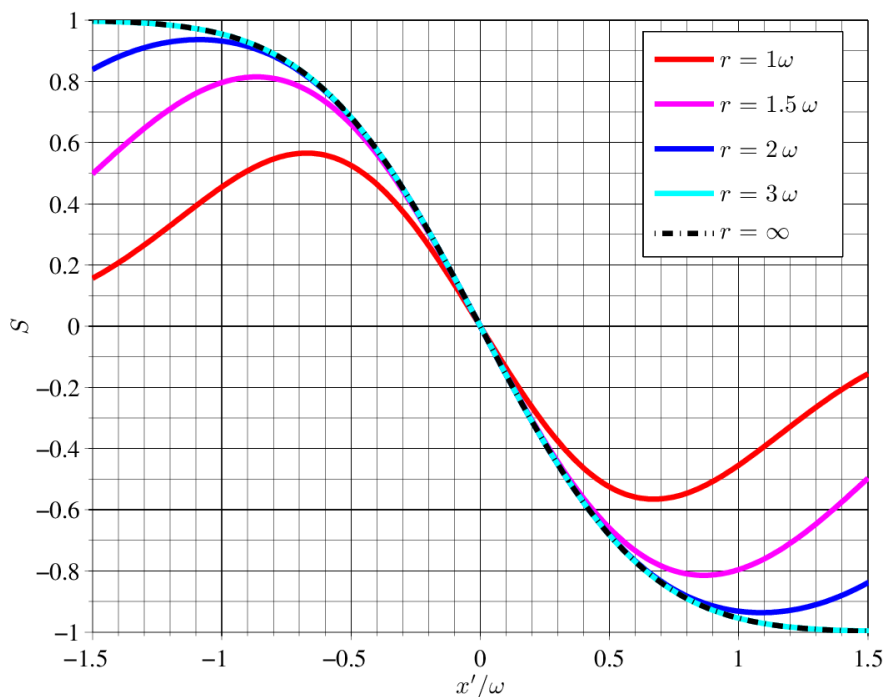


Figure 3.15: Quadrant photodiode response S vs. relative movement x'

From Figure 3.15 we see that to obtain accurate measurements in laser beam movements, the initial laser beam should be centered, and its radius well adapted to the extent of the movement of the laser beam.

There are two types of laser beam movements, angular and positional, denoted as $\delta\alpha$ and Δ , respectively¹⁷. In principle, a thorough characterization of laser beam pointing stability requires two (or more) measurements at different distances of the laser beam to distinguish these two types of movements. In practice, for convenience, a single measurement can also lead to useful information on laser beam pointing stability by assuming that all the movements are either angular or positional. Moreover, by putting the quadrant photodiode at the focus of a lens, we measure only the angular movements, while by putting the quadrant photodiode at the beam waist of the beam of interest (which may not be always possible), we measure only the lateral movements.

¹⁷ISO 11670:2003, Lasers and laser-related equipment – Test methods for laser beam parameters – Beam positional stability

Another possibility in measuring beam pointing stability is to couple the laser beam into a cavity, and measure the relative field amplitudes of the TEM₁₀ and the TEM₀₁ modes [146–148]. This technique does not tell apart $\delta\alpha$ and Δ , but as we will see in the next section, there exists an invariant $|\epsilon|$ in Gaussian beam propagation through optical systems

$$|\epsilon| = \sqrt{\left(\frac{\Delta}{\omega_0}\right)^2 + \left(\frac{\delta\alpha}{\theta}\right)^2}, \quad (3.50)$$

where ω_0 is the beam waist radius and θ is the half divergence angle of a given Gaussian beam.

3.8 Invariance of Gaussian Beam Pointing Stability

As demonstrated in [149], a Gaussian beam may be represented by the complex beam parameter $q(z)$,

$$\frac{1}{q} = \frac{1}{R(z)} - i\frac{\lambda}{\pi\omega(z)^2}, \quad (3.51)$$

where $R(z)$ is the radius of curvature at a distance z from the beam waist, λ is the wavelength and $\omega(z)$ is the beam radius at z . Together with the commonly used $ABCD$ matrix M for optical systems,

$$M = \begin{bmatrix} A & B \\ C & D \end{bmatrix} \\ |M| = AD - BC = 1, \quad (3.52)$$

the Gaussian beam propagation in an optical system may be derived by matrix operation:

$$\begin{bmatrix} q_2 \\ 1 \end{bmatrix} = \begin{bmatrix} A & B \\ C & D \end{bmatrix} \begin{bmatrix} q_1 \\ 1 \end{bmatrix}, \quad (3.53)$$

or:

$$q_2 = \frac{Aq_1 + B}{Cq_1 + D}. \quad (3.54)$$

After some algebra on Equation 3.51, one can show that:

$$q(z) = z + iz_R, \quad (3.55)$$

where z_R is the Rayleigh distance:

$$z_R = \pi \frac{\omega_0^2}{\lambda}. \quad (3.56)$$

At the beam waist, $z = 0$, by defining q_0 as

$$q_0 \equiv q(0) = iz_R. \quad (3.57)$$

and propagating q_0 with the $ABCD$ matrix, we have:

$$\begin{aligned} q_{0,i} &= iz_{R,i} \\ &= \frac{BD + ACz_{R,o}^2}{D^2 + C^2z_{R,o}^2} + i\frac{(AD - BC)z_{R,o}}{D^2 + C^2z_{R,o}^2}, \end{aligned} \quad (3.58)$$

where the subscripts o and i denote the object space and the image space, respectively, inferring

$$\frac{BD + ACz_{R,o}^2}{D^2 + C^2z_{R,o}^2} = 0 \longrightarrow z_{R,o}^2 = -\frac{BD}{AC} \quad (3.59)$$

and

$$z_{R,i} = \frac{(AD - BC)z_{R,o}}{D^2 + C^2z_{R,o}^2} = \left(\frac{A}{D}\right) \cdot z_{R,o}. \quad (3.60)$$

In the $ABCD$ matrix formulation, a geometrical optical ray is represented by the ray vector

$$\begin{bmatrix} y \\ u \end{bmatrix}, \quad (3.61)$$

where y is the distance of the ray and u is angle of inclination of the ray with respect to the optical axis. Similarly, the beam pointing parameters may be combined into a vector

$$\begin{bmatrix} \Delta \\ \delta\alpha \end{bmatrix}, \quad (3.62)$$

and propagated by the $ABCD$ matrix formulation such that

$$\begin{bmatrix} \Delta_i \\ \delta\alpha_i \end{bmatrix} = \begin{bmatrix} A & B \\ C & D \end{bmatrix} \begin{bmatrix} \Delta_o \\ \delta\alpha_o \end{bmatrix}, \quad (3.63)$$

which results in:

$$\begin{aligned} \Delta_i &= A\Delta_o + B\delta\alpha_o \\ \delta\alpha_i &= C\Delta_o + D\delta\alpha_o. \end{aligned} \quad (3.64)$$

The invariance in Equation 3.50, squared, in the object space, $|\epsilon_o|^2$, can be represented as:

$$\begin{aligned} |\epsilon_o|^2 &= \left(\frac{\Delta}{\omega_0}\right)^2 + \left(\frac{\delta\alpha}{\theta}\right)^2 \\ &= \frac{\pi}{\lambda} \cdot \left[\frac{\Delta_o^2}{z_{R,o}} + z_{R,o} \cdot \delta\alpha_o^2 \right] \end{aligned} \quad (3.65)$$

with the introduction of the relations:

$$\begin{aligned} \omega &= \sqrt{\frac{\lambda}{\pi}} \cdot \sqrt{z} \\ \theta &= \sqrt{\frac{\lambda}{\pi}} \cdot \sqrt{\frac{1}{z}}. \end{aligned}$$

Similarly, in the image space, $|\epsilon_i|^2$, with the introduction of Equations 3.59 and 3.60, as:

$$\begin{aligned}
|\epsilon_i|^2 &= \left(\frac{\pi}{\lambda}\right) \left[\frac{A\Delta_o + B\delta\alpha_o^2}{\omega_{0,i}} + \frac{C\Delta_o + D\delta\alpha_o^2}{\theta_{0,i}} \right] \\
&= \left(\frac{\pi}{\lambda}\right) \left[\frac{D}{A} (A^2\Delta_o^2 + B^2\delta\alpha_o^2 + AB\Delta_o\delta\alpha_o) \frac{1}{z_{R,o}} \right. \\
&\quad \left. + \frac{A}{D} (C^2\Delta_o^2 + D^2\delta\alpha_o^2 + CD\Delta_o\delta\alpha_o) z_{R,o} \right] \\
&= \left(\frac{\pi}{\lambda}\right) \left\{ \Delta_o^2 \left[\frac{AD}{z_{R,o}} + \frac{AC^2}{D} z_{R,o} \right] + \delta\alpha_o^2 \left[\frac{DB^2}{z_{R,o}} + ADz_{R,o} \right] \right. \\
&\quad \left. + \Delta\delta\alpha_o \left[\frac{BD}{z_{R,o}} + ACz_{R,o} \right] \right\}. \tag{3.66}
\end{aligned}$$

With Equations 3.52 and 3.59, we have:

$$\begin{aligned}
\frac{AD}{z_{R,o}} + \frac{AC^2}{D} z_{R,o} &= \frac{1}{z_{R,o}} \left[AD + \left(\frac{AC^2}{D}\right) \left(-\frac{BD}{AC}\right) \right] = \frac{1}{z_{R,o}} [AD - BC] = \frac{1}{z_{R,o}} \\
\frac{DB^2}{z_{R,o}} + ADz_{R,o} &= z_{R,o} \left[\left(\frac{DB^2}{A}\right) \left(-\frac{AC}{BD}\right) + AD \right] = z_{R,o} [-BC + AD] = z_{R,o} \\
\frac{BD}{z_{R,o}} + ACz_{R,o} &= \frac{1}{z_{R,o}} \left[BD + AC \left(-\frac{BD}{AC}\right) \right] = 0. \tag{3.67}
\end{aligned}$$

Plugging Equation 3.67 into Equation 3.66 yields

$$|\epsilon_i|^2 = \left(\frac{\pi}{\lambda}\right) \left\{ \Delta_o^2 \left[\frac{1}{z_{R,o}} \right] + \delta\alpha_o^2 [z_{R,o}] + \Delta\delta\alpha_o [0] \right\} = |\epsilon_o|^2, \tag{3.68}$$

thus proving the invariance of Equation 3.50.

Another physical aspect, given the condition $|\epsilon| \ll 1$, for the demonstrated invariance is to expand Δ and $\delta\alpha$ into Hermite–Gauss modes in the total field Φ [146–148, 150]:

$$\Phi \approx \text{TEM}_{00} + \epsilon_x \text{TEM}_{10} + \epsilon_y \text{TEM}_{01}. \tag{3.69}$$

The value $|\epsilon|^2$ is then the power of the TEM_{10} or the TEM_{01} modes and is therefore invariant when propagated through ideal optical systems.

3.9 Beam Profile Measurement

The transverse modal contents in a laser beam can be analyzed by a scanning Fabry–Perot cavity [147]. Moreover, by using a ring cavity with an odd number of optics, the TEM_{xy} modes and the TEM_{yx} modes become non-degenerate when x is odd, and therefore may be discriminated to give more information on the transverse modal contents of the laser beam under diagnosis. In some of our experiments a scanning triangular optical cavity was used to analyze the laser beam.

Using an optical cavity for beam profile analysis, however, requires some electronics and alignment. An easier approach to know how much TEM_{00} content is in

the laser beam is to couple the beam into a single-mode fiber. The linearly polarized mode LP_{01} matches well with the TEM_{00} mode [79, 80] and therefore provides a good estimate.

Another common method is to use a beam profiler. We commonly use a beam profiler with scanning slits¹⁸ to determine the beam parameters such as the size and the location of the beam waist. By fitting the measurements to a TEM_{00} Gaussian beam, the fitting error reflects the beam quality. A MATLAB script, as presented in Appendix F, is implemented to make such fitting.

3.10 Transverse Modes: LP_{01} in Fiber vs. Gaussian TEM_{00} in Free-Space

For weakly guiding fibers, the transverse field may be constructed to be essentially polarized in one direction, resulting in the commonly known linearly polarized (LP) fiber modes [79]. The matching, in power transmission, between the fundamental fiber LP mode in a step-index fiber and the fundamental Gaussian transverse electromagnetic (TEM) mode is $> 93\%$ for $V \geq 1.5$, and $> 99\%$ for $V \approx 2$ [80], where V is the normalized frequency parameter (Equation 2.5).

Below we use the wave optics formulation of fiber modes [151] to give an estimate on the TEM_{00} – LP_{01} matching with the parameters of the polarization-maintaining single-mode fibers used in our experiments (Figure 4.4):

- Mode Field Diameter (MFD): $7.2 \mu\text{m}$ @ $\lambda = 1064 \text{ nm}$
- Numerical Aperture (NA): 0.120

and assume a step-index profile in which the cladding is composed of silica, which has a refractive index $n_{clad} = 1.4496$ [152]¹⁹. The refractive index of the core may then be derived by definition (Equation 2.5) as $n_{core} = 1.4546$. From these two parameters, Equations 2.5 and 2.6 may be numerically solved to yield $V \sim 2.0923$, which in turn gives the radius $a \sim 2.9526 \mu\text{m}$ ²⁰ of the fiber core. It is customary to define the following parameters:

$$\begin{aligned} u &= a \cdot \sqrt{k^2 n_{core}^2 - \beta^2} \\ w &= a \cdot \sqrt{\beta^2 - k^2 n_{clad}^2}, \end{aligned} \quad (3.70)$$

where $k = 2\pi/\lambda$ is the wave number in free space, and β is the propagation constant of the fiber mode. The general solution of the wave equation of the LP_{01} mode for

¹⁸BeamScan, Model 1080 Slit Scan

¹⁹<http://refractiveindex.info/?shelf=main&book=SiO2&page=Malitson>

²⁰We note that this value is different from that specified in Figure 4.4. Since we do not know the exact composition and structure of the fiber, we note the specified uncertainty in MFD, but do not comment on the discrepancy. The purpose in this section is however instead to justify the similarity of the fundamental fiber LP and Gaussian TEM modes.

a step-index fiber can then be written as [151]:

$$\begin{aligned}\Phi_{core}(r) &= C_{core} \cdot J_0\left(\frac{u}{a} \cdot r\right) \\ \Phi_{clad}(r) &= C_{clad} \cdot K_0\left(\frac{w}{a} \cdot r\right),\end{aligned}\quad (3.71)$$

where J is the Bessel function of the first kind, and K is the modified Bessel function of the second kind, which describe the field Φ in the fiber core and that in the fiber cladding, respectively. The constant C is introduced to ensure the continuity condition. The value of β , can be solved by establishing the continuity of the two fields at $r = a$:

$$\begin{aligned}\Phi_{core}(a) &= \Phi_{clad}(a) \\ \frac{\partial}{\partial r}\Phi_{core}(a) &= \frac{\partial}{\partial r}\Phi_{clad}(a),\end{aligned}\quad (3.72)$$

which, after some algebra, leads to:

$$\begin{aligned}C_{core} \cdot J_0(u) &= C_{clad} \cdot K_0(w) \\ \frac{J_0(u)}{u \cdot J_1(u)} &= \frac{K_0(w)}{w \cdot K_1(w)}.\end{aligned}\quad (3.73)$$

We then arrive numerically at $\beta \sim 8.5742 \times 10^6 \text{ m}^{-1}$ and $C_{clad} \sim 2.1767 \cdot C_{core}$. The fundamental fiber LP mode field Φ_F can then be derived and be compared to that of the fundamental Gaussian TEM mode Φ_G , as shown in Figure 3.16. We note that here the Gaussian field is defined as [80]:

$$\Phi_G = \frac{2}{\omega_0} \cdot \sqrt{\frac{1}{2\pi}} \cdot e^{-\left(\frac{r}{\omega_0}\right)^2}, \quad (3.74)$$

and the fiber field Φ_F is scaled by $1/\sqrt{P}$, where

$$P = \int_0^{2\pi} d\phi \int_0^\infty r \Phi_F^2 dr \quad (3.75)$$

so that the two fields both have an integral squared value of unity. We see that the two modes match well, with a power transmission value $T = |c|^2 = 0.9946$ where c is the integral of the modal overlapping:

$$c = \int_0^{2\pi} d\phi \int_0^\infty r \Phi_F \Phi_G dr. \quad (3.76)$$

3.11 Power Spectral Density Measurement

Almost all the probes in the experiments end up as voltage signals. A multimeter can give simple statistical measures on the voltage signals such as the average DC value and the root-mean-square value.

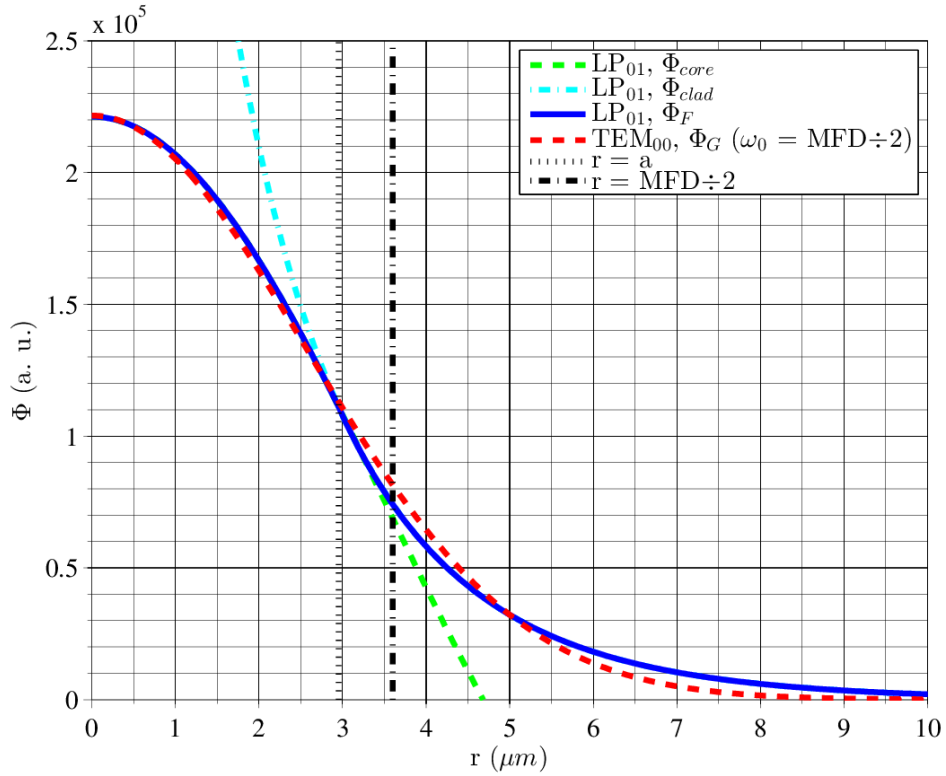


Figure 3.16: Comparison on the fields of the fundamental fiber LP and Gaussian TEM modes.

To perform frequency-domain spectral analyses, we use instruments based on either Fourier transform (SR780²¹) or swept-tuned super-heterodyning (HP8591A²²). The key characteristics of these instruments are summarized as follow.

SR780 Specifications

- Input Impedance: $1 \text{ M}\Omega + 50 \text{ pF}$.
- Frequency Range: 102.4 kHz.
- Input Noise (RMS): $< 10 \text{ nV } \sqrt{\text{Hz}}^{-1}$ ($< -160 \text{ dBV } \sqrt{\text{Hz}}^{-1}$) above 200 Hz.

HP8591A Specifications

- Input Impedance: 50Ω .
- Frequency Range: 9 kHz to 1.8 GHz.
- Displayed Average Noise Level (input terminated, 0 dB attenuation, 1 kHz RBW, 30 Hz VBW):
 - 400 kHz to 1.5 GHz: $\leq -115 \text{ dBm}$.
 - Equivalent to an input noise of $13 \text{ nV } \sqrt{\text{Hz}}^{-1}$.

²¹Stanford Research Systems, SR780 Network Signal Analyzer

²²Hewlett-Packard, HP 8591A Spectrum Analyzer

We use the SR780 for the frequency range from 10 Hz to 100 kHz, and the HP8591A for the frequency range from 100 kHz to 100 MHz. To ensure that the results are comparable, GPIB commands wrapped in Perl²³ are used to make automatic measurements (Appendix G).

Another all-round solution is to use analog-to-digital converters (ADC) which simply registers the voltage signal time series. Statistical and/or frequency domain analyses can then be carried out through post-processing. We use mostly the ADC cards from National Instruments (USB-6229, USB-6210 and USB-6009²⁴), while an ADC card from Measurement Computing (PCI-DAS1000²⁵) is used in the mapping setup for photodiode responsivity. A general issue with ADC cards is that the input noise is generally higher than that of dedicated instruments, with some noise peaks. For example, the specifications of National Instruments USB-6229 on the random noise (RMS) vs. the input range are

- ± 10 V: 244 μ V (772 nV $\sqrt{\text{Hz}}^{-1}$)
- ± 5 V: 122 μ V (386 nV $\sqrt{\text{Hz}}^{-1}$)
- ± 1 V: 30 μ V (95 nV $\sqrt{\text{Hz}}^{-1}$)
- ± 0.2 V: 13 μ V (41 nV $\sqrt{\text{Hz}}^{-1}$)

where the input noise levels in the parenthesis are calculated assuming 100 kHz bandwidth. A noise floor of ~ 500 nV $\sqrt{\text{Hz}}^{-1}$ was measured with the USB-6229 with ± 5 V input range. The Ni-DAQmx library was wrapped in Perl for data acquisition with the National Instrument ADC cards (Appendix H).

3.12 Transfer Function Measurement

With a network analyzer, it is straightforward to obtain the transfer function of a given system. We use the SR780 for transfer function measurement below 100 kHz, and the HP3577A²⁶.

In the case of a servo control loop, a useful measure is the open-loop transfer function (OLTF). Figure 3.17 shows a control loop diagram: δ is the free-running noise, p is the perturbation input ϵ_1 and ϵ_2 are the error signal probes. We characterize the servo control loop by sending a calibrated signal through the perturbation input p to the system, and measuring the response of the system through the error signals ϵ_1 and ϵ_2 . In the loop there is an amplifier with gain A , and a feedback network B . When the loop is closed, at steady-state, $\epsilon_2 \rightarrow 0$. Hence,

$$\epsilon_1 = \delta - ABp - AB\epsilon_1 = \frac{\delta - ABp}{1 + AB}, \quad (3.77)$$

²³<https://www.perl.org/>

²⁴National Instruments, USB-6229 (16-bit, 250 kHz), USB-6210 (16-bit, 250 kHz) and USB-6009 (14-bit, 48 kHz)

²⁵Measurement Computing, PCI-DAS1000 (12-bit, 250 kHz)

²⁶Hewlett-Packard, HP 3577A Network Analyzer

and

$$\epsilon_2 = \epsilon_1 + p = \frac{p + \delta}{1 + AB}. \quad (3.78)$$

If the perturbation p is significantly greater than δ , $p \gg \delta$, the ratio between ϵ_1 and ϵ_2 is

$$\frac{\epsilon_1}{\epsilon_2} = -AB, \quad (3.79)$$

where AB is referred to as the OLF. It is a useful measure because when $p = 0$, the residual noise after the servo control loop is

$$\epsilon_2 = \epsilon_1 = \frac{\delta}{1 + AB} = \frac{\delta}{1 + OLF}. \quad (3.80)$$

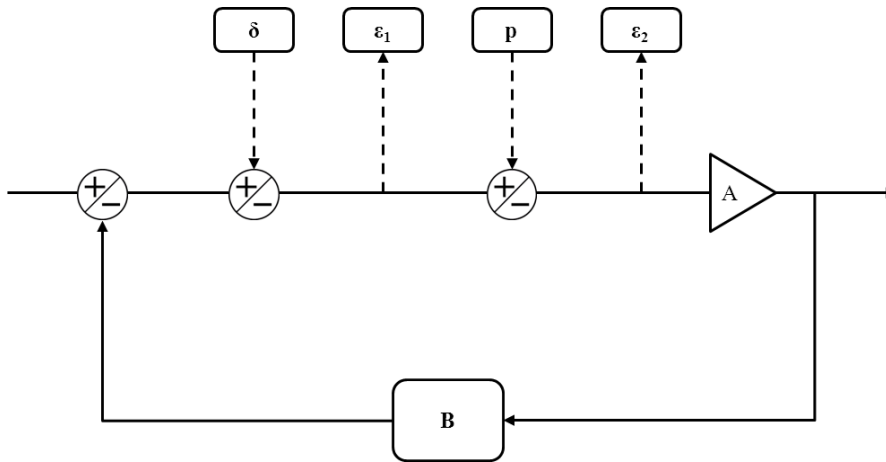


Figure 3.17: A control loop diagram with negative feedback amplifier.

3.13 Automated Data Acquisition

During the course of this study efforts, have been made to standardize, in particular, the power spectral density (PSD) measurements. Since we had the FFT-based and the swept-tuned spectrum analyzers in hand, the first effort was to standardize, in particular, the frequency spans and the resolution bandwidths of our PSD measurements in order to make uncorrelated measurements more comparable. Moreover, even with a defined measurement procedure, it is often tedious and complicated to manually operate all the steps, register the data, perform necessary conversion etc., without making mistakes from time to time. The time required for manual operation is therefore also a lot longer than computer-assisted operations, reducing the simultaneity of correlated measurement, and making the rendering of the results more difficult when the measurands of interest are non-stationary. Automated operation and data acquisition of the spectrum analyzers are therefore implemented through the GPIB interface with the commands wrapped in Perl (Appendix G). The developed Perl script works well, but inherently the spectrum analyzers have very limited numbers of input channels, in our case two for the FFT-based spectrum analyzer and one for the swept-tuned spectrum analyzer. Unless computer-controlled

electric switches are implemented, manual operation is still required when multiple signal channels are considered.

Analog-to-digital conversion (ADC) cards are therefore considered, which often come with a bunch of input channels. The input noise level of commercially available ADC cards may be significant, especially when the input range is set large, limiting its sensitivity in relative measurements. Such limit can nevertheless be overcome with the use of low-noise operational amplifiers, in which ARTEMIS is experienced.

Certainly when sampling frequency up to ~ 100 MHz is considered, the number of input channels also becomes more limited. It should be noted however the possibility to register digitized time series with an ADC card in comparison to a swept-tuned spectrum analyzer. Digitized time series enable various data analyses which do not have to be decided upon the acquisition of the data.

Fast Fourier transform (FFT) is probably the most common analysis, among which a logarithmic frequency scale is often used in our application. We note that some techniques may be applied to improve the Fourier frequency spectrum estimation on a logarithmic frequency axis [153, 154].

An ADC acquisition script written in Perl using the NiDAQ-mx library may be found in Appendix [H](#).

Chapter 4

Master Oscillator Fiber Power Amplifier

As illustrated in Figure 2.15, Advanced Virgo foresees the use of fiber amplifiers to attain the required power level. This Chapter briefly summarizes our experience to date on some fiber amplifiers, and eventually focuses on the test results of our most recent MOFPA setup which consists of commercially available fiber amplifiers seeded by fiber-coupled NPRO lasers. The setup was continually tested for a few thousands of hours. The noise performance was compliant with the Advanced Virgo specifications. Despite the shortcoming of output power which may be remedied by coherent beam combination as will be presented in the Chapter 5, in terms of noise aspects, the test results of the MOFPA setup are reassuring for its application in interferometric gravitational wave detectors.

This Chapter starts with a discussion on the seed lasers for fiber laser amplifiers, taking into account the requirements of fiber-optic components as well as those imposed by Advanced Virgo and its facility. Results on the fiber-coupling of NPRO lasers are then presented, as well as an experiment on the probing of the stimulated Brillouin scattering threshold of the fiber of interest.

We then characterize and present the results on the fiber laser amplifiers from Nufern, Eolite and Azur Light Systems.

4.1 Seed Lasers for Fiber Amplifiers

A fiber amplifier cannot work by itself without a seed laser signal. Moreover, in some cases the lack of a seed laser signal while the gain medium is being actively pumped may result in devastating consequences in the fiber amplifier system.

Since in Advanced Virgo, the use of multiple fiber amplifiers is considered, we use the term *fibered seed lasers* to refer to the conceptual building block that precedes the *phase actuators* building block and the *fiber amplifiers* building block, and the term *laser source* for the beam before branching, as illustrated in Figure 4.1.

For Advanced Virgo, the construction of the *fibered seed lasers* building block depends on a few criteria:

- The laser source has to fulfill the noise requirements described in Section 2.7.

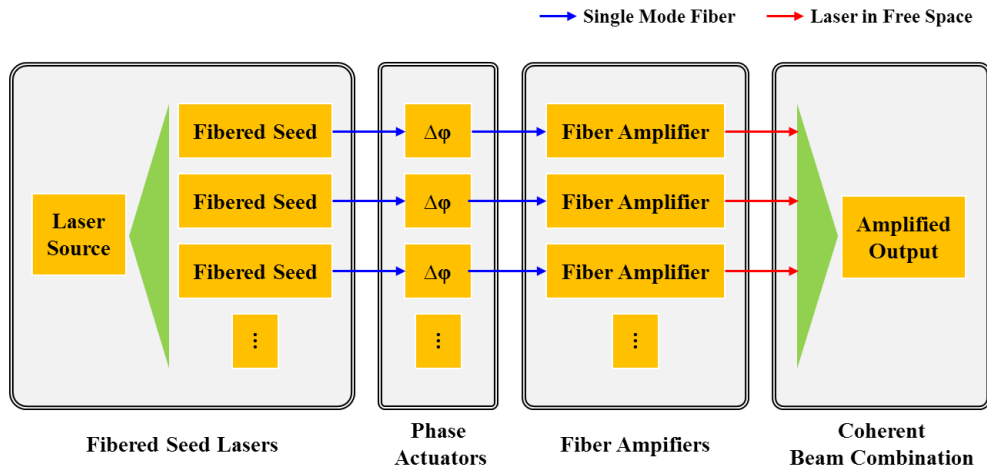


Figure 4.1: Conceptual building blocks for coherently combined master oscillator fiber power amplifiers.

In theory, an ideal laser amplifier inherits the properties of its input laser signal, so having a stable laser source makes things easier from the beginning.

- The laser source should deliver a few hundred mW of optical power. This criterion is bounded by two observations, and scaled by the number of fiber amplifiers to be combined. The input power required by fiber amplifiers can be as low as ~ 15 mW, while the maximum power rating of fiber electro-optic phase modulators is 100 mW ¹. To account for the considerable loss (~ 0.7 dB, cf. IL, insertion loss, in Figure 4.4) of common fiber connectors, we should consider 100 mW per fiber amplifier as limited by the fiber phase modulators. Accordingly, if the combination of more than three fiber amplifiers is considered, the laser source should deliver $> 300 \text{ mW}$.
- A strong plus if the laser source is intrinsically guided in an optical fiber, or if the laser head may be separated from its electronic driver.

The last criterion come from additional environmental considerations in the Advanced Virgo facilities, where there are the physically separated ($\sim 10 \text{ m}$):

- *laser room* dedicated to core optics and laser components; has better cleanliness.
- *electronics room* for equipments that should not be placed in the *laser room*; has lower level of cleanliness.

Then, first of all, to avoid noise contaminations such as electromagnetic interference and acoustic coupling on various control loop signals, all noisy equipment should be placed in the *electronics room*. Secondly, in terms of cleanroom management, components that may require maintenance should also be placed in the *electronics*

¹See, e.g., Photline electro-optic phase modulator, NIR-MPX-LN-0.1, <http://www.photline.com/product/view/52/pdf/>

room. Last, to facilitate heat management and to avoid temperature gradients, highly thermal dissipative equipments should also be placed in the *electronics room*.

As discussed in Section 2.1, the NPRO laser is the state of the art when both high power and good noise performance are considered, so the *fibered seed lasers* building block may be construct simply by the fiber-coupling and the beam-splitting of the NRPO laser, as will be shown in the next section.

Currently Advanced Virgo foresees to place also the NPRO laser in the *electronics room*. On the one hand, it is not clear whether this leads to other concerns. On the other hand, the fan in the electronic driver of the NPRO laser is known to cause noise problems during the integration of the PSL and the INJ subsystems. Owing to the finite range (~ 1.5 m) of the proprietary electric cable between the NPRO laser and its electronic driver, we are not able to separate and place them in the two rooms. The NPRO laser will thus be located in the *electronics room* and the beam delivery to the *laser room* will be made with optical fiber connections.

We do not know whether the laser head and the electronics of other alternatives laser sources are separable by the physical distance required in Advanced Virgo facilities, but as long as the laser sources are intrinsically fibered and therefore do not require bulk optics, their placement in the *electronics room* will at least be less prone to dust and other environmental factors.

Taking all these considerations into account, Figure 4.2 shows a possible configuration for the Advanced Virgo laser system, where the NPRO laser is used as the laser source for the *fibered seed lasers* building block.

A possible alternative is to use low-noise single-frequency laser sources that are inherently fibered (cf. Section 2.1). These laser sources often have limited output power (≤ 100 mW), and therefore require amplification. Since we are dealing with fiber amplifiers, this may be done by simply adding another fiber amplifier stage, while another possibility is to use the semiconductor optical amplifier (SOA). An all-fiber configuration of the *fibered seed lasers* building block is shown in Figure 4.3, with which the high-power system will be fibered until the *coherent beam combination* building block and thus require neither optical alignment nor demanding cleanroom environment.

4.2 Fiber Coupling of the NPRO Laser

During the course of this study, three NPRO lasers were used, hereinafter denoted as NPRO-400, NPRO-800 and NPRO-900, in which the number indicates roughly the output power in mW. All three NPRO lasers had been coupled to polarization-maintaining single-mode fibers.

Fiber of Interest

PM980-XP alike polarization-maintaining (PM) single-mode (SM) fibers are used in our experiments. The specifications from various providers are shown in Figure 4.4 among which we extract the following:

- Numerical Aperture (NA): 0.120.

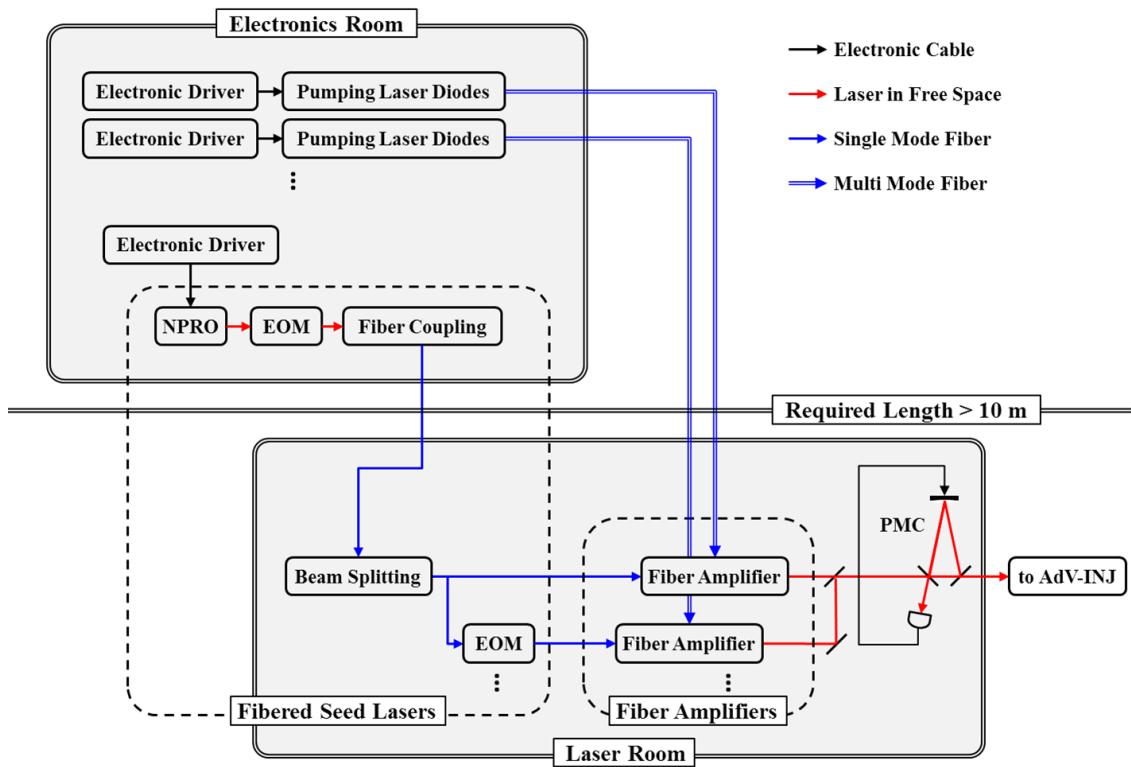


Figure 4.2: A possible configuration for the Advanced Virgo laser system.

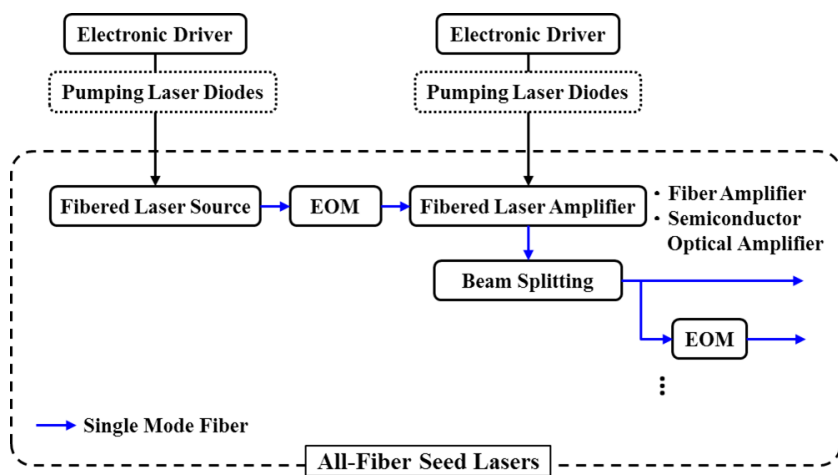


Figure 4.3: An all-fiber configuration of the *fibered seed lasers* building block.

- Core Diameter: 5.5 μm .
- Mode Field Diameter (MFD): 7.2 μm @ $\lambda = 1064 \text{ nm}$.
- Insertion Loss (Fiber Connection): 0.7 dB.

Also, we generally use fiber patch cords with uncoated FC/APC (fiber connector, angled physical contact) facets and launch the linearly-polarized laser beam with its polarization aligned to the slow axis of the PM fiber, which is also the industry standard of the orientation of the FC/APC key. We generally use the narrow key (Type R) format.

The APC angle is $\theta_{fiber} \sim 8^\circ$ in the plane of the fast axis (crossing the fiber axis), therefore the beam is S-polarized when its polarization is aligned along the slow axis. Apply Snell's law (or *la lois de Descartes*), we have:

$$(n_{silica} \sim 1.45) \cdot \sin(\theta_{fiber} \sim 8^\circ) = (n_{air} \sim 1) \cdot \sin(\theta_{air} \sim 11.6^\circ), \quad (4.1)$$

and by assuming silica-air interface with a refractive index contrast of $n_{silica} \approx 1.45$ and $n_{air} \approx 1$, we obtain the reflection losses R_{APC}

$$\begin{aligned} R_{APC}^S &= \left| \frac{n_{silica} \cdot \cos(\theta_{fiber}) - n_{air} \cdot \cos(\theta_{air})}{n_{silica} \cdot \cos(\theta_{fiber}) + n_{air} \cdot \cos(\theta_{air})} \right|^2 \approx 3.6\% \\ R_{APC}^P &= \left| \frac{n_{air} \cdot \cos(\theta_{fiber}) - n_{silica} \cdot \cos(\theta_{air})}{n_{air} \cdot \cos(\theta_{fiber}) + n_{silica} \cdot \cos(\theta_{air})} \right|^2 \approx 3.2\%. \end{aligned} \quad (4.2)$$

Following Equation 2.4, the SBS threshold of this fiber is $\sim 17 \text{ W m}^{-1}$. The configuration shown in Figure 4.2 comprises fiber beam delivery with $> 10 \text{ m}$ length.

To ensure that the beam delivery over such length does not introduce problems, simple experimental verifications were performed using the setup illustrated in Figure 4.5. The comparison of PD1 and PD2 provides information on the fiber coupling process, and the comparison of PD2 and PD3/Calorimeter provides information on the beam delivery process.

More than 1 W of single- frequency optical power was injected into the 25 m long fiber. The output power was measured to be proportional to the input power (Figure 4.6), and no additional noise was observed (Figure 4.7).

We note that the variable attenuator was inserted only for power noise measurements with PD3. Optical power levels between 35 mW and 997 mW were injected to the 25 m fiber, and by tuning the variable attenuator we ensured that the shot noise measurement floors were comparable. All the measured power noise levels after the 25 m fiber were comparable, among which only the result with the maximum injected power is shown.

The measurement result infers that the SBS threshold is $> 25 \text{ W m}^{-1}$, which is higher than the theoretical value. It can therefore be suggested that in a typical fiber implementation, the SBS gain is broadened due to mechanisms described in Section 2.3. The feasibility of fiber beam delivery of $\sim 1 \text{ W}$ of optical power over $\sim 10 \text{ m}$ length, as illustrated in Figure 4.2, is therefore justified.

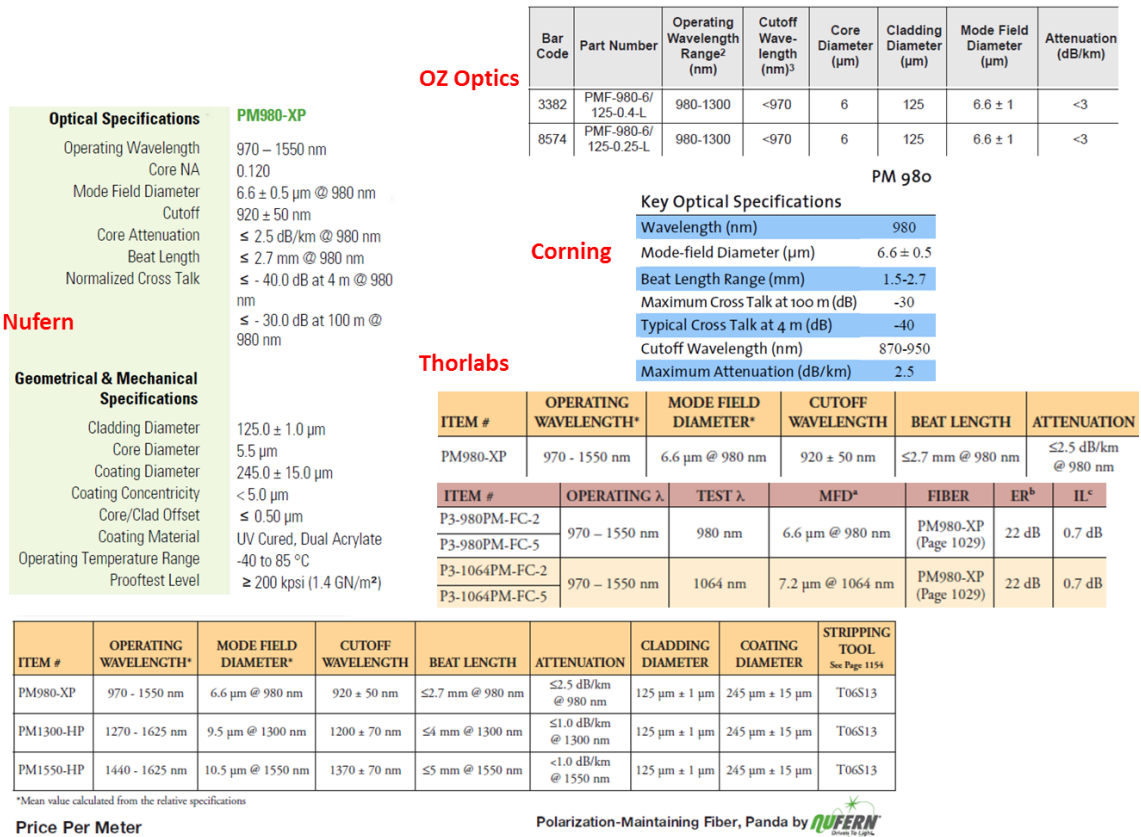


Figure 4.4: Specifications of PM980-XP polarization-maintaining single-mode fiber from various providers.

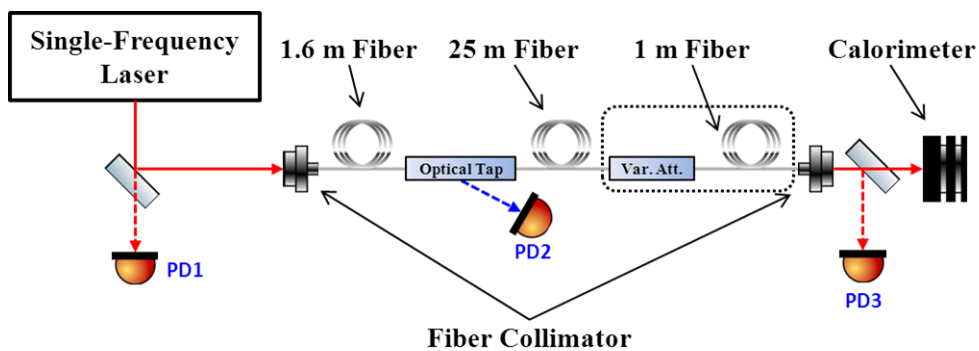


Figure 4.5: Setup for testing fiber coupling and beam delivery with up to ~ 1W optical power.

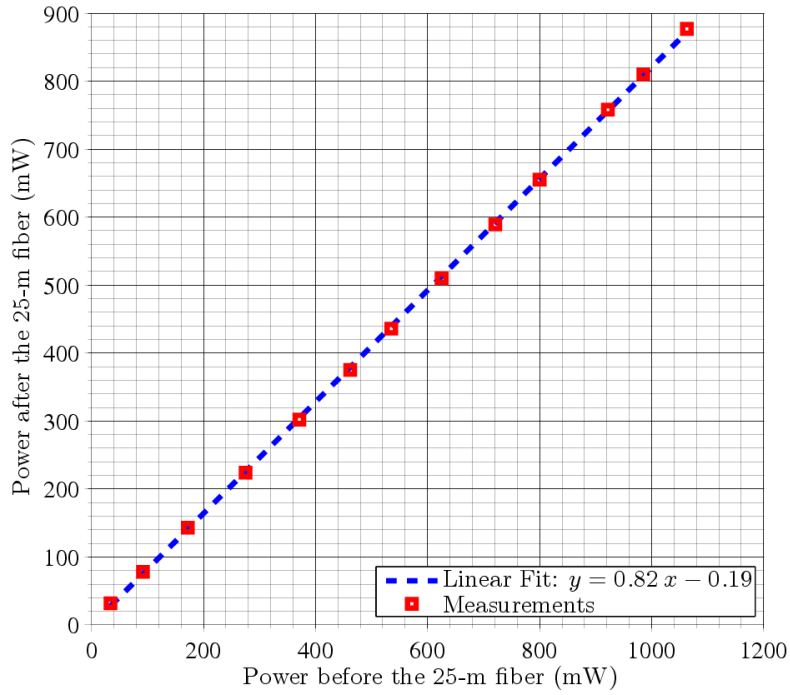


Figure 4.6: Output power vs. input power of the 25 m long PM980-XP like fiber.

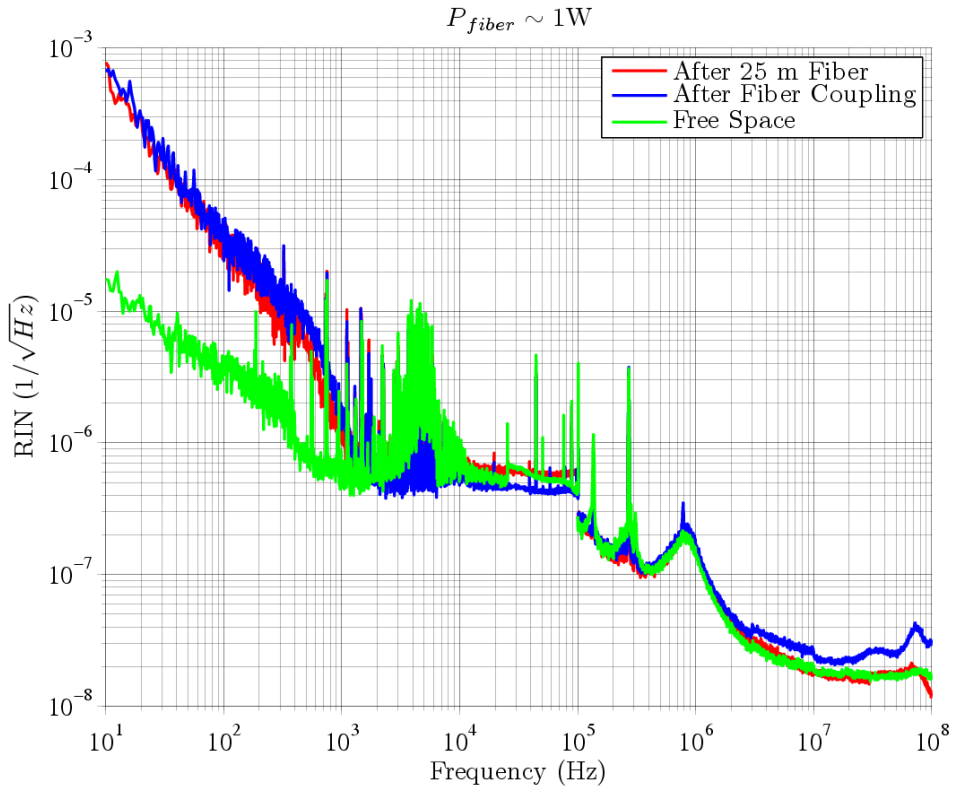


Figure 4.7: Power noise of a laser beam before and after fiber coupling (~ 1 W coupled), and after a 25m long PM980-XP alike fiber. We note that the *After Fiber Coupling* (blue) curve was measured with lower photocurrent and therefore the measurement floor was higher at high frequencies.

Fiber Coupling Loss and Noise

From Figure 4.7 we also see that fiber coupling introduces additional power noise in the low frequency range. This is very likely due to mechanical and acoustic vibrations in the setup, as explained in the following.

Consider two Gaussian fields defined as in Equation 3.74 whose waist locations are identical,

$$\begin{aligned}\Phi_G &= \frac{2}{\omega_0} \cdot \sqrt{\frac{1}{2\pi}} \cdot e^{-\left(\frac{r}{\omega_0}\right)^2} \\ \Phi'_G &= \frac{2}{\omega'_0} \cdot \sqrt{\frac{1}{2\pi}} \cdot e^{-\left(\frac{r+\Delta_r}{\omega'_0}\right)^2},\end{aligned}\tag{4.3}$$

where Δ_r is the separation of the beam axes.² The power transmission T is then the square of the integral of the modal overlapping of these two fields, as defined in Equation 3.76. The power noise coupling factor κ due to beam pointing instability defined in Equation 3.6 is then

$$\kappa = \frac{1}{T} \cdot \frac{\partial T}{\partial \Delta_r}.\tag{4.4}$$

As one can see, the κ induced by fiber coupling is linearly dependent on Δ_r , following the property of the exponential function.

Noting that since the separation Δ_r of the beam axes breaks the axial symmetry, it is more straightforward to consider the integral in Cartesian coordinates. The results obtained numerically³ assuming identical beam waist radius are shown in Figure 4.8.

Figure 4.9 shows some commercially available fiber collimators designed for 1064 nm wavelength. The output beam diameter (BD) is calculated with the formula: $BD = 2 \times f \times NA$, and the numerical aperture (NA) is calculated with the half divergence angle associated with the mode field diameter (MFD). We note that the NA value obtained this way is different from that shown in Figure 4.4, but the derived beam diameter values fit experimental measurements (Figure 4.10).

For example, if we assume a beam waist radius of $\omega_0 = 600 \mu\text{m}$ for fiber coupling and a centering error of $6 \mu\text{m} = \omega_0/100$, the resulting κ is $\sim 17 \text{m}^{-1}$, which is significant and may thus explain the additional power noise introduced by fiber coupling at low frequencies.

On the other hand, the loss due to misalignment is insignificant, only $\sim 1\%$ loss takes place for a lateral misalignment of $\sim 0.1 \omega_0$. We do not discuss losses due to other geometrical origins, while Figure 5.6 — although compiled for a study on coherent beam combination efficiency — also gives some ideas on this topic. The approximated expansions of general misalignments in [150] may also be used to estimate the effect of misalignment on coupling loss.

²The formulation here may give the impression of a non-Gaussian shape for Φ'_G . To avoid confusion, a vector form should be used for Δ_r but is dropped here for simplicity.

³Calculation window: $6 \omega_0 \times 6 \omega_0$; step resolution: $dx = dy = 0.01 \omega_0$.

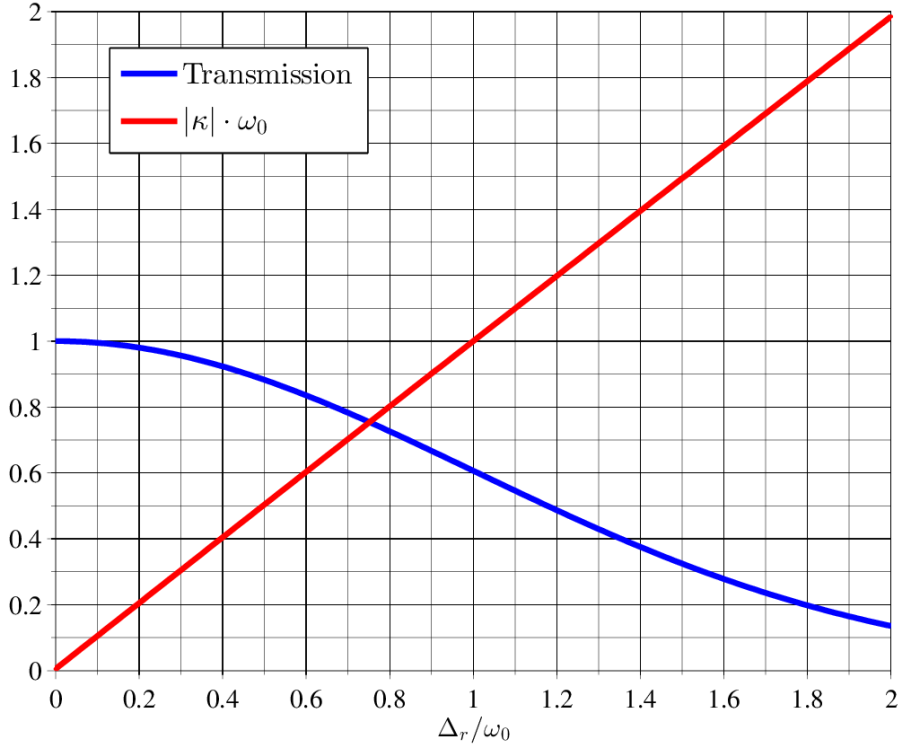


Figure 4.8: κ due to fiber coupling.

NPRO-400

The beam waist of NPRO-400 was measured to be $\omega_0^x = 157 \mu\text{m}$ in the horizontal plane, and $\omega_0^y = 173 \mu\text{m}$ in the vertical plane for a pumping current of 1.1 A.

With a typical coupling setup shown in Figure 4.11 (but without the isolator⁴), a coupling efficiency of $> 85\%$ was obtained. Assuming reflection loss of $\sim 3.6\%$ (Equation 4.2) per FC/APC, the mode-matching reaches $> 92\%$. The coupling efficiency time series is shown in Figure 4.12, and the histogram in Figure 4.13. The fluctuation follows normal distribution, with a standard deviation of $\sim 0.5\%$.

The NPRO-400 setup was initially mounted on an optical table under a hood, and later transferred onto a $450 \text{ mm} \times 450 \text{ mm}$ optical breadboard.

NPRO-900

The NPRO-900 was temporarily used⁵ to provide the input power required ($> 400 \text{ mW}$) for the Nufern and the Eolite fiber amplifiers discussed in the next sections.

The output power vs. pumping current of NPRO-900 is shown in Figure 4.14. The beam propagation measurement is shown in Figure 4.15.

⁴Since after the fiber coupling process, the optical power reduces to $\sim 300 \text{ mW}$, a miniature fiber isolator/circulator may be used for convenience and compactness. Miniature fiber-optic components generally have a maximum power rating of $\sim 300 \text{ mW}$, with few exceptional cases of $\sim 500 \text{ mW}$.

⁵We acknowledge the kind loan from European Gravitational Observatory (EGO), Cascina, Italy.

PM980-XP	Wavelength	1064	nm
	MFD	7.2	um
	Divergence Half Angle	0.09	radian
	Numerical Aperture	0.09	
Collimator Nominal Focal Length (mm)	Output Beam Diameter (mm)	Remark	Focal Shift at 1064 nm
1.14	0.21	OZ Optics, For Focuser Only	
1.47	0.28	OZ Optics	
2.03	0.38	OZ Optics	
2.76	0.52	OZ Optics	
3.95	0.74	OZ Optics	
5.07	0.95	OZ Optics	
6.34	1.19	OZ Optics	
8.11	1.52	OZ Optics	
8.13	1.53	Thorlabs F240APC-C	-0.0509 mm
11.17	2.10	Thorlabs F220APC-1064	
11.32	2.13	OZ Optics	
14.24	2.68	OZ Optics	
15.52	2.92	Thorlabs F260APC-C	-0.0786 mm
18.67	3.51	Thorlabs F280APC-C	-0.0951 mm
18.68	3.51	OZ Optics	

Figure 4.9: Some commercially available fiber collimators designed for 1064 nm wavelength. The ones highlighted in yellow were used in our experiments.

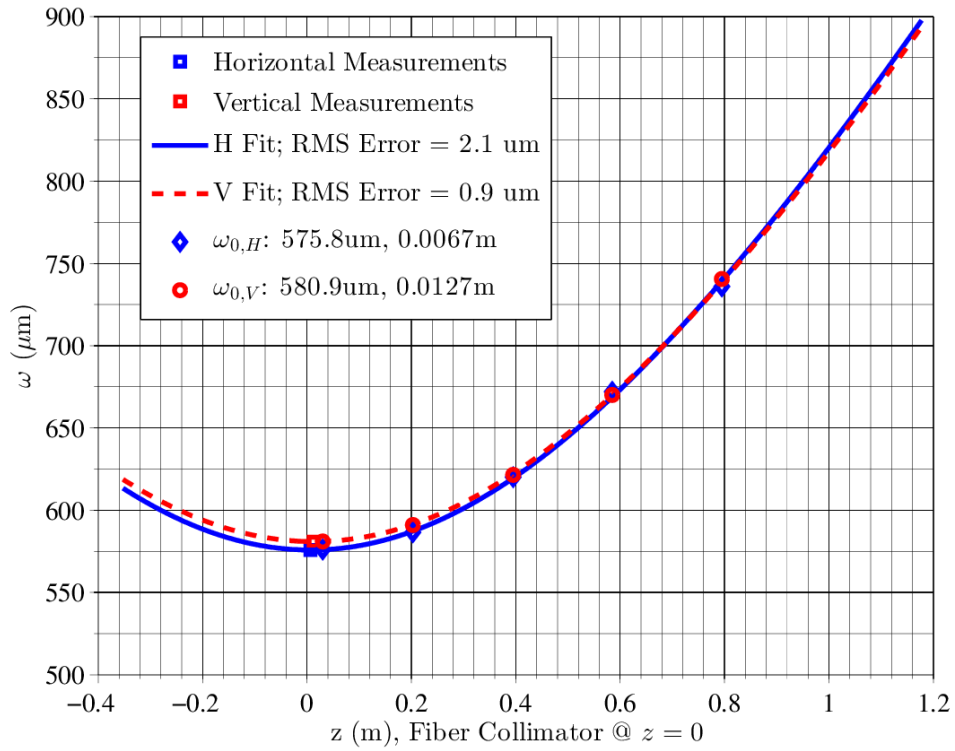


Figure 4.10: Beam propagation measurement of the PM980-XP fiber using a collimator with focal length $f \sim 6.34 \text{ mm}$.

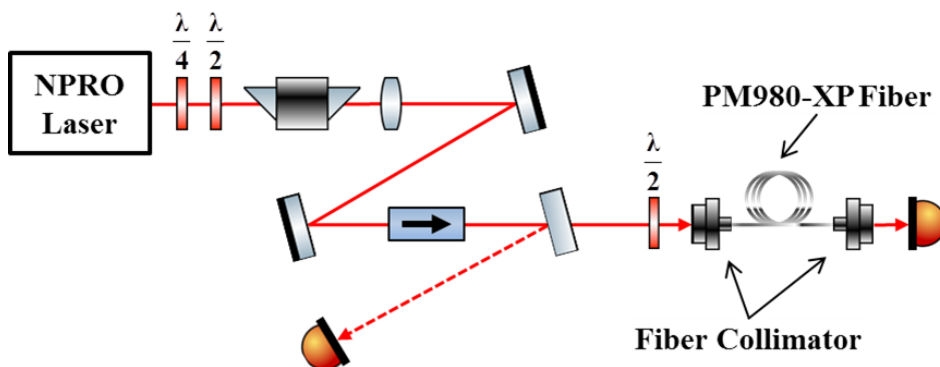


Figure 4.11: Fiber coupling of the NPRO laser.

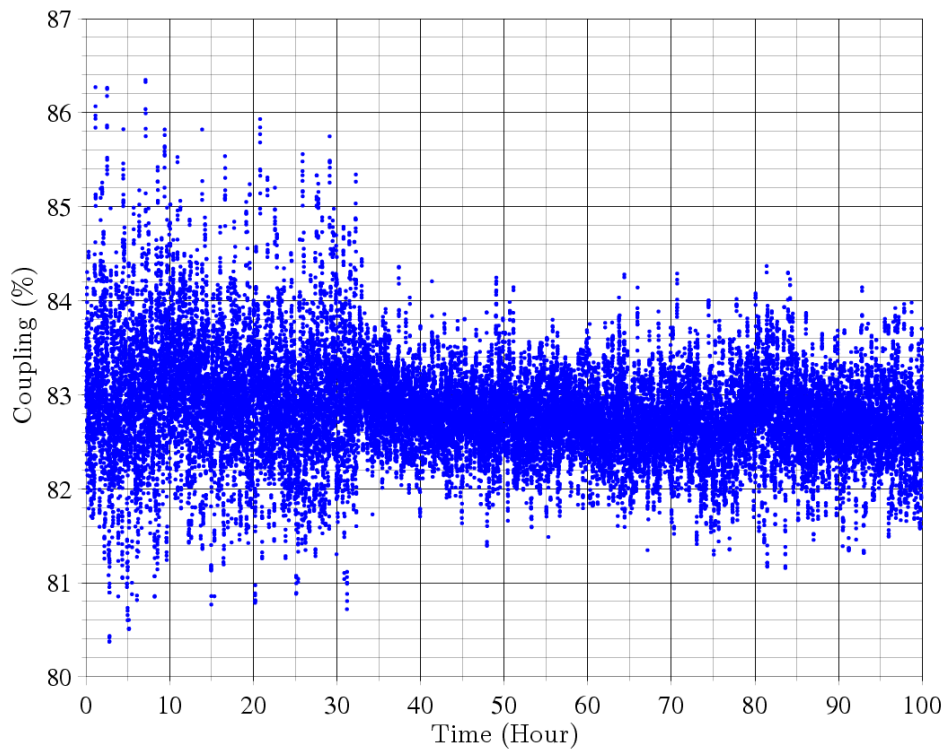


Figure 4.12: Fiber coupling efficiency time series of NPRO-400.

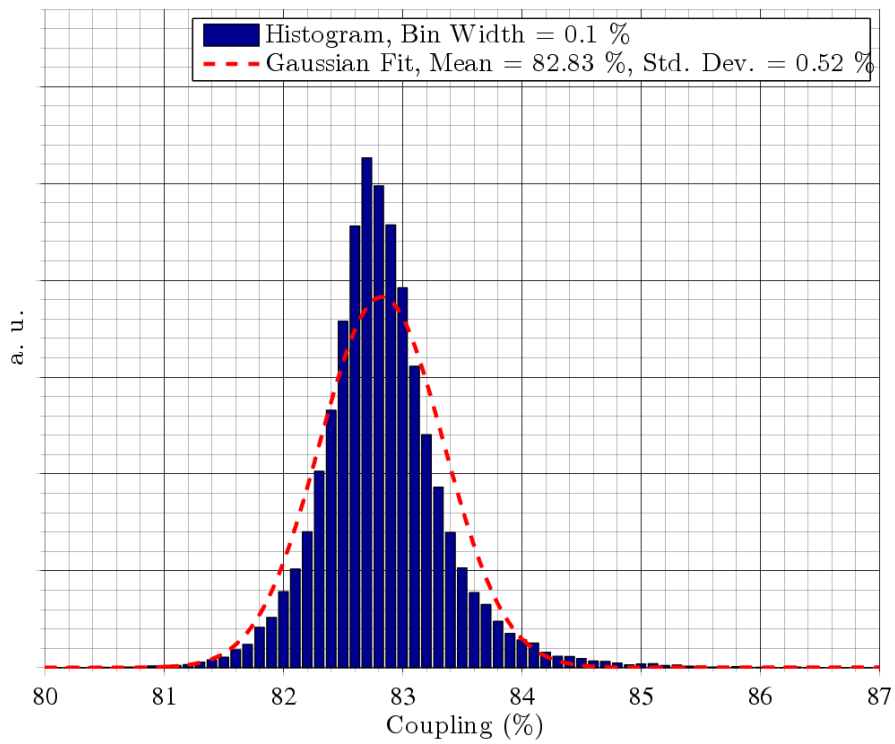


Figure 4.13: Fiber coupling efficiency histogram of NPRO-400.

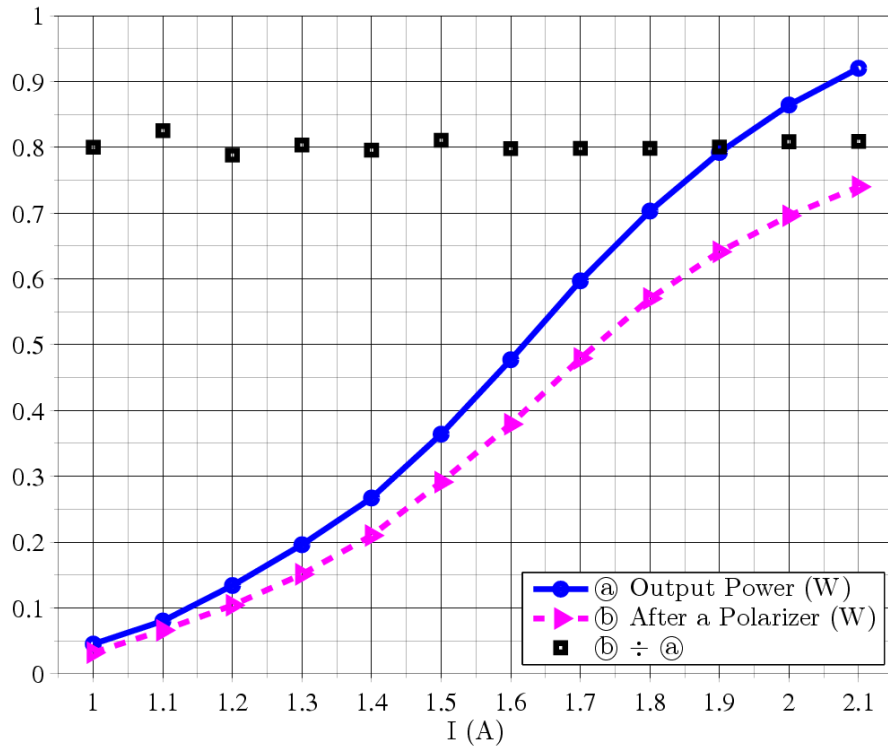


Figure 4.14: Output power vs. pumping current of NPRO-900.

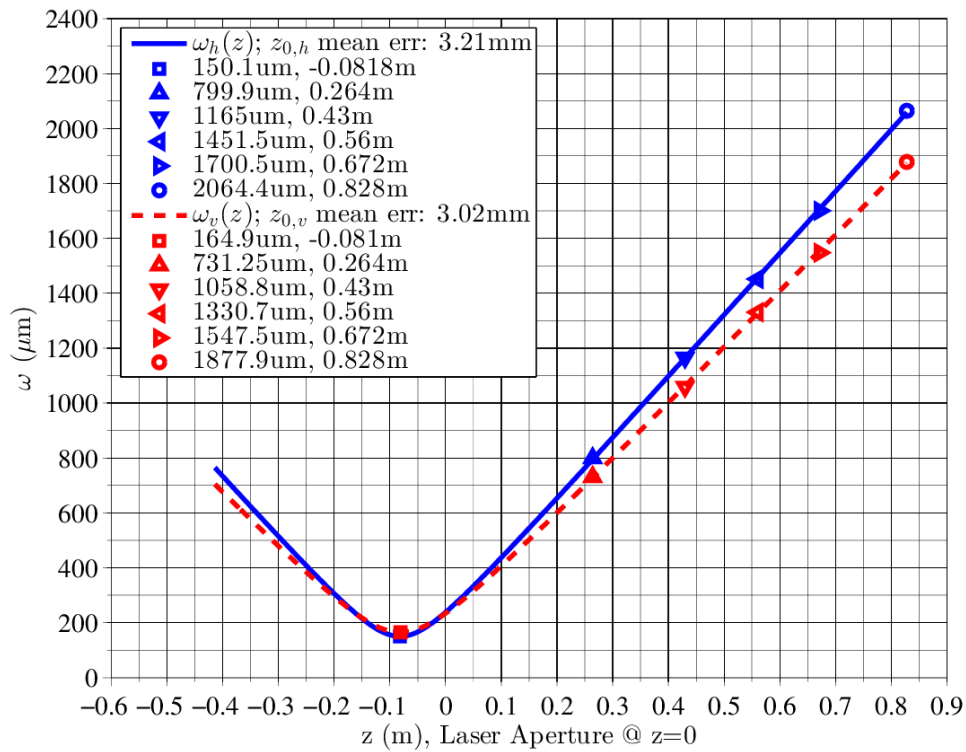


Figure 4.15: Beam propagation measurement of NPRO-900. Pumping current $I = 2$ A.

Using the setup shown in Figure 4.11 led to $\sim 90\%$ coupling efficiency (Figure 4.16). In deriving the coupling slope efficiency, the power injected to the fiber was adjusted with both the tuning of the polarization (by rotating the first half-wave plate in Figure 4.11) and the tuning of the pump current of the NPRO (Figure 4.14). We see from the results that the beam profile of the NPRO is dependent on the pump current.

The fiber coupling efficiency time series is shown in Figure 4.17, which encompasses obviously daily 24 h oscillations. The histogram is shown in Figure 4.18. We see that the short term stability of the fiber coupling for NPRO-900 is much better than that for NPRO-400. There was no systematic study based on this observation, but we recall that an optical isolator was installed for NPRO-900 but not for NPRO-400. This might be one possible reason of the instability of the setup with NPRO-400, as later in our experiments we noticed that back reflected light induced instability in the NPRO laser.

The NPRO-900 setup was mounted on an optical table under a hood.

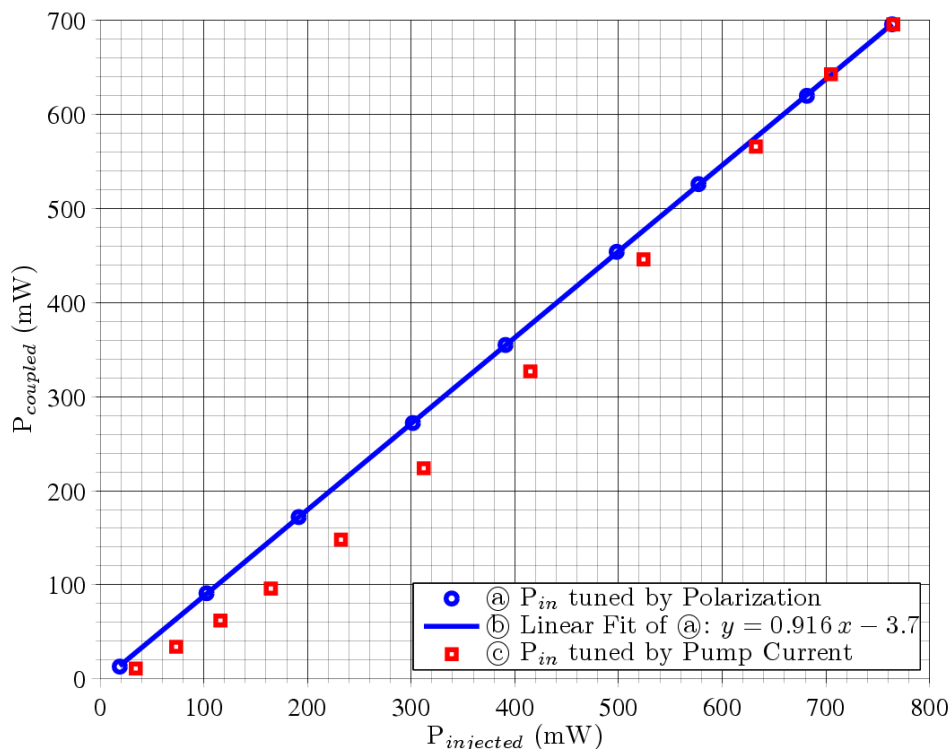


Figure 4.16: Fiber coupling efficiency of NPRO-900.

NPRO-800

The coupling setup for NPRO-900 was stable and delivered decent output power to seed the fiber amplifiers, but owing to the need of the Advanced Virgo project, we could not keep NPRO-900 and consequently had to use the very old NPRO-800, which had been lent to the Eolite company during the collaboration on rod fiber amplifiers.

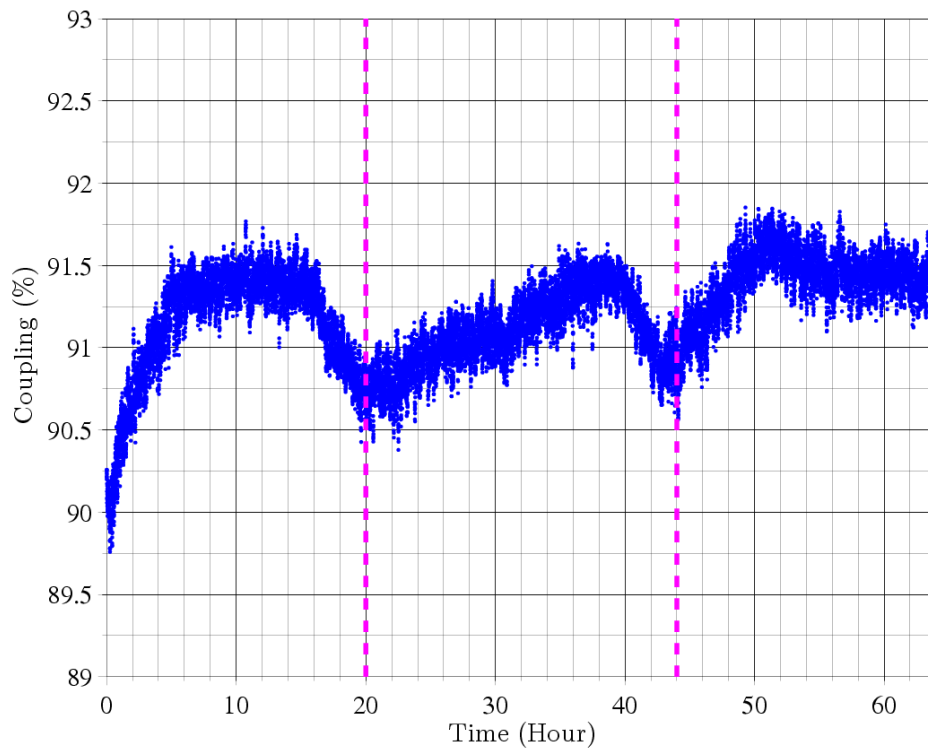


Figure 4.17: Fiber coupling efficiency time series of NPRO-900.

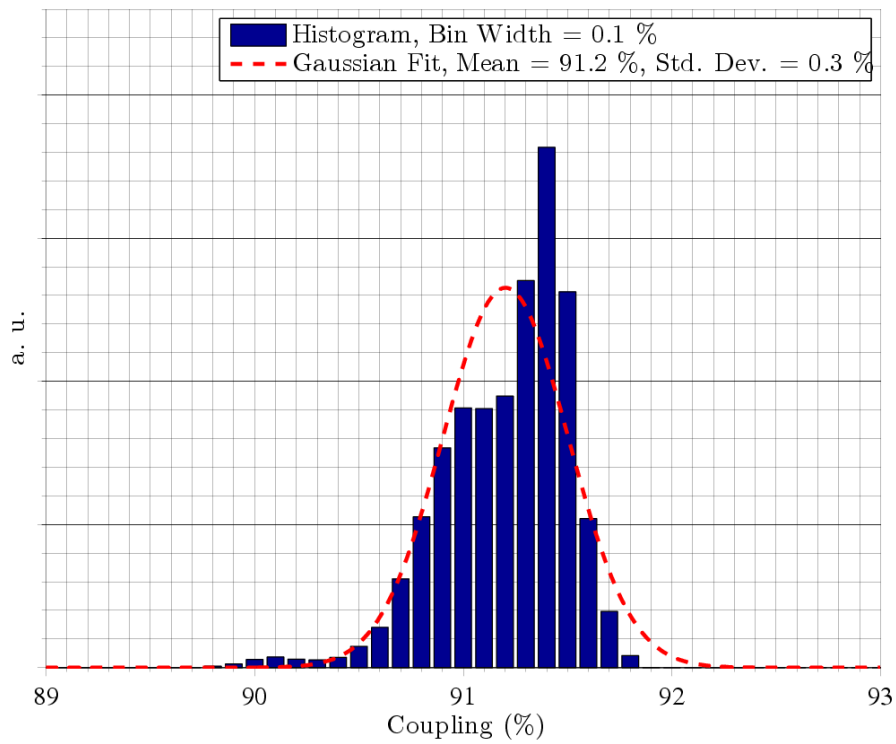


Figure 4.18: Fiber coupling efficiency histogram of NPRO-900.

The beam propagation measurement of NPRO-800 is shown in Figure 4.19. A more complicated setup (Figure 4.20) was used for the fiber coupling of the NPRO-800, with the intention to better characterize the fiber coupling of the NPRO laser. The setup was designed to fit onto a 450 mm \times 450 mm optical breadboard.

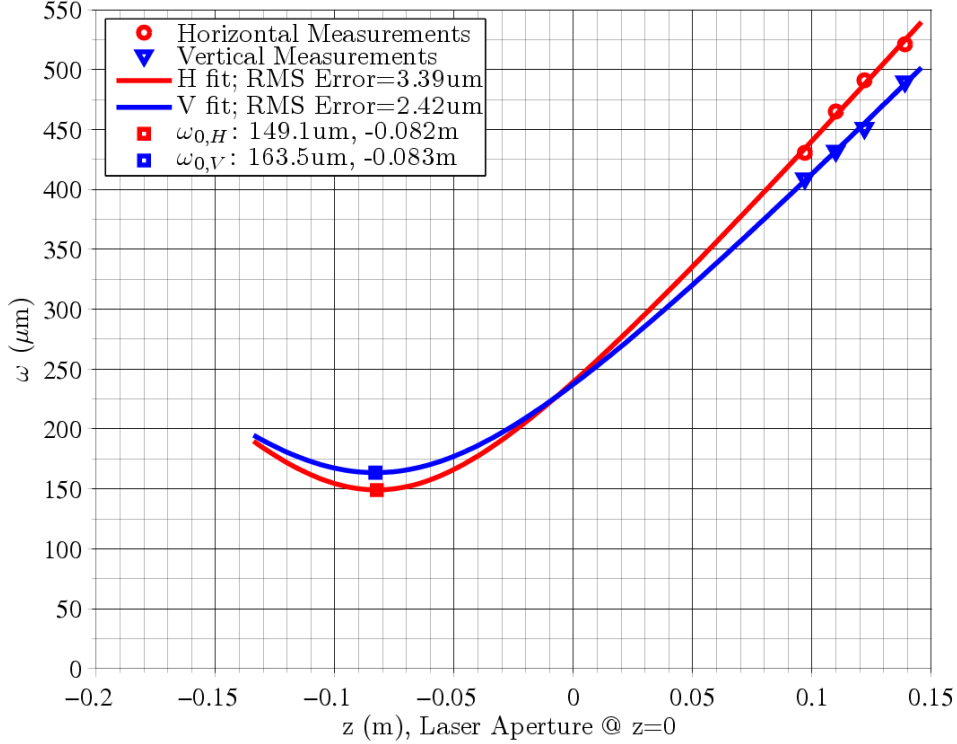


Figure 4.19: Beam propagation measurement of NPRO-800. Pumping current $I = 1.8$ A.

Despite the effort, the NPRO-800 encountered failure and consequently discouraged the systematic study planned. Some remarks may be added with respect to this effort for future attempts:

- A circulator was implemented to probe back scattered light in fiber connections. A polarization beam splitter (PBS) is used as the first polarizer for the circulator as well as to fold the optical path.
- The power ratio between the reflected beam and the transmitted beam of the PBS was maximized to $\sim 382 : 1$ ⁶.
- The power transmission of the Faraday rotator was measured to be $\sim 97\%$, while the total power transmission of the optical isolator was measured to be $\sim 90\%$.
- There was some reflection off the second surface of the Faraday rotator arriving at the photodiode PD2, affecting the sensitivity on the probing of the back-reflected light coming from the fiber. This may be avoided with better AR

⁶We note that the measurement was limited by the dynamic range of the optical power meter and ambient light. The true ratio should therefore be higher than this.

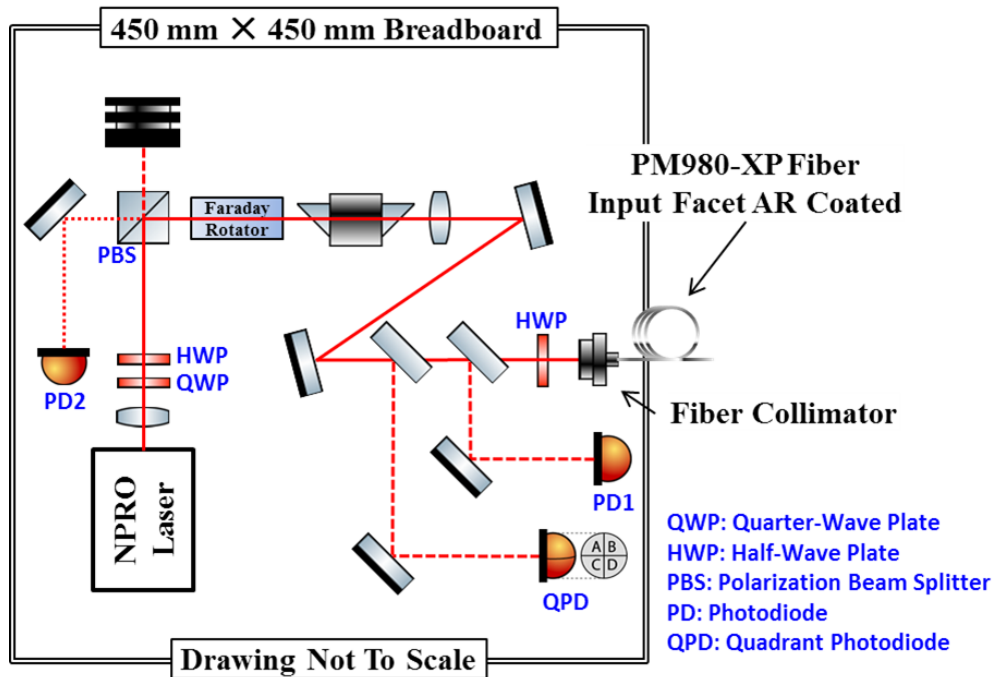


Figure 4.20: Fiber coupling of NPRO-800.

coatings on the Faraday crystal, or by tilting the crystal to segregate the beams and with the use of a diaphragm.

- A fiber with anti-reflection (AR) coated input facet was used, but the maximum coupling efficiency obtained by tuning the aligning mirrors was only $\sim 82\%$, even lower than that of NPRO-400 and NPRO-900.
- Although mode mismatching may well be a good reason to explain the low coupling efficiency, in principle the coupling losses due to common tolerances on the size and the location of the beam waist should be fairly limited [155, 156]. We note that the previous attempt on the fiber coupling of NPRO-800 on an optical table with a simpler setup also resulted in limited coupling efficiency.
- The fiber coupling efficiency time series together with the injected and coupled optical power are shown in Figure 4.21. We see that the output power of the NPRO-800 underwent abrupt jumps, which might be a sign for its loss of stability due to aging. Also, the coupling efficiency showed some correlation with the power of the NPRO laser, inferring once again that the beam profile of the NPRO laser is dependent on its operating condition. Like NPRO-900, the short term stability of the coupling stability was better than NPRO-400, likely due to the implementation of the optical isolator.
- The alignment of the laser beam into the fiber is often done with low optical power to avoid damaging the fiber facet. As demonstrated in Figure 4.16, the operating condition of the NPRO laser affects its beam profile and therefore should be decided in the fiber coupling design. We note that using neutral

density filters is not an option as thermal lensing effects can also leading to misleading results. Figure 4.23 shows the change in the beam profile at a given location when a neutral density filter with optical density (OD) of ~ 0.4 was introduced in the beam path for attenuation.

- The histogram on coupling efficiency is shown in Figure 4.22. The Gaussian fit parameters are also given, although the scattering does not match that of normal distribution.

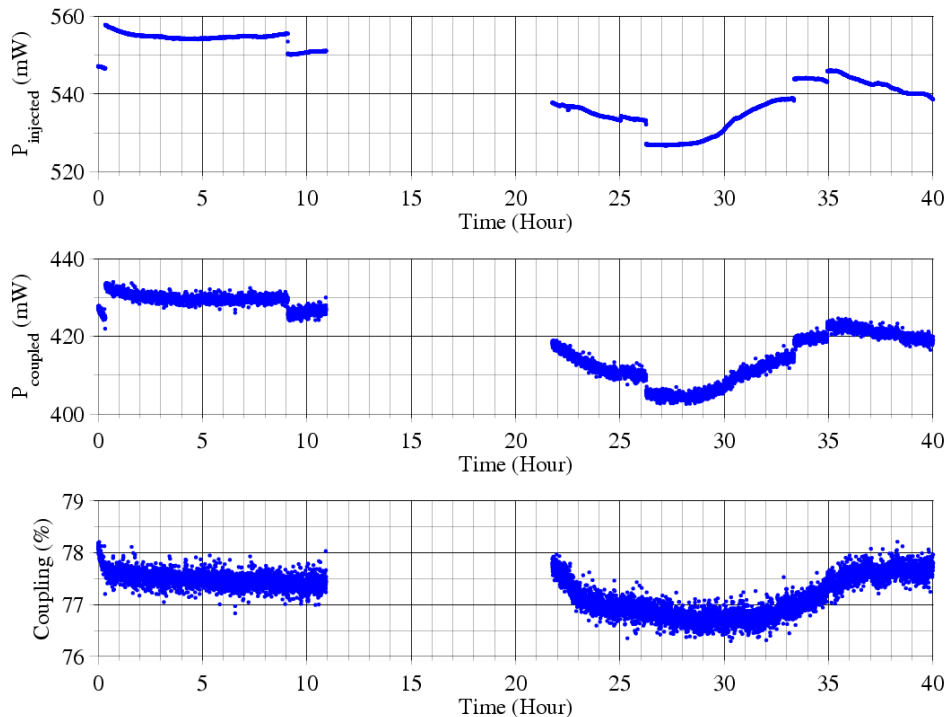


Figure 4.21: Fiber coupling efficiency time series of NPRO-800.

Summary on the Fiber Coupling of the NPRO Laser

Although we did not perform a systematic characterization on the NPRO lasers and their fiber coupling, and the results shown in this section are somewhat fractional, it should be nevertheless fair to conclude that using a fibered NPRO laser in seeding the fiber amplifiers is compatible with the requirements imposed by Advanced Virgo.

The coupling efficiency we obtained at the fiber injection level generally ranged between 80% and 90%, with a possible improvement of up to $\sim 7.2\%$ if anti-reflection coated fiber facets are used. Commercially available fiber-coupled NPRO lasers specify $> 60\%$ coupling efficiency and typically reach 70% to 80% [157]. We note that in order to make a fair comparison, the optical loss in our setup, coming from the isolator for example, might also have to be taken into account, although we do not know whether optical isolation is implemented in the commercial model.

One problem we had encountered was the optical damage at the fiber facet (Figure 4.24), which was likely due to laser beam misalignment and/or dust con-

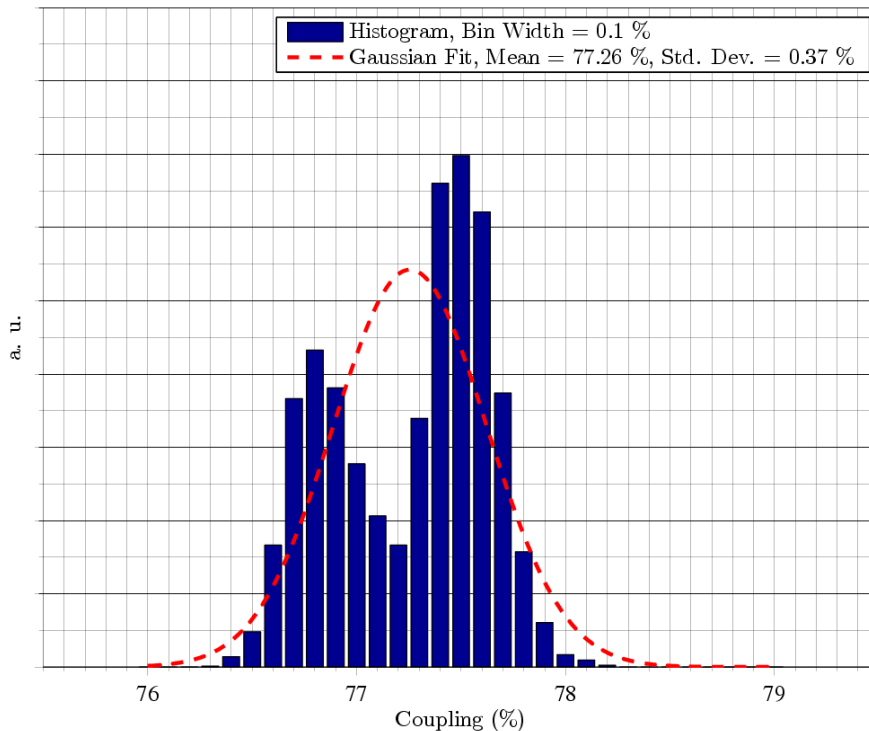


Figure 4.22: Fiber coupling efficiency histogram of NPRO-800.

tamination. This may be avoided by using sealed pigtailed fiber collimators, or by fusing the fiber to a silica rod⁷ to mitigate the effect of possible dust contamination.

Another issue for the experiments was that the NPRO lasers used were rather aged, especially NPRO-800, and went into unknown failures from time to time.

Last, although the use of a fiber-coupled NPRO laser is justified, based on the considerations discussed in Section 4.1, having an intrinsically fibered laser source and an all-fiber configuration in the *fibered seed lasers* building block is advantageous in relieving the need for optical alignment and cleanliness.

4.3 Fiber Coupling for General Beam Delivery

In the previous section we show the coupling and the delivery of the beam of an NPRO laser with an optical fiber.

Similarly, fiber coupling might provide some additional degree of freedom to tackle with the coupling factor κ coming from the inhomogeneous responsivity of photodiodes, which is a concern in the laser power stabilization system for Advanced Virgo. If the photodiode is clamped to the fiber facet such that there is no or little relative motion in between, the inhomogeneity is no longer a concern. The coupling issue is then simplified to that of finite aperture and finite alignment accuracy.

In both the case of a photodiode and the case of fiber coupling, as long as the impinging laser beam is centered with normal incidence, the coupling factor κ is null. Misalignments will have stronger effects in the case of fiber coupling as it

⁷<http://www.lightpath.com/PDFFiles/Collimators.pdf>

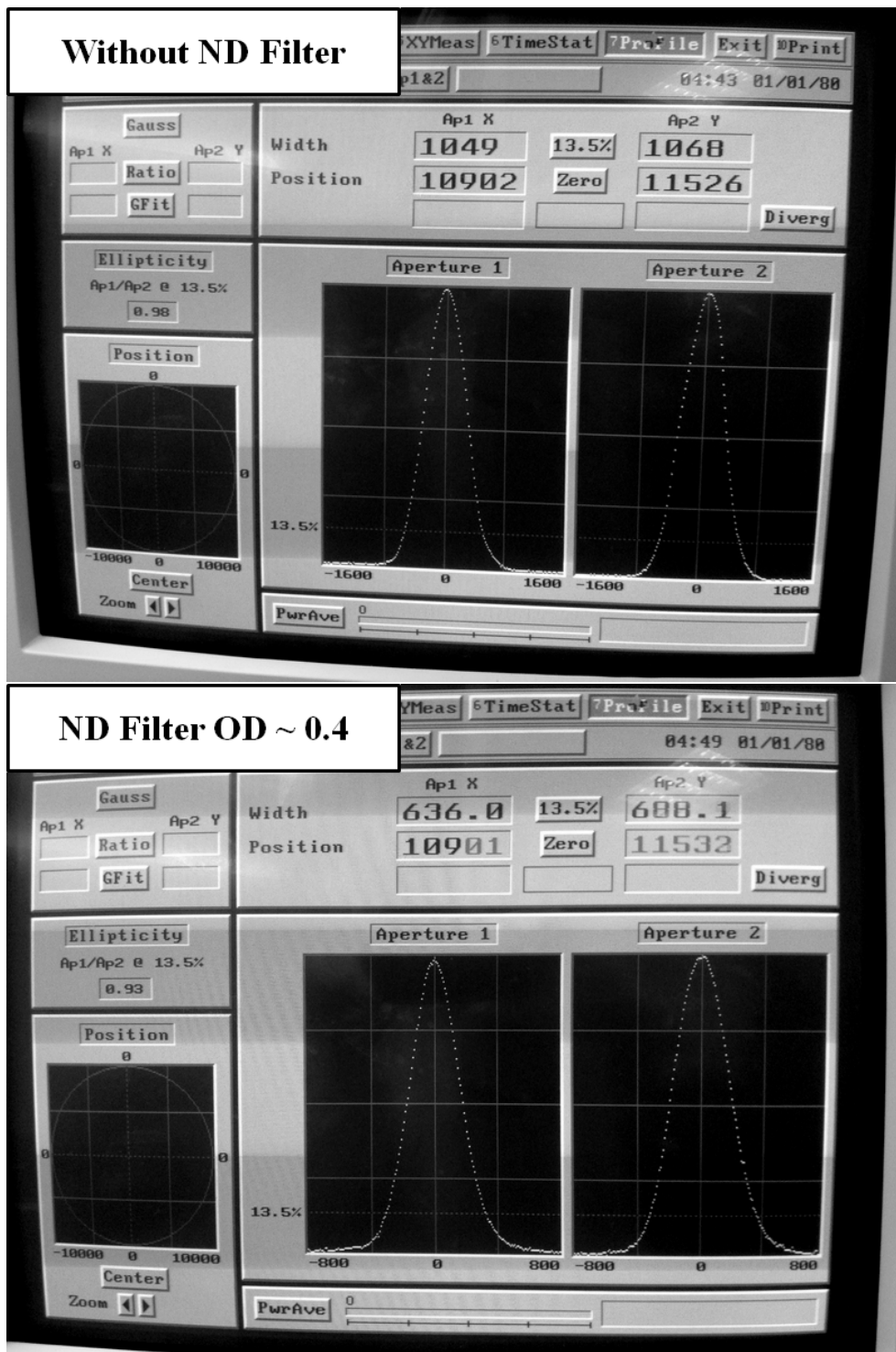


Figure 4.23: Thermal lensing of neutral density filters. The optical power was ~ 0.7 W. We note that the horizontal scales of the cross-section plots are different by a factor 2.

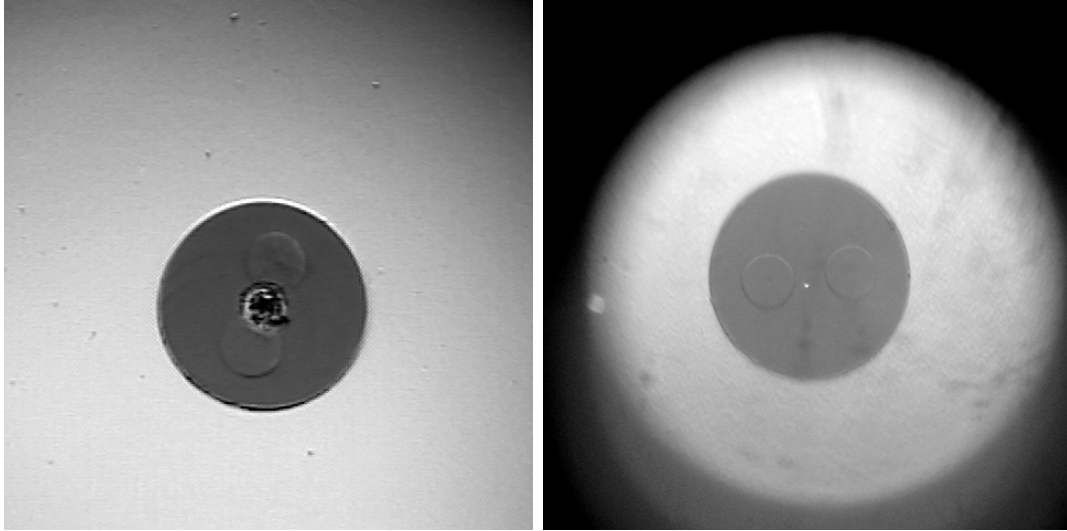


Figure 4.24: A damaged (left) facet and a normal facet (right) of a PM980-XP fiber. We note that the scale of the image may be deduced from the cladding diameter ($125\ \mu\text{m} \approx 38\%$ of the field of view) specified in Figure 4.4

depends on the overlapping of two Gaussian profiles, instead of that of a Gaussian profile and a *top hat* profile in the case of a photodiode. The *top hat*, however, has more limited dimension. The aperture of the fiber collimator, on the other hand, is generally large enough for the clipping effect to be negligible, and the output mode radius can be at the order of a few mm (Figure 4.9). In comparison, the mode waist radius of the Input Mode Cleaner (IMC) of Advanced Virgo is 5.17 mm (cf. Section 2.7).

If we assume a beam waist radius of $\omega_0 = 5\ \text{mm}$ (half divergence angle $\theta \sim 68\ \mu\text{rad}$) and a centering error of $5\ \mu\text{m}$. the coupling factor κ is then $0.2\ \text{m}^{-1}$ according to Figure 4.8. We note that in this case the equivalent pointing error required derived from the analogy in Figure 5.6 is $0.001 \times \theta \sim 68\ \text{nrad}$, which might not be feasible. A more realistic case might be to have $\omega_0 = 500\ \mu\text{m}$ ($\theta \sim 680\ \mu\text{rad}$) and a relative centering/pointing error of 0.1%, which in absolute terms is $0.5\ \mu\text{m}$ for centering, and $\sim 0.68\ \mu\text{rad}$ for pointing. We do not know the exact performance on laser beam alignment in Advanced Virgo and in normal laboratory conditions, but some ideas may be inferred from Figures 2.14 and 2.19 in which the AC counterparts are drawn.

One may argue that the photodiode may also be clamped to a certain optics for a larger apparent aperture size. This may be possible if only one photodiode is considered. In the case where multiple photodiodes are combined to deliver a high photocurrent for better RIN sensitivity, it may be difficult to clamp the whole bulk optical setup required. In other words, to reduce the coupling factor κ , the choice lies between a bigger *Gaussian hat* and a smaller *flat-top hat* with finite homogeneity.

In a fibered setup, beam-splitting can take the form of fiber couplers and therefore greatly reduces the size of the optical setup. The drawback, however, is that standard miniature fiber couplers often have a maximum power rating of 300 mW to 500 mW, and the loss of cube-like fiber beam splitters is rather significant from

our experience. In any case the maximum power rating of 500 mW matches already the power foreseen to be injected to the photodiode array for laser power stabilization in Advanced Virgo. A sealed fibered photodiode is also less prone to dust contamination, which might be advantageous for some applications.

Once the laser beam to be characterized in terms of power noise is coupled to a single-mode fiber, the optical AC coupling [114] technique may also be implemented with reduced difficulty thanks to the good beam quality, if a free-space cavity is to be used. All-fiber optical AC coupling is also possible, except that it might not be effective for low frequencies owing to the optical power damage threshold in fiber Fabry–Perot interferometers⁸. On the other hand, if laser beam quality is not an issue and only the optical power is considered, multi-mode fibers may also be considered for laser beam delivery.

4.4 Nufern Fiber Amplifiers

Prior to this study, a 100 W customized fiber amplifier from Nufern⁹ was tested in ARTEMIS and encountered an unknown failure after just a few tens of hours of operation.

In 2013, we received an engineering demo unit of a ~ 50 W commercially available fiber amplifier from Nufern. On start, the fiber amplifier delivered 49 W output power with an input power of 120 mW. Two continuous runs were carried out; the first run lasted 62 h and the second run lasted 57 h. The intended interruption between the first and the second runs was about 15 min, while the second run was interrupted due to a shutdown of the seed NPRO laser. The amplifier failed to restart after the interruption.

There were two major issues with this fiber amplifier. The first was the continuous and monotonic drop in the output power. The output power dropped by $\sim 4.5\%$ during the first 62 h run, and $\sim 1.5\%$ during the second 57 h run (Figure 4.25).

The fiber amplifier was cooled with water chillers. By lowering the temperature setting of the water chiller from 23 °C to 21 °C, the output power dropped by $\sim 6\%$. Such process is reversible, and indicates a $\sim 3\%$ per °C temperature dependence of the output power. Since the temperature of the water chiller was regulated to within ± 0.2 °C with a time constant in the order of a few minutes, the excessive output power drop of the fiber amplifier over several tens of hours should not be associated solely with temperature effects. In other words, the loss in the output power was intrinsic to the fiber amplifier.

The second major issue was the power noise plateau that extended from ~ 1 MHz to ~ 10 MHz (Figure 4.26), thereby exceeding the noise budget of the reference design of the PSL for Advanced Virgo by more than an order of magnitude. The beam pointing stability in the horizontal plane of this fiber amplifier is shown in Figure 4.27.

⁸For example, < 100 mW for finesse $\mathcal{F} = 200$, $FSR\nu_0 > 10$ MHz (Equation 2.10), Micron Optics, Fiber Fabry–Perot Scanning Interferometer, FFP-SI. The spectral resolution ($= \nu_0/\mathcal{F} > 50$ kHz)

⁹<http://www.nufern.com/>

More information on the test results of this fiber amplifier from Nufern is attached in Appendix A [158].

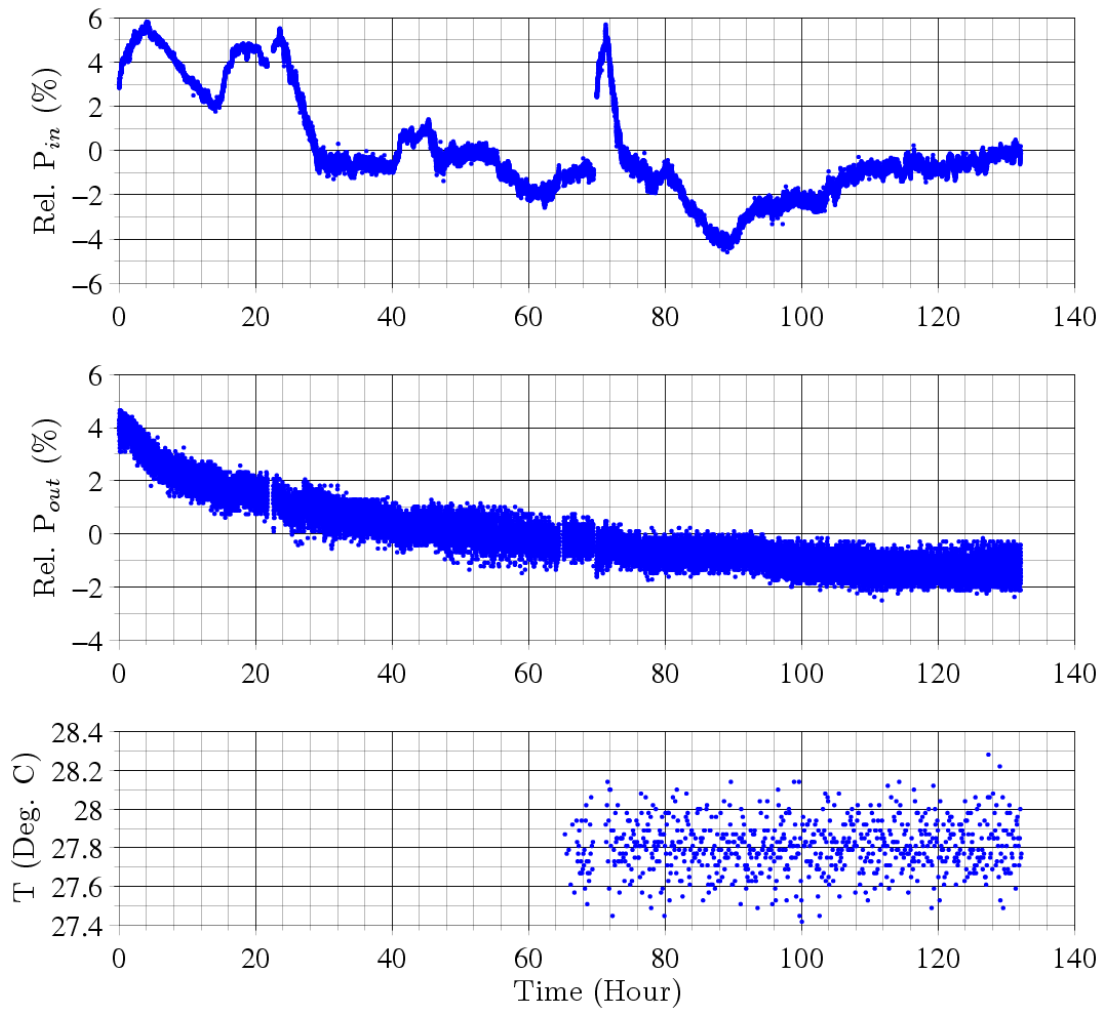


Figure 4.25: Input power, output power and temperature time series of the Nufern ~ 50 W fiber amplifier.

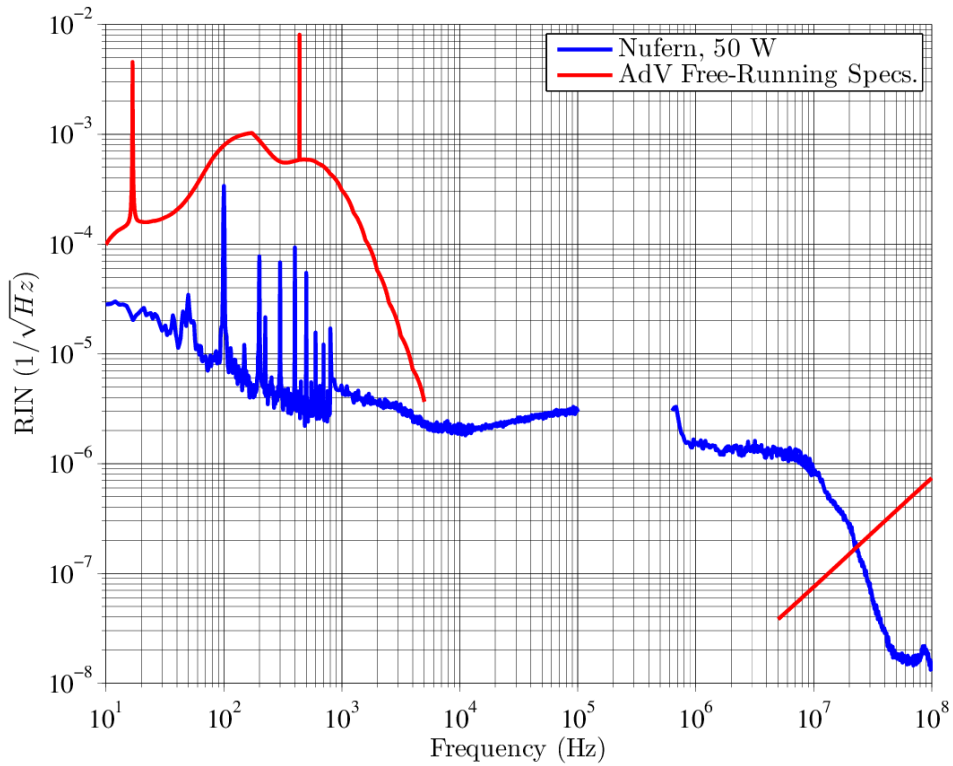


Figure 4.26: Power noise of the Nufern ~ 50 W fiber amplifier.

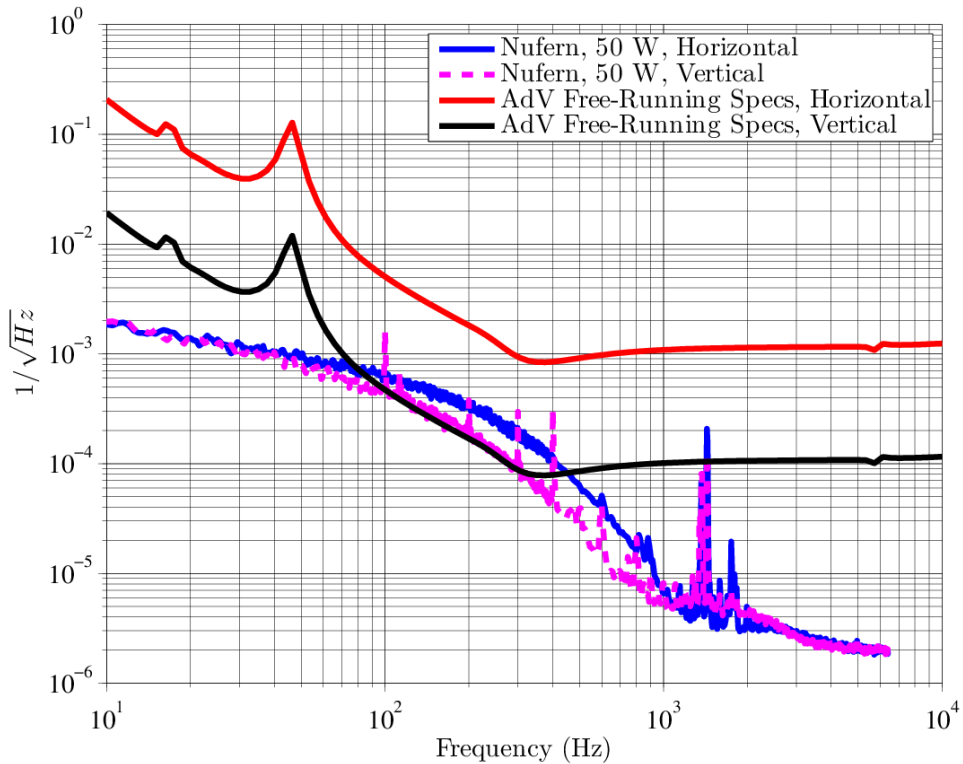


Figure 4.27: Beam pointing stability of the Nufern ~ 50 W fiber amplifier.

4.5 Eolite Fiber Amplifiers

In 2011, ARTEMIS started a collaboration with Eolite on the investigation of rod fiber amplifier technologies. The target output power, as a start, was ~ 50 W. The major problem of the rod fiber amplifier was its transverse mode instability at high power levels, as discussed in Section 2.3.

The collaboration then turned its focus to more conventional fibers, and in 2013, a fiber amplifier with ~ 27 W output power was delivered to ARTEMIS where it was tested for more than 500 h, over which the output power evolved incrementally by 2% (Figure 4.28). The measured power noise is shown in Figure 4.29, and the beam pointing stability in Figure 4.30.

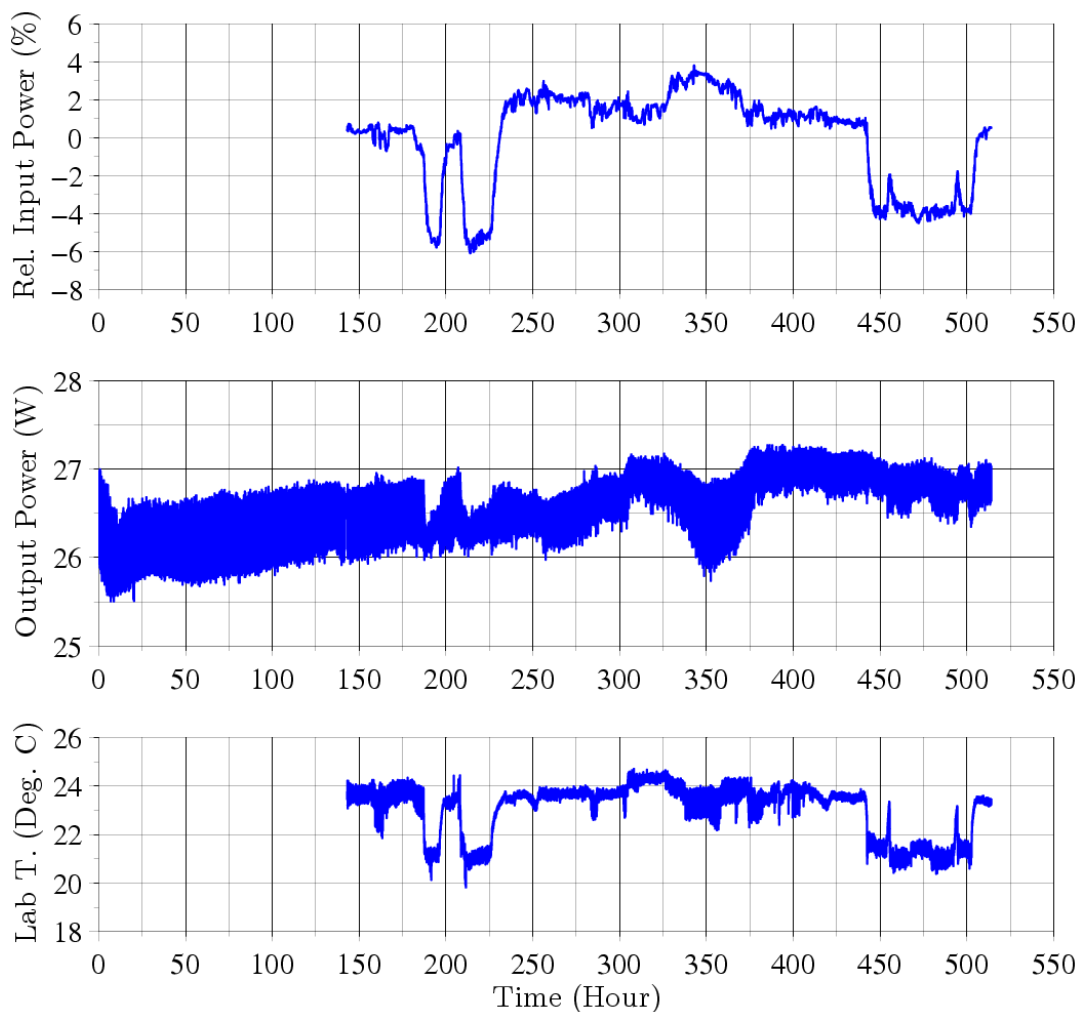


Figure 4.28: Output power time series of the Eolite ~ 27 W fiber amplifier.

The main problem with this fiber amplifier, obviously, is the shortcoming of output power. Moreover, this fiber amplifier required > 400 mW at its input. An additional pre-amplifier stage would be necessary if we had continued the collaboration in this direction.

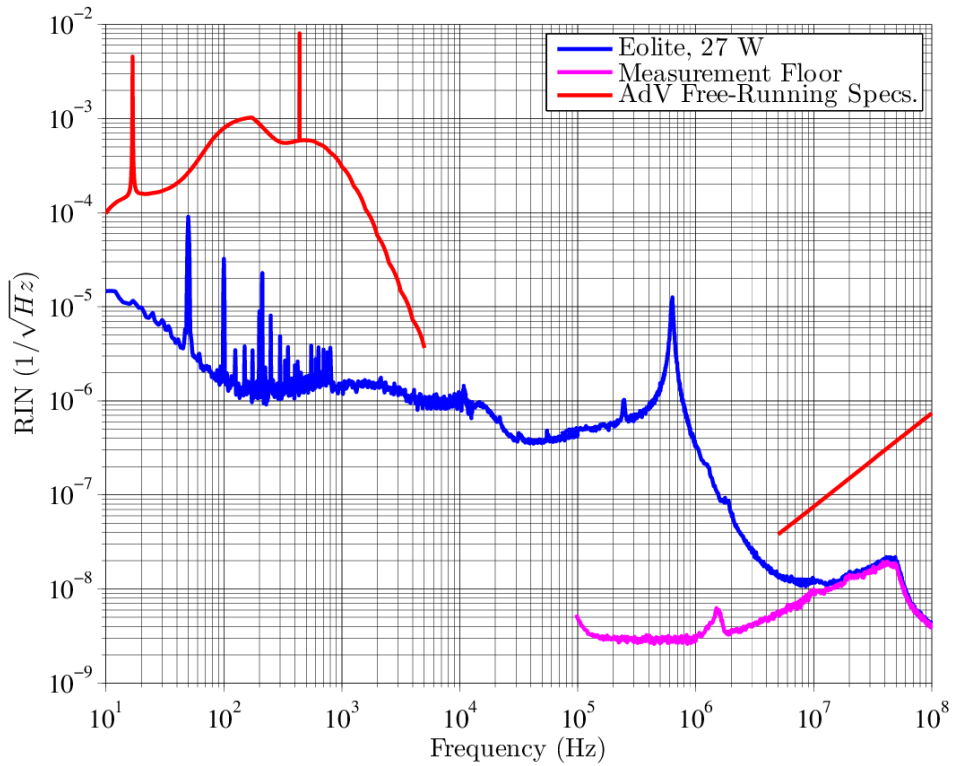


Figure 4.29: Power noise spectrum of the Eolite ~ 27 W fiber amplifier.

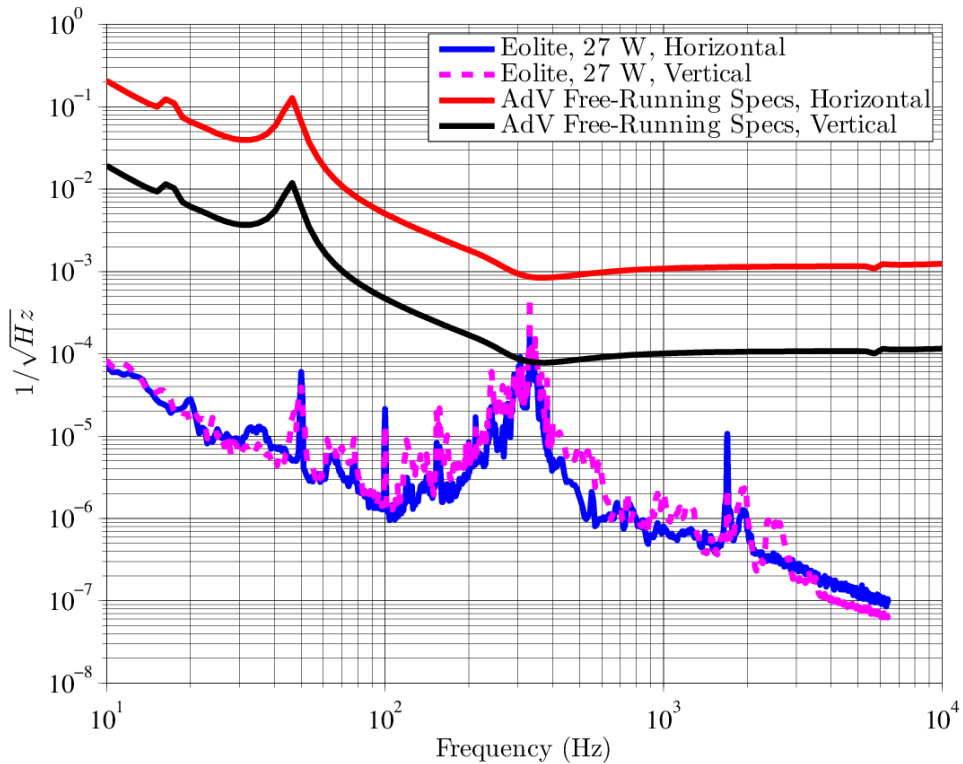


Figure 4.30: Beam pointing stability of the Eolite ~ 27 W fiber amplifier.

4.6 Azur Light Systems Fiber Amplifiers

In 2013, we made contact with Azur Light Systems, a French company, in having 50 W fiber amplifiers. Owing to the frustrating experiences we had with Nufern and Eolite, we visited the company and tested a 30 W demo unit as a cautious start. The output power, according to the company, was limited by available pump power. The demo unit had only one pumping laser diode, while the design of the active fiber was meant for as high as 70 W [159].

The test results (Appendix B) of this demo unit were satisfactory, and an order of two 50 W (two pumping laser diodes) fiber amplifiers were placed. After a considerable delay, the two fiber amplifiers (hereinafter denoted as ALS 1 and ALS 2) were delivered, one of which (ALS 1) were returned shortly to the company following the failure of the pre-amplifier.

Figure 4.31 is a schematic diagram of the fiber amplifiers. An input beam of > 20 mW is required to seed the amplifier. The input beam is pre-amplified to a few hundred mW and then amplified to a maximum of ~ 55 W before the output optical isolator (Figure 4.35). The power throughput of the isolator is $\sim 85\%$. Two laser diodes are combined to pump the ytterbium-doped double-clad large-mode-area fiber in a co-propagation setup. Rack A and Rack B are standard 19-inch racks. Rack A is cooled by forced air, while Rack B is cooling-free. Rack A and Rack B are connected by three optical fibers of about 2 m length. Rack B and Laser Head is connected by a 60 cm fiber. Some photos of the fiber amplifier system ALS 2 are shown in Figure 4.32. The leakage beam from the optical isolator of ALS 2, as shown in Figure 4.33, indicates that the isolator is aligned with respect to the extinction ratio instead of the power transmission.

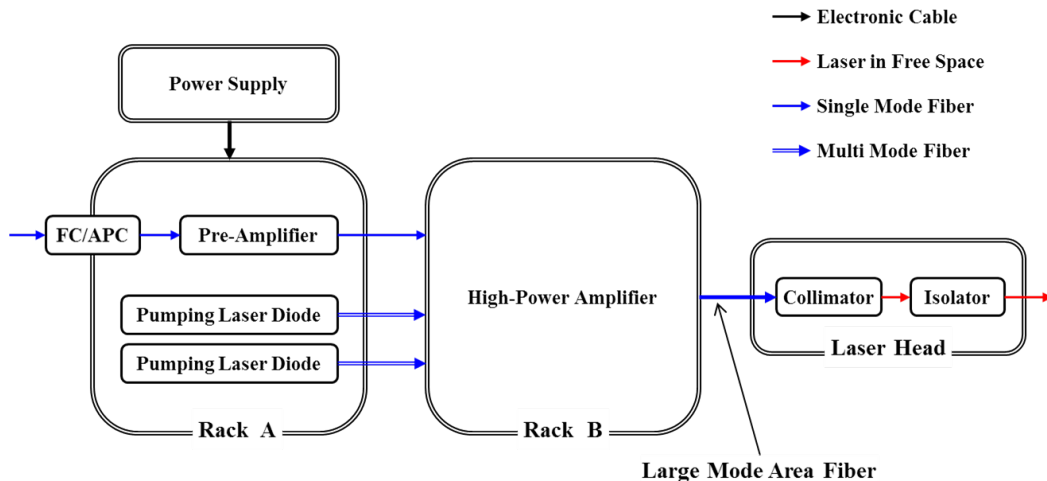


Figure 4.31: Schematic diagram of the tested fiber amplifiers

We note that the forced air cooling of Rack A introduces significant acoustic noise between 200 Hz and 200 kHz (Figure 4.34). Originally water cooling was foreseen, but due to communication errors the delivered units came with forced air cooling. As we will see later, the acoustic noise associated with the fan potentially spoils many of our measurements, but in any case, for Advanced Virgo, water cooling can

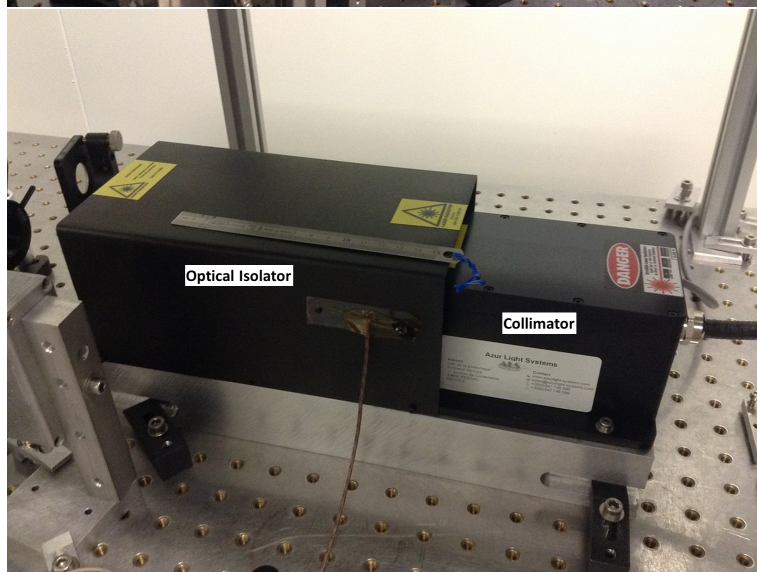
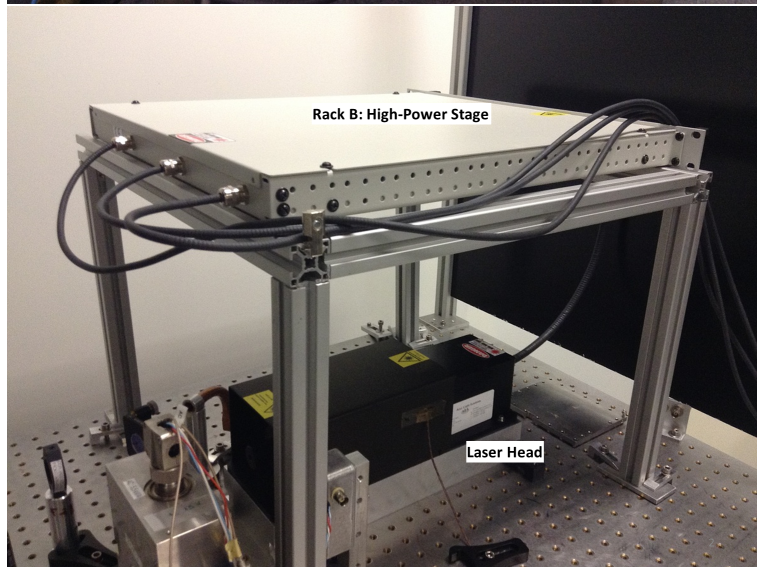
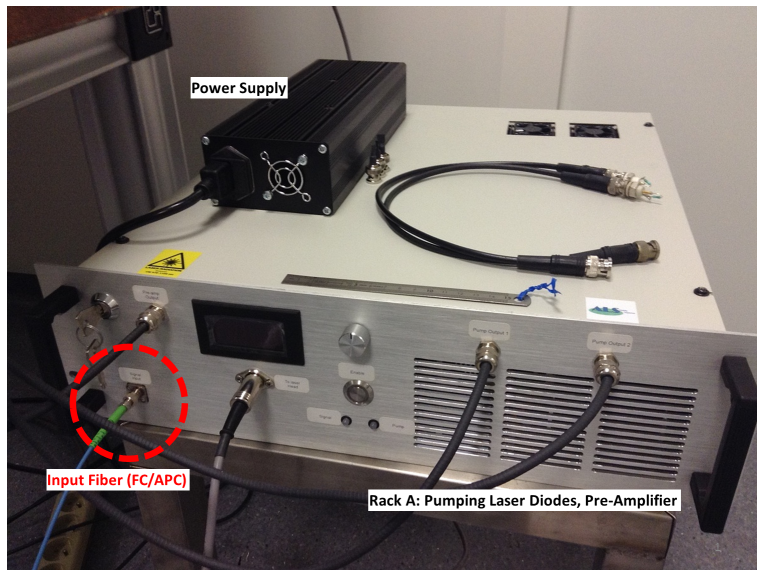


Figure 4.32: Photos of ALS fiber amplifier.

always be opted for to avoid problems.

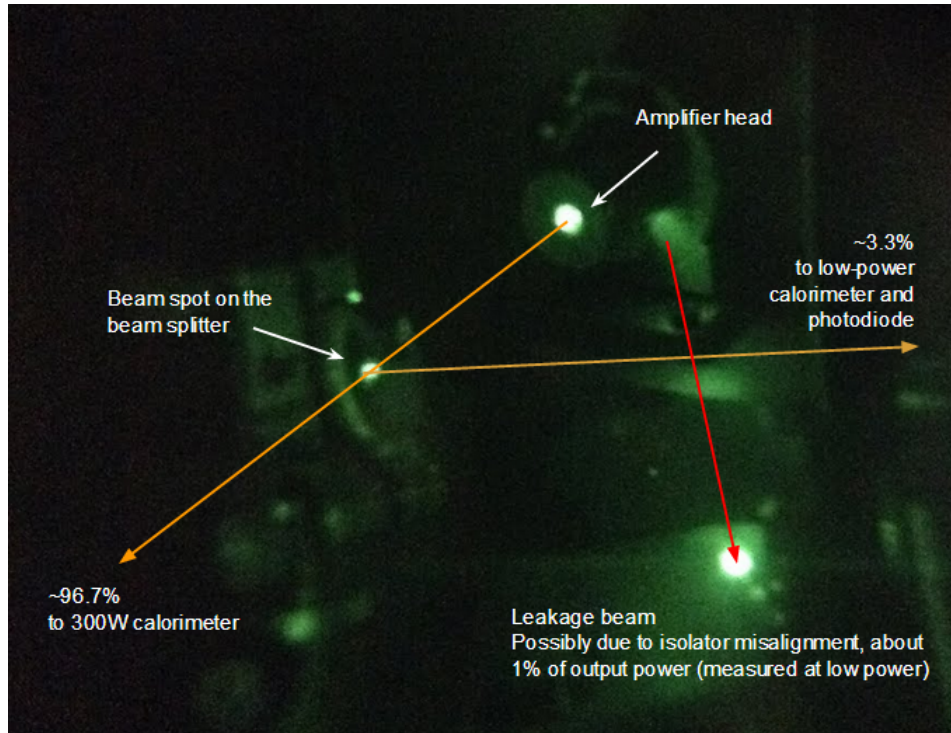


Figure 4.33: The leakage beam from the optical isolator of ALS 2.

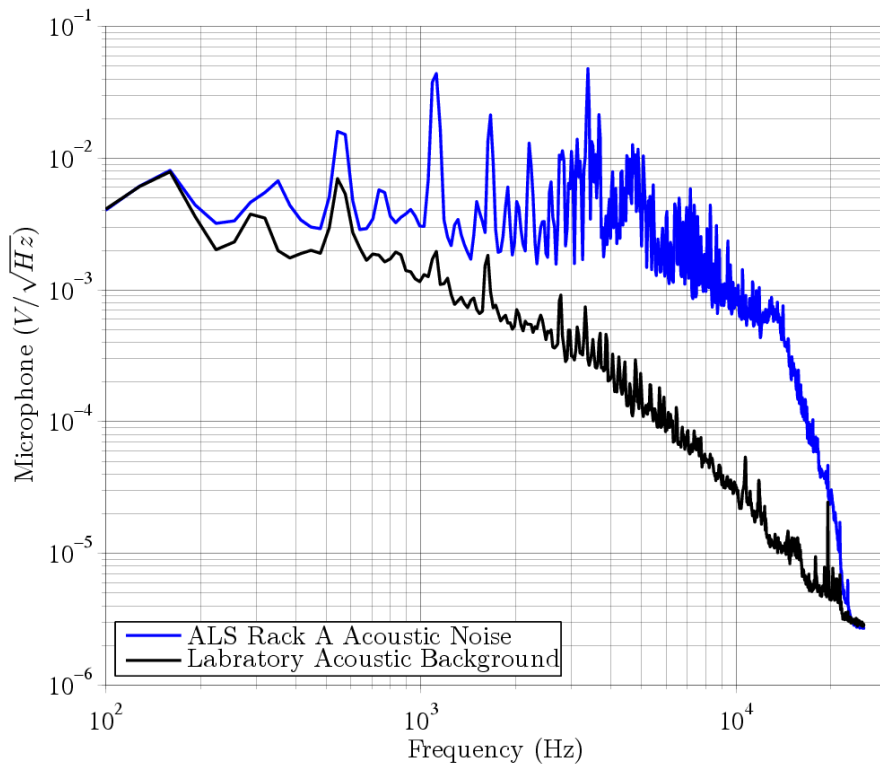


Figure 4.34: Acoustic noise of Rack A. Measured with ALS 2.

In the following, we show results on the characterization of our MOFPA setup in comparison with Advanced Virgo requirements. In short, the MOFPA setup qualifies for the use in Advanced Virgo in terms of power noise, frequency noise and beam pointing stability, while the shortcoming in available output power is obvious. A partial workaround is coherent beam combination, as will be presented in Chapter 5, but for practical concerns in terms of system complexity, having an MOFPA delivering ~ 100 W output power is highly favored. Last, the long-term stability of the system is promising, but further studies are required to come to a conclusion.

Output Power

Figure 4.36 shows the output power of the fiber amplifiers after the optical isolator¹⁰ versus the current of the pumping laser diodes. We see that the curves are linear. Both amplifiers were put in continuous operation whenever possible with constant pump current of 9.6 A for ALS 1 and 9 A for ALS 2, which were the maximum set values available.

The output power was monitored constantly by a photodiode, and most of the time also by a calorimeter, separated by a beam splitter. Data were registered using analog-to-digital converter (ADC) at 10 s interval for $t < 650$ h, and at 60 s interval otherwise. The correlated trends of the photodiode and the calorimeter justify the overall validity of the output power history, among which the less noisy data from the photodiode are shown in Figure 4.36. Also, amidst the monitoring process the calorimeters were calibrated with respect to traceable standard from NIST to an uncertainty of $\pm 2.5\%$.

As ALS 1 was shipped back to the manufacture for repair, we began with the monitoring of ALS 2, and saw an increase in output power during the first 650 h. The trend interruption of ALS 2 at ~ 300 h was due to computer crash, while the amplifier ALS 2 remained operational. On the opposite, other trend interruptions in Figure 4.36 generally corresponded to the off-state of the amplifiers ALS 1 and ALS 2. The shutdown of the amplifiers was caused by either the built-in security electronics, the shutdown of the seed NPRO laser (likely also due to security electronics), or power outage of the lab. Either case, the fiber amplifiers could be easily restarted and thus showed their robustness.

Restarting the amplifiers caused relatively large fluctuations in output power which might last a few hours before reaching relative steady-state operation, as shown in Figure 4.38, and resulted in the downward spikes in the time series.

Oscillating output power fluctuations with 24 h period were present for both ALS 1 and ALS 2, as shown in Figure 4.37. In addition to the daily oscillation, the oscillation with ~ 25 min period corresponded to environmental fluctuations of the laboratory associated with the air conditioning system. No other obvious oscillations were observed. We note that ALS 1 and ALS 2 were placed in different rooms; the room with ALS 1 was with less disturbance. Also, other characterizations apart from output power monitoring were made with ALS 2. The output power time

¹⁰Thorlabs IO-5-1064-VHP

series of ALS 1 shown in Figure 4.36 should therefore reflect the intrinsic character of the fiber amplifier.

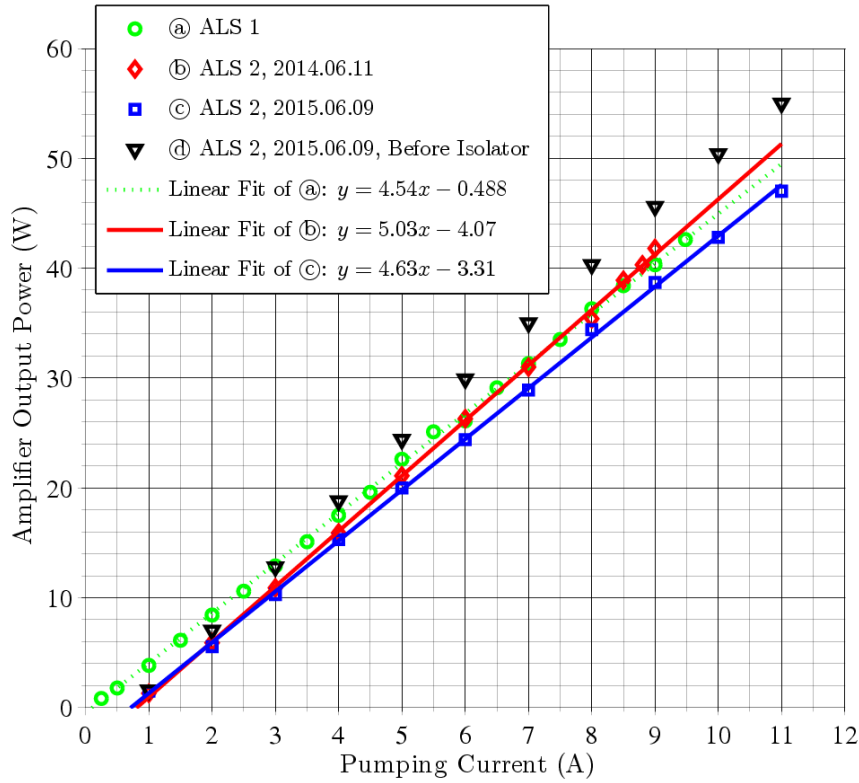


Figure 4.35: ALS fiber amplifiers: output power vs. laser diode pump current.

The most important objective in monitoring the output power was to gain some insight on lifetime and stability of fiber amplifiers, as photo-darkening [102, 103, 160] has long been a concern in high-power ytterbium-doped fiber amplifiers for long-term operation. Both ALS 1 and ALS 2 experienced gradual loss of output power. Simple linear fitting of the output power trend between ~ 3800 h and ~ 6400 h indicates loss rate of 1.1 mW h^{-1} for ALS 1 and 0.9 mW h^{-1} for ALS 2. It should be noted that there was no measurement dedicated to photo-darkening, so the loss of output power was a collective effect of many factors including but not limited to photo-darkening. For example, the degradation of the fiber coupler bringing together the signal beam the two pumping beams might also be liable for the loss of output power.

To our knowledge, this is the first report on the output power trend of high-power ytterbium-doped fiber amplifiers with quasi-continuous operation over a few thousand hours. The accumulative operational hours before necessary maintenance, which are ~ 2400 h for ALS 1 and ~ 3900 h for ALS 2, are reasonable for applications like interferometric GWDs which require continuous laser operation over months.

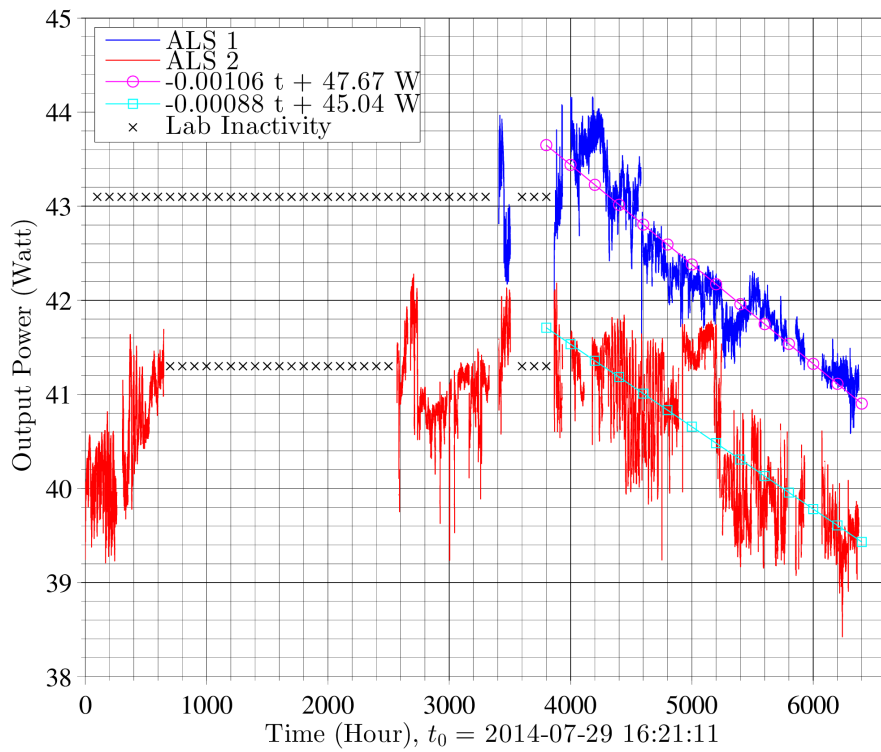


Figure 4.36: ALS fiber amplifiers: output power time series.

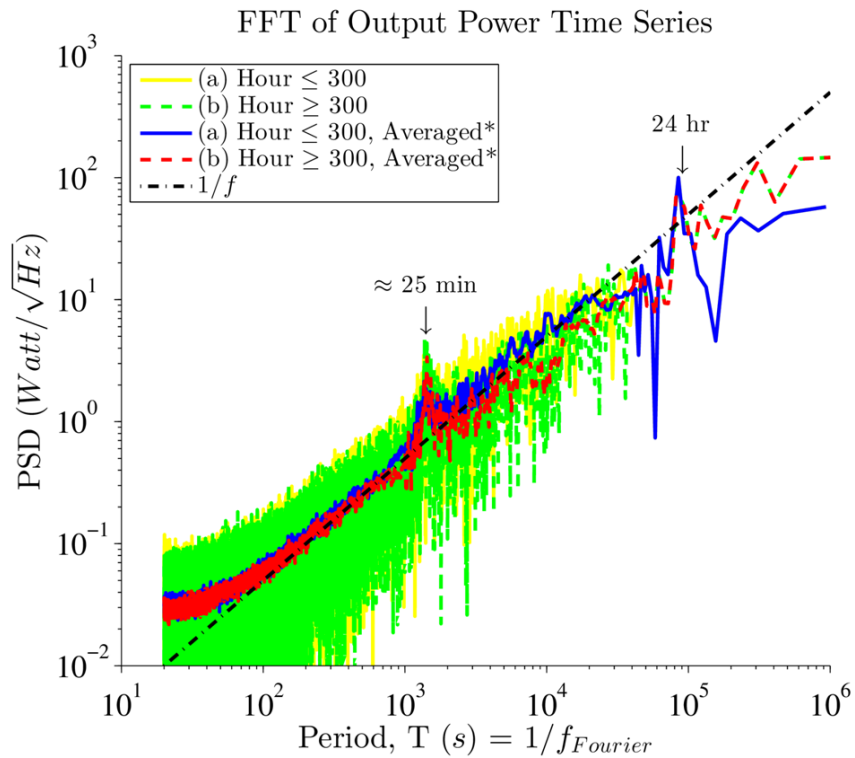


Figure 4.37: Fourier transform of ALS 2 output power time series for $t < 650$ h. *Moving average of 50 bins for $T < 10^3$, and 10 bins for $10^3 < T < 5 \times 10^4$. FFT resolution $\sim 8.17 \times 10^{-7}$ Hz $\approx 1.22 \times 10^6$ s.

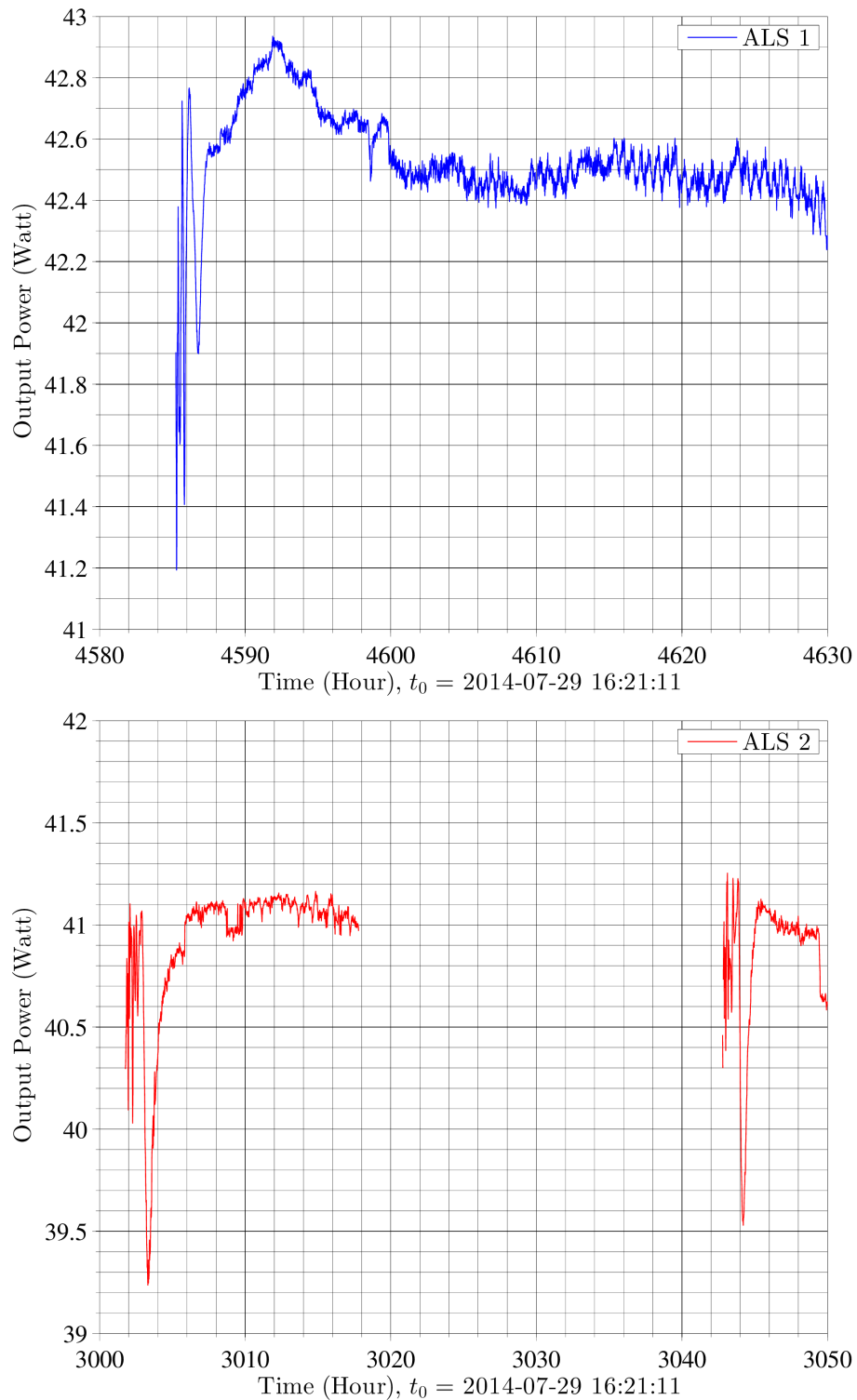


Figure 4.38: Some exemplary excerpts of the output power time series after the restart of the ALS fiber amplifiers.

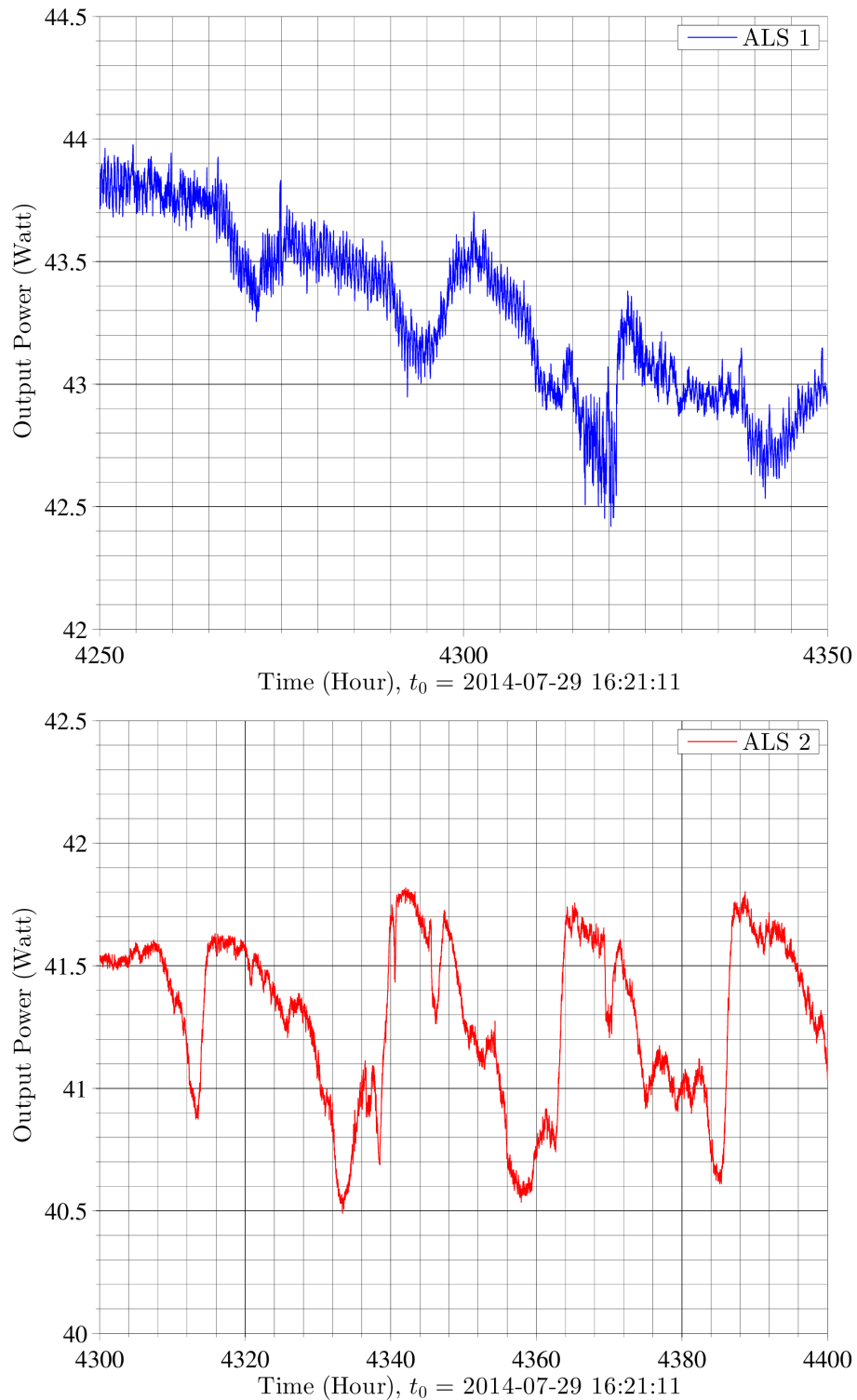


Figure 4.39: Some exemplary excerpts of the 24 h oscillations in the output power time series of the ALS fiber amplifiers.

Time Domain Stability Analysis of ALS 2 Fiber Amplifier for $t = 0$ h to $t = 650$ h

During the first ~ 650 h of operation, ALS 2 was left mostly untouched, except that the computer used for monitoring crashed and therefore required a restart at ~ 260 h. The fiber amplifier remained running despite the computer crash.

To better understand the stability of the output power and its potential correlation with operational and environmental factors, we monitored various signals and performed time domain stability analysis using the Allan deviation (ADEV) statistics [135]. The Allan deviation is the square root of the Allan variance (AVAR), which is also known as the two-sample variance and is defined as:

$$\sigma_x^2(\tau) = \frac{1}{2} \langle (x_{i+1} - x_i)^2 \rangle_\tau. \quad (4.5)$$

Although time consuming, to make better use of the whole data set, we applied overlapping all-tau ADEV calculations with a MATLAB routine¹¹.

Figure 4.40 shows the ADEV results on various signals associated with ALS 2 between ~ 2 h and ~ 240 h (the head and the tail of the time series are removed to avoid spurious results due to disturbance). Figure 4.41 shows those between ~ 305 h and ~ 647 h. We note that the time series plotted are only to indicate their evolution with time; the units on the vertical axis are chosen arbitrarily, so direct comparisons are only valid with quantities that are alike.

From the time series plots we can see that (a) Amplifier Input Power shows some correlation with the Amplifier Output Power (d) and (e). Since in a separate experiment we verified that the fiber amplifier was saturated that the change of input power from 20 mW to 45 mW had no effect on the output power, and ~ 27 mW was injected to seed ALS 2, such correlation suggests that there might have been some systematic errors in our overall measurement setup, such as electronic drifts in the ADC readout, for example. The Power of Pumping Laser Diodes (c) and (d) correlate to each other, and also slightly with the Pumping Current (b). The Beam Pointings (g) and (h) also correlate to each other.

From the ADEV results, two notches are present, one at ~ 1500 s and one at $\sim 80\,000$ s, which correspond to the ~ 25 min time constant of air conditioning and the daily oscillation, respectively. The correlations basically follow the discussions on the times series in the above paragraph. One thing that may be interesting to note is that the stability of the reading from the calorimeter is a lot worse than that from the photodiode for timescales below ~ 200 s, which might correspond to the thermal time constant of the calorimeter.

Beam Quality

We were able to couple a fraction of the ~ 40 W beam of ALS 2 into a polarization-maintaining single-mode fiber with $> 88\%$ efficiency using a simple setup like that in Figure 4.11. Assuming 3.6% Fresnel reflection loss (Equation 4.2) for each uncoated FC/APC facet, this means that $> 95\%$ of the output beam is matched to the fiber

¹¹<http://www.mathworks.com/matlabcentral/fileexchange/26659-allan-v3-0>

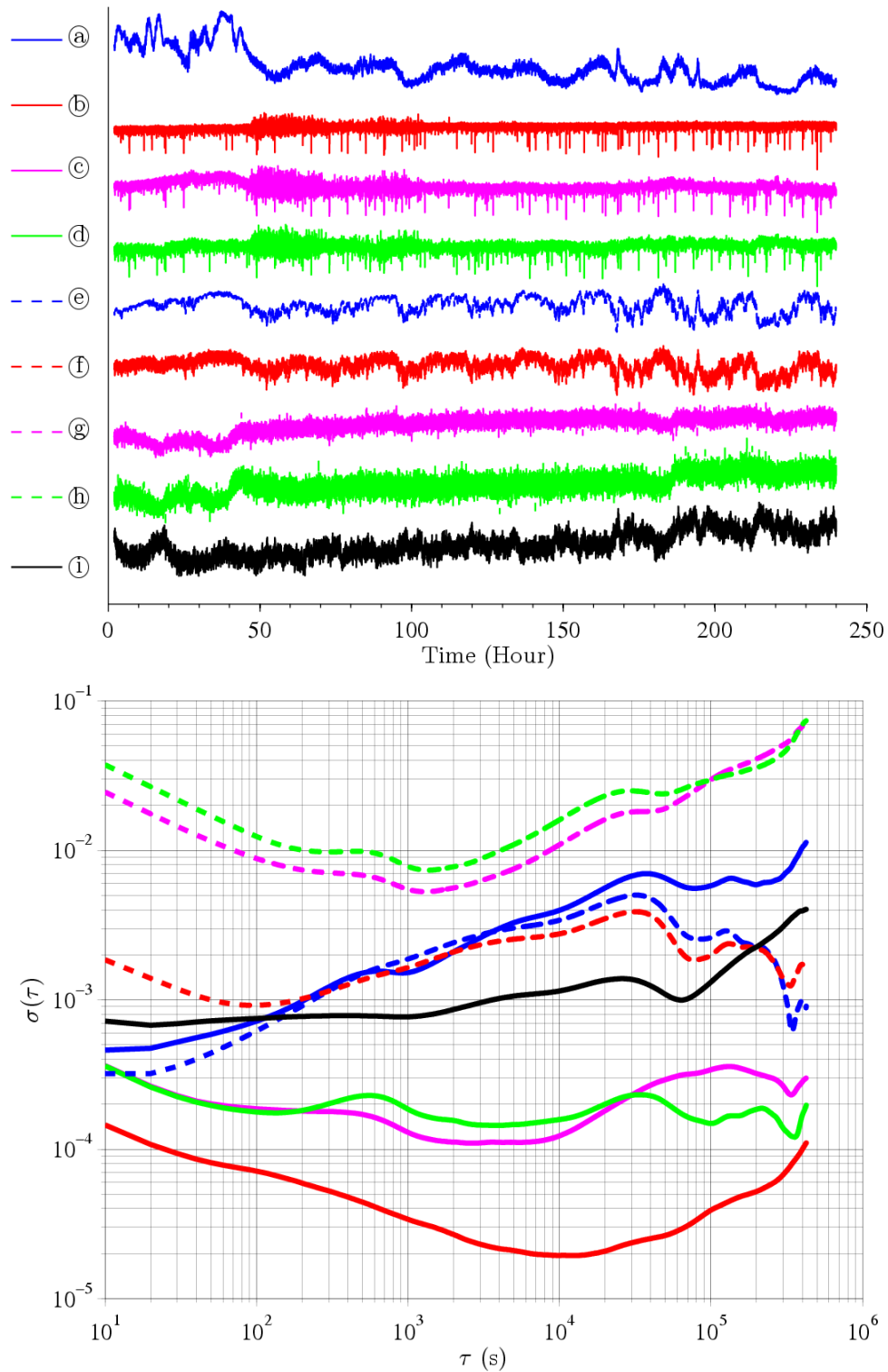


Figure 4.40: Time series and ADEV of various signals associated with ALS 2 between ~ 2 h and ~ 240 h: (a) Amplifier Input Power; (b) Pumping Current; (c) Power of Pumping Laser Diode 1; (d) Power of Pumping Laser Diode 2; (e) Amplifier Output Power, Photodiode; (f) Amplifier Output Power, Calorimeter; (g) Horizontal Beam Pointing; (h) Vertical Beam Pointing; (i) Laser Head Temperature.

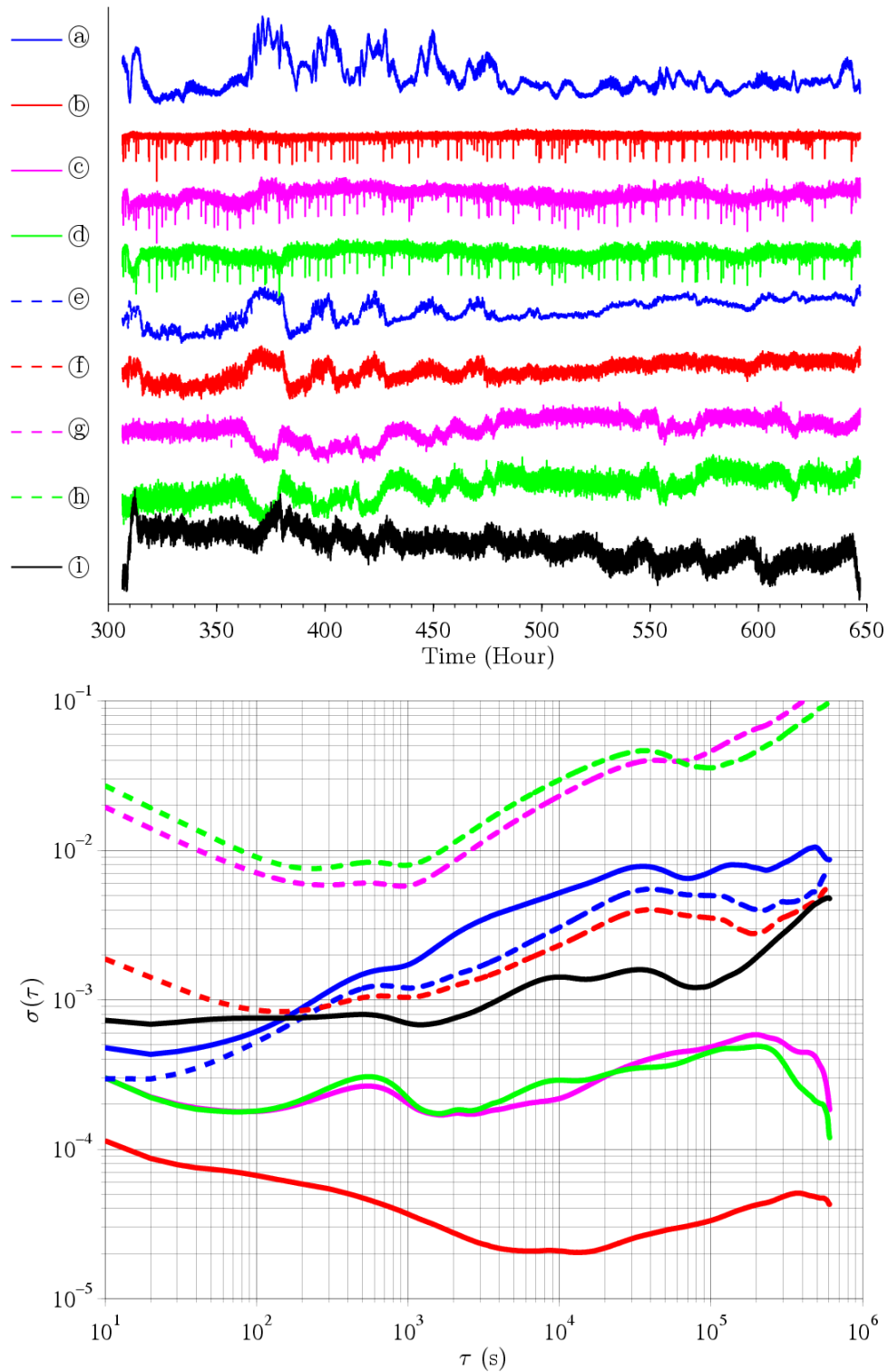


Figure 4.41: Time series and ADEV of various signals associated with ALS 2 between ~ 305 h and ~ 647 h: (a) Amplifier Input Power; (b) Pumping Current; (c) Power of Pumping Laser Diode 1; (d) Power of Pumping Laser Diode 2; (e) Amplifier Output Power, Photodiode; (f) Amplifier Output Power, Calorimeter; (g) Horizontal Beam Pointing; (h) Vertical Beam Pointing; (i) Laser Head Temperature.

LP₀₁ mode, whose mode profile highly resembles that of the Gaussian TEM₀₀ mode (cf. Section 3.10).

Also, the beam propagation measurement of ALS 2 after a lens shown in Figure 4.42 also fits well to a fundamental Gaussian beam.

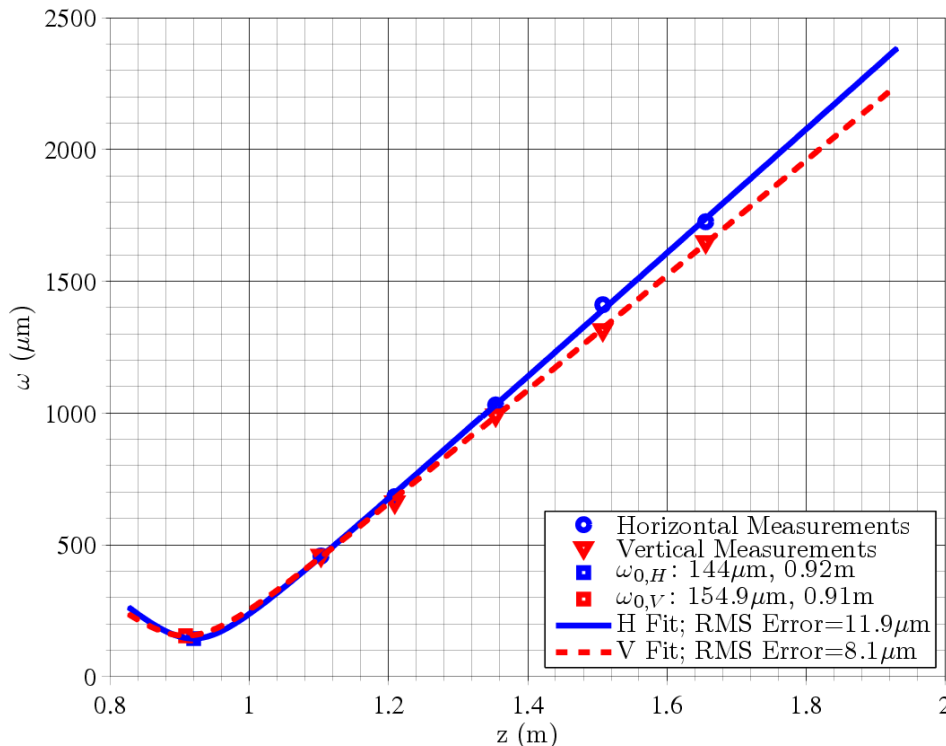


Figure 4.42: Beam propagation measurement of ALS 2 after a lens.

Power Noise

Due to the experience with the Nufern ~ 50 W fiber amplifier which had excessive power noise in the MHz range, we first wanted to know if the power noise of the ALS fiber amplifiers were acceptable in this frequency range. An 1 mm diameter photodiode was used to ensure fast response up to ~ 100 MHz, and the measured power noise at high frequencies is shown in Figure 4.43

Then we tried to measure the power noise at lower frequencies, but observed the difficulty in obtaining consistent values across measurements. Multiple cross-checking power noise measurements were then taken to understand better the difficulty, with the results shown in Figure 4.44.

A few observations may be commented accordingly:

- The 1 mm diameter photodiode measures higher power noise level at low frequencies due to beam clipping effects discussed in Section 3.4 (Curves ② vs. ③, and ⑤ vs. ⑥.).
- The clipping effect can extend up to ~ 1 kHz (Curves ① and ④ vs. ③).

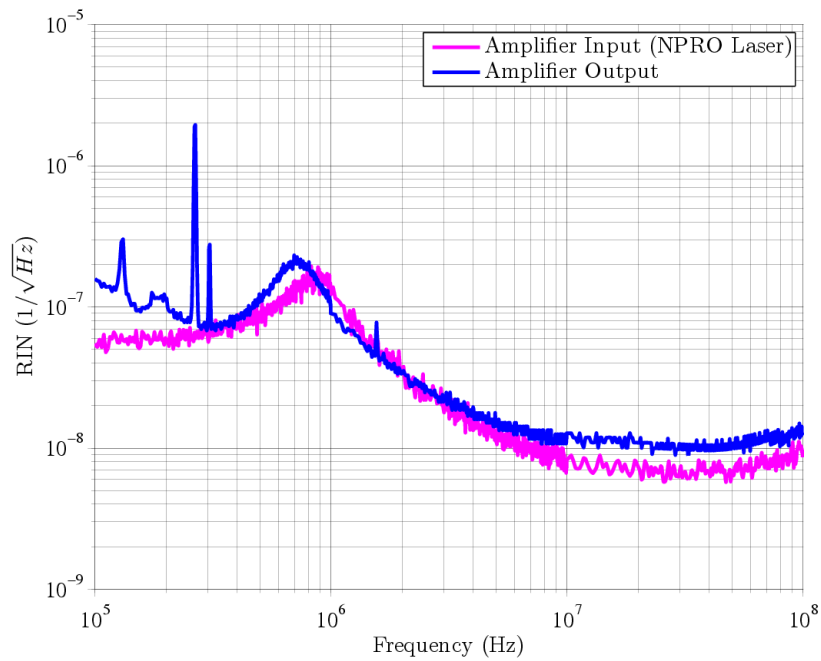


Figure 4.43: Power noise at ALS 2 fiber amplifier input and output between 100 kHz and 100 MHz. The power of the NPRO laser was tuned slightly and hence the move of the lump at ~ 800 kHz.

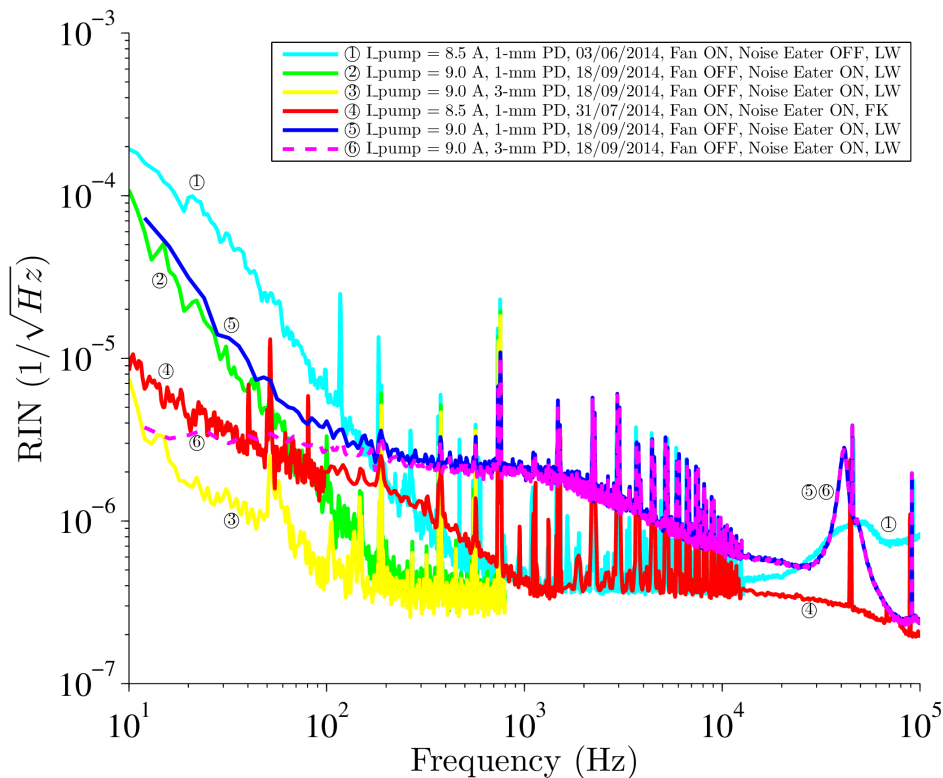


Figure 4.44: Power noise at ALS 2 fiber amplifier input and output between 10 Hz and 100 kHz. Noise Eater is the built-in power stabilization of the NPRO laser, and here *Fan* refers to that of the calorimeter.

- The power noise is non-stationary, and can sometimes dominate over the clipping effect down to ~ 200 Hz (Curves ⑥ and ⑥ vs. ① and ④).
- The power noise level may change between ~ 200 Hz and ~ 10 kHz, but the amplitudes and frequencies of the forest peaks therein remain constant.

To better understand the output power noise, correlation measurements were made to seek its possible origin. Figure 4.45 shows that the peak forest appears at the pumping current level and imprints onto the power of the pumping laser diodes, and Figure 4.46 shows that the peak forest eventually continues on from the pumping laser diode power to the output power. From these measurements, seemingly the peak forest in the output power originated from the current source. There were however situations in which the relation was not very visible (Figure 4.47).

In terms of the non-stationary behavior, one order of magnitude in output power noise was observed. The process seemed to be rather random. Sometimes it evolved slowly, while sometimes it jumped abruptly. Sometimes we were able to trigger the evolution by perturbing the system with a slight change of pump current, while sometimes the system was just not affected. Figures 4.48 and 4.49 are another two measurements showing the power noise dynamics.

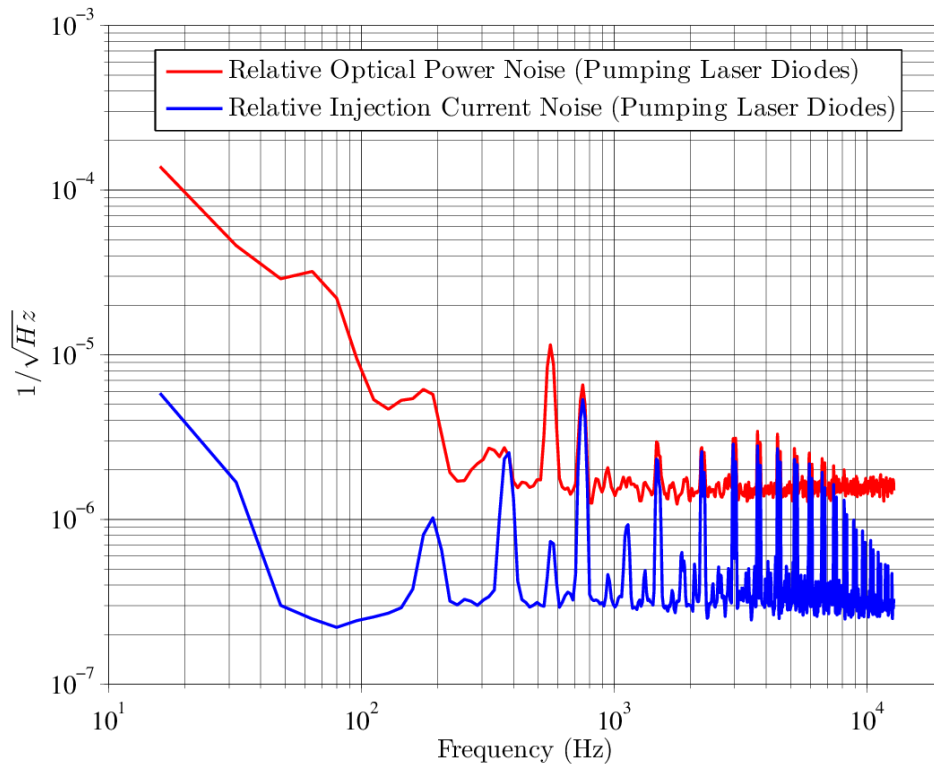


Figure 4.45: Relative optical power noise vs. relative injection current noise, of the pumping laser diodes of the ALS 2 fiber amplifier.

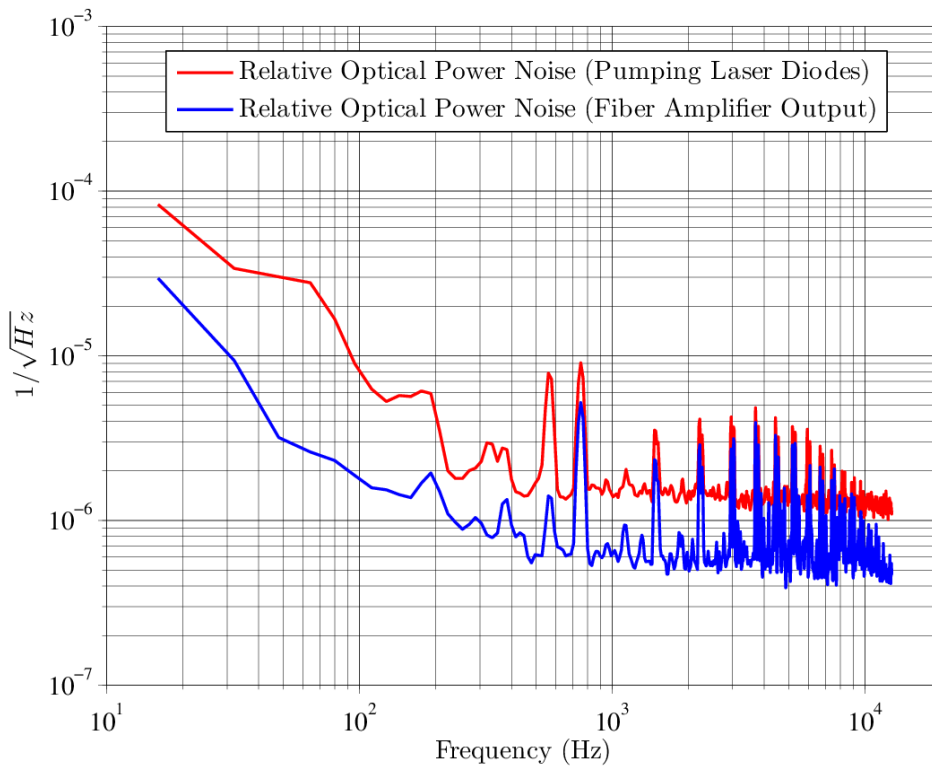


Figure 4.46: Relative power noise of ALS 2 fiber amplifier output vs. relative optical power noise of the pumping laser diodes (1/4).

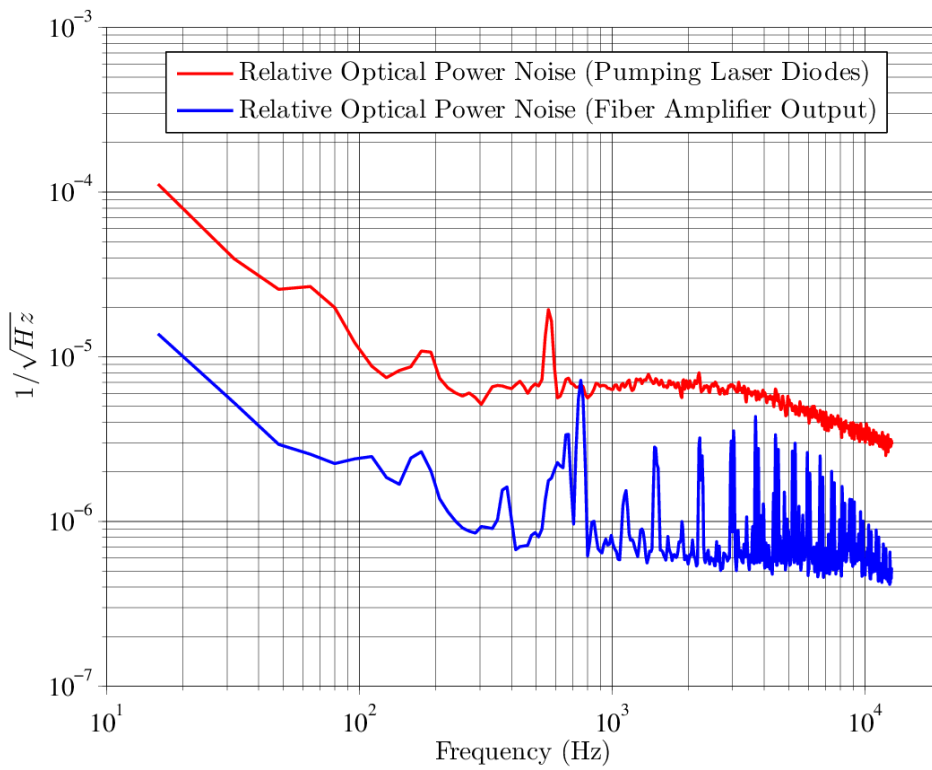


Figure 4.47: Relative power noise of ALS 2 fiber amplifier output vs. relative optical power noise of the pumping laser diodes (2/4).

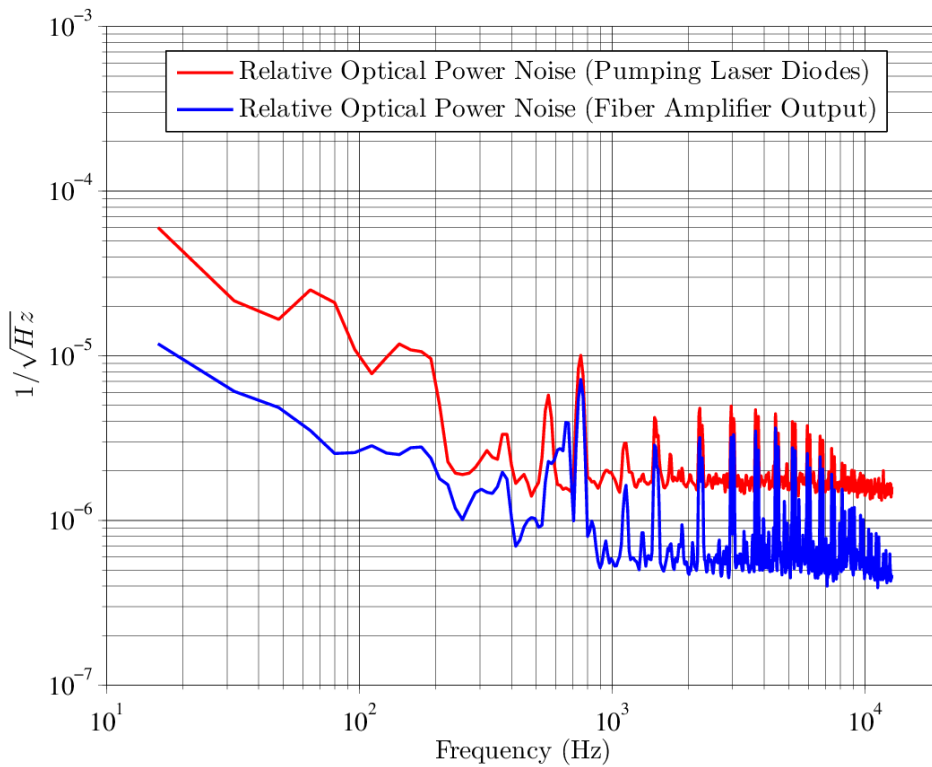


Figure 4.48: Relative power noise of ALS 2 fiber amplifier output vs. relative optical power noise of the pumping laser diodes (3/4).

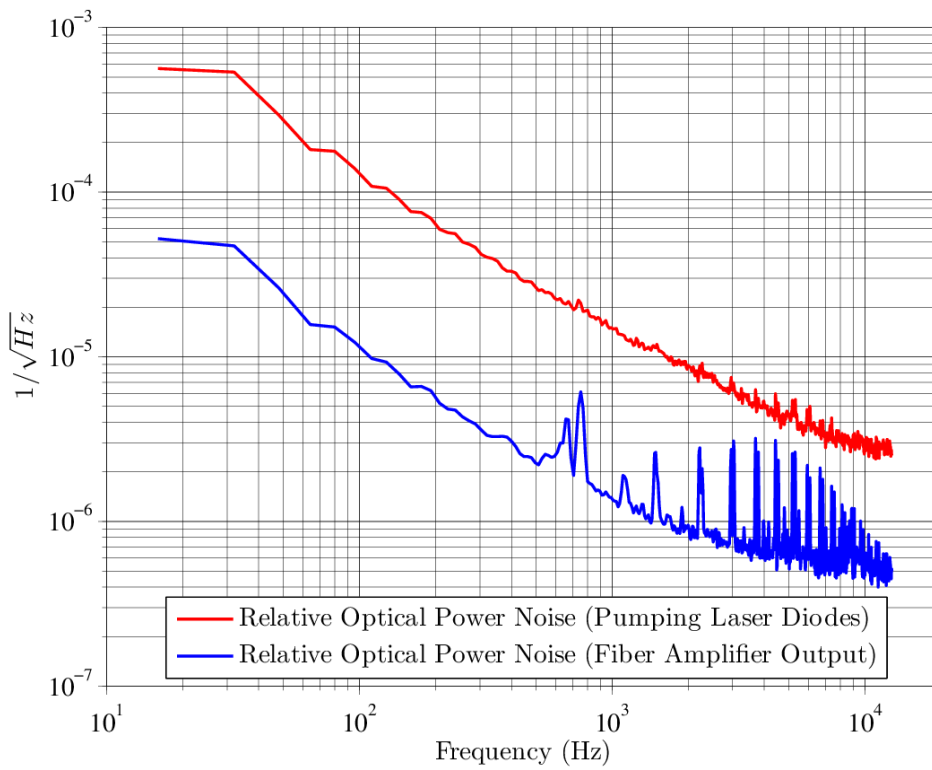


Figure 4.49: Relative power noise of ALS 2 fiber amplifier output vs. relative optical power noise of the pumping laser diodes (4/4).

Although it may be interesting to understand better the characteristics and the dynamics of fiber amplifier output power noise, for Advanced Virgo, what matters more is whether the noise of the system stay within the requirements despite the fluctuations.

We therefore monitored the output power noise of ALS 2 over 60 h (starting at ~ 5787 h) with a ~ 15 min measurement interval¹² to obtain the spectrograms shown in Figures 4.50 & 4.51 for an estimate on the range and in particular the upper limit.

We note that owing to non-optimized ratio between the radius of the impinging beam and that of the 1 mm diameter photodiode used for the monitoring, and the presence of non-negligible beam pointing instability (Figure 4.53), the power noise for $f < 1$ kHz shown in Figure 4.50 was overestimated.

From the spectrograms we see that there were stationary peaks as well as non-stationary peaks, and that there were periods where the system appeared to be noisier as well as those where the system appeared to be more stable. For example, many peaks appeared at few kHz when the system was relatively noisier.

In any case, the power noise generally fit the free-running specifications of Advanced Virgo, excepted for the noise peaks at $3 \text{ kHz} \leq f \leq 5 \text{ kHz}$. As discussed above, the power noise at these frequencies likely come from the noise in the current source of the pumping diode lasers, and accordingly may be remedied simply by regulating the current source, which, as claimed by the manufacturer, is implemented in the newer model of the same fiber amplifier product family.

Moreover, the free-running specifications we use was tailored to the Virgo solid-state laser system with a more reserved power stabilization loop unity gain frequency at ~ 20 kHz (cf. Figure 2.18), while previous experiences shown that the power stabilization loop unity gain frequency may be pushed up to ~ 80 kHz, which can also cover the excess power noise even without modification to the current source of the pumping laser diodes. It should be nevertheless acknowledged that when it comes to the performance of the power stabilization loop, the fiber amplifier itself also has to be considered, as will be discussed in Section 4.7.

Frequency Noise

The output beam of the amplifier was coupled into a polarization-maintaining (PM) single-mode (SM) fiber, and fed to one arm of a fiber-optic Mach–Zehnder interferometer (Figure 3.12). A passive fiber was connected to the other arm. The mismatch in arm length was ~ 25 m.

A fiber-optic EOM was used to create the dithering phase signal ($f = 14$ MHz)

¹²The measurement was automatized with GPIB commands wrapped in Perl (Appendix G). Owing to unknown reasons, the GPIB connection with SR780 could sometimes fail during the acquisition. Since it would be effort costly to handle all error exceptions in the Perl script, a simple trick is to call the Perl script in a batch command file and run repeatedly until the acquisition succeeds. Once succeeded, the Perl script holds on for the set time interval before it terminates. The same was applied to HP8591A, with another batch command file. In short, the power noise acquisitions at high frequencies and at low frequencies were made in parallel, but were interwoven instead of synchronized, and the measurement intervals could drift due to GPIB connection problems, especially for SR780.

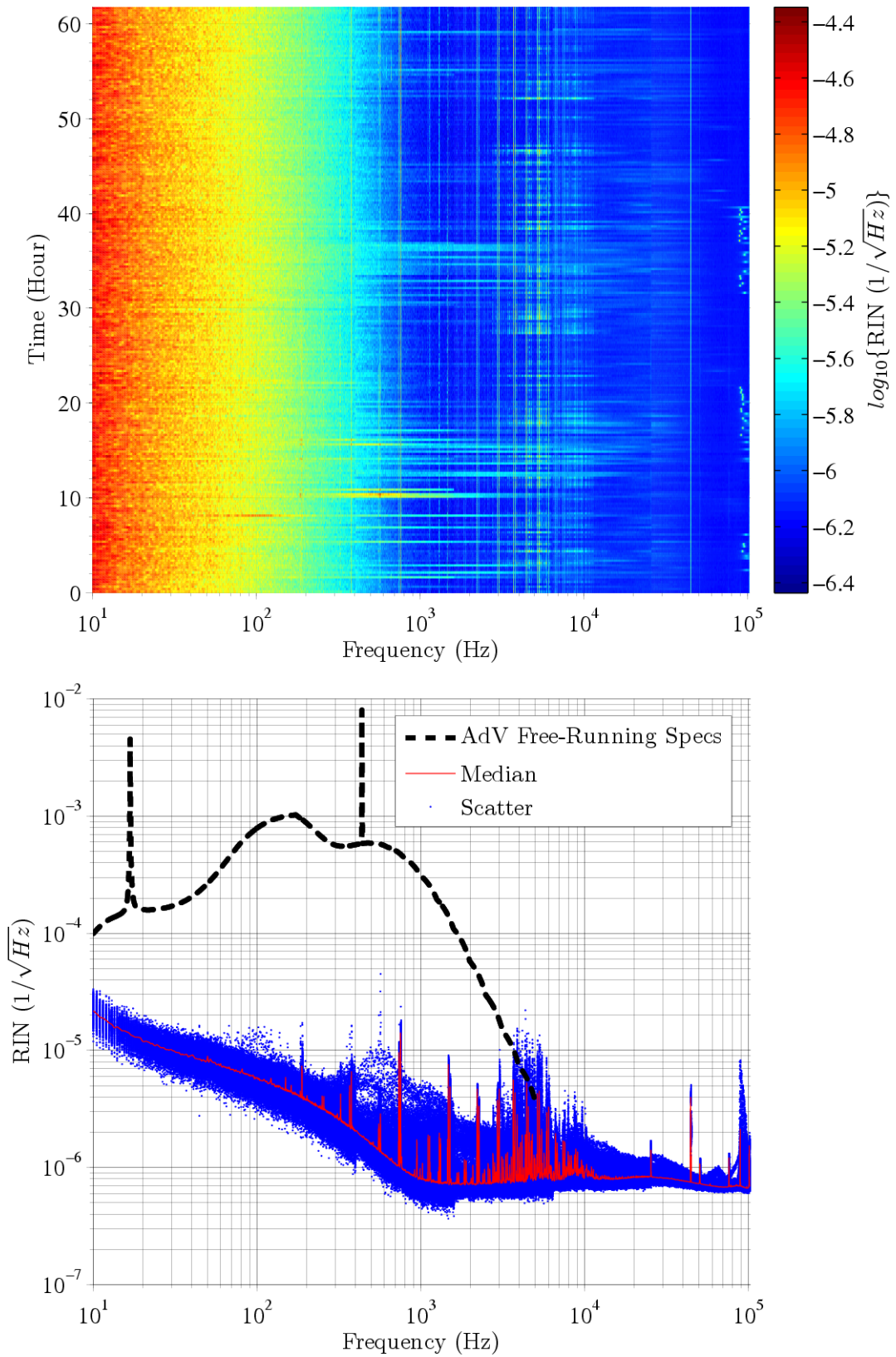


Figure 4.50: Output power noise spectrogram of ALS 2 at low frequencies.

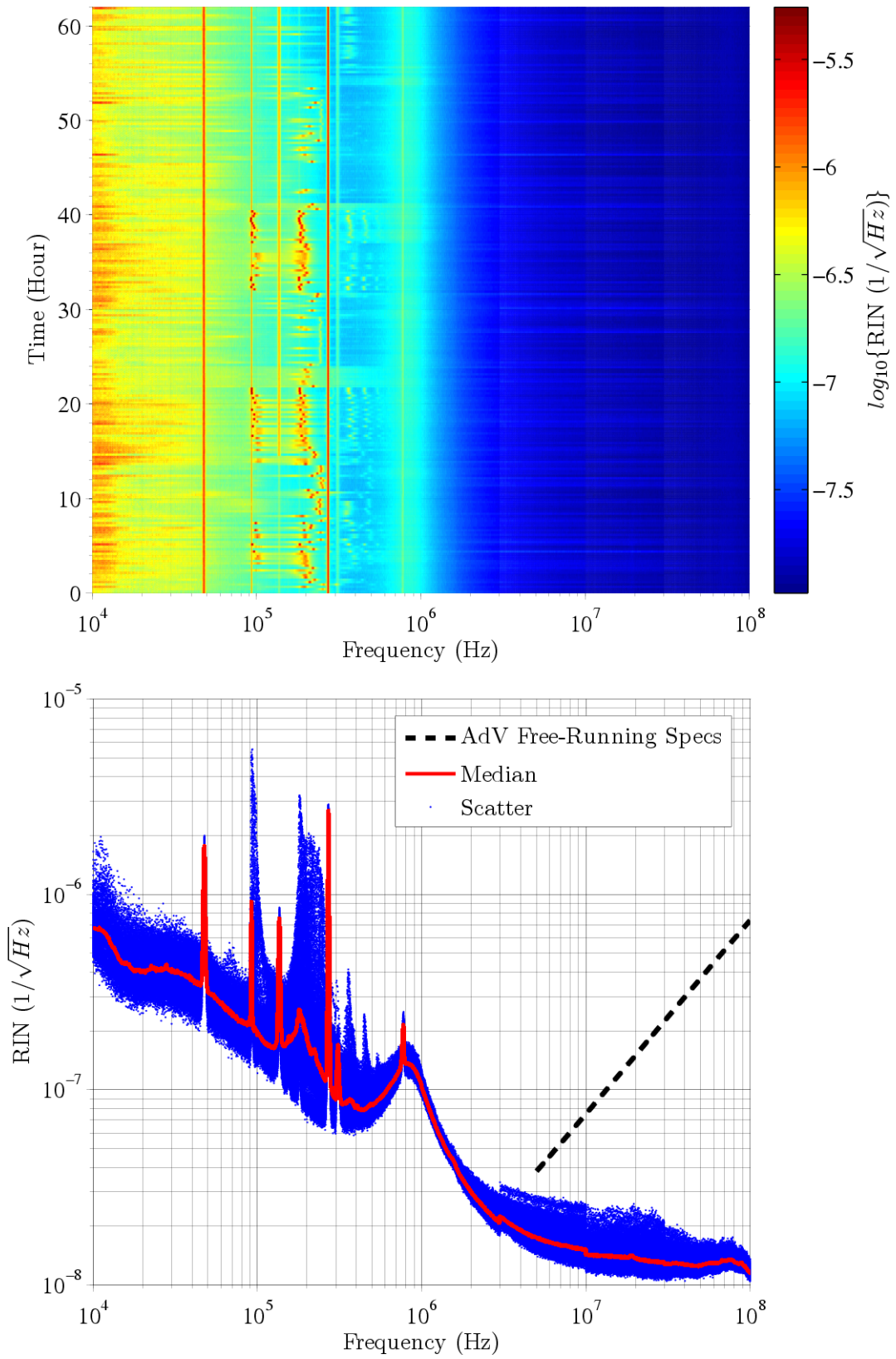


Figure 4.51: Output power noise spectrogram of ALS 2 at high frequencies.

required to lock the interferometer as well as to correct fast differential phase fluctuations. A unity gain frequency of ~ 1 MHz was obtained for the phase lock. Slow phase drift with large dynamic range (~ 2200 rad peak-peak in 15 h, cf. Figure 5.2) was corrected by thermally tuning the optical frequency of the NPRO laser crystal.

The dynamic range of the fast phase actuation by the EOM was ~ 8.6 rad ($V_{\pi, \text{EOM}} \sim 2.2$ V with ± 6 V voltage range), and that of the slow actuation was about ± 943 rad (thermal tuning of the NPRO laser frequency $3 \text{ GHz } ^\circ\text{C}^{-1}$ via voltage control $1 \text{ } ^\circ\text{C V}^{-1}$, with ± 0.6 V voltage range and 25 m interferometer asymmetry ΔL ; cf. Equation 3.36). The crossing frequency of these two phase actuation paths was of the order of a few Hz.

The differential phase noise between the two fiber amplifiers in the frequency band of interest was obtained by probing the correction signal sent to the EOM. After the conversion to frequency noise by multiplying the Fourier frequency (Equation 3.19), the results are shown in Figure 4.52. Typical $10 \text{ kHz}/f \text{ Hz } \sqrt{\text{Hz}}^{-1}$ frequency noise of the NPRO laser is shown for comparison; the measurement floor is defined by the coupling of the NPRO frequency noise and arm length mismatch (Equation 3.36). Here we do not plot the Advanced Virgo free-running specifications for comparison, as the measured frequency noise was orders of magnitude below the requirements (cf. Figure 2.18).

It may be confusing in Figure 4.52 that the measured frequency noise at the output of the fiber amplifier is lower than that of a typical NPRO laser, which was used to seed the fiber amplifier. This is in fact because the measurement setup inherits the frequency noise of its input beam through the arm length asymmetry. In our setup this contribution is small (cf. the estimated Measurement Floor in Figure 4.52) compared to the measurements undertaken. In other words, the measured frequency noise of the fiber amplifier presented in the Figure 4.52 is an additional contribution to the frequency noise that is already present in the beam entering the Mach–Zehnder interferometer.

A 25 m passive fiber was used to replace the arm with the fiber amplifier to obtain experimentally the measurement floor of this setup. Although this was measured with a different frequency resolution bandwidth, it is shown in Figure 4.52 for information. We see that the measurement floor matches calculation, while some noise structures are also present. It may be worth noting the similarity of the noise forest in the kHz range to that seen in the acoustic noise (Figure 4.34), and that in the power noise of the current source (Figure 4.45).

From these results we can fairly say that the fiber amplifier does not introduce significant phase/frequency noise to its input beam, and qualifies for the use in Advanced Virgo.

Beam Pointing Stability

A 3 mm diameter InGaAs quadrant photodiode¹³ was used to measure the beam pointing stability of the output beam of the fiber amplifiers. The results, expressed in $|\epsilon|$ as defined in Equation 3.50, are shown in Figure 4.53.

¹³OSI Optoelectronics, FCI-InGaAs-Q3000

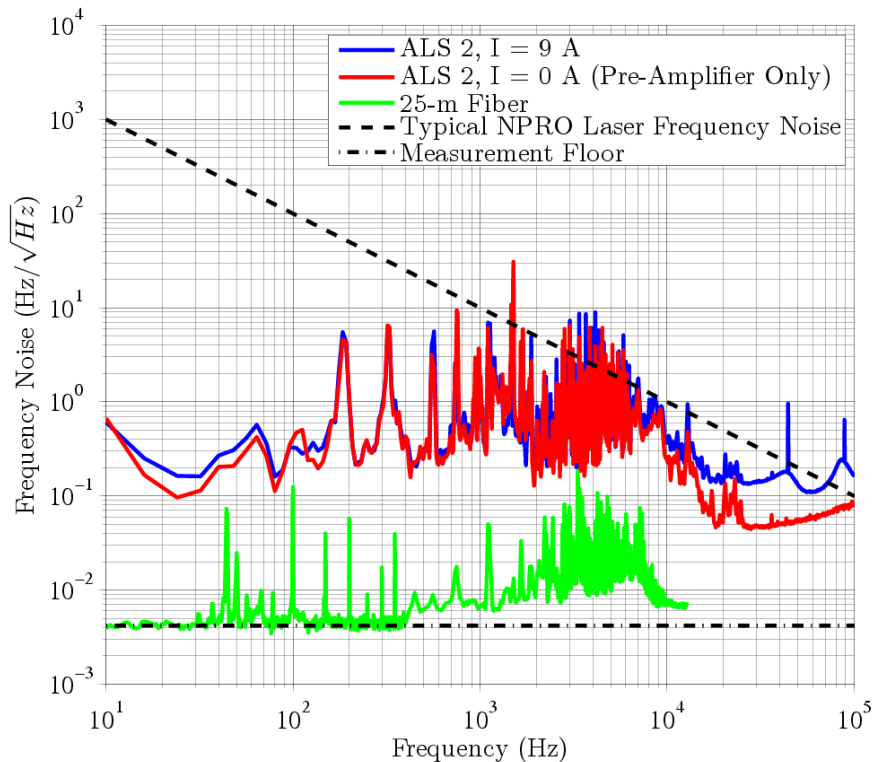


Figure 4.52: Frequency noise of ALS 2.

We see that despite the noisy environment, the beam pointing stability is within the free-running requirements of Advanced Virgo.

4.7 Actuation Paths for Power Stabilization

In Section 2.5 and in the discussion on the power noise measurement of the ALS fiber amplifier, it is stated that when it comes to power stabilization, the actuation path has also to be considered, especially if Advanced Virgo adopts the same power stabilization scheme as that of Virgo, which is based on the current shunt on the pumping laser diodes¹⁴.

Figure 4.54 is the schematics showing the current shunt used in Virgo and its relation to the laser system [161]. A bipolar junction transistor (BJT) is used as the electric switch to stand high current levels. By applying a voltage signal on the *base* (B), the current flowing through the *collector* (C) and the *emitter* (E) changes accordingly as well as the current flowing through the pump laser diodes.

Figure 4.55 shows the amplitude transfer function (*base* to *emitter*) of the current shunt with different voltages across the current shunt. The voltage across the current shunt depends on the operation condition of the laser system. For example, that of ALS 2 is shown in Figure 4.56.

¹⁴In Virgo the current shunt was implemented on the pumping laser diodes for the injection-locked slave laser, while for the Virgo+ laser which has an additional stage of solid-state laser amplifier, the current shunt is implemented on those for the amplifier.

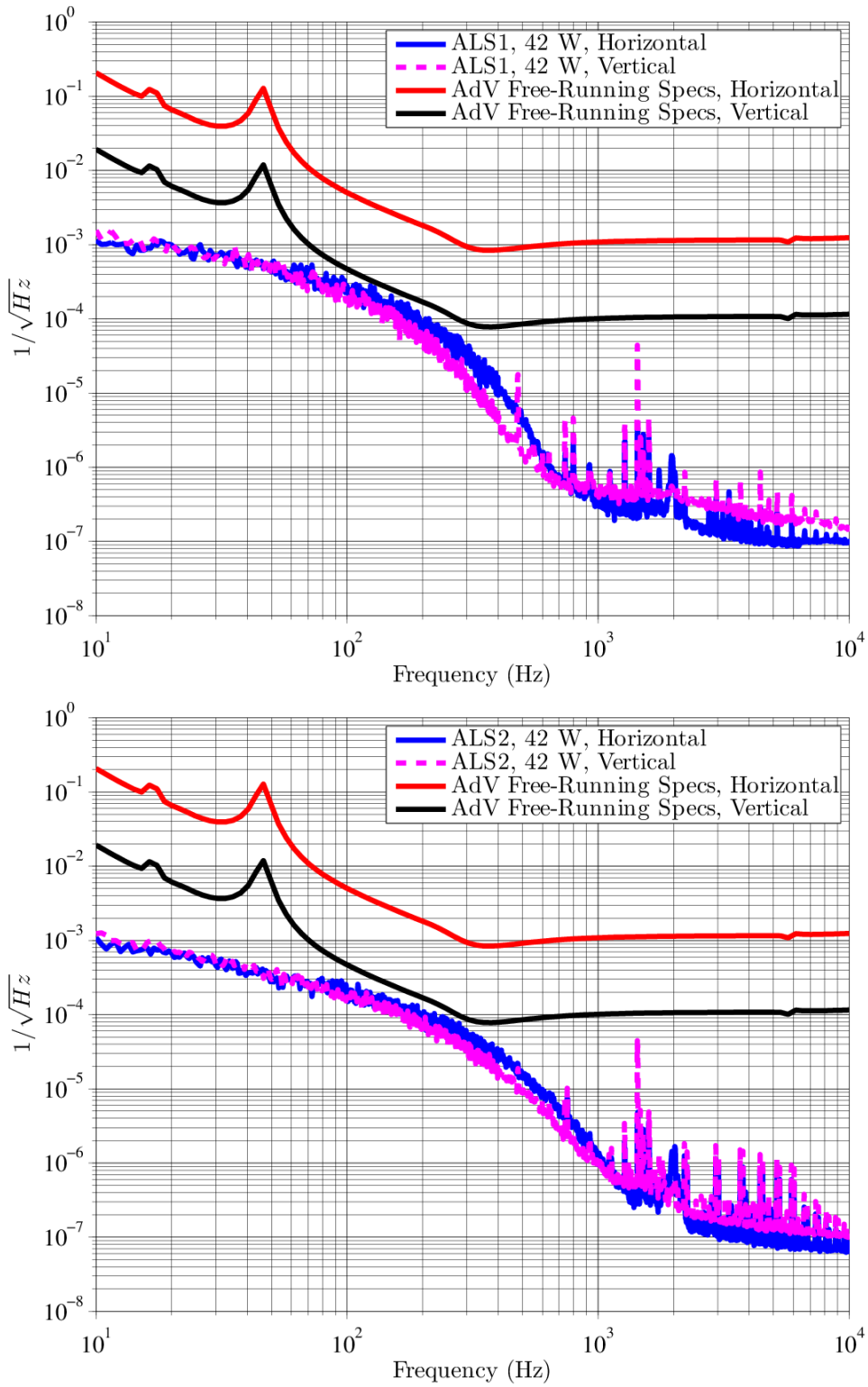


Figure 4.53: Output beam pointing stability of ALS fiber amplifiers.

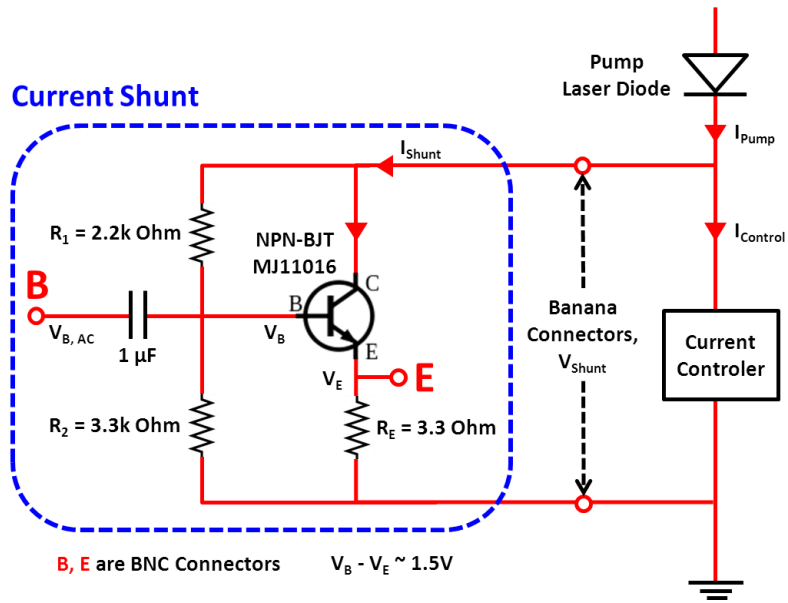


Figure 4.54: Current shunt for power stabilization.

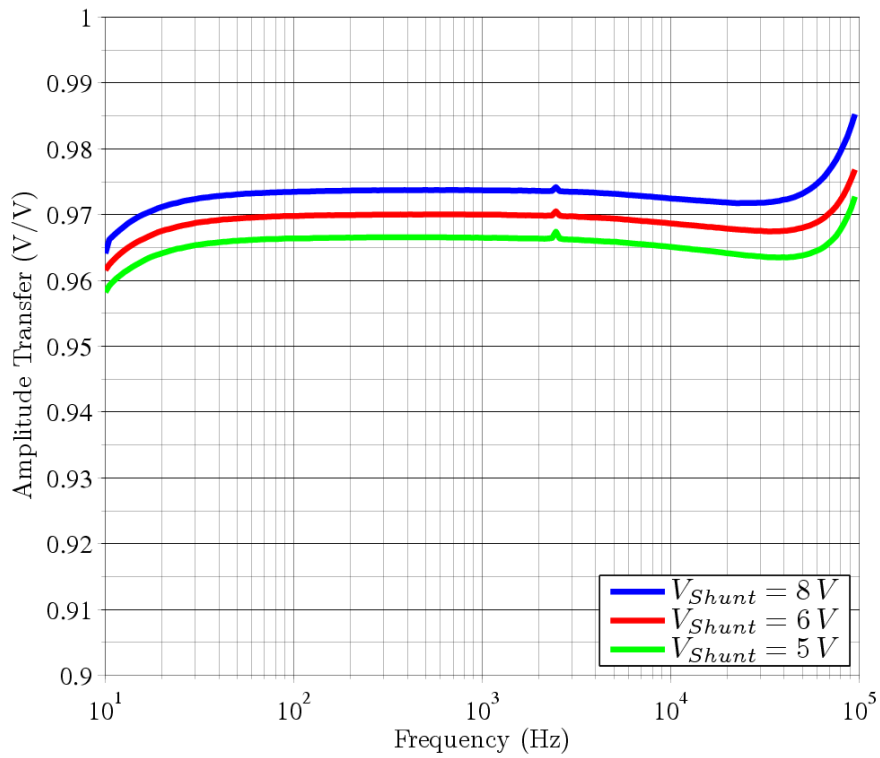


Figure 4.55: Amplitude transfer function of the current shunt for laser power stabilization.

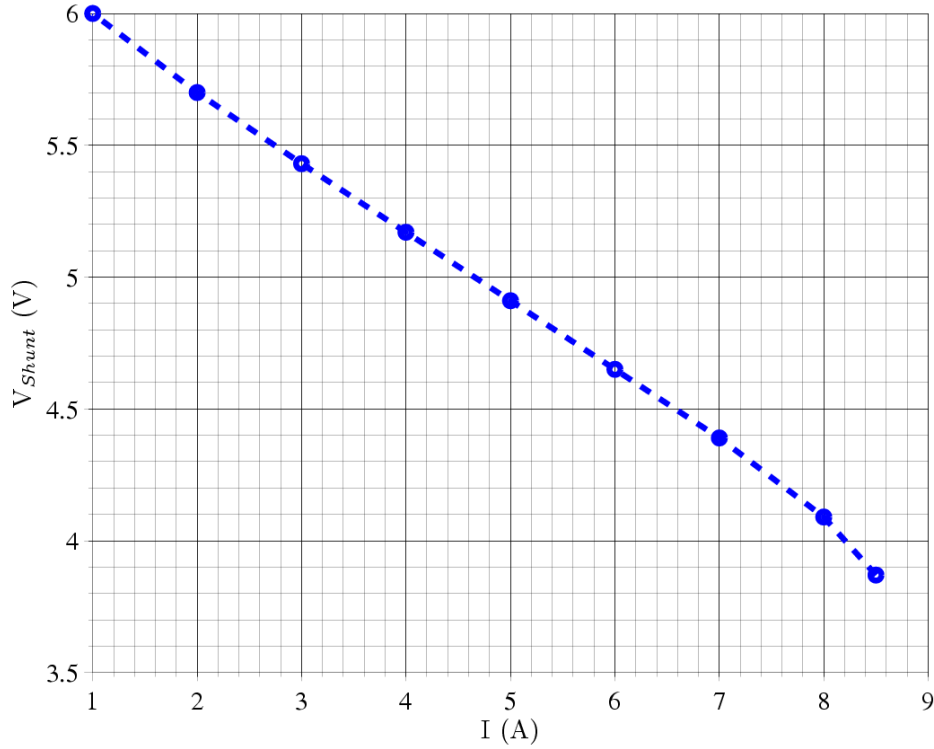


Figure 4.56: Voltage across the current shunt vs. pump current, ALS 2.

What we are then interested in is the amplitude transfer from the current shunt to the output power of the fiber amplifier. In fiber amplifiers, the analytic model for gain modulation in a quasi-three-level ($n = 1, 2, 3$, Figure 4.57) laser system such as erbium-doped and ytterbium-doped fiber laser amplifiers suggests the introduction of the corner frequency ω_{eff} [162, 163] defined as:

$$\omega_{eff} = P_S^0(L)B_S + P_P^0(L)B_P + \frac{1}{\tau}, \quad (4.6)$$

where L is the length of the fiber, P_S^0 is the mean seed power, P_P^0 is the mean pump power¹⁵, and τ is the fluorescence lifetime. B_S and B_P account for the confinement factors Γ_P and Γ_S which account for the overlapping between the beam and the doped region, the absorption and emission cross sections $\sigma_{nm'}$, and the effective area A of the fiber:

$$\begin{aligned} B_P &= \Gamma_P \cdot \frac{\sigma_{13} + \sigma_{31}}{A} \\ B_S &= \Gamma_S \cdot \frac{\sigma_{12} + \sigma_{21}}{A}. \end{aligned} \quad (4.7)$$

Physically, ω_{eff} denotes the low-pass cutoff frequency for pump-to-output power modulation transfer. Only if the modulation frequency of the pump power is below ω_{eff} will the populations be able to follow. On the other hand, slow variations in the seed power will be auto-corrected by the population and therefore suppressed

¹⁵Here the power is in unit *photons per second*.

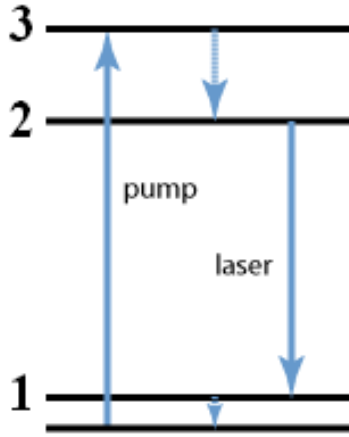


Figure 4.57: A quasi-three-level system for laser action.

[164]. Figure 4.58 illustrates the first-order filter like amplitude modulation transfer of quasi-three-level fiber amplifiers. Due to the lack of knowledge in the parameters of our fiber amplifiers, we are not able to construct models using this analytic model.

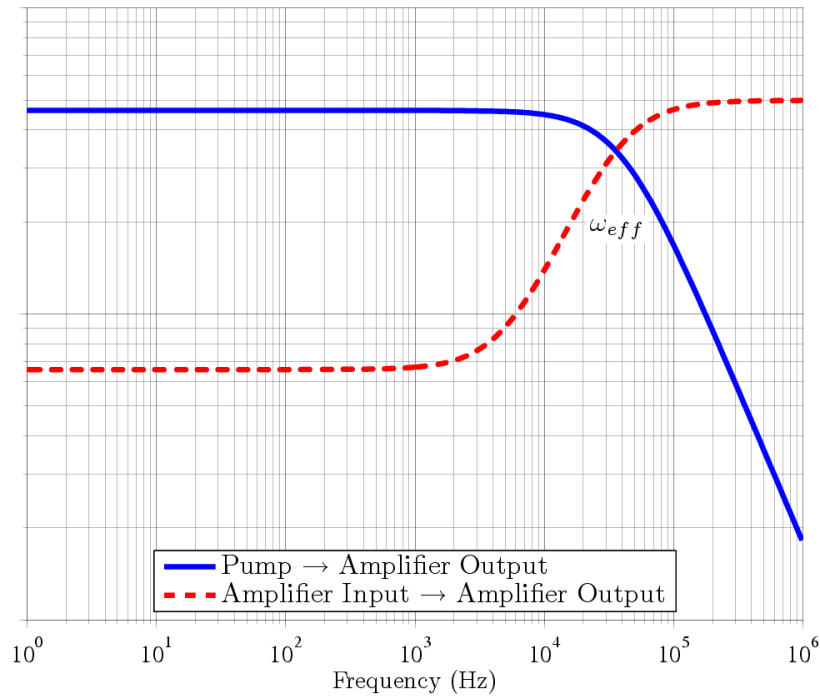


Figure 4.58: Qualitative illustration on the amplitude modulation transfer of pump/input power to output power and the corner frequency ω_{eff} of a fiber amplifier.

In Equation 4.6, for ytterbium, the fluorescence lifetime is ~ 1 ms [164], whose inverse is ~ 1 kHz, a rather low frequency. In an ideal amplifier setup, the unabsorbed pump power $P_p^0(L)$ is also low and therefore Equation 4.6 is dominated by the first term and may be approximated by

$$\omega_{eff} \approx P_S^0(L)B_S, \quad (4.8)$$

which infers that the higher the output power, the higher the corner frequency ω_{eff} . Figure 4.59 shows the amplitude modulation transfer of pump current to output power of ALS 2 fiber amplifier at different output power levels, measured using the current shunt, which confirms this tendency.

We see that for $I \geq 6\text{ A}$, the shape of the transfer function was somewhat abnormal. We did not go into investigations, as the measurement was made to give an idea on how fast we could act on the fiber amplifier using the same power stabilization scheme for Virgo. The cutoff frequency, as plotted, falls in the range of several tens of kHz. Therefore, the power stabilization scheme previously used for the Virgo laser systems may be also be used with the master oscillator fiber power amplifier setup.

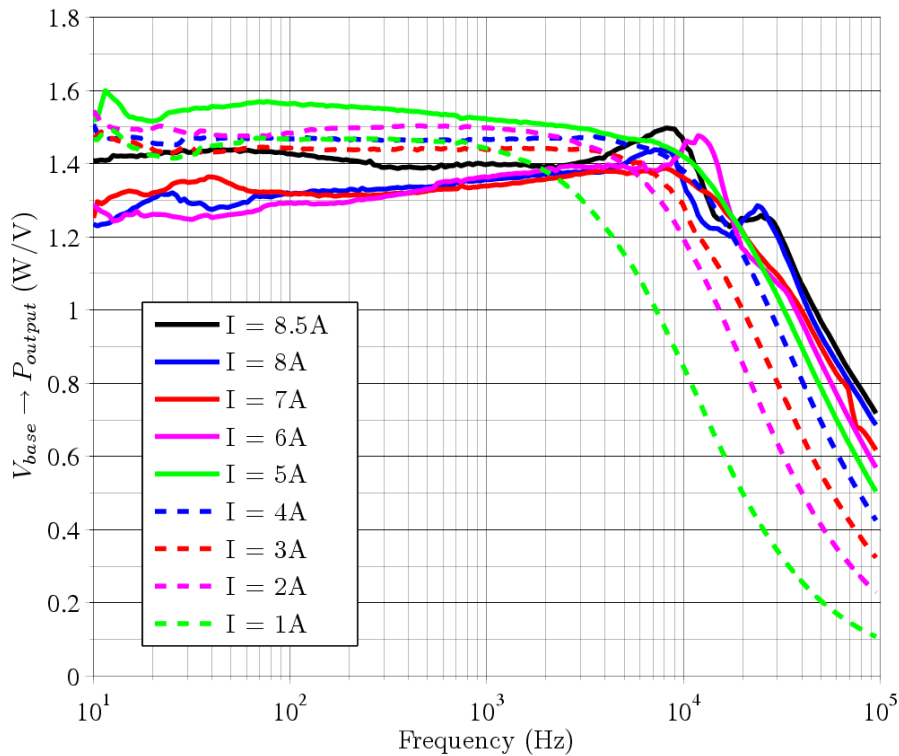


Figure 4.59: Amplitude transfer function of the current shunt to the output power of ALS 2.

Chapter 5

Coherent Beam Combination

To obtain high power, coherent beam combination is an alternative to the power scaling of fiber amplifiers. To date, there have been numerous proposed schemes on laser beam combining [109], notably those focused on ytterbium fiber amplifiers [110, 165]. For our application, given the stringent specifications aforementioned, we limit ourselves to the use of Mach–Zehnder interferometry, just as the earliest report in using coherent combination to obtain higher available laser power for interferometric gravitational wave detectors [166].

In fact, the stringent constraints on the laser beam as required by Advanced Virgo, or interferometric gravitational wave detectors alike, actually facilitates coherent beam combination. The line of thought is logically symmetric:

- We use laser interferometry to probe gravitational waves.
- To achieve good interferometry for gravitational wave detection, we need good laser beams.
- We may also use laser interferometry for coherent beam combination.
- To achieve good interferometry for coherent beam combination, we also need good laser beams.

So, essentially we are using interferometry for interferometry, and the argument is simple: if we do find a decent laser beam for one *interferometry*, there is no reason to not use it for the other *interferometry*. If one is justified, so should be the other.

In the case where a Mach–Zehnder interferometer is used, coherent beam combination equates the locking of an interferometer, which has been extensively studied in the gravitational wave detector community [144, 167, 168].

Coherent beam combination (CBC) techniques using Mach–Zehnder interferometry based on the configurations discussed in Section 3.6 have all been reported, which are: heterodyne [143], phase dithering [165] and frontal phase modulation [169].

In this chapter, results on the coherent combination of the two ALS fiber amplifiers will be presented. A dither-locked free-space Mach–Zehnder interferometer as discussed in Section 3.6 was implemented for the combination. As the simple argument above suggests, given qualified laser beams as those from the fiber amplifiers

discussed in the Chapter 4, the coherently combined laser beam also qualifies the requirements posed by Advanced Virgo and therefore should be naturally considered in the scaling of laser power for gravitational wave detectors.

5.1 Dither-Locked Free-Space Mach–Zehnder Interferometry for Coherent Beam Combination

The two ALS fiber amplifiers presented in Section 4.6 were coherently combined using a dither-locking scheme similar to that used for the measurement of laser frequency noise (Figure 3.12). The main differences are that the Mach–Zehnder interferometer for combination was set up in free-space and that a piezoelectric fiber stretcher¹ with about 300 rad total actuation range was implemented to compensate for the differential phase drift between the arms. The setup is shown in Figure 5.1.

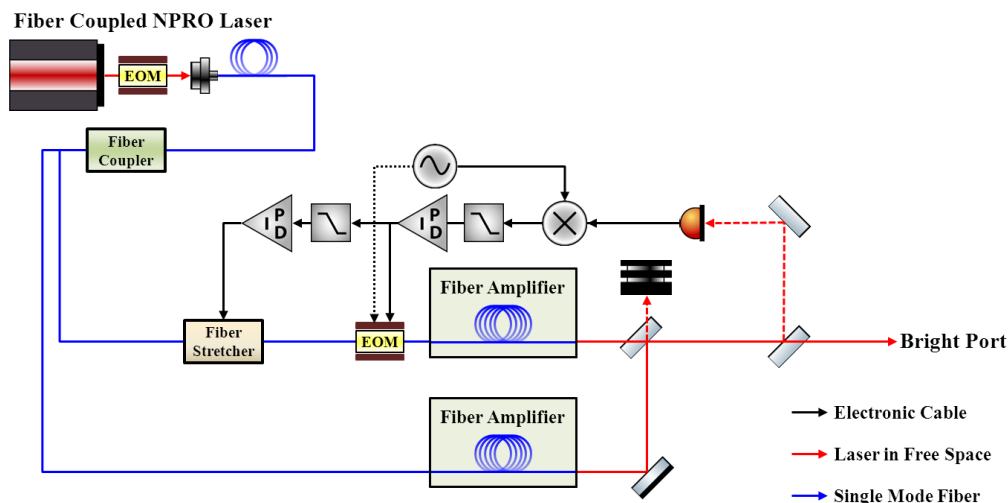


Figure 5.1: Schematic diagram of the setup for the CBC of two MOFPAs

The path length difference between the two arms was accordingly minimized to:

- Achieve better mode-matching. Since the two fiber amplifiers use identical large-mode-area fibers and therefore have almost identical beam parameters, minimizing the path length difference brings together the locations of the beam waists and leads to good mode-matching.
- Reduce the noise coupling of the laser frequency noise and the asymmetry, although the induced phase noise is rather negligible for a reasonable asymmetry.
- Take into account the compatibility with the laser frequency stabilization of Advanced Virgo (cf. Figure 2.15). Since the laser frequency adapts to various cavities which may drift, it is wise to minimize the arm length difference so that the induced phase change due to the change in laser frequency (Equation

¹OPTIPHASE, PZ1-PM1: $\sim 0.3 \text{ rad V}^{-1}$, $\pm 500 \text{ V}$, first resonance at $\sim 56 \text{ kHz}$.

3.36) may be correspondingly minimized and thus reduces the dynamic range needed for phase actuation.

- To relieve the differential phase drift due to the asymmetry coming from thermal fluctuations for example.

The path difference of the two arms in our beam combination setup was minimized to about 0.5 m. The path difference was measured by tuning the laser frequency and observing the resultant differential phase change, as related by Equation 3.36.

5.2 Phase Dynamic of Azur Light Systems Fiber Amplifiers

When performing the frequency noise measurement of the ALS 2 fiber amplifier (Figure 4.52), a phase drift of ~ 2200 rad in ~ 15 h was observed (Figure 5.2). The phase drift was compensated for by the coupling of laser frequency tuning and the ~ 25 m asymmetry, which had $\sim \pm 943$ rad phase actuation range.

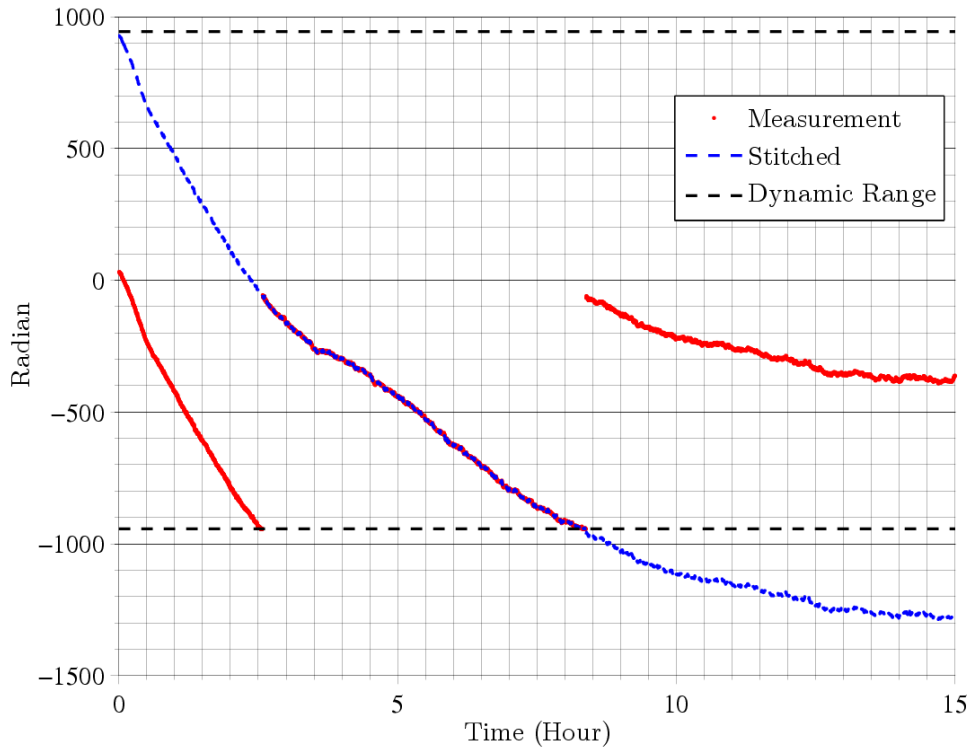


Figure 5.2: Differential phase time series of an asymmetric Mach-Zehnder interferometer in which one arm is a passive fiber and the other is the fiber amplifier ALS 2.

A continuous, uninterrupted operation of the laser system is required for interferometric GWDs, so it is important to make sure that the phase actuation range suffices the relative drifts in the Mach-Zehnder interferometer.

Previously, an increase in the path length of nearly 2000 waves was observed during the first 8 minutes of operation of a fiber amplifier, indicating that the heating of the fiber persisted even after the fiber amplifier had reached full power [143].

On the one hand, the phase drift rate is likely to decrease as the system approaches steady-state, and a continuous combination may be obtained even with limited phase actuation range, but at the cost of increased downtime of the laser interferometric GWD once a failure takes place. This suggests that a more active measure be taken.

On the other hand, ideally, when two fiber amplifiers of an identical structure are combined, we can expect that most of the phase evolution takes place in common-mode, and only some residual takes place in differential-mode. It has been reported, however, that mismatches of 10% can be expected from nominally identical fiber amplifiers [110, 143].

A similar study showed that the duration of continuous combination was limited by available actuation range [165], while another study showed that even with ~ 30 m asymmetry, by using a piezoelectric fiber stretcher, the combination system remained locked even when the pump power was tuned between 0 W and 18 W [169].

Although it is still inconclusive whether minimizing the asymmetry helps reduce the differential-mode phase drift, with our setup where the asymmetry was measured to be < 0.5 m, we were able to maintain the phase lock for combination over the course of a few hours to few tens of hours, depending on whether the system was disturbed.

Figure 5.3 shows three time series of the differential phase evolution between the two ALS fiber amplifiers in the coherent beam combination setup. We note that during the periods ① and ③ marked in the figure the system was left untouched, while some laboratory activities were undertaken during the period ②. Whenever the dynamic range is reached and that the power of the combined beam drops to a certain threshold ($\sim 15\%$ from the maximum), the locking loop stops functioning with the control signal set to zero, and re-locks again when the same threshold is triggered by spontaneous fluctuations. The re-locking process is rather fast, so we can assume that it does not interfere the combination system. We may then estimate the dynamic of the differential phase drift by stitching together the discontinuities at the unlocks, as shown in the lower half of Figure 5.3.

Accordingly, with the ~ 300 rad peak-peak phase dynamic range of the piezoelectric fiber stretcher used, an uninterrupted continuous lock may be marginally achieved given an undisturbed environment. Robustness may be improved by using multiple piezoelectric fiber stretcher of the same type in serie, or by using models with larger dynamic range. Regarding the latter, up to 4 times phase dynamic range, i.e., ~ 1200 rad, is readily available on the market².

To obtain a large phase actuation range, apart from using piezoelectric fiber stretchers, other possibilities include exploiting the Kramers–Kronik relation, as demonstrated in [169], and the use of thermal controllers. Electronically, a fast $2n\pi$ phase snapback circuit like that in [170] may also be considered.

²OPTIPHASE, PZI-PM4

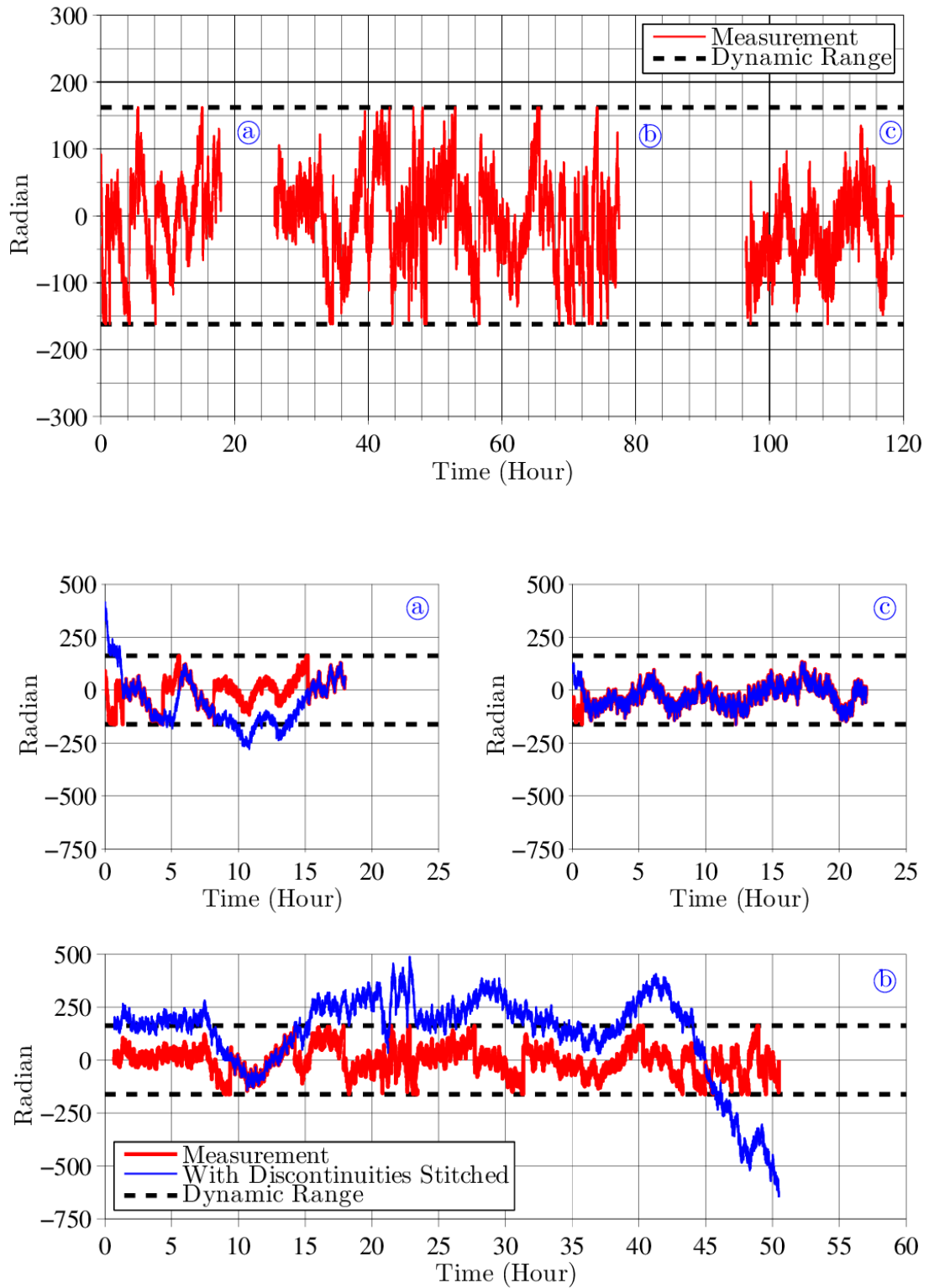


Figure 5.3: Time series of the differential phase evolution between the two ALS fiber amplifiers in the coherent beam combination setup. The raw measurement data at the top were split into the three plots at the bottom with the discontinuities stitched for an estimate on the differential phase dynamics.

5.3 Combining Efficiency and Power Penalty

In an interferometric setup, unbalanced optical power of the beams reduces the fringe contrast and results in the power penalty of beam combination. Since we might not be able to arbitrarily choose the reflectivity of the beam splitter, some studies use polarization beam splitters for coherent beam combination [171] and argue that it is a more versatile approach.

The power penalty due to power mismatch is however insignificant. Consider the interference setup shown in Figure 5.4, following Equation 3.22, we have:

$$\begin{aligned} P_3 &= TP_1 + RP_2 + 2 \cdot \sqrt{TP_1 \cdot RP_2} \cdot \cos(\phi_\Delta) \\ P_4 &= TP_2 + RP_1 + 2 \cdot \sqrt{TP_2 \cdot RP_1} \cdot \cos(\phi_\Delta + \pi) \end{aligned} \quad (5.1)$$

By letting

$$\begin{aligned} P_1 &= P_0 \\ P_2 &= P_0 + \Delta P, \end{aligned} \quad (5.2)$$

and locking P_3 at the bright fringe, the combination efficiency η is defined as

$$\begin{aligned} \eta &= \frac{P_3}{P_1 + P_2} \\ &= \frac{(1 - R)P_0 + R(P_0 + \Delta P) + 2\sqrt{(1 - R)P_0 \cdot R(P_0 + \Delta R)}}{2P_0 + \Delta P} \end{aligned} \quad (5.3)$$

and plotted in Figure 5.5. We see that the resulting power penalty due to optical power mismatch is insignificant. Loss origins related to geometrical alignment are discussed in [155, 156] (Figure 5.6), which are also rather insignificant.

The loss of combination efficiency is mainly due to uncorrelated non-TEM₀₀ modal contents in the combining beams. In other words, the combination efficiency also reflects to some extent the beam quality of the combining beams.

The percentage of the optical power in TEM₀₀ of one of the fiber amplifiers was estimated to be > 95 % (cf. Section 4.6), while that of the other fiber amplifier was not directly measured. Assuming however that they have the same optical power in TEM₀₀ and that their non-TEM₀₀ contents are uncorrelated, 95 % is a good estimate on the maximum attainable combination efficiency of our CBC setup.

After some pick-off plates for diagnostic purposes, ~ 35 W of optical power of each ALS fiber amplifier was sent to the beam-splitter. The combining efficiency at the beam-splitter level was measured to be > 87 % with direct optical power measurements. Then, after some optimization in alignment, a fringe contrast (visibility) of 92 % was measured. By combining the definition of fringe contrast and Equation 3.22, we have:

$$\begin{aligned} \text{Contrast} &= \frac{P_{Max} - P_{Min}}{P_{Max} + P_{Min}} \\ 2 \cdot \sqrt{P_1 \cdot P_2} &= \text{Contrast} \cdot (P_1 + P_2) \end{aligned} \quad (5.4)$$

such that when 50–50 beam-splitting ratio is assumed, the combination efficiency η is:

$$\eta = \frac{1}{2} \cdot \frac{P}{P_1 + P_2} = \frac{1}{2} \cdot (1 + \text{Contrast}) \quad (5.5)$$

The measured fringe contrast of 92% therefore inferred a combination efficiency of 96%, which was close to the measurement result on the beam quality of the ALS 2 fiber amplifier.

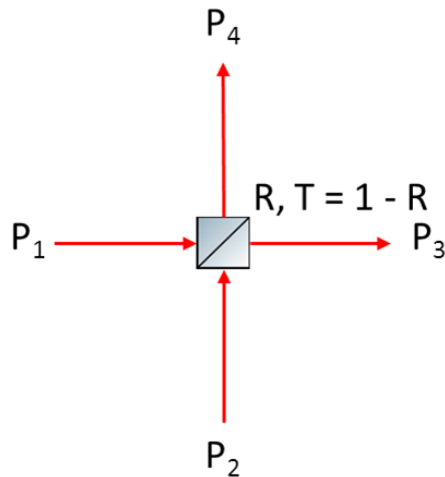


Figure 5.4: Optical interference: P_1 , P_2 are the optical power at the input ports, P_3 , P_4 are the optical power at the output ports. R is the reflectivity, and $T = 1 - R$ is the transmittance of the beam splitter.

Another power penalty for our coherent beam combination setup lies in the modulation sidebands. Figure 5.7 shows the Bessel function of the first kind of the orders 0 to 4 versus modulation depth β . In our setup, for a phase-locking unity gain frequency of ~ 1 MHz, a modulation depth $\beta \sim 0.05$ rad was implemented. According to Equation 3.30, this means that $\sim 0.06\%$ ($= 1 - J_0(0.05)$) power was taken from the carrier beam, which is negligible.

5.4 Power Noise

Figure 5.8 shows the power noise of the laser beam after coherent beam combination. At low frequencies, the power noise is generally within the Advanced Virgo requirements, except for $f > \sim 3$ kHz, just as the result of the individual fiber amplifier ALS 2 shown in Figure 4.50. Some additional noise peaks are clearly visible in the 100 Hz to 1 kHz range, with also the increased $1/f$ content below 1 kHz likely coming from the coupling of the beam pointing instability.

At high frequencies, the power noise floor is also that of the result of the individual fiber amplifier ALS 2 (Figure 4.51), with additional peaks due to the modulation ($f \sim 14$ MHz) for the phase-dithering technique. The noise peaks at the even harmonics of the modulation frequency come from dither locking. In Equation 3.30,

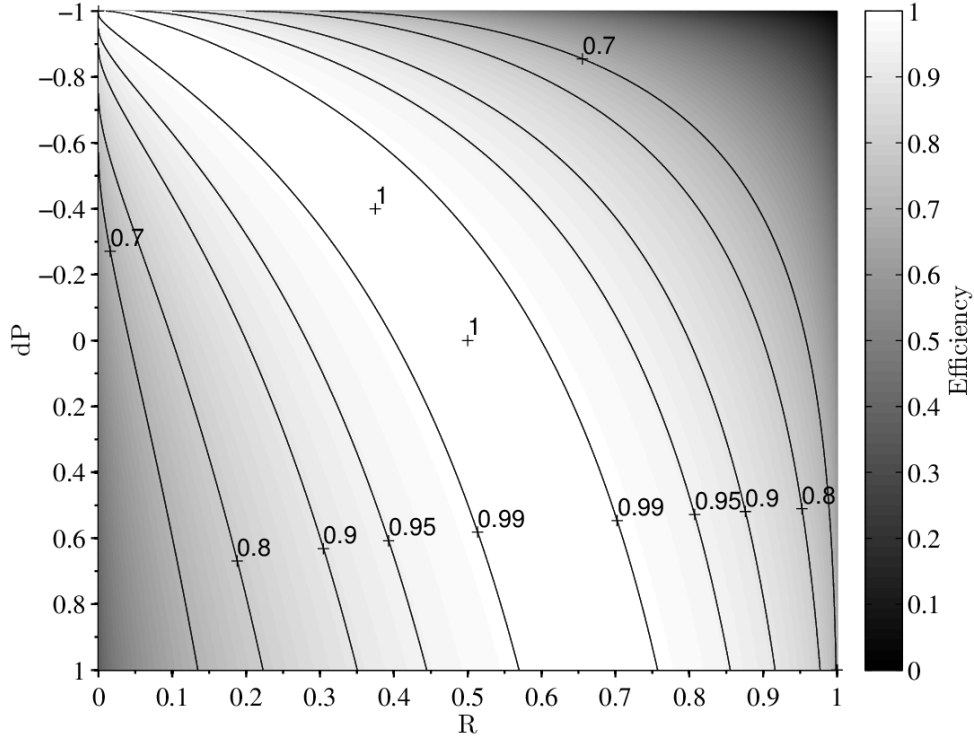


Figure 5.5: Coherent beam combination efficiency vs. optical power mismatch.

we see that when the system is locked at $\phi_\Delta = 0$, the *sin* terms vanish, but the *cos* terms remain.

The noise peaks at the modulation frequency and its odd harmonics are likely a result of residual amplitude modulation [172–176], which is a well-known effect in electro-optic modulation, and is in general significant in fiber EOMs. Any offset ϕ_ϵ in the phase lock such that $\phi_\Delta - \phi_\epsilon \rightarrow 0$ will also lead to the presence of these peaks.

In order to not interfere with the Advanced Virgo specifications, the modulation frequency for phase dithering has to be carefully chosen. Apart from this, coherent beam combination complies with the requirements in power noise.

To better understand the sources of possible noise contribution, we plot the measurements of power noise of individual fiber amplifier beams and that of the combined beam together in Figure 5.9. The measurement noise floor, which is the dark noise of the photo-detection setup, is also shown. We note that the power noise of the combined beam is plotted first, then on top it the power noise of the ALS 2 fiber amplifier, the power noise of the ALS 1 fiber amplifier, and finally the measurement noise floor. This way, the uncovered parts of the power noise curve of the combined beam may be regarded as additional noise.

An important remark is that there was a significant difference in the optical power of the two beams that were combined, owing to the abrupt loss of power of ALS 1 which eventually led to its failure. The power ratio during the time of these measurements was $\sim 1.8 : 1$.

In Figure 5.9 we see that the power noise peak set with fundamental frequency $1f \sim 185\text{Hz}$ is only visible in the combined beam, and resemble that seen in the frequency noise of the ALS 2 fiber amplifier in Figure 4.52. The reason for the

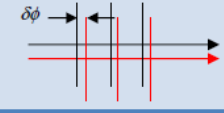
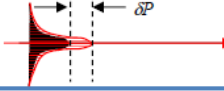
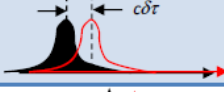
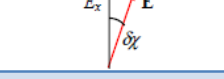
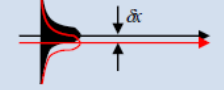
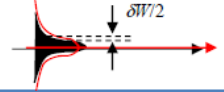
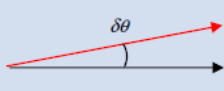
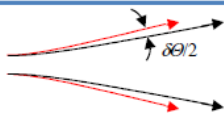
RMS Parameter Variation	Combining Loss, $1-\eta$	Value for 1% Loss	Schematic	Notes
Piston phase, σ_ϕ	σ_ϕ^2	$\sigma_\phi = 0.1$ rad		Also applies to non-common path, intensity-weighted wavefront aberrations
Power fraction, σ_P/P	$\frac{1}{4}(\sigma_P/P)^2$	$\sigma_P/P = 20\%$		$P \sim A^2$, so $\delta P \sim 2\delta A$; hence $\sigma_P/P = 2\sigma_A/A$
Optical path mismatch, $c\sigma_\tau$	$\frac{\pi^2}{2\ln(2)}\Delta f_{FWHM}^2\sigma_\tau^2$	$\Delta f_{FWHM} = 11$ GHz, $c\sigma_\tau = 1$ mm		Loss due to dephasing between beams
Polarization angle, σ_χ	σ_χ^2	$\sigma_\chi = 0.1$ rad		Equivalent to depolarized power loss
Fractional spot displacement, σ_x/W	$2\ln(2)(\sigma_x/W)^2$	$\sigma_x/W = 7\%$		δx = beam position error W = FWHM spot size Loss is for a single transverse axis x .
Fractional spot size, σ_W/W	$\frac{1}{2}(\sigma_W/W)^2$	$\sigma_W/W = 14\%$		W = FWHM spot size Loss is for a single transverse axis x .
Fractional pointing, σ_θ/Θ	$2\ln(2)(\sigma_\theta/\Theta)^2$	$\sigma_\theta/\Theta = 7\%$		$\delta\theta$ = beam pointing error Θ = FWHM divergence Loss is for a single transverse axis x .
Fractional divergence, σ_Θ/Θ	$\frac{1}{2}(\sigma_\Theta/\Theta)^2$	$\sigma_\Theta/\Theta = 14\%$		Θ = FWHM divergence Loss is for a single transverse axis x .

Figure 5.6: Loss analysis of mismatched Gaussian beams for coherent combination. From [155].

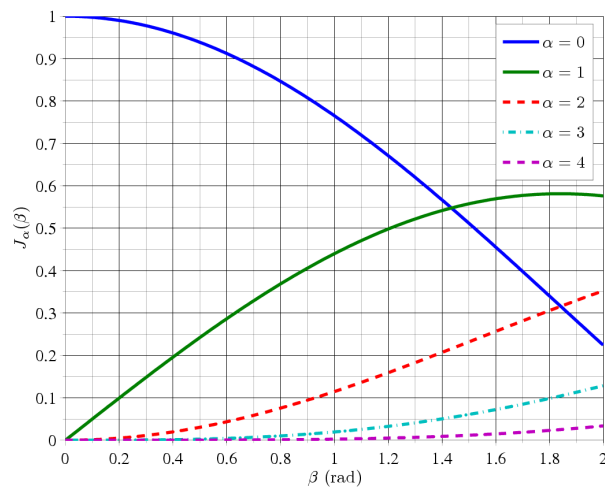


Figure 5.7: Bessel function of the first kind.

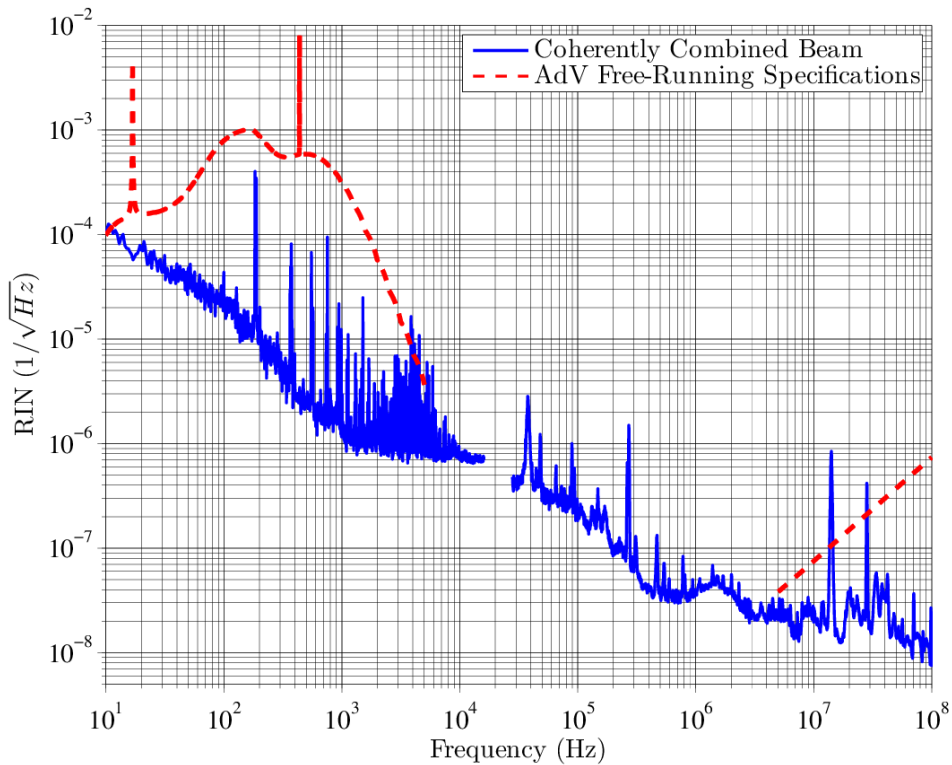


Figure 5.8: Power noise of the coherently combined beam.

correlation is not clear. Possible explanations include:

- Noise coupling effects. If the two combining beams are not perfectly collinear, the correction of their differential phase noise can translate into beam pointing instability. The finite aperture of the photodiode then translates the beam pointing instability to power noise. This seems to be one likely contribution, as the correlation between the fiber amplifier frequency noise and the beam pointing instability was also observed, not only for the noise peak set with fundamental frequency $f_0 \sim 185$ Hz but also in the kHz range (Figures 4.52 and 5.13).
- A loophole in our frequency/phase sensitive measurement setup. This, however, does not seem to be the case according to the calibration measurement of a 25 m fiber (Figure 4.52).

At high frequencies, we see from Figure 5.9 that the coherent beam combination process does not alter much the noise performance, except at frequencies associated with the phase modulation signal. We see clearly the effect of the radio frequency modulation at 14 MHz, which is the strongest in the ALS 2 fiber amplifier output beam, where the phase modulation takes place, due to residual amplitude modulation (RAM). It is also visible in the combined beam, and even the output beam of ALS 1. The latter may be explained by electromagnetic coupling, as is seen in the dark noise which defines the measurement floor. The former, at first glance, may seem to due to RAM, while we note that the phase locking loop normally should render RAM into an offset in the locking point such that the signal at 14 MHz is null.

To further explain, we note that the differential phase noise at Fourier frequencies higher than the loop bandwidth (~ 1 MHz), as can be inferred from Figure 5.11, not only renders itself into power noise at the output of the combined beam, but also induces the residual of the modulation sidebands due to non-zero ϕ_Δ in Equation 3.30. We also recall that the even harmonics of the 14 MHz modulation are present due to the dither-locking technique (Equation 3.30).

5.5 Frequency Noise and Beam Quality

It was planned to couple part of the beam after the combination to a single-mode fiber for the assessment on beam profile and the measurement of frequency noise.

The coupling efficiency of the individual beams and the combined beam will provide information on the beam quality of each beam, and a cross comparison will provide information on mode-matching. A scanning Fabry–Perot cavity will also be used to precisely characterize the transverse modal contents of each beam.

The fiber-coupled beam will then be sent to a fiber Mach–Zehnder interferometer in which the beam in one arm is frequency-shifted with an acousto-optic modulator. Following the discussions in Section 3.6, we can then measure the differential phase noise and convert it to frequency noise with Equation 3.19.

Unfortunately, due to the failure of the two fiber amplifiers, we have not been able to perform such task to date.

In principle, in the MZI beam combination scheme, since one beam is locked with respect to the other beam, the frequency noise of the combined beam should resemble that of the reference beam. Although only experimental verification could give a real measure on the frequency noise of the combined beam, the expected result of the coherently combined beam should not differ too much from that shown in Figure 4.52.

Once locked, the differential frequency noise between the two fiber amplifiers may be assessed using the control signal sent to the fast phase actuator, the EOM, as shown in Figure 5.10. It should be noted that due to a communication error³ in the implementation of the locking electronics, the crossing frequency between the fast EOM path and the slow piezoelectric fiber stretcher path was ~ 300 Hz instead of the few Hz foreseen, so the results at lower frequencies may be biased.

The differential frequency noise also resembles that of ALS 2 shown in Figure 4.52 in terms of the floor and roughly the peak frequencies, especially the set with $f_0 \sim 185$ Hz.

Another way to assess the differential frequency noise is to measure the power noise of the combined beam when the system is left free-running. The results obtained this way are however only qualitative, as the coupling from frequency noise to power noise is dependent on the fringe state. Therefore, to properly recover from the measured power noise to frequency noise, the time series has to be acquired with a sampling rate that is high enough in comparison to the frequency band of interest, followed by tedious data analysis. It is however interesting to compare the power

³We forgot to include the 50 V/V gain of the high-voltage amplifier for the piezoelectric fiber stretcher.

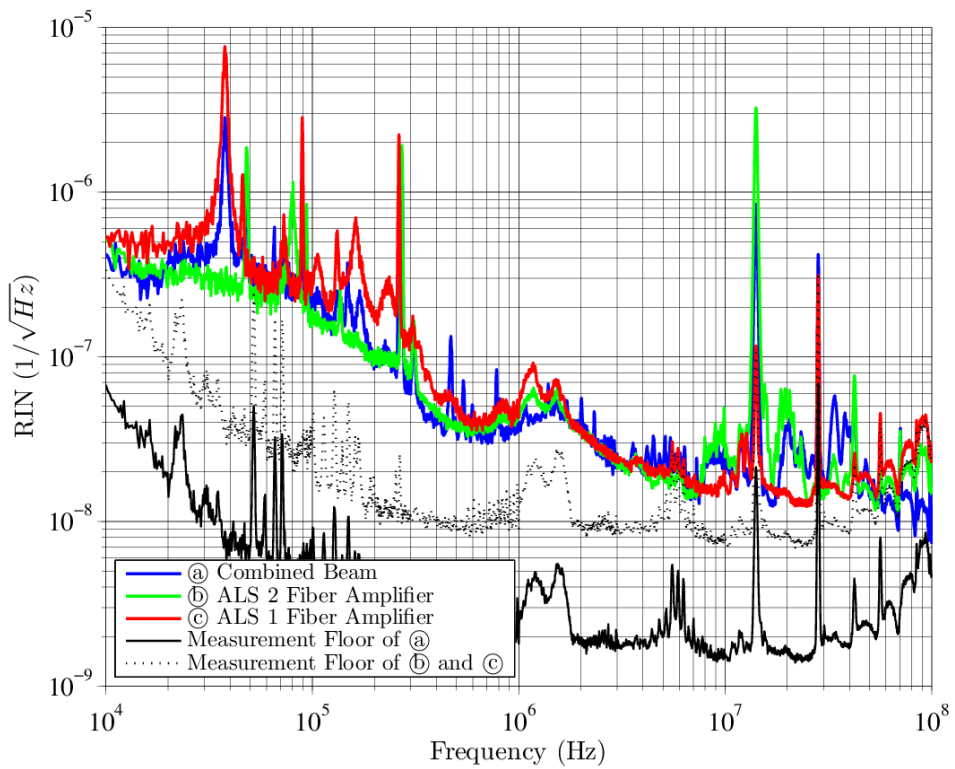
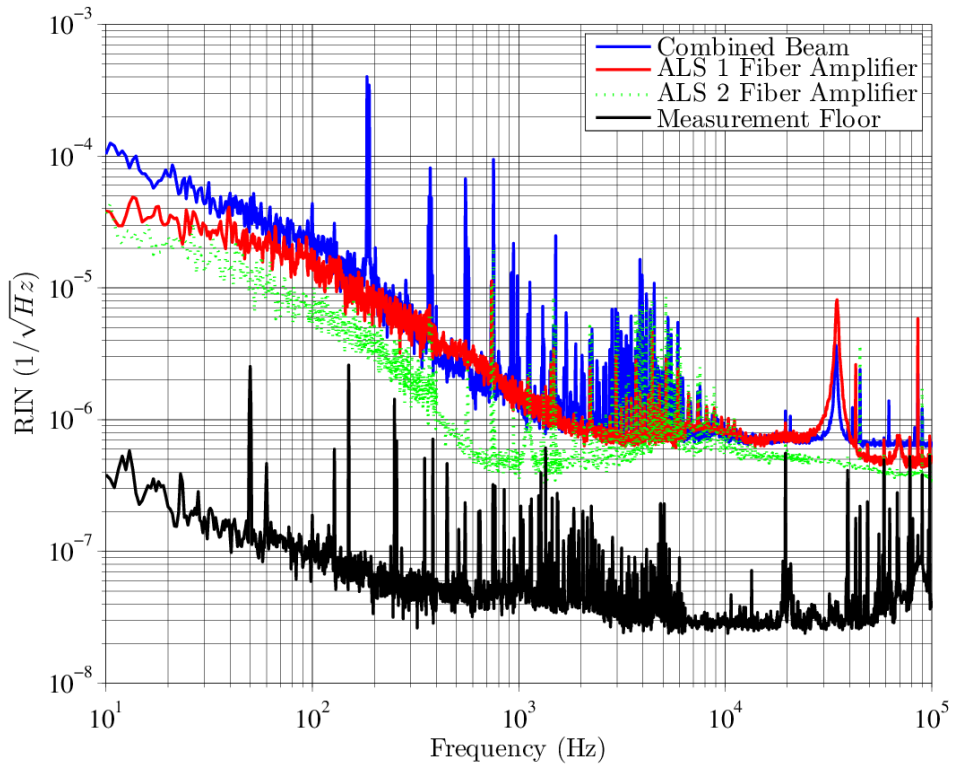


Figure 5.9: Power noise of the individual fiber amplifier beams and the coherently combined beam.

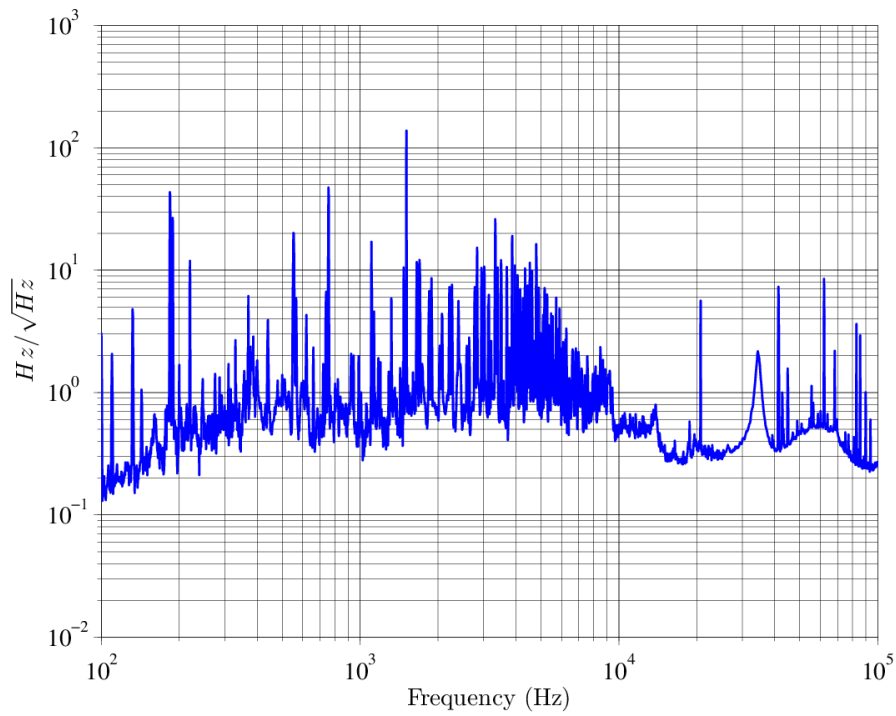


Figure 5.10: Differential frequency noise between the two fiber amplifiers used for coherent beam combination. This measurement is derived from the differential phase correction signal.

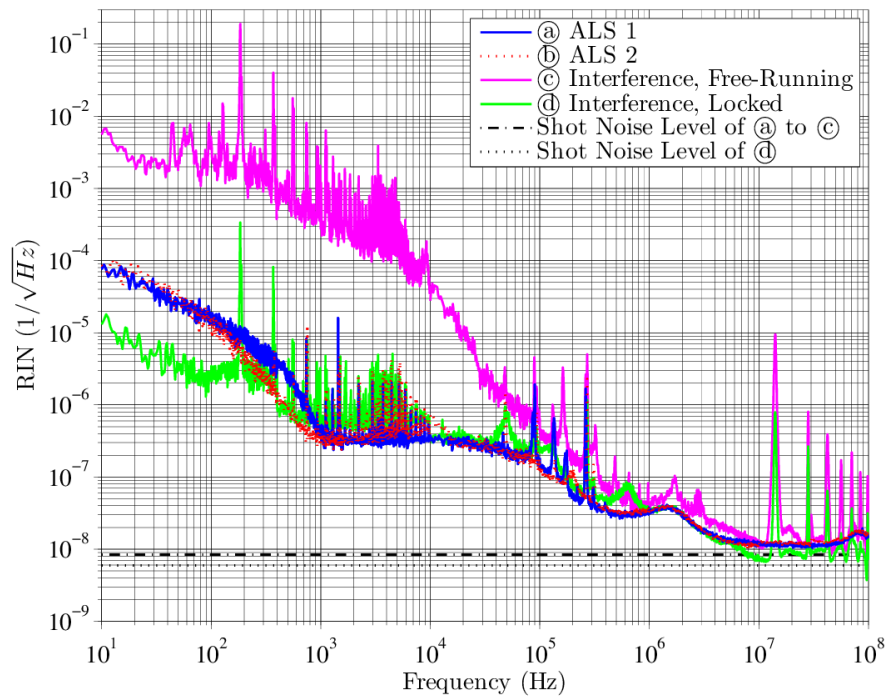


Figure 5.11: Power noise of the combined beam when free-running and when phase-locked.

noise of the combined beam when it is phase-locked, to the free-running counterpart, as shown in Figure 5.11.

5.6 Beam Pointing Stability

Figure 5.12 shows the beam pointing stability after the coherent combination, which is within the Advanced Virgo free-running specifications. The results also resemble those of individual fiber amplifiers shown in Figure 4.53, except for the noise peak set with $f_0 \sim 185$ Hz, and the peak forest between ~ 1 kHz and ~ 10 kHz, which correspond to those measured in the frequency noise of ALS 2 shown in Figure 4.52, and those in the differential frequency noise shown in Figure 5.10.

This observation confirms the argument that due to the misalignment of the two combining beams, the correction of differential phase noise couples to beam pointing instability, which then couples with the clipping effect of the finite dimension of the photodiode and results in the peaks seen in the power noise measurement in Figure 5.9.

For a clearer comparison, the beam pointing stability of the the individual beams and the combined beam are brought together in Figure 5.13. We note that the photocurrents used for the measurement were different and therefore resulted in the different measurement floors visible in the figure for readings reaching $\sim 10^{-7} \sqrt{\text{Hz}}^{-1}$. The additional noise peaks in the pointing instability of the combined beam associated with the frequency noise measurement shown in Figures 4.52 and 5.10 are then easily identified.

In any case, these additional noise peaks do not exceed the requirements of Advanced Virgo and thereby once again justifying coherent beam combination a suitable means for power scaling. Moreover, the presence of such noise coupling mechanism automatically serves as a probe for the degree of alignment of the two combining beams, as illustrated in [150], if any auto-alignment effort is to be taken.

5.7 Long Term Monitoring Results

To check the stability of the coherent beam combination system, in addition to the differential phase dynamics shown in Figure 5.3, an ADC card was used to monitor and generate the spectrogram of various signals. We note that although the input noise of the ADC card was significant, as well as the dark noise of the photodiode and the transimpedance amplifier used for the ALS 1 fiber amplifier, according to the calibration measurements shown in Figure 5.14, the results obtained this way are still relevant, at least for $f < \sim 10$ kHz. The measurement setup for the combined beam is similar to that for ALS 2.

The resulting spectrograms are: Figure 5.15 for the power noise of the ALS 1 fiber amplifier, Figure 5.16 for the power noise of the ALS 2 fiber amplifier, Figure 5.17 for the power noise of the combined beam, and Figure 5.18 for the differential phase noise between the two fiber amplifiers. The blank gaps are the periods where the relevant data are not available, either due to the security shutdown of the fiber

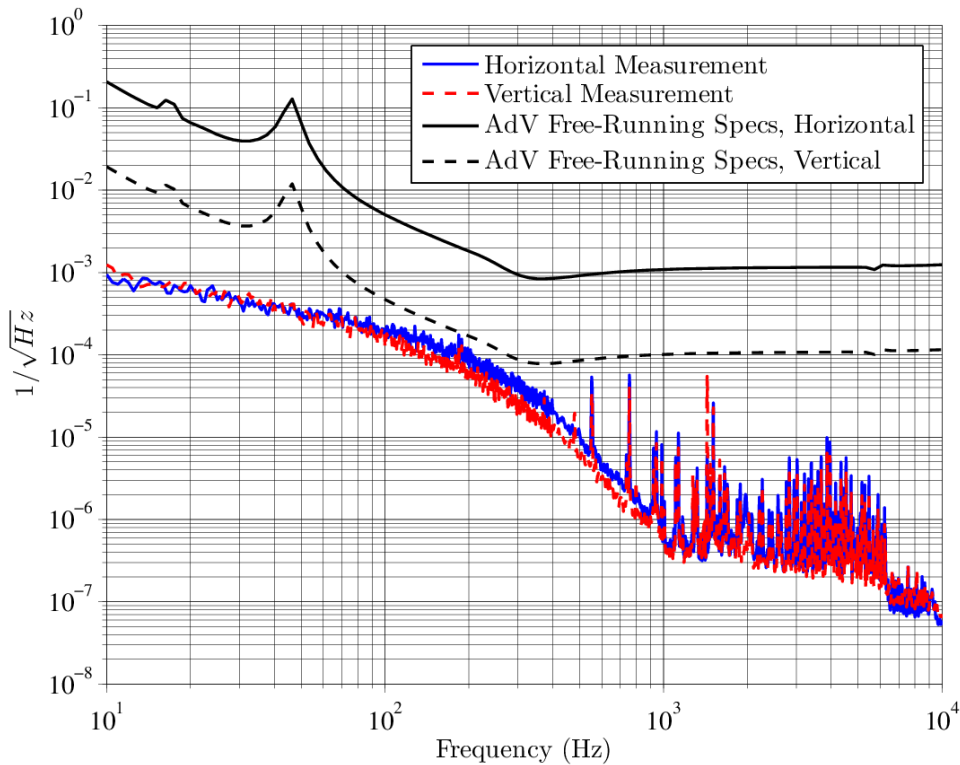


Figure 5.12: Beam pointing stability of the coherently combined beam vs Advanced Virgo free-running specifications.

amplifiers or experimental purposes. We note that in the coherent beam combination experiment the fiber amplifiers were relocated to the same room.

We see from the spectrograms that the power noise of ALS 1 is different from that of ALS 2. The peak forest in ALS 1 is less visible. Considerable fluctuations in the power noise level are again observed in both ALS fiber amplifiers. The power noise of the combined beam is higher than that of the combining beams, notably at the set of frequencies with $f_0 \sim 185$ Hz.

The frequency set with $f_0 \sim 185$ Hz, as well as many frequency peaks, has constant and stable appearance in the differential phase/frequency noise spectrum. It may therefore be suggested that these peaks are stable oscillations in the individual fiber amplifiers with different frequencies.

5.8 Laser Power Stabilization On Top of Coherent Beam Combination

Coherent beam combination provides an additional actuation path for power stabilization. Using a dither-locked Mach—Zehnder interferometer, by offsetting the locking point from the bright fringe, we get some slope for power actuation, at the cost of decreased combination efficiency and increased phase noise. The former is not really an issue as all power stabilization schemes would require some power reserve anyway. The latter, judging from the need of our application, Advanced Virgo,

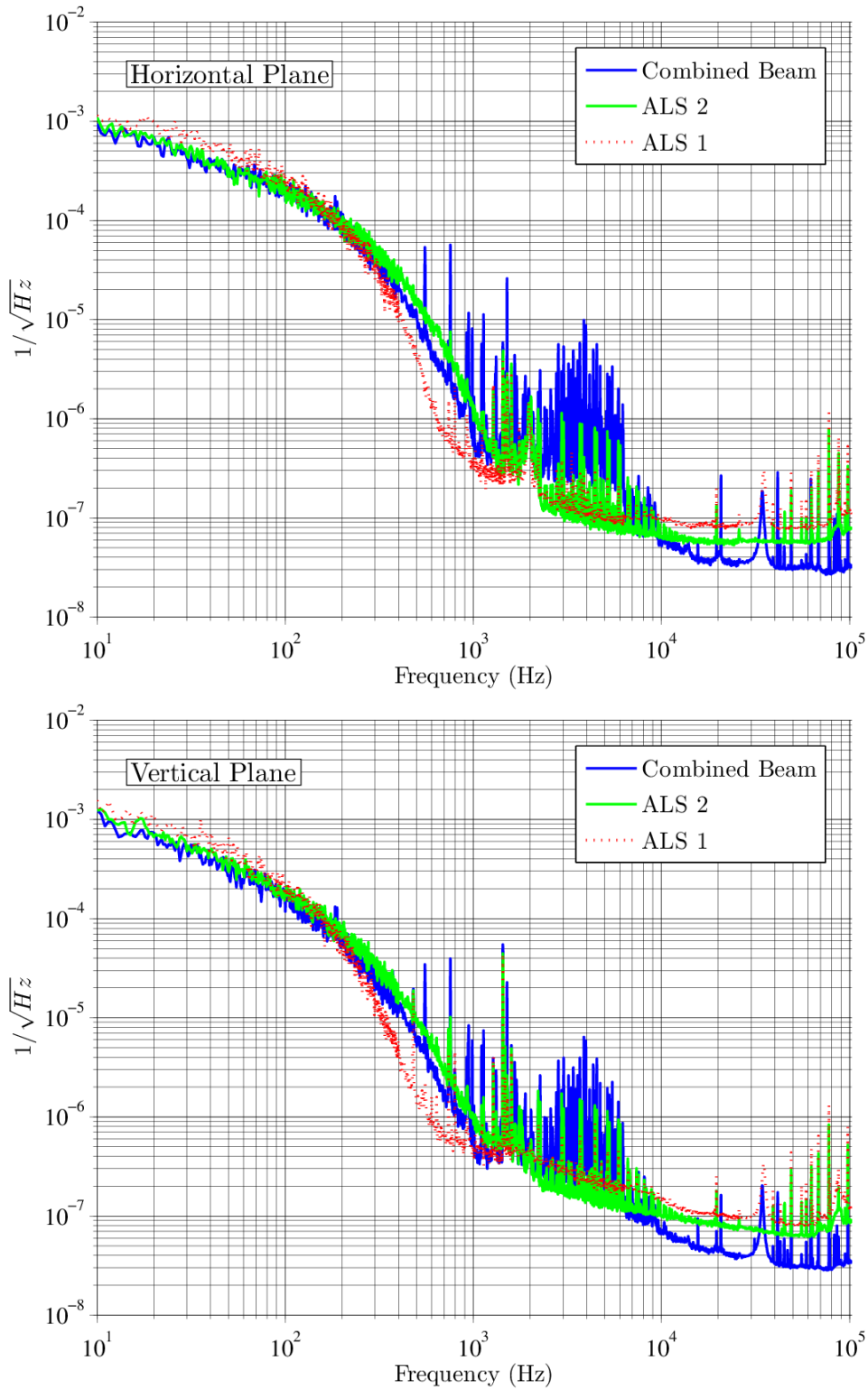


Figure 5.13: Beam pointing stability of the individual beams and the combined beam.

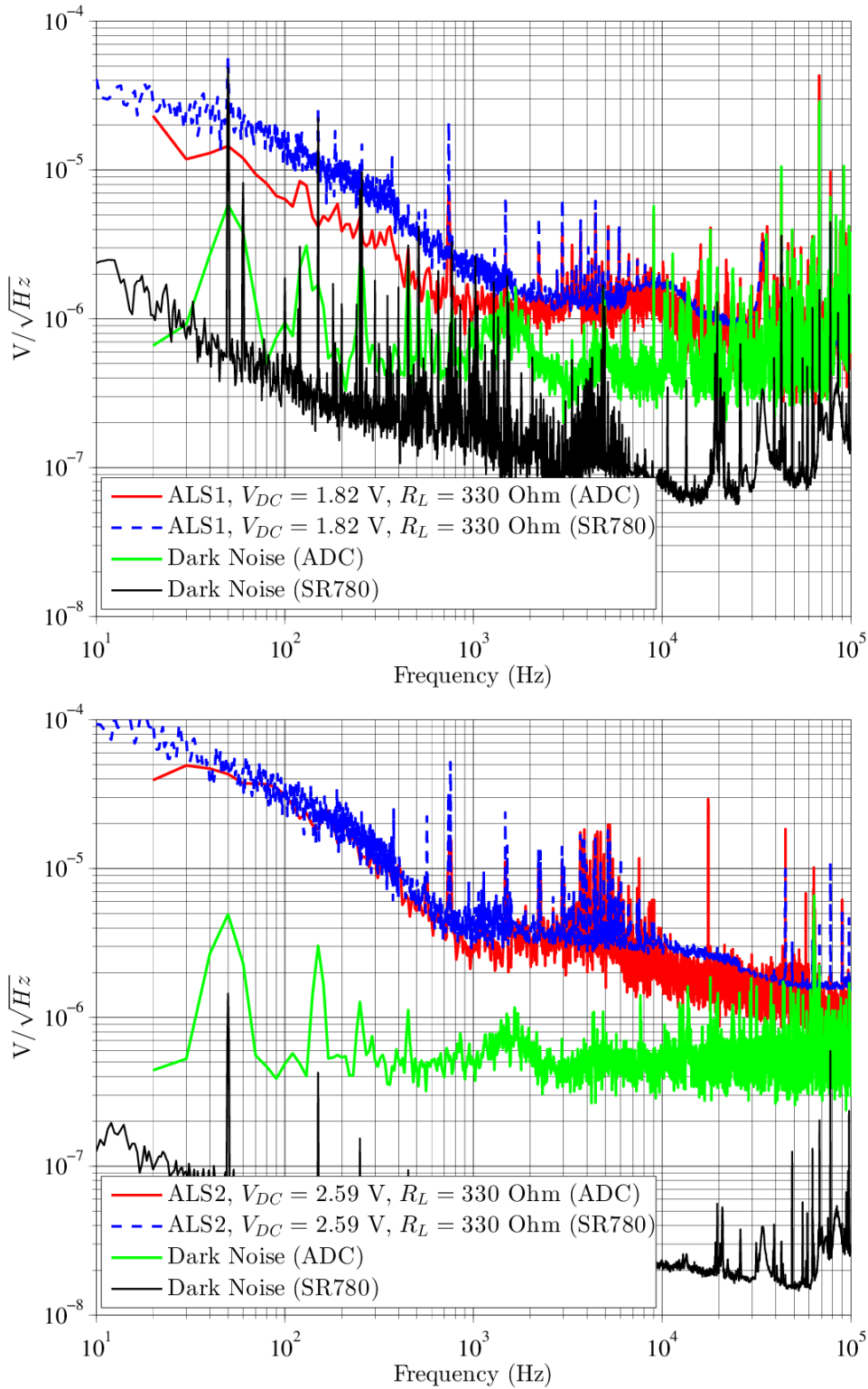


Figure 5.14: Power noise measurement with an ADC card calibrated against the SR780 spectrum analyzer. Note that these are raw voltage measurements, not RIN measurements.

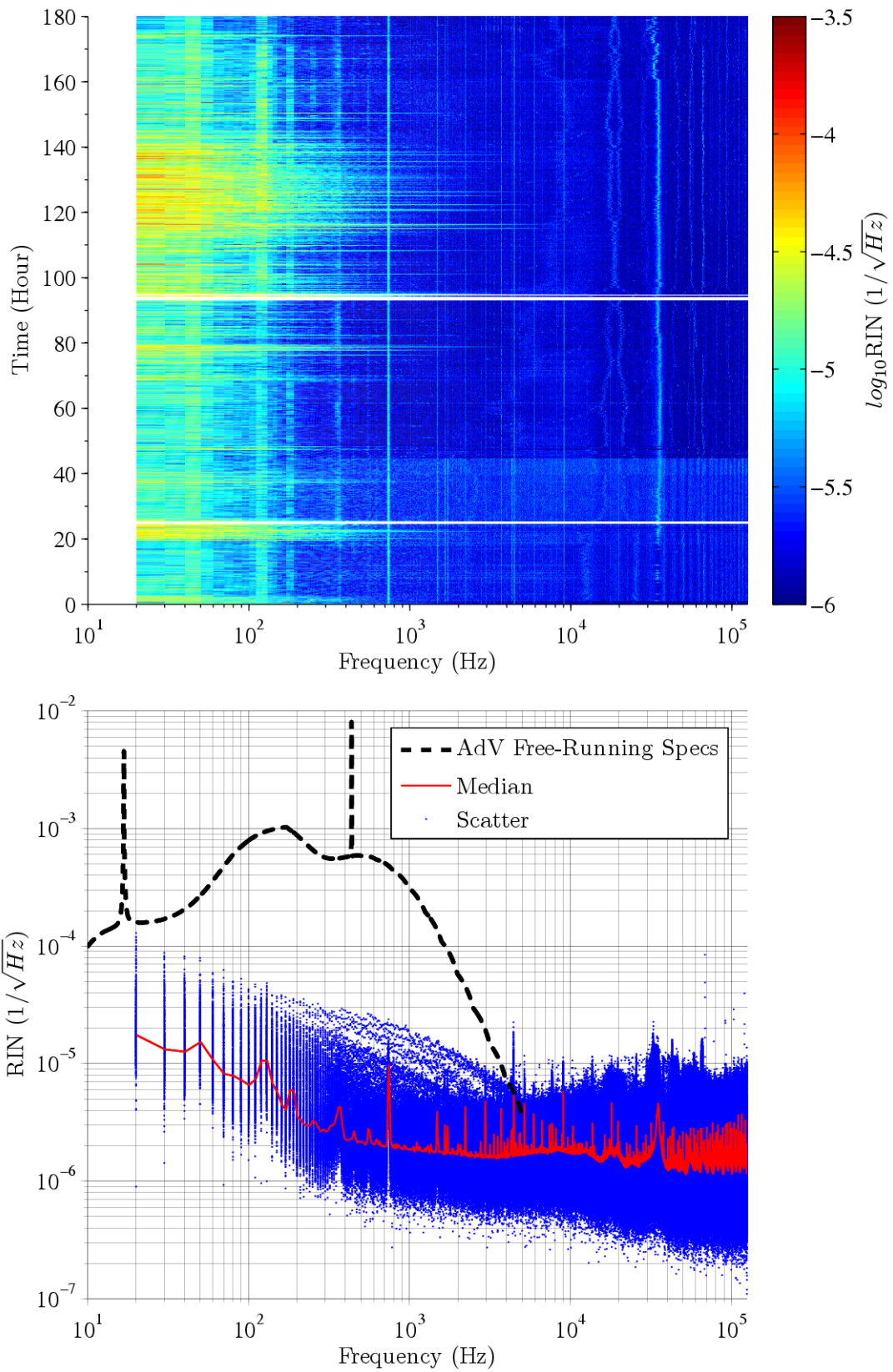


Figure 5.15: Spectrogram of the power noise of the ALS 1 fiber amplifier in the coherent beam combination experiment.

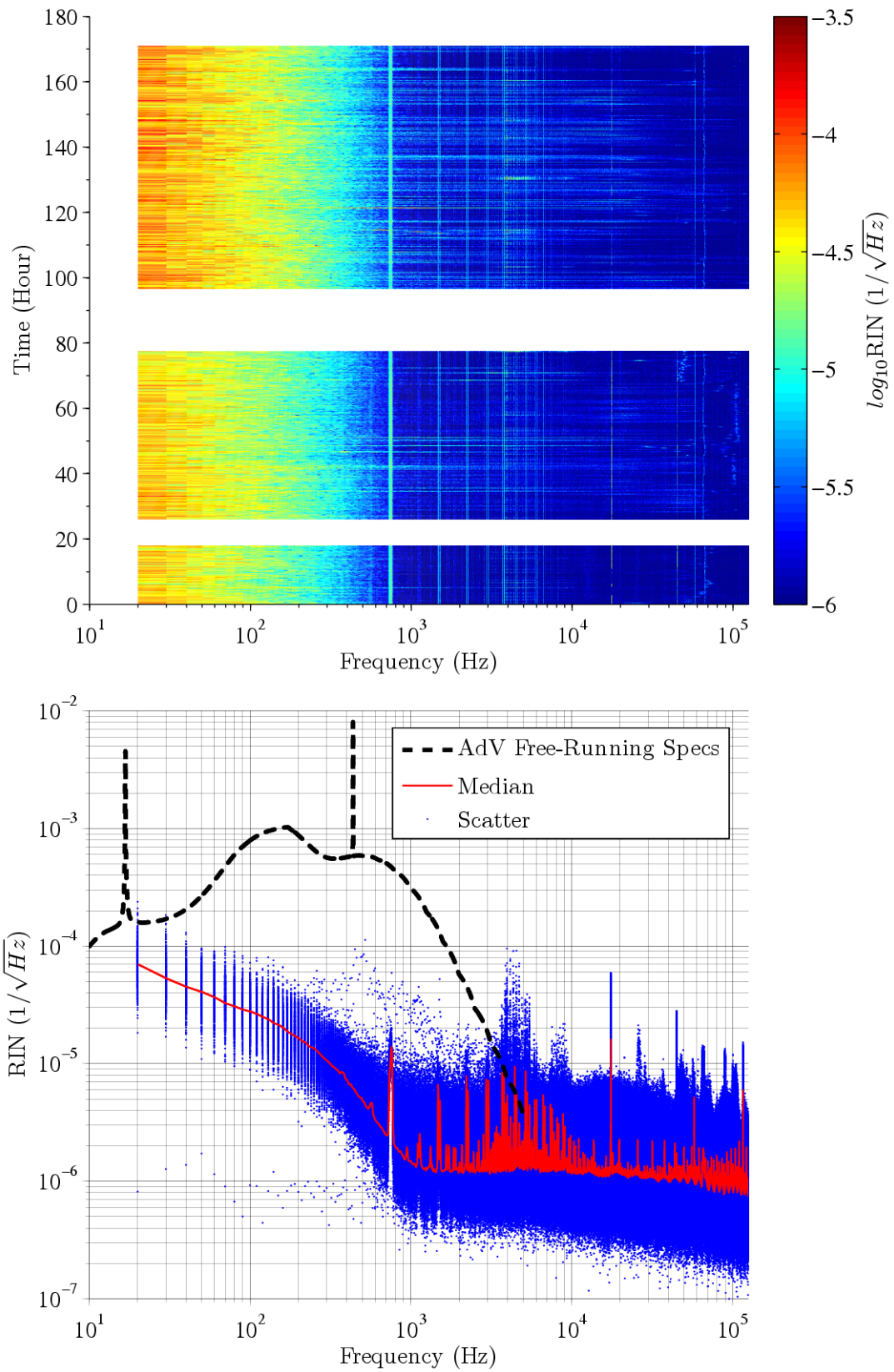


Figure 5.16: Spectrogram of the power noise of the ALS 2 fiber amplifier in the coherent beam combination experiment.

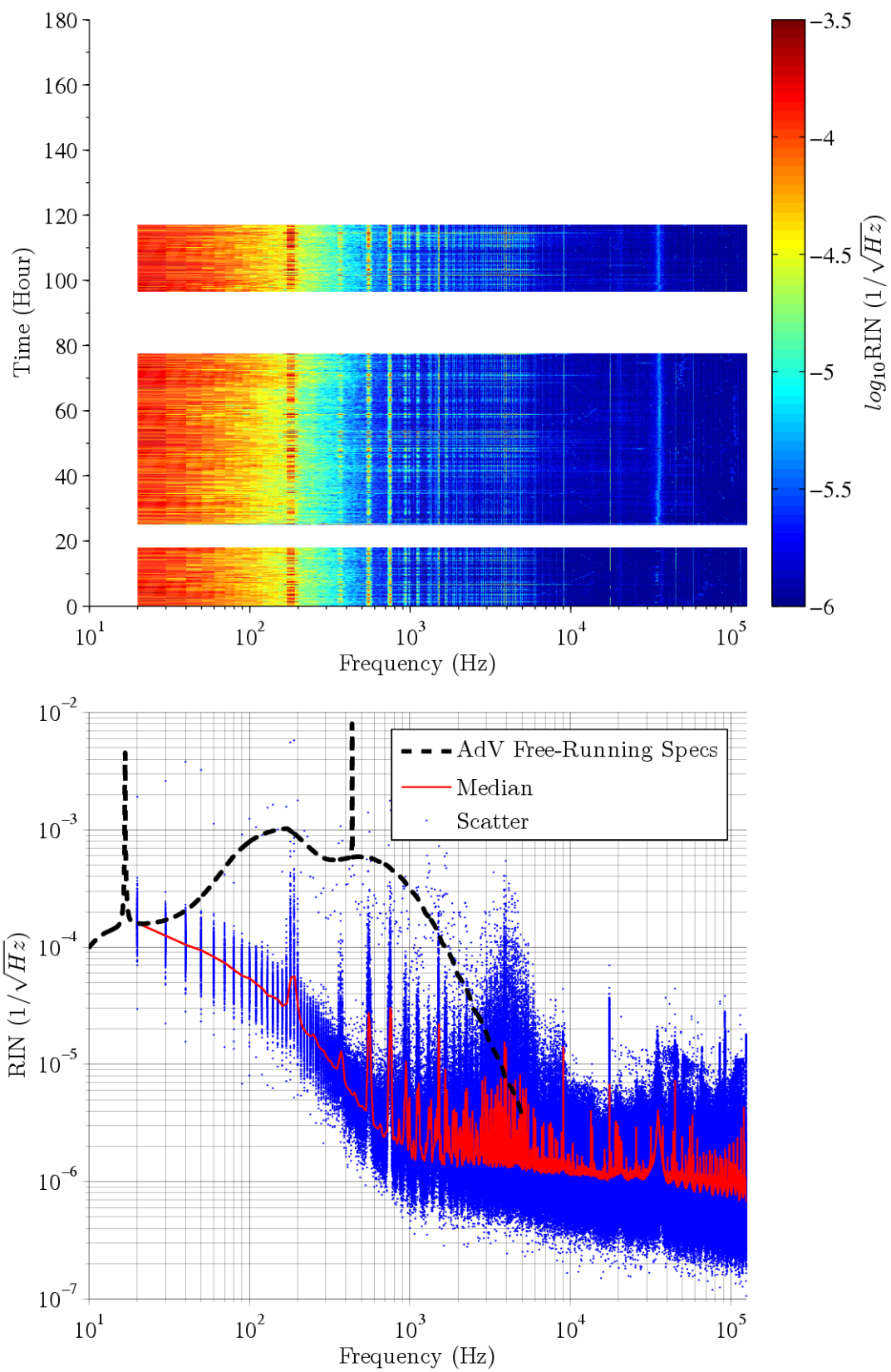


Figure 5.17: Spectrogram of the power noise of the combined beam in the coherent beam combination experiment.

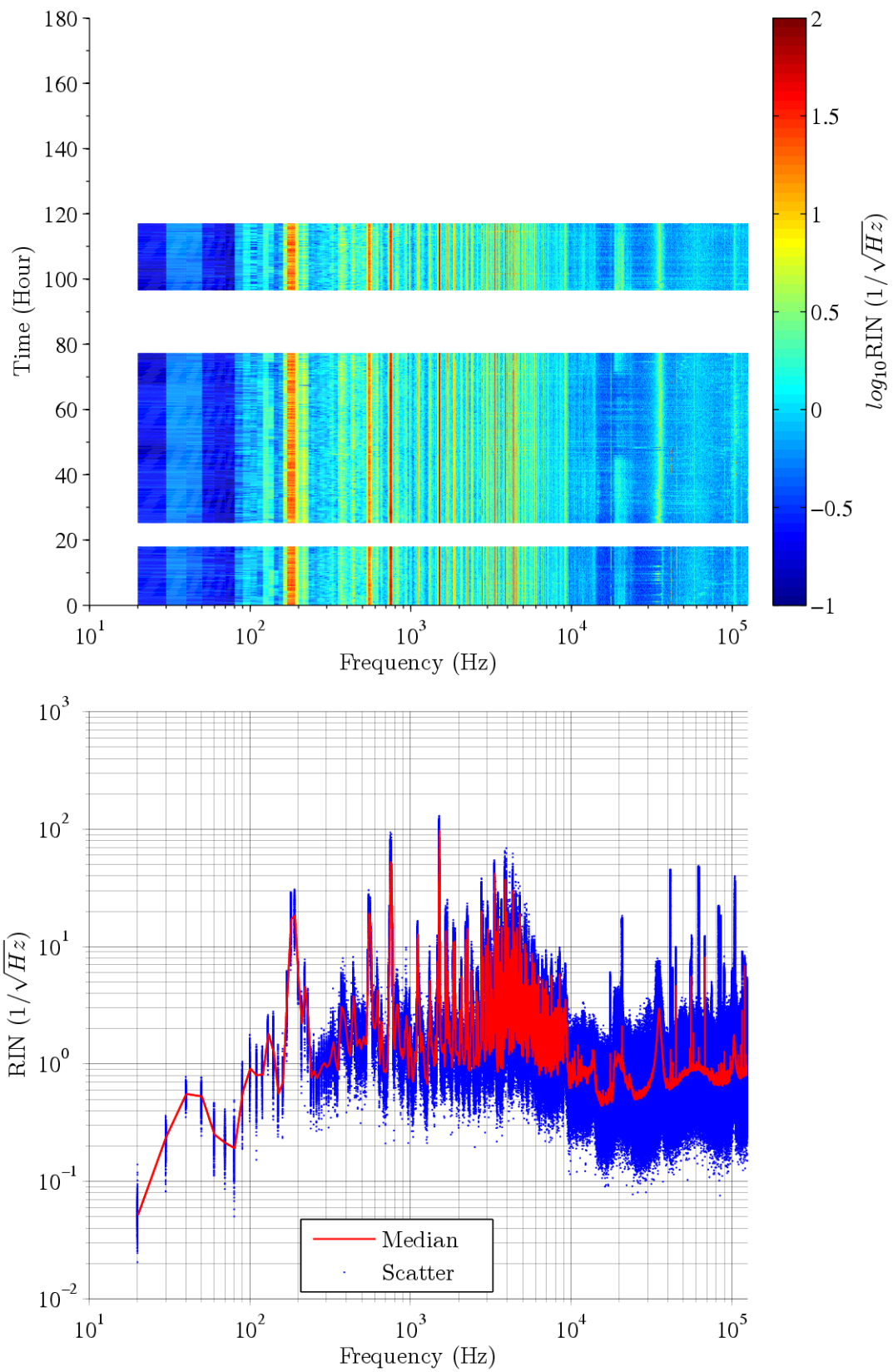


Figure 5.18: Spectrogram of the differential phase noise in the coherent beam combination experiment.

is tolerable, as discussed below.

Consider Figure 5.4 and let $P_1 = P_2 = P_0$, we have

$$P_3 = P_0 \cdot (1 + \cos\phi_\Delta), \quad (5.6)$$

whose derivative with respect to ϕ_Δ is

$$\frac{\delta P_3}{\delta\phi_\Delta} = -P_0 \cdot \sin\phi_\Delta. \quad (5.7)$$

To control P_3 and suppress RIN (here $\text{RIN} = \delta P_3/P_3$) by tuning ϕ_Δ , following the definition in Equation 3.1, we define the conversion factor Γ as:

$$\Gamma \equiv \frac{\delta \text{RIN}}{\delta\phi_\Delta} = -\frac{\sin\phi_\Delta}{1 + \cos\phi_\Delta}. \quad (5.8)$$

The induced phase in the combined beam, $\delta\phi_{CBC}$, is half of $\delta\phi_\Delta$:

$$\begin{aligned} \delta\phi_{CBC} &= \frac{1}{2} \cdot \delta\phi_\Delta \\ &= \frac{1}{2} \cdot \frac{\delta \text{RIN}}{\Gamma}. \end{aligned} \quad (5.9)$$

Equation 5.9 relates the translation of RIN to phase noise in the combined beam. The effect of such translation may be assessed, at first glance, by looking at the free-running laser frequency noise specifications for Advanced Virgo (Figure 2.18), in which large attenuation is present at low frequencies, and the free-running power noise of the coherently combined fiber amplifiers (Figure 5.8). If we approximate the latter by an upper limit of $0.1/f \sqrt{\text{Hz}}^{-1}$, and assume a 0.3 rad offset in ϕ_Δ which leads to $\Gamma \approx -0.15$, the resulting frequency noise is:

$$\begin{aligned} \delta\nu_{CBC} &= f \cdot \delta\phi_{CBC} \\ &= f \cdot \frac{1}{2} \cdot \frac{\delta \text{RIN}}{\Gamma} \\ &= f \cdot \frac{1}{2} \cdot \frac{-0.1/f \sqrt{\text{Hz}}^{-1}}{-0.15} \\ &= \frac{1}{3} \text{Hz} \sqrt{\text{Hz}}^{-1}, \end{aligned} \quad (5.10)$$

which is within the specifications (cf. Figure 2.18). It is also below the frequency noise of a typical NPRO laser and the ALS fiber amplifier (cf. Figure 4.52). The power penalty for a 0.3 rad offset is $\sim 4.5\%$, which is a reasonable value as all power stabilization scheme would require some actuation reserve.

5.9 Combining More Beams

Considering the shortcoming of available output power of individual fiber amplifiers, to reach the required 200 W for Advanced Virgo, the combination of more than two fiber amplifiers may have to be considered. As presented throughout the chapter,

the setup shown in Figure 5.1 are compatible with Advanced Virgo, and may be scaled to incorporate more fiber amplifiers.

Figure 5.19 shows a schematic diagram in which three fiber amplifiers are combined. By using different phase modulation frequencies, in principle all the phase locking may be done using a single fast photodiode. Moreover, if we consider the frontal phase dithering scheme as presented in Section 3.6, it may be possible to use only one EOM on which multiple phase modulation frequencies are applied accordingly to the arm length difference between the interfering beams.

An additional path for the overall frequency/phase noise measurement of the combined beam is also shown in Figure 5.19 for information. The additional fibered beams, one from the laser source and one after the coherent beam combination, will be useful for diagnostic purposes as well as the phase reference for the phase camera in the Thermal Compensation System (TCS) of Advanced Virgo [177].

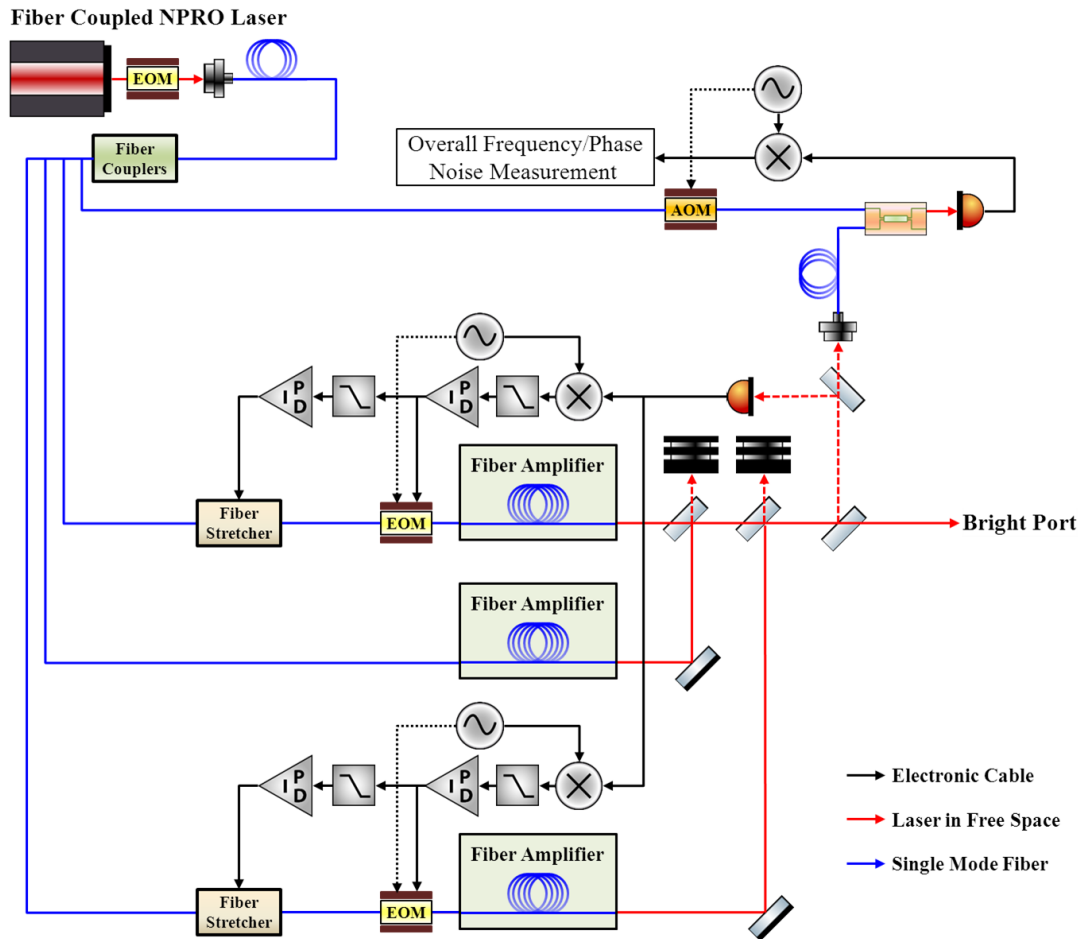


Figure 5.19: A schematic diagram on the coherent beam combination with three fiber amplifiers.

Chapter 6

Conclusions and Perspectives

6.1 High-Power Fiber Amplifiers

The test results in Chapter 4 show that the master oscillator fiber power amplifier (MOFPA) configuration can deliver stable low-noise output power of ~ 42 W for a timescale of months. As we have shown, in terms of noise performance, the system complies with the requirements of Advanced Virgo.

What is not yet fully proven, is the attainable output power for stable operation while maintaining the low-noise characteristics that we have measured. Although the output power level of fiber amplifiers tested in this work does not meet the expectation of the reference design shown in Figure 2.15, the long-term operation capacity of fiber amplifiers justified in this work, which to our knowledge has not been systematically reported, is nevertheless encouraging for their use in laser interferometric GWDs.

In terms of research and development, as discussed in Section 2.3, in recent years there have been extensive researches focused on the transverse mode instability and photo-darkening which are the current limiting factors in the power-scaling of fiber amplifiers. The solution-seeking process is still ongoing, and will hopefully provide valuable results in view of more advanced fiber designs and the know-how in handling critical fiber-optic components.

On the system level for their application in laser interferometric GWDs, in future long-term monitoring tests of fiber amplifiers, one can consider introducing additional probes to distinguish the effect of photo-darkening and the aging of critical fiber-optic components. This may be done, for example, by the co-injection of a laser beam with a visible wavelength into the fiber amplifier. The possible advantage is two-fold. First, it has been shown that the rate of photo-darkening is higher towards shorter wavelengths [104, 106]. Therefore, the co-injected visible light serves as a more sensitive probe for the 1064 nm wavelength of interest. Second, it has been reported that the co-injection of visible light suppresses the photo-darkening induced losses [178, 179], and such photo-bleaching effect has also been reported by the exposure to ultraviolet light [106].

On the other hand, probes may also be introduced at the combiner level (tapered fiber bundle) where the signal beam and the pump beam(s) are brought together to assess component aging effects.

The introduction of either additional probe will thus bring more insight in future long-term tests of fiber amplifiers and lead to a better planning for their use in laser interferometric GWDs.

A minor consideration lies in the actuation path for laser power stabilization. As Equation 4.6 suggests, the corner frequency is dependent on amplifier configuration, notably the seed signal power and the pump power. If the existing know-how in laser power stabilization for the Virgo GWD based on shunting the pump current is to be implemented in Advanced Virgo, it may be useful to include the corner frequency into consideration in defining the MOFPA configuration.

6.2 Coherent Beam Combination

In Chapter 5 we show that, if single-frequency single-mode laser beams are used, the coherent beam combination technique itself is fully compatible with Advanced Virgo. The technique is arbitrarily scalable, but at the cost of increased system complexity. Also, considering the finite rate of failure per amplifier, it may not be wise to have a large number of amplifiers when continuous uninterrupted operation is desired.

Taking these considerations into account and also the currently attainable output power of fiber amplifiers, 3 to 4 should be reasonable limit for the final system for Advanced Virgo. This then implies the need of fiber amplifiers with minimum output power level of 50 W to 70 W. Fiber amplifiers with ~ 100 W are still certainly a strong plus, but may be unrealistic when the project time line is also to be considered.

6.3 Besides High-Power Laser

Higher laser power is not the only mean to advance the quantum limit in detector sensitivity. Moreover, radiation pressure noise at the test mass mirrors scales with impinging laser power, higher laser power also means that heavier test masses have to be used to achieve an overall gain in the standard quantum limit (SQL) [30, 37, 38]. The extreme high intra cavity power also induces parametric instabilities in the resonant cavities [180–183], as is observed in Advanced LIGO [184];

As mentioned in the beginning of Chapter 2, the use of squeezed light can also improve the sensitivity of laser interferometric GWDs. Up to 3.7 dB sensitivity improvement has been demonstrated with the GEO-HF project [39, 185, 186], and up to 2.15 dB with the LIGO project [187]. Among other factors, the improvement with squeezed light is inversely proportional to optical losses. For example, a 10% total loss will limit the improvement by a maximum of 10 dB. For Advanced LIGO, the estimated total loss is 20% to 32%, which equates maximum squeezing of 5 dB to 7 dB, and the projected total loss after a future effort on loss reduction is 9% to 17%, inferring 8 dB to 10 dB maximum squeezing [188]. A 10 dB squeezing is equivalent to the increase in optical power by a factor 10, and is therefore a powerful technique in advancing further the detection limit of laser interferometric GWDs.

If we take a closer look at Figure 1.5, we see that the Brownian noise of the mirror coating dominates in the mid frequency range. Therefore, the development of better mirror coating technologies should be born in mind in addition to the improvements in the standard quantum limit.

Last, a different interferometer configuration, the Sagnac speed meter, which has better SQL detection sensitivity at low frequencies, has also been proposed [189].

6.4 Beyond Advanced Gravitational Wave Detectors

The construction of the two Advanced LIGO detectors was completed in March, 2015, and the first observing run has recently started on September 18th, 2015, marking the start of the second generation of the search of gravitational waves, almost a century since the prediction of their existence by Einstein in 1916.

Meanwhile, the construction of Advanced Virgo is underway, and expected to be completed in 2016. The launch of LISA Pathfinder¹, whose objective is to test the technologies for the eLISA² project, is scheduled in late 2015. All these scientific efforts will bring valuable experimental data to fundamental physics, and hopefully open up a new window to the Universe.

If the detection of gravitational wave would be possible with the first-generation interferometers, and probable with the second-generation, advanced, interferometers³, it is natural to wonder what the objective for future gravitational wave projects would be.

A design study of future generation gravitational wave detectors based on currently proven technologies suggests an optimal baseline of 40 km with which the detection of gravitational waves may be extended to cosmological distances [190]. On the other hand, it has also been evaluated that the detection sensitivity of current advanced detectors may be doubled by reducing the limiting noise sources [191].

As shown in Figure 1.3, Einstein Telescope (ET), a third-generation GWD featuring 10 km baselines has been proposed and its design well studied [192] with more than an order of magnitude of improvement in detection sensitivity. The design of ET calls for 500 W of laser power [192] at the input, which is 4 times that of the advanced detectors.

The development of ultra-stable high-power single frequency lasers will therefore always be appealed to in the quest of higher and higher sensitivity in precision interferometry, among which the search of gravitational waves, and eventually the gravitational wave astronomy, are the most intriguing applications.

The accidental discovery of the cosmic wave background (CWB) led to the Nobel Prize in Physics in 1978 to Arno A. Penzias and Robert W. Wilson [193] and the portrait of the *young* Universe at $\sim 380\,000$ yr after the Big Bang⁴, which was

¹<http://sci.esa.int/lisa-pathfinder/>

²Evolved Laser Interferometer Space Antenna

³Physics: Wave of the future, Nature 511, 278–81 (17 July 2014) doi:10.1038/511278a

⁴<http://sci.esa.int/planck/53103-planck-cosmology/>

the time when the first light emerged. So, even with infinite vision in terms of electromagnetic waves, we *see* as far as $\sim 380\,000$ yr after the Big Bang.

Also, the lambda cold dark matter (Λ -CDM) cosmological model together with the recent results of the Planck mission suggests the following cosmic *reci*pe⁵: 4.9 % ordinary matter, 26.8 % dark matter, 68.3 % dark energy. That is to say, even with infinite vision in electromagnetic waves, we *see* at most 4.9 % of the Universe.

The rest, in time and in space, remains as known unknowns — or unknown unknowns — that will hopefully be partially unveiled with the gravitational wave *hearing* of laser interferometers.

⁵<http://sci.esa.int/planck/51557-planck-new-cosmic-recipe/>

Bibliography

1. Blair, D. G. *The Detection of Gravitational Waves* ISBN: 9780521021029 (Cambridge University Press, 1991).
2. Blair, D. G. *Advanced Gravitational Wave Detectors* ISBN: 9780521874298 (Cambridge University Press, 2012) (Cited on page 51).
3. *The Nobel Prize in Physics 1993* Accessed: 2015-03-10. <http://www.nobelprize.org/nobel_prizes/physics/laureates/1993> (Cited on pages 1, 160).
4. Hulse, R. A. *The Discovery of The Binary Pulsar* Accessed: 2015-03-10. <http://www.nobelprize.org/nobel_prizes/physics/laureates/1993/hulse-lecture.pdf> (1993) (Cited on pages 1, 160).
5. Joseph H. Taylor, J. *Binary Pulsars and Relativistic Gravity* Accessed: 2015-03-10. <http://www.nobelprize.org/nobel_prizes/physics/laureates/1993/taylor-lecture.pdf> (1993) (Cited on pages 1, 160).
6. Jones., E. M. *Apollo 15 Lunar Surface Journal: The Hammer and the Feather* Accessed: 2015-03-10. <<https://www.hq.nasa.gov/alsj/a15/a15.clsout3.html>> (1996) (Cited on pages 1, 160).
7. Lequeux, J. *The Discovery of Neptune (1845-1846) in Le Verrier—Magnificent and Detestable Astronomer* http://www.springer.com/cda/content/document/cda_downloadocument/9781461455646-c1.pdf, 21–53 (Springer-Verlag New York, 2013). ISBN: 9781461455653. doi:10.1007/978-1-4614-5565-3 (Cited on pages 1, 160).
8. Wheeler, J. & Ford, K. *Geons, Black Holes, and Quantum Foam: A Life in Physics* ISBN: 9780393079487 (W. W. Norton, 2010) (Cited on pages 1, 2, 160).
9. Carlip, S. *Does Gravity Travel at the Speed of Light?* Accessed: 2015-03-10. <http://math.ucr.edu/home/baez/physics/Relativity/GR/grav_speed.html> (2011) (Cited on pages 1, 160).
10. Taylor, J. H. & Weisberg, J. M. A new test of general relativity - Gravitational radiation and the binary pulsar PSR 1913+16. *The Astrophysical Journal* **253**, 908–920. doi:10.1086/159690 (Feb. 1982) (Cited on pages 2, 160).
11. Weisberg, J. M. & Taylor, J. H. *Relativistic Binary Pulsar B1913+16: Thirty Years of Observations and Analysis* version 1. arXiv: [astro-ph/0407149v1](https://arxiv.org/abs/astro-ph/0407149v1) [[astro-ph](https://arxiv.org/abs/astro-ph), [gr-qc](https://arxiv.org/abs/gr-qc)]. (2004) (Cited on page 3).

12. Einstein, A. *The Experimental Confirmation of the General Theory of Relativity in Relativity : the Special and General Theory* trans. by Lawson, R. W. (Methuen & Co Ltd, 1920). ISBN: 9781936690015. <<http://www.gutenberg.org/ebooks/5001>> (Cited on pages 2, 161).
13. Ashby, N. Relativity in the Global Positioning System. *Living Reviews in Relativity* **6**. doi:[10.12942/lrr-2003-1](https://doi.org/10.12942/lrr-2003-1) (2003) (Cited on pages 2, 161).
14. Will, C. M. The Confrontation between General Relativity and Experiment. *Living Reviews in Relativity* **9**. doi:[10.12942/lrr-2006-3](https://doi.org/10.12942/lrr-2006-3) (2006) (Cited on pages 2, 161).
15. Sathyaprakash, B. & Schutz, B. F. Physics, Astrophysics and Cosmology with Gravitational Waves. *Living Reviews in Relativity* **12**. doi:[10.12942/lrr-2009-2](https://doi.org/10.12942/lrr-2009-2) (2009) (Cited on pages 2, 161).
16. Pitkin, M., Reid, S., Rowan, S. & Hough, J. Gravitational Wave Detection by Interferometry (Ground and Space). *Living Reviews in Relativity* **14**. doi:[10.12942/lrr-2011-5](https://doi.org/10.12942/lrr-2011-5) (2011) (Cited on pages 4, 161).
17. Blair, D. G. *Sources of gravitational waves in The detection of gravitational waves* 16–42 (Cambridge University Press, 1991). ISBN: 9780521021029 (Cited on pages 4, 161).
18. Moore, C. J., Cole, R. H. & Berry, C. P. L. Gravitational-wave sensitivity curves. *Classical and Quantum Gravity* **32**, 015014. <<http://stacks.iop.org/0264-9381/32/i=1/a=015014>> (2015) (Cited on pages 4, 161).
19. Giazotto, A. Status of gravitational wave detection. *Journal of Physics: Conference Series* **120**, 032002. <<http://stacks.iop.org/1742-6596/120/i=3/a=032002>> (2008) (Cited on pages 4, 161).
20. Forward, R. L. Wideband laser-interferometer gravitational-radiation experiment. *Physical Review D* **17**, 379–390. doi:[10.1103/PhysRevD.17.379](https://doi.org/10.1103/PhysRevD.17.379) (Jan. 1978) (Cited on pages 4, 161).
21. Michelson, A. A. & Morley, E. W. On the Relative Motion of the Earth and of the Luminiferous Ether. *Sidereal Messenger* **6**, 306–310. <<http://adsabs.harvard.edu/abs/1887SidM....6..306M>> (Nov. 1887) (Cited on pages 4, 161).
22. Hobbs, G. *et al.* The International Pulsar Timing Array project: using pulsars as a gravitational wave detector. *Classical and Quantum Gravity* **27**, 084013. <<http://stacks.iop.org/0264-9381/27/i=8/a=084013>> (2010) (Cited on pages 4, 161).
23. Seljak, U. & Zaldarriaga, M. Signature of Gravity Waves in the Polarization of the Microwave Background. *Physical Review Letters* **78**, 2054–2057. doi:[10.1103/PhysRevLett.78.2054](https://doi.org/10.1103/PhysRevLett.78.2054) (Mar. 1997) (Cited on pages 4, 161).
24. Accadia, T. *et al.* Virgo: a laser interferometer to detect gravitational waves. *Journal of Instrumentation* **7**, P03012. <<http://stacks.iop.org/1748-0221/7/i=03/a=P03012>> (2012) (Cited on pages 5, 6, 161, 162).

25. The Virgo Collaboration. *Virgo Sensitivity Curves* Accessed: 2015-10-16. <<https://wwwcascina.virgo.infn.it/DataAnalysis/Calibration/Sensitivity/>> (2011) (Cited on pages 5, 162).
26. The Virgo Collaboration. *Advanced Virgo overview in Advanced Virgo Technical Design Report* 3–12 (2012). <<https://tds.ego-gw.it/ql/?c=8940>> (Cited on pages 5, 23, 162).
27. Mei, S. *et al.* The ACS Virgo Cluster Survey. XIII. SBF Distance Catalog and the Three-dimensional Structure of the Virgo Cluster. *The Astrophysical Journal* **655**, 144. <<http://stacks.iop.org/0004-637X/655/i=1/a=144>> (2007) (Cited on pages 5, 162).
28. Abadie, J. *et al.* Predictions for the rates of compact binary coalescences observable by ground-based gravitational-wave detectors. *Classical and Quantum Gravity* **27**, 173001. <<http://stacks.iop.org/0264-9381/27/i=17/a=173001>> (2010) (Cited on pages 5, 162).
29. Acernese, F. *et al.* Advanced Virgo: a second-generation interferometric gravitational wave detector. *Classical and Quantum Gravity* **32**, 024001. <<http://stacks.iop.org/0264-9381/32/i=2/a=024001>> (2015) (Cited on pages 5, 6, 9, 10, 162).
30. Corbitt, T. & Mavalvala, N. Review: Quantum noise in gravitational-wave interferometers. *Journal of Optics B: Quantum and Semiclassical Optics* **6**, S675. <<http://stacks.iop.org/1464-4266/6/i=8/a=008>> (2004) (Cited on pages 6, 9, 140, 162, 163, 169).
31. Kwee, P. *et al.* Stabilized high-power laser system for the gravitational wave detector advanced LIGO. *Optics Express* **20**, 10617–10634. doi:10.1364/OE.20.010617 (May 2012) (Cited on pages 6, 14, 162).
32. Takeno, K., Ozeki, T., Moriwaki, S. & Mio, N. 100 W, single-frequency operation of an injection-locked Nd:YAG laser. *Optics Letters* **30**, 2110–2112. doi:10.1364/OL.30.002110 (Aug. 2005) (Cited on pages 6, 162).
33. Richardson, D. J., Nilsson, J. & Clarkson, W. A. High power fiber lasers: current status and future perspectives. *Journal of the Optical Society of America B* **27**, B63–B92. doi:10.1364/JOSAB.27.000B63 (Nov. 2010) (Cited on pages 6, 15, 19, 162).
34. Black, E. D. & Gutenkunst, R. N. An introduction to signal extraction in interferometric gravitational wave detectors. *American Journal of Physics* **71**, 365–378. doi:<http://dx.doi.org/10.1119/1.1531578> (2003) (Cited on pages 9, 51).
35. The LIGO Scientific Collaboration *et al.* Advanced LIGO. *Classical and Quantum Gravity* **32**, 074001. <<http://stacks.iop.org/0264-9381/32/i=7/a=074001>> (2015) (Cited on page 9).
36. Somiya, K. Detector configuration of KAGRA-the Japanese cryogenic gravitational-wave detector. *Classical and Quantum Gravity* **29**, 124007. <<http://stacks.iop.org/0264-9381/29/i=12/a=124007>> (2012) (Cited on page 9).

37. Caves, C. M. Quantum-mechanical noise in an interferometer. *Physical Review D* **23**, 1693–1708. doi:[10.1103/PhysRevD.23.1693](https://doi.org/10.1103/PhysRevD.23.1693) (Apr. 1981) (Cited on pages [9](#), [140](#), [163](#), [169](#)).
38. Caves, C. M. Quantum-Mechanical Radiation-Pressure Fluctuations in an Interferometer. *Physical Review Letters* **45**, 75–79. doi:[10.1103/PhysRevLett.45.75](https://doi.org/10.1103/PhysRevLett.45.75) (July 1980) (Cited on pages [9](#), [140](#), [163](#), [169](#)).
39. Affeldt, C. *et al.* Advanced techniques in GEO 600. *Classical and Quantum Gravity* **31**, 224002. <<http://stacks.iop.org/0264-9381/31/i=22/a=224002>> (2014) (Cited on pages [9](#), [140](#), [163](#), [169](#)).
40. Drever, R. W. P. *Fabry-Perot cavity gravity-wave detectors* in *The detection of gravitational waves* (Editor: Blair, D. G.) 306–328 (Cambridge University Press, 1991). ISBN: 9780521021029 (Cited on pages [9](#), [163](#)).
41. Sato, S. *et al.* High-gain power recycling of a Fabry–Perot Michelson interferometer for a gravitational-wave antenna. *Applied Optics* **39**, 4616–4620. doi:[10.1364/AO.39.004616](https://doi.org/10.1364/AO.39.004616) (Sept. 2000) (Cited on pages [9](#), [163](#)).
42. Punturo, M. *Advanced Virgo Sensitivity Curve: a possible scenario* VIR-NOT-PER-1390-283 (The Virgo Collaboration, 2004). <<https://tds.ego-gw.it/ql/?c=1509>> (Cited on page [10](#)).
43. Losurdo, G. *Advanced Virgo sensitivity curve: cavity finesse and signal recycling tuning* VIR-0024A-07 (The Virgo Collaboration, 2007). <<https://tds.ego-gw.it/ql/?c=1871>> (Cited on page [10](#)).
44. The Virgo Collaboration. *Optical simulation and design* in *Advanced Virgo Technical Design Report* 13–73 (2012). <<https://tds.ego-gw.it/ql/?c=8940>> (Cited on page [10](#)).
45. The Virgo Collaboration. *Interferometer sensing and control* in *Advanced Virgo Technical Design Report* 311–360 (2012). <<https://tds.ego-gw.it/ql/?c=8940>> (Cited on pages [11](#), [22](#), [23](#), [25–27](#)).
46. Kravtsov, N. V. & Naniš, O. E. High-stability single-frequency solid-state lasers. *Quantum Electronics* **23**, 272. <<http://stacks.iop.org/1063-7818/23/i=4/a=R03>> (1993) (Cited on page [11](#)).
47. Tunnermann, A., Zellmer, H., Schone, W., Giesen, A. & Contag, K. *New Concepts for Diode-Pumped Solid-State Lasers* in *High-Power Diode Lasers* (Editor: Diehl, R.) 369–408 (Springer Berlin Heidelberg, 2000). ISBN: 9783540666936. doi:[10.1007/3-540-47852-3_10](https://doi.org/10.1007/3-540-47852-3_10) (Cited on page [11](#)).
48. Kane, T. J. & Byer, R. L. Monolithic, unidirectional single-mode Nd:YAG ring laser. *Optics Letters* **10**, 65–67. doi:[10.1364/OL.10.000065](https://doi.org/10.1364/OL.10.000065) (Feb. 1985) (Cited on page [11](#)).
49. Kwee, P. & Willke, B. Automatic laser beam characterization of monolithic Nd:YAG nonplanar ring lasers. *Applied Optics* **47**, 6022–6032. doi:[10.1364/AO.47.006022](https://doi.org/10.1364/AO.47.006022) (Nov. 2008) (Cited on pages [11](#), [12](#)).
50. Numata, K. *et al.* Characteristics of the single-longitudinal-mode planar-waveguide external cavity diode laser at 1064 nm. *Optics Letters* **39**, 2101–2104. doi:[10.1364/OL.39.002101](https://doi.org/10.1364/OL.39.002101) (Apr. 2014) (Cited on pages [11](#), [13](#)).

51. Numata, K. & Camp, J. Precision laser development for interferometric space missions NGO, SGO, and GRACE Follow-On. *Journal of Physics: Conference Series* **363**, 012054. <<http://stacks.iop.org/1742-6596/363/i=1/a=012054>> (2012) (Cited on pages 11, 13).
52. Fan, T. & Sanchez, A. Pump source requirements for end-pumped lasers. *IEEE Journal of Quantum Electronics* **26**, 311–316. doi:10.1109/3.44963 (Feb. 1990) (Cited on page 14).
53. Freitag, I., Tunnermann, A. & Welling, H. Power scaling of diode-pumped monolithic Nd:YAG lasers to output powers of several watts. *Optics Communications* **115**, 511–515. doi:10.1016/0030-4018(95)00020-9 (Apr. 1995) (Cited on page 14).
54. Liem, A., Limpert, J., Zellmer, H. & Tünnermann, A. 100-W single-frequency master-oscillator fiber power amplifier. *Optics Letters* **28**, 1537–1539. doi:10.1364/OL.28.001537 (Sept. 2003) (Cited on pages 14, 15, 17).
55. Farinas, A. D., Gustafson, E. K. & Byer, R. L. Frequency and intensity noise in an injection-locked, solid-state laser. *Journal of the Optical Society of America B* **12**, 328–334. doi:10.1364/JOSAB.12.000328 (Feb. 1995) (Cited on page 14).
56. Siegman, A. E. *Laser Injection Locking in Lasers* 1129–1170 (University Science Books, 1986). ISBN: 0935702115 (Cited on page 14).
57. Cregut, O. *et al.* 18 W single-frequency operation of an injection-locked, CW, Nd:YAG laser. *Physics Letters A* **140**, 294–298. doi:10.1016/0375-9601(89)90623-3 (1989) (Cited on page 14).
58. Freitag, I. *et al.* Amplitude and frequency stability of a diode-pumped Nd:YAG laser operating at a single-frequency continuous-wave output power of 20 W. *Optics Letters* **20**, 462–464. doi:10.1364/OL.20.000462 (Mar. 1995) (Cited on page 14).
59. Zawischa, I. *et al.* The GEO 600 laser system. *Classical and Quantum Gravity* **19**, 1775. <<http://stacks.iop.org/0264-9381/19/i=7/a=374>> (2002) (Cited on page 14).
60. Takeno, K., Ozeki, T., Moriwaki, S. & Mio, N. Development of a 100-W, single-frequency Nd:YAG laser for large-scale cryogenic gravitational wave telescope. *Journal of Physics: Conference Series* **32**, 276. <<http://stacks.iop.org/1742-6596/32/i=1/a=041>> (2006) (Cited on page 14).
61. Frede, M. *et al.* Fundamental mode, single-frequency laser amplifier for gravitational wave detectors. *Optics Express* **15**, 459–465. doi:10.1364/OE.15.000459 (Jan. 2007) (Cited on page 15).
62. Man, N. *Virgo+ laser system: specifications* VIR-0028A-14 (The Virgo Collaboration, 2014). <<https://tds.ego-gw.it/ql/?c=10005>> (Cited on page 15).
63. Giesen, A. *et al.* Scalable concept for diode-pumped high-power solid-state lasers. English. *Applied Physics B* **58**, 365–372. doi:10.1007/BF01081875 (1994) (Cited on page 15).

64. Karszewski, M. *et al.* 100 W TEM₀₀ Operation of Yb:YAG Thin Disc Laser with High Efficiency in *Advanced Solid State Lasers* (Optical Society of America, 1998), HP1. doi:[10.1364/ASSL.1998.HP1](https://doi.org/10.1364/ASSL.1998.HP1) (Cited on page 15).
65. Ganija, M., Ottaway, D., Veitch, P. & Munch, J. Cryogenic, high power, near diffraction limited, Yb:YAG slab laser. *Optics Express* **21**, 6973–6978. doi:[10.1364/OE.21.006973](https://doi.org/10.1364/OE.21.006973) (Mar. 2013) (Cited on page 15).
66. Kafka, J. *Laser diode pumped fiber lasers with pump cavity* US Patent 4,829,529; see also: <http://ao.osa.org/abstract.cfm?URI=ao-30-15-1864>. May 1989. <<https://www.google.com/patents/US4829529>> (Cited on page 15).
67. Snitzer, E., Po, H., Hakimi, F., Tumminelli, R. & McCollum, B. *Double Clad, Offset Core Nd Fiber Laser in Optical Fiber Sensors* (Optical Society of America, 1988), PD5. doi:[10.1364/OFS.1988.PD5](https://doi.org/10.1364/OFS.1988.PD5) (Cited on page 15).
68. Zawischa, I. *et al.* All-solid-state neodymium-based single-frequency master-oscillator fiber power-amplifier system emitting 5.5 W of radiation at 1064 nm. *Optics Letters* **24**, 469–471. doi:[10.1364/OL.24.000469](https://doi.org/10.1364/OL.24.000469) (Apr. 1999) (Cited on pages 15, 17).
69. Höfer, S. *et al.* Single-frequency master-oscillator fiber power amplifier system emitting 20 W of power. *Optics Letters* **26**, 1326–1328. doi:[10.1364/OL.26.001326](https://doi.org/10.1364/OL.26.001326) (Sept. 2001) (Cited on pages 15, 17).
70. Jeong, Y. *et al.* Power Scaling of Single-Frequency Ytterbium-Doped Fiber Master-Oscillator Power-Amplifier Sources up to 500 W. *IEEE Journal of Selected Topics in Quantum Electronics* **13**, 546–551. doi:[10.1109/JSTQE.2007.896639](https://doi.org/10.1109/JSTQE.2007.896639) (May 2007) (Cited on pages 15, 18).
71. Theeg, T., Sayinc, H., Neumann, J. & Kracht, D. All-Fiber Counter-Propagation Pumped Single Frequency Amplifier Stage With 300-W Output Power. *IEEE Photonics Technology Letters* **24**, 1864–1867. doi:[10.1109/LPT.2012.2217487](https://doi.org/10.1109/LPT.2012.2217487) (Oct. 2012) (Cited on pages 15, 17–19).
72. Agrawal, G. P. *Nonlinear Fiber Optics* Fourth Edition. ISBN: 9780123695161. doi:[10.1016/B978-012369516-1/50009-1](https://doi.org/10.1016/B978-012369516-1/50009-1) (Academic Press, San Diego, 2006) (Cited on page 15).
73. Chiao, R. Y., Townes, C. H. & Stoicheff, B. P. Stimulated Brillouin Scattering and Coherent Generation of Intense Hypersonic Waves. *Physical Review Letters* **12**, 592–595. doi:[10.1103/PhysRevLett.12.592](https://doi.org/10.1103/PhysRevLett.12.592) (May 1964) (Cited on page 15).
74. Agrawal, G. P. *Stimulated Brillouin Scattering in Nonlinear Fiber Optics* Fourth Edition, 329–367 (Academic Press, San Diego, 2006). ISBN: 9780123695161. doi:[10.1016/B978-012369516-1/50009-1](https://doi.org/10.1016/B978-012369516-1/50009-1) (Cited on pages 15, 16).
75. Ippen, E. & Stolen, R. Stimulated Brillouin scattering in optical fibers. *Applied Physics Letters* **21**, 539–541. doi:[10.1063/1.1654249](https://doi.org/10.1063/1.1654249) (1972) (Cited on page 15).
76. Smith, R. G. Optical Power Handling Capacity of Low Loss Optical Fibers as Determined by Stimulated Raman and Brillouin Scattering. *Applied Optics* **11**, 2489–2494. doi:[10.1364/AO.11.002489](https://doi.org/10.1364/AO.11.002489) (Nov. 1972) (Cited on page 15).

77. Cotter, D. Stimulated Brillouin Scattering in Monomode Optical Fiber. *Journal of Optical Communications* **4**, 10–19. doi:[10.1515/JOC.1983.4.1.10](https://doi.org/10.1515/JOC.1983.4.1.10) (1983) (Cited on page 15).
78. Kobayakov, A., Sauer, M. & Chowdhury, D. Stimulated Brillouin scattering in optical fibers. *Advances in Optics and Photonics* **2**, 1–59. doi:[10.1364/AOP.2.000001](https://doi.org/10.1364/AOP.2.000001) (Mar. 2010) (Cited on page 15).
79. Gloge, D. Weakly Guiding Fibers. *Applied Optics* **10**, 2252–2258. doi:[10.1364/AO.10.002252](https://doi.org/10.1364/AO.10.002252) (Oct. 1971) (Cited on pages 16, 57).
80. Marcuse, D. Gaussian approximation of the fundamental modes of graded-index fibers. *Journal of the Optical Society of America* **68**, 103–109. doi:[10.1364/JOSA.68.000103](https://doi.org/10.1364/JOSA.68.000103) (Jan. 1978) (Cited on pages 16, 57, 58).
81. Marcuse, D. Loss analysis of single-mode fiber splices. *The Bell System Technical Journal* **56**, 703–718. doi:[10.1002/j.1538-7305.1977.tb00534.x](https://doi.org/10.1002/j.1538-7305.1977.tb00534.x) (May 1977) (Cited on page 16).
82. Knight, J. C. Photonic crystal fibres. *Nature* **424**, 847–851. doi:[10.1038/nature01940](https://doi.org/10.1038/nature01940) (Aug. 14, 2003) (Cited on page 16).
83. Pulford, B. *et al.* 400-W near diffraction-limited single-frequency all-solid photonic bandgap fiber amplifier. *Optics Letters* **40**, 2297–2300. doi:[10.1364/OL.40.002297](https://doi.org/10.1364/OL.40.002297) (May 2015) (Cited on page 16).
84. Shiraki, K., Ohashi, M. & Tateda, M. Suppression of stimulated Brillouin scattering in a fibre by changing the core radius. *Electronics Letters* **31**, 668–669. doi:[10.1049/el:19950418](https://doi.org/10.1049/el:19950418) (Apr. 1995) (Cited on page 17).
85. Shiraki, K., Ohashi, M. & Tateda, M. SBS threshold of a fiber with a Brillouin frequency shift distribution. *Journal of Lightwave Technology* **14**, 50–57. doi:[10.1109/50.476136](https://doi.org/10.1109/50.476136) (Jan. 1996) (Cited on page 17).
86. Yoshizawa, N. & Imai, T. Stimulated Brillouin scattering suppression by means of applying strain distribution to fiber with cabling. *Journal of Lightwave Technology* **11**, 1518–1522. doi:[10.1109/50.249889](https://doi.org/10.1109/50.249889) (Oct. 1993) (Cited on page 17).
87. Boggio, J. M. C., Marconi, J. D. & Fragnito, H. L. Experimental and Numerical Investigation of the SBS-Threshold Increase in an Optical Fiber by Applying Strain Distributions. *Journal of Lightwave Technology* **23**, 3808. <<http://jlt.osa.org/abstract.cfm?URI=jlt-23-11-3808>> (Nov. 2005) (Cited on page 17).
88. Zhang, L., Cui, S., Liu, C., Zhou, J. & Feng, Y. 170 W, single-frequency, single-mode, linearly-polarized, Yb-doped all-fiber amplifier. *Optics Express* **21**, 5456–5462. doi:[10.1364/OE.21.005456](https://doi.org/10.1364/OE.21.005456) (Mar. 2013) (Cited on pages 17, 18).
89. Hansryd, J., Dross, F., Westlund, M., Andrekson, P. A. & Knudsen, S. N. Increase of the SBS Threshold in a Short Highly Nonlinear Fiber by Applying a Temperature Distribution. *Journal of Lightwave Technology* **19**, 1691. <<http://jlt.osa.org/abstract.cfm?URI=jlt-19-11-1691>> (Nov. 2001) (Cited on page 17).

90. Robin, C. A. *Novel approaches to power scaling of single-frequency photonic crystal fiber amplifiers* PhD thesis (University of New Mexico, Department of Electrical and Computer Engineering, July 2011). <<http://repository.unm.edu/handle/1928/13126>> (Cited on page 17).
91. Kovalev, V. I. & Harrison, R. G. Suppression of stimulated Brillouin scattering in high-power single-frequency fiber amplifiers. *Optics Letters* **31**, 161–163. doi:[10.1364/OL.31.000161](https://doi.org/10.1364/OL.31.000161) (Jan. 2006) (Cited on page 17).
92. Paschotta, R. *Encyclopedia of Laser Physics and Technology: Amplified Spontaneous Emission* Accessed: 2015-09-10. <https://www.rp-photonics.com/amplified_spontaneous_emission.html> (Cited on page 17).
93. Kobayakov, A. *et al.* Design concept for optical fibers with enhanced SBS threshold. *Optics Express* **13**, 5338–5346. doi:[10.1364/OPEX.13.005338](https://doi.org/10.1364/OPEX.13.005338) (July 2005) (Cited on page 17).
94. Li, M.-J. *et al.* Al/Ge co-doped large mode area fiber with high SBS threshold. *Optics Express* **15**, 8290–8299. doi:[10.1364/OE.15.008290](https://doi.org/10.1364/OE.15.008290) (June 2007) (Cited on page 17).
95. Jahn, P., Tünnermann, H., Puncken, O., Quetschke, V. & Weßels, P. *Suppression of stimulated Brillouin scattering with modulation/demodulation techniques* Talk given by V. Quetschke during the LSC-VIRGO Collaboration Meeting in Nice on Mar. 18, 2014 (Cited on page 17).
96. Gray, S. *et al.* 502 Watt, single transverse mode, narrow linewidth, bidirectionally pumped Yb-doped fiber amplifier. *Optics Express* **15**, 17044–17050. doi:[10.1364/OE.15.017044](https://doi.org/10.1364/OE.15.017044) (Dec. 2007) (Cited on page 18).
97. Dawson, J. W. *et al.* Analysis of the scalability of diffraction-limited fiber lasers and amplifiers to high average power. *Optics Express* **16**, 13240–13266. doi:[10.1364/OE.16.013240](https://doi.org/10.1364/OE.16.013240) (Aug. 2008) (Cited on pages 18, 19).
98. Eidam, T. *et al.* Experimental observations of the threshold-like onset of mode instabilities in high power fiber amplifiers. *Optics Express* **19**, 13218–13224. doi:[10.1364/OE.19.013218](https://doi.org/10.1364/OE.19.013218) (July 2011) (Cited on page 18).
99. Otto, H.-J., Modsching, N., Jauregui, C., Limpert, J. & Tünnermann, A. Impact of photodarkening on the mode instability threshold. *Optics Express* **23**, 15265–15277. doi:[10.1364/OE.23.015265](https://doi.org/10.1364/OE.23.015265) (June 2015) (Cited on page 18).
100. Jauregui, C., Eidam, T., Limpert, J. & Tünnermann, A. Impact of modal interference on the beam quality of high-power fiber amplifiers. *Optics Express* **19**, 3258–3271. doi:[10.1364/OE.19.003258](https://doi.org/10.1364/OE.19.003258) (Feb. 2011) (Cited on page 18).
101. Hansen, K. R., Alkeskjold, T. T., Broeng, J. & Lægsgaard, J. Theoretical analysis of mode instability in high-power fiber amplifiers. *Optics Express* **21**, 1944–1971. doi:[10.1364/OE.21.001944](https://doi.org/10.1364/OE.21.001944) (Jan. 2013) (Cited on page 18).
102. Ye, C., Petit, L., Koponen, J., Hu, I.-N. & Galvanauskas, A. Short-Term and Long-Term Stability in Ytterbium-Doped High-Power Fiber Lasers and Amplifiers. *IEEE Journal of Selected Topics in Quantum Electronics* **20**, 188–199. doi:[10.1109/JSTQE.2014.2310657](https://doi.org/10.1109/JSTQE.2014.2310657) (Sept. 2014) (Cited on pages 18, 93).

103. Paschotta, R. *et al.* Lifetime quenching in Yb-doped fibres. *Optics Communications* **136**, 375–378. doi:[10.1016/S0030-4018\(96\)00720-1](https://doi.org/10.1016/S0030-4018(96)00720-1) (1997) (Cited on pages [18](#), [93](#)).
104. Koponen, J. J., Söderlund, M. J., Hoffman, H. J. & Tammela, S. K. T. Measuring photodarkening from single-mode ytterbium doped silica fibers. *Optics Express* **14**, 11539–11544. doi:[10.1364/OE.14.011539](https://doi.org/10.1364/OE.14.011539) (Nov. 2006) (Cited on pages [18](#), [139](#), [168](#)).
105. Piccoli, R., Mechin, D., Robin, T. & Taccheo, S. Lifetime reduction due to photodarkening phenomenon in ytterbium-doped fibers and rate equation term. *Optics Letters* **38**, 4370–4373. doi:[10.1364/OL.38.004370](https://doi.org/10.1364/OL.38.004370) (Nov. 2013) (Cited on page [18](#)).
106. Manek-Hönninger, I. *et al.* Photodarkening and photobleaching of an ytterbium-doped silica double-clad LMA fiber. *Optics Express* **15**, 1606–1611. doi:[10.1364/OE.15.001606](https://doi.org/10.1364/OE.15.001606) (Feb. 2007) (Cited on pages [18](#), [139](#), [168](#)).
107. Koponen, J., Soderlund, M., Hoffman, H. J., Kliner, D. & Koplow, J. Photodarkening measurements in large mode area fibers. *SPIE Proceedings* **6453**. doi:[10.1117/12.712545](https://doi.org/10.1117/12.712545) (2007) (Cited on page [18](#)).
108. DiGiovanni, D. & Stentz, A. *Tapered fiber bundles for coupling light into and out of cladding-pumped fiber devices* US Patent 5,864,644. Jan. 1999. <<http://www.google.com/patents/US5864644>> (Cited on page [19](#)).
109. Fan, T. Laser beam combining for high-power, high-radiance sources. *IEEE Journal of Selected Topics in Quantum Electronics* **11**, 567–577. doi:[10.1109/JSTQE.2005.850241](https://doi.org/10.1109/JSTQE.2005.850241) (May 2005) (Cited on pages [19](#), [115](#), [167](#)).
110. Augst, S. J., Ranka, J. K., Fan, T. Y. & Sanchez, A. Beam combining of ytterbium fiber amplifiers (Invited). *Journal of the Optical Society of America B* **24**, 1707–1715. doi:[10.1364/JOSAB.24.001707](https://doi.org/10.1364/JOSAB.24.001707) (Aug. 2007) (Cited on pages [19](#), [115](#), [118](#), [167](#)).
111. Tünnermann, H. *et al.* Beam quality and noise properties of coherently combined ytterbium doped single frequency fiber amplifiers. *Optics Express* **19**, 19600–19606. doi:[10.1364/OE.19.019600](https://doi.org/10.1364/OE.19.019600) (Sept. 2011) (Cited on page [19](#)).
112. Kwee, P., Willke, B. & Danzmann, K. New concepts and results in laser power stabilization. English. *Applied Physics B* **102**, 515–522. doi:[10.1007/s00340-011-4399-1](https://doi.org/10.1007/s00340-011-4399-1) (2011) (Cited on page [19](#)).
113. Black, E. D. An introduction to Pound-Drever-Hall laser frequency stabilization. *American Journal of Physics* **69**, 79–87. doi:[10.1119/1.1286663](https://doi.org/10.1119/1.1286663) (2001) (Cited on pages [19](#), [20](#), [45](#)).
114. Kwee, P., Willke, B. & Danzmann, K. Optical ac coupling to overcome limitations in the detection of optical power fluctuations. *Optics Letters* **33**, 1509–1511. doi:[10.1364/OL.33.001509](https://doi.org/10.1364/OL.33.001509) (July 2008) (Cited on pages [20](#), [84](#)).
115. Kwee, P., Willke, B. & Danzmann, K. Shot-noise-limited laser power stabilization with a high-power photodiode array. *Optics Letters* **34**, 2912–2914. doi:[10.1364/OL.34.002912](https://doi.org/10.1364/OL.34.002912) (Oct. 2009) (Cited on page [20](#)).

116. Cleva, F., Coulon, J. P. & Merzougui, M. *Pstab Boxes Status for PSL VIR-0140A-13* (The Virgo Collaboration, 2013). <<https://tds.ego-gw.it/ql/?c=9486>> (Cited on pages 20, 26, 195).
117. Drever, R. *et al.* Laser phase and frequency stabilization using an optical resonator. English. *Applied Physics B* **31**, 97–105. doi:10.1007/BF00702605 (1983) (Cited on pages 20, 45).
118. Bondu, F. *L'interféromètre Virgo : propriétés optiques, stabilisation en fréquence du laser* Habilitation à diriger des recherches (Université Nice Sophia Antipolis, June 2008). <<https://tel.archives-ouvertes.fr/tel-00284986>> (Cited on pages 21, 26, 29).
119. Calloni, E. & Vajente, G. *Conceptual design of the second stage of frequency stabilization for Advanced Virgo* VIR-0013C-12 (The Virgo Collaboration, 2012). <<https://tds.ego-gw.it/ql/?c=8815>> (Cited on pages 21, 26, 29).
120. Canuel, B., Genin, E., Marque, J. & Benoit, P. *Reference Cavity characterization* VIR-0231A-13 (The Virgo Collaboration, 2013). <<https://tds.ego-gw.it/ql/?c=9577>> (Cited on pages 21, 26).
121. Rudiger, A. *et al.* A Mode Selector to Suppress Fluctuations in Laser Beam Geometry. *Optica Acta: International Journal of Optics* **28**, 641–658. doi:10.1080/713820609 (1981) (Cited on page 21).
122. Willke, B. *et al.* Spatial and temporal filtering of a 10-W Nd:YAG laser with a Fabry–Perot ring-cavity premode cleaner. *Optics Letters* **23**, 1704–1706. doi:10.1364/OL.23.001704 (Nov. 1998) (Cited on page 21).
123. Born, M. & Wolf, E. *Elements of the Theory of Interference and Interferometers* in *Principles of Optics* Sixth Edition, 256–369 (Pergamon, 1980). ISBN: 9780080264820. doi:10.1016/B978-0-08-026482-0.50014-1 (Cited on page 21).
124. Barriga, P. *Optical Cavity Designs for Interferometric Gravitational Wave Detectors* Accessed: 2015-10-16. <<http://www.gravity.uwa.edu.au/docs/EGR/LecturePablo/Cavity%20Designs.pdf>> (2009) (Cited on pages 21, 22).
125. The Virgo Collaboration. *Injection in Advanced Virgo Technical Design Report* 93–170 (2012). <<https://tds.ego-gw.it/ql/?c=8940>> (Cited on pages 22–25).
126. van-der-Schaaf, L. *Status of AdV phase cameras* LIGO-G1501160 (2015). <<https://dcc.ligo.org/LIGO-G1501160>> (Cited on page 25).
127. Chiummo, A. *Requirements for technical noise with ITF asymmetries* VIR-0517A-11 (The Virgo Collaboration, 2011). <<https://tds.ego-gw.it/ql/?c=8573>> (Cited on pages 22, 23, 25–27).
128. Gouaty, R. *Laser RIN specifications at Advanced Virgo modulation frequencies* VIR-0328A-13 (The Virgo Collaboration, 2013). <<https://tds.ego-gw.it/ql/?c=9681>> (Cited on pages 22, 23).

129. The Virgo Collaboration. *Prestabilized laser in Advanced Virgo Technical Design Report* 75–92 (2012). <<https://tds.ego-gw.it/ql/?c=8940>> (Cited on pages 25, 27, 28).
130. Cleva, F. personal communication (Cited on page 28).
131. Cleva, F. personal communication (Cited on page 29).
132. Zhu, T. C. *et al.* Absolute calibration of optical power for PDT: Report of AAPM TG140. *Medical Physics* **40**. doi:[10.1118/1.4813897](https://doi.org/10.1118/1.4813897) (2013) (Cited on page 33).
133. The Virgo Collaboration. *Advanced Virgo Technical Design Report VIR-0128A-12* (Centre national de la recherche scientifique *CNRS*, Istituto nazionale di fisica nucleare *INFN*, Nationaal instituut voor subatomaire fysica *NIKHEF*, and European Gravitational Observatory *EGO*, 2012). <<https://tds.ego-gw.it/ql/?c=8940>> (Cited on page 34).
134. Obarski, G. E. & Splett, J. D. Transfer standard for the spectral density of relative intensity noise of optical fiber sources near 1550 nm. *Journal of the Optical Society of America B* **18**, 750–761. doi:[10.1364/JOSAB.18.000750](https://doi.org/10.1364/JOSAB.18.000750) (June 2001) (Cited on page 34).
135. David W. Allan, C. C. H. Neil Ashby. *The Science of Timekeeping* Application Note 1289 (Hewlett-Packard, 1997). <<http://literature.agilent.com/litweb/pdf/5965-7984E.pdf>> (Cited on pages 43, 97).
136. Comité Consultatif International Des Radiocommunications (CCIR). *Characterization of Frequency and Phase Noise in Characterization of Clocks and Oscillators* Report 580 of the CCIR, reprinted as NIST Technical Note 1337, 142–150 (National Institute of Standards and Technology, 1986). <<http://tf.nist.gov/general/pdf/868.pdf>> (Cited on page 45).
137. Siegman, A. E. *Linear Pulse Propagation in Lasers* 331–361 (University Science Books, 1986). ISBN: 0935702115 (Cited on page 45).
138. Hansch, T. & Couillaud, B. Laser frequency stabilization by polarization spectroscopy of a reflecting reference cavity. *Optics Communications* **35**, 441–444. doi:[10.1016/0030-4018\(80\)90069-3](https://doi.org/10.1016/0030-4018(80)90069-3) (1980) (Cited on page 45).
139. Shaddock, D. A., Gray, M. B. & McClelland, D. E. Frequency locking a laser to an optical cavity by use of spatial mode interference. *Optics Letters* **24**, 1499–1501. doi:[10.1364/OL.24.001499](https://doi.org/10.1364/OL.24.001499) (Nov. 1999) (Cited on page 45).
140. Cusack, B. J. *et al.* Double pass locking and spatial mode locking for gravitational wave detectors. *Classical and Quantum Gravity* **19**, 1819. <<http://stacks.iop.org/0264-9381/19/i=7/a=379>> (2002) (Cited on page 45).
141. Miller, J. & Evans, M. Length control of an optical resonator using second-order transverse modes. *Optics Letters* **39**, 2495–2498. doi:[10.1364/OL.39.002495](https://doi.org/10.1364/OL.39.002495) (Apr. 2014) (Cited on page 45).
142. Saleh, B. & Teich, M. *Wave Optics in Fundamentals of Photonics* 41–79 (Wiley, 2001). ISBN: 9780471358329 (Cited on page 45).

143. Augst, S. J., Fan, T. Y. & Sanchez, A. Coherent beam combining and phase noise measurements of ytterbium fiber amplifiers. *Optics Letters* **29**, 474–476. doi:[10.1364/OL.29.000474](https://doi.org/10.1364/OL.29.000474) (Mar. 2004) (Cited on pages [47](#), [115](#), [118](#)).
144. Takahashi, R., Mizuno, J., Miyoki, S. & Kawashima, N. Control of a 10 m delay-line laser interferometer using the pre-modulation method. *Physics Letters A* **187**, 157–162. doi:[10.1016/0375-9601\(94\)90054-X](https://doi.org/10.1016/0375-9601(94)90054-X) (1994) (Cited on pages [51](#), [115](#)).
145. Panduputra, Y., Ng, T. W., Neild, A. & Robinson, M. Intensity influence on Gaussian beam laser based measurements using quadrant photodiodes. *Applied Optics* **49**, 3669–3675. doi:[10.1364/AO.49.003669](https://doi.org/10.1364/AO.49.003669) (July 2010) (Cited on page [52](#)).
146. Anderson, D. Z. Alignment of resonant optical cavities. *Applied Optics* **23**, 2944–2949. doi:[10.1364/AO.23.002944](https://doi.org/10.1364/AO.23.002944) (Sept. 1984) (Cited on pages [54](#), [56](#)).
147. Kwee, P., Seifert, F., Willke, B. & Danzmann, K. Laser beam quality and pointing measurement with an optical resonator. *Review of Scientific Instruments* **78**. doi:[10.1063/1.2754400](https://doi.org/10.1063/1.2754400) (2007) (Cited on pages [54](#), [56](#)).
148. Kwee, P. *Laser Characterization and Stabilization for Precision Interferometry* PhD thesis (Gottfried Wilhelm Leibniz Universität Hannover, Jan. 2010). ISBN: 9783868442908. <https://gwic.ligo.org/thesisprize/2010/kwee_thesis.pdf> (Cited on pages [54](#), [56](#)).
149. Kogelnik, H. & Li, T. Laser Beams and Resonators. *Applied Optics* **5**, 1550–1567. doi:[10.1364/AO.5.001550](https://doi.org/10.1364/AO.5.001550) (Oct. 1966) (Cited on page [54](#)).
150. Morrison, E., Meers, B. J., Robertson, D. I. & Ward, H. Automatic alignment of optical interferometers. *Applied Optics* **33**, 5041–5049. doi:[10.1364/AO.33.005041](https://doi.org/10.1364/AO.33.005041) (Aug. 1994) (Cited on pages [56](#), [70](#), [128](#)).
151. Mitschke, F. *Treatment with Wave Optics* in *Fiber Optics: Physics and Technology* 25–45 (Springer Berlin Heidelberg, 2010) (Cited on pages [57](#), [58](#)).
152. Malitson, I. H. Interspecimen Comparison of the Refractive Index of Fused Silica. *Journal of the Optical Society of America* **55**, 1205–1208. doi:[10.1364/JOSA.55.001205](https://doi.org/10.1364/JOSA.55.001205) (Oct. 1965) (Cited on page [57](#)).
153. Trobs, M. & Heinzl, G. Improved spectrum estimation from digitized time series on a logarithmic frequency axis. *Measurement* **39**, 120–129. doi:[10.1016/j.measurement.2005.10.010](https://doi.org/10.1016/j.measurement.2005.10.010) (2006) (Cited on page [62](#)).
154. Trobs, M. & Heinzl, G. Corrigendum to “Improved spectrum estimation from digitized time series on a logarithmic frequency axis” [Measurement 39 (2006) 120–129]. *Measurement* **42**, 170–. doi:[10.1016/j.measurement.2008.04.004](https://doi.org/10.1016/j.measurement.2008.04.004) (2009) (Cited on page [62](#)).
155. Goodno, G. D., Shih, C.-C. & Rothenberg, J. E. Perturbative analysis of coherent combining efficiency with mismatched lasers: errata. *Optics Express* **20**, 23587–23588. doi:[10.1364/OE.20.023587](https://doi.org/10.1364/OE.20.023587) (Oct. 2012) (Cited on pages [79](#), [120](#), [123](#)).

156. Goodno, G. D., Shih, C.-C. & Rothenberg, J. E. Perturbative analysis of coherent combining efficiency with mismatched lasers. *Optics Express* **18**, 25403–25414. doi:[10.1364/OE.18.025403](https://doi.org/10.1364/OE.18.025403) (Nov. 2010) (Cited on pages 79, 120).
157. Freitag, I. personal communication (Cited on page 80).
158. Cleva, F. & Wei, L.-W. *Nufern 50W fiber amplifier test - first part* VIR-0102B-13 (The Virgo Collaboration, 2013). <<https://tds.ego-gw.it/ql/?c=9447>> (Cited on page 85).
159. Boulet, J. personal communication (Cited on page 89).
160. Koponen, J. *et al.* Photodarkening rate in Yb-doped silica fibers. *Applied Optics* **47**, 1247–1256. doi:[10.1364/AO.47.001247](https://doi.org/10.1364/AO.47.001247) (Mar. 2008) (Cited on page 93).
161. Coulon, J.-P. personal communication (Cited on page 109).
162. Novak, S. & Moesle, A. Analytic Model for Gain Modulation in EDFAs. *Journal of Lightwave Technology* **20**, 975. <<http://jlt.osa.org/abstract.cfm?URI=jlt-20-6-975>> (June 2002) (Cited on page 112).
163. Tünnermann, H. *Fiber Amplifiers for Gravitational Wave Detectors: Temporal Dynamics and Coherent Beam Combining* PhD thesis (Gottfried Wilhelm Leibniz Universität Hannover, Feb. 2013). <<http://d-nb.info/1037456440>> (Cited on page 112).
164. Tünnermann, H., Neumann, J., Kracht, D. & Weßels, P. Gain dynamics and refractive index changes in fiber amplifiers: a frequency domain approach. *Optics Express* **20**, 13539–13550. doi:[10.1364/OE.20.013539](https://doi.org/10.1364/OE.20.013539) (June 2012) (Cited on page 113).
165. Tünnermann, H. *et al.* Beam quality and noise properties of coherently combined ytterbium doped single frequency fiber amplifiers. *Optics Express* **19**, 19600–19606. doi:[10.1364/OE.19.019600](https://doi.org/10.1364/OE.19.019600) (Sept. 2011) (Cited on pages 115, 118, 167).
166. Man, C. N. & Brillat, A. Injection locking of argon-ion lasers. *Optics Letters* **9**, 333–334. doi:[10.1364/OL.9.000333](https://doi.org/10.1364/OL.9.000333) (Aug. 1984) (Cited on pages 115, 167).
167. Man, C., Shoemaker, D., Tu, M. P. & Dewey, D. External modulation technique for sensitive interferometric detection of displacements. *Physics Letters A* **148**, 8–16. doi:[10.1016/0375-9601\(90\)90565-6](https://doi.org/10.1016/0375-9601(90)90565-6) (1990) (Cited on page 115).
168. Hild, S. *et al.* DC-readout of a signal-recycled gravitational wave detector. *Classical and Quantum Gravity* **26**, 055012. <<http://stacks.iop.org/0264-9381/26/i=5/a=055012>> (2009) (Cited on page 115).
169. Tünnermann, H., Feng, Y., Neumann, J., Kracht, D. & Weßels, P. All-fiber coherent beam combining with phase stabilization via differential pump power control. *Optics Letters* **37**, 1202–1204. doi:[10.1364/OL.37.001202](https://doi.org/10.1364/OL.37.001202) (Apr. 2012) (Cited on pages 115, 118).

170. Vornehm, J. E., Schweinsberg, A., Shi, Z., Gauthier, D. J. & Boyd, R. W. Phase locking of multiple optical fiber channels for a slow-light-enabled laser radar system. *Optics Express* **21**, 13094–13104. doi:[10.1364/OE.21.013094](https://doi.org/10.1364/OE.21.013094) (June 2013) (Cited on page 118).
171. Uberna, R., Bratcher, A. & Tiemann, B. G. Power scaling of a fiber master oscillator power amplifier system using a coherent polarization beam combination. *Applied Optics* **49**, 6762–6765. doi:[10.1364/AO.49.006762](https://doi.org/10.1364/AO.49.006762) (Dec. 2010) (Cited on page 120).
172. Whittaker, E. A., Gehrtz, M. & Bjorklund, G. C. Residual amplitude modulation in laser electro-optic phase modulation. *Journal of the Optical Society of America B* **2**, 1320–1326. doi:[10.1364/JOSAB.2.001320](https://doi.org/10.1364/JOSAB.2.001320) (Aug. 1985) (Cited on page 122).
173. Wong, N. C. & Hall, J. L. Servo control of amplitude modulation in frequency-modulation spectroscopy: demonstration of shot-noise-limited detection. *Journal of the Optical Society of America B* **2**, 1527–1533. doi:[10.1364/JOSAB.2.001527](https://doi.org/10.1364/JOSAB.2.001527) (Sept. 1985) (Cited on page 122).
174. Foltynowicz, A., Silander, I. & Axner, O. Reduction of background signals in fiber-based NICE-OHMS. *Journal of the Optical Society of America B* **28**, 2797–2805. doi:[10.1364/JOSAB.28.002797](https://doi.org/10.1364/JOSAB.28.002797) (Nov. 2011) (Cited on page 122).
175. Silander, I., Ehlers, P., Wang, J. & Axner, O. Frequency modulation background signals from fiber-based electro optic modulators are caused by crosstalk. *Journal of the Optical Society of America B* **29**, 916–923. doi:[10.1364/JOSAB.29.000916](https://doi.org/10.1364/JOSAB.29.000916) (May 2012) (Cited on page 122).
176. Kokeyama, K. *et al.* Residual amplitude modulation in interferometric gravitational wave detectors. *Journal of the Optical Society of America A* **31**, 81–88. doi:[10.1364/JOSAA.31.000081](https://doi.org/10.1364/JOSAA.31.000081) (Jan. 2014) (Cited on page 122).
177. The Virgo Collaboration. *Thermal compensation in Advanced Virgo Technical Design Report* 187–234 (2012). <<https://tds.ego-gw.it/ql/?c=8940>> (Cited on page 137).
178. Piccoli, R., Robin, T., Brand, T., Klotzbach, U. & Taccheo, S. Effective photodarkening suppression in Yb-doped fiber lasers by visible light injection. *Optics Express* **22**, 7638–7643. doi:[10.1364/OE.22.007638](https://doi.org/10.1364/OE.22.007638) (Apr. 2014) (Cited on pages 139, 168).
179. Taccheo, S. *et al.* *Photodarkening: Investigation, Measurement and Standards in Advanced Photonics* (Optical Society of America, 2014), SoW2B.6. doi:[10.1364/SOF.2014.SoW2B.6](https://doi.org/10.1364/SOF.2014.SoW2B.6) (Cited on pages 139, 168).
180. Braginsky, V., Strigin, S. & Vyatchanin, S. Parametric oscillatory instability in Fabry-Perot interferometer. *Physics Letters A* **287**, 331–338. doi:[10.1016/S0375-9601\(01\)00510-2](https://doi.org/10.1016/S0375-9601(01)00510-2) (2001) (Cited on pages 140, 169).
181. Braginsky, V., Strigin, S. & Vyatchanin, S. Analysis of parametric oscillatory instability in power recycled LIGO interferometer. *Physics Letters A* **305**, 111–124. doi:[10.1016/S0375-9601\(02\)01357-9](https://doi.org/10.1016/S0375-9601(02)01357-9) (2002) (Cited on pages 140, 169).

182. Zhao, C., Ju, L., Degallaix, J., Gras, S. & Blair, D. G. Parametric Instabilities and Their Control in Advanced Interferometer Gravitational-Wave Detectors. *Physical Review Letters* **94**, 121102. doi:[10.1103/PhysRevLett.94.121102](https://doi.org/10.1103/PhysRevLett.94.121102) (Apr. 2005) (Cited on pages 140, 169).
183. Ju, L. *et al.* Strategies for the control of parametric instability in advanced gravitational wave detectors. *Classical and Quantum Gravity* **26**, 015002. <<http://stacks.iop.org/0264-9381/26/i=1/a=015002>> (2009) (Cited on pages 140, 169).
184. Evans, M. *et al.* Observation of Parametric Instability in Advanced LIGO. *Physical Review Letters* **114**, 161102. doi:[10.1103/PhysRevLett.114.161102](https://doi.org/10.1103/PhysRevLett.114.161102) (Apr. 2015) (Cited on pages 140, 169).
185. Khalaidovski, A. *et al.* Status of the GEO 600 squeezed-light laser. *Journal of Physics: Conference Series* **363**, 012013. <<http://stacks.iop.org/1742-6596/363/i=1/a=012013>> (2012) (Cited on pages 140, 169).
186. A gravitational wave observatory operating beyond the quantum shot-noise limit. *Nat Phys* **7**, 962–965. doi:[10.1038/nphys2083](https://doi.org/10.1038/nphys2083) (Dec. 2011) (Cited on pages 140, 169).
187. J., A. *et al.* Enhanced sensitivity of the LIGO gravitational wave detector by using squeezed states of light. *Nature Photonics* **7**, 613–619. doi:[10.1038/nphoton.2013.177](https://doi.org/10.1038/nphoton.2013.177) (Aug. 2013) (Cited on pages 140, 169).
188. Oelker, E., Barsotti, L., Dwyer, S., Sigg, D. & Mavalvala, N. Squeezed light for advanced gravitational wave detectors and beyond. *Optics Express* **22**, 21106–21121. doi:[10.1364/OE.22.021106](https://doi.org/10.1364/OE.22.021106) (Aug. 2014) (Cited on pages 140, 169).
189. Gräf, C. *et al.* Design of a speed meter interferometer proof-of-principle experiment. *Classical and Quantum Gravity* **31**, 215009. <<http://stacks.iop.org/0264-9381/31/i=21/a=215009>> (2014) (Cited on pages 141, 169).
190. Dwyer, S. *et al.* Gravitational wave detector with cosmological reach. *Physical Review D* **91**, 082001. doi:[10.1103/PhysRevD.91.082001](https://doi.org/10.1103/PhysRevD.91.082001) (Apr. 2015) (Cited on pages 141, 170).
191. Miller, J. *et al.* Prospects for doubling the range of Advanced LIGO. *Physical Review D* **91**, 062005. doi:[10.1103/PhysRevD.91.062005](https://doi.org/10.1103/PhysRevD.91.062005) (Mar. 2015) (Cited on pages 141, 170).
192. ET Science Team. *Einstein gravitational wave Telescope Conceptual Design Study* ET-0106C-10 (2011). <<https://tds.ego-gw.it/ql/?c=7954>> (Cited on pages 141, 170).
193. *The Nobel Prize in Physics 1978* Accessed: 2015-10-08. <http://www.nobelprize.org/nobel_prizes/physics/laureates/1978> (Cited on pages 141, 170).

Traduction partielle en français

Chapitre 1 Introduction (intégral)

1.1 Gravité, la relativité générale, et les ondes gravitationnelles

Le prix Nobel de physique 1993 a été attribué à Russell A. Hulse et Joseph H. Taylor Jr. “pour la découverte d’un nouveau type de pulsar, une découverte qui a ouvert de nouvelles possibilités quand à l’étude de la gravitation [3–5].”

L’étude moderne de la gravitation remonte à la découverte par Galileo Galilei durant le 16–17^{ème} siècle de la constance de l’accélération des objets en chute libre. La mission Apollo 15 a fait la preuve du célèbre test de la chute du poids de plume et du poids de plomb sur la lune [6].

En 1687 Isaac Newton publie *Philosophiæ Naturalis Principia Mathematica* dans lequel la loi de la gravitation universelle est présentée; nous connaissons tous l’anecdote de la pomme qui a présidé à sa découverte. Le succès de la loi de la gravitation universelle a été confortée par la découverte de Neptune, la première planète dont l’existence a été déduite par les lois de la physique avant son observation directe. En 1846 Johann Gottfried Galle découvrit Neptune sur la base des calculs d’Urbain Le Verrier [7]. La théorie de Newton ne pouvait néanmoins pas expliquer le taux de précession du périhélie rendu par l’observation. Il faut attendre la théorie de la relativité générale d’Albert Einstein publiée en 1915 pour obtenir une prise en compte précise de ce phénomène.

En relativité générale l’espace et le temps, qui sont considérés comme absolu dans la théorie de Newton, sont liés au sein d’une variable appelée espace-temps. Dans la théorie de Newton la présence d’une particule massive crée un potentiel de gravitation et l’interaction matière–matière est décrite par la force de gravitation. En relativité générale la gravitation est considérée comme une courbure de l’espace-temps induite par la présence d’une masse et la gravitation est “véhiculée” par la variable espace-temps (figure 1.1). Comme cité par John Archibald Wheeler: “l’espace temps indique à la matière comment se mouvoir; la matière indique à l’espace temps comment se déformer [8].”

La théorie de la gravitation de Newton considère que les masses interagissent de façon instantanée, indépendamment de la distance qui les sépare, ce qui implique que la vitesse d’interaction est infinie et que les masses d’épreuve sont corrélées en temps réel [9]. En relativité générale le déplacement de particules massives crée des ondulations de l’espace-temps, qui sont les ondes de gravitation. De la même façon que la relativité restreinte étend les lois du mouvement aux vitesses proches de celle de la lumière, la relativité générale étend les lois de la gravitation dans le cas des champs de gravitation fort.

En 1974, Hulse et Taylor découvre PSR B1913+16, un pulsar associé à un système binaire. La décroissance orbitale de PSR B1913+16 a été expliquée par la perte d’énergie et du moment angulaire induite par l’émission d’onde de gravitation prédite par le relativité générale (figure 1.2) [10]. C’est une preuve indirecte de l’existence des ondes gravitationnelles et une confirmation de la validité de la relativité générale dans le cadre des champs gravitationnels forts.

Jusqu’à aujourd’hui, en plus de la prédiction précise du taux de précession du

périhélie de Mercure et de la décroissance orbitale du pulsar Hulse–Taylor, la théorie d’Albert Einstein a permis des prédictions dans deux autres cas [12]: la déviation de la lumière par le soleil ainsi que le décalage gravitationnel vers le rouge dont la prise en compte est essentielle pour garantir la précision du GPS (géo-positionnement par satellite) [13, 14].

Une observation directe des ondes de gravitation n’apportera pas seulement une confirmation de la relativité générale mais aussi permettra une nouvelle appréhension de l’univers pour une meilleure connaissance [15].

1.2 Les sources et détecteurs d’ondes gravitationnelles

Un effort généralisé est en cours pour la détection directe⁶ des ondes de gravitation. La détection des ondes gravitationnelles nécessite la modélisation des possibles sources et la mise au point de détecteurs adaptés.

Le passage d’une onde gravitationnelle induit une déformation relative d’amplitude h proportionnelle à $\Delta L/L$ où ΔL est la variation de distance entre deux masses test séparées de la distance L [16]. Les sources d’ondes gravitationnelles considérées comme les candidats les plus probables sont les supernovæ, les étoiles binaires coalescentes, et les étoiles non-axisymétriques en rotation rapide [17]. La figure 1.3 montre l’amplitude d’ondes de gravitation induites par des sources typiques et probables ainsi que la sensibilité de détecteurs actuels [18].

Afin de détecter les ondes gravitationnelles, Joseph Weber développa en 1960 le premier détecteur basé sur des barres résonantes [19]. On peut considérer les barres résonantes comme un diapason dont la sensibilité est d’autant plus grande que son facteur de qualité mécanique est élevé.

Une détection large-bande peut être envisagée par l’utilisation de détecteur interférométrique d’ondes gravitationnelles [20]. Dans l’expérience de Michelson–Morley [21] l’interféromètre de Michelson a prouvé son efficacité en permettant de donner une valeur limite supérieure de l’anisotropie de la vitesse de la lumière, mettant en évidence sa constance. De la même façon, l’interféromètre de Michelson peut aussi être utilisé pour mesurer la contrainte induite par le passage d’une onde gravitationnelle et constitue le cœur des détecteurs interférométriques d’ondes gravitationnelles. Les détecteurs interférométriques actuels ont perfectionné les concepts initiaux de l’interféromètre de Michelson en intégrant de nouveaux concepts, comme par exemple l’utilisation de cavités Fabry–Perot.

D’autres techniques de mesures des ondes gravitationnelles mettent en œuvre des réseaux synchronisés de pulsar [22], et la mesure de la polarisation du fond cosmique de micro-ondes [23].

1.3 Le projet Advanced Virgo

Virgo est un interféromètre de Michelson dédié à la détection des ondes gravitationnelles (figure 1.6) [24]. Avec des bras de 3 km Virgo atteint une sensibilité de l’ordre

⁶For the viewpoint of Joseph H. Taylor Jr. on indirect vs. direct detections, see “An Interview with Joseph Hooton Taylor, Jr.” in LIGO Magazine, Issue 7, September 2015. Online: <http://www.ligo.org/magazine/LIGO-magazine-issue-7.pdf#page=22>

de $10^{-22} \sqrt{\text{Hz}}^{-1}$ (figure 1.4) [25] et permet la détection de système binaire d'étoiles à neutron spirales distant de 12 Mpc [26]. En comparaison, Virgo, le plus proche amas de galaxies se trouve à 16.5 Mpc [27].

En plus de l'amplitude de la déformation (qui définit la sensibilité minimale de l'interféromètre), le taux d'événement et le type de population des sources potentielles d'ondes gravitationnelles interviennent également dans le taux de détection. Ainsi, des sources induisant une onde gravitationnelle de forte amplitude seront facilement détectables mais ne seront intéressantes que dans la mesure où leur probabilité d'apparition sera "raisonnablement" élevée. Considérant l'ensemble de ces facteurs, le réseau de détecteurs formé par LIGO⁷ et Virgo aurait un taux de détection de 0.02 événement par an (sur la base de la détection de coalescence de binaire à neutron) [28].

Des améliorations majeures de Virgo sont en cours avec le projet Advanced Virgo (AdV). Celui-ci vise une sensibilité 10 fois plus élevée, permettant l'accès à une déformation relative de $10^{-23} \sqrt{\text{Hz}}^{-1}$ [29]. De telles améliorations sont également prévues pour le projet LIGO; le nouveau réseau de détecteurs ainsi optimisé aura un taux de détection de 40 événements par an [28].

1.4 Motivation, objectif et organisation de la thèse

La nature quantique de la lumière impose des limitations sur les mesures de type interférométrique. Ainsi, la coexistence du bruit de grenaille (bruit de détection) et du bruit de pression de radiation des photons sur les optiques de Virgo définit une limite dite "limite quantique standard" [30].

Le bruit de grenaille limite la sensibilité de l'interféromètre en haute fréquence. Afin d'atteindre la sensibilité prévue pour Advanced Virgo la contrainte due au bruit de grenaille impose une puissance du laser de 175 W, pour une fréquence et répartition dans le mode transverse TEM₀₀ de l'interféromètre.

Au contraire des configurations adoptées par Advanced LIGO [31], KAGRA [32] et Virgo [24] pour le laser, à savoir, un laser à solide amplifié par un amplificateur optique à solide, Advanced Virgo prévoit la mise en œuvre de la combinaison cohérente d'amplificateurs à fibre alimentés par un même laser de faible puissance.

Les amplificateurs laser à fibre sont une technologie émergente qui est largement utilisée dans les applications nécessitant une puissance élevée [33]. Grâce à la structure guidante de la fibre et au rapport surface/volume favorable ils permettent d'obtenir des faisceaux de bonne qualité associés à des puissances élevées. Enfin, leur compacité, l'absence de besoin d'alignement et leur haute efficacité énergétique en font des candidats idéaux pour les détecteurs d'ondes gravitationnelles de nouvelle génération.

La puissance optique n'est pas la seule spécification pour Advanced Virgo. Le bruit de puissance, le bruit de fréquence, le bruit de pointé du faisceau sont aussi contraints à de faibles niveaux de fluctuations. Il est donc essentiel de connaître le comportement de ces systèmes fibrés du point de vue de ces spécifications. De

⁷Laser Interferometer Gravitational-Wave Observatory, consists of two detectors similar to Virgo located in the Washington and Louisiana States of America.

plus l'obtention de systèmes fibrés aux niveaux de puissance qui nous intéresse devient problématique. La combinaison cohérente de plusieurs systèmes de puissance réduite est une des solutions possibles. L'objet de cette thèse est l'étude de la faisabilité d'un système laser pour Advanced Virgo basé sur la combinaison cohérente d'amplificateurs laser à fibre.

Le chapitre 2 donne un aperçu des technologies associées ainsi qu'un résumé des spécifications pour Advanced Virgo. Le chapitre 3 donne un aperçu des techniques de caractérisation utilisées. Le chapitre 4 montre les performances d'un amplificateur à fibre considéré comme une unité de puissance. Le chapitre 5 montre les résultats de la combinaison cohérente de deux unités de puissance. Le chapitre 6 conclue l'étude et présente les perspectives pour le système à venir.

Chapitre 2 Système laser pré-stabilisé pour les détecteurs interférométriques d'ondes gravitationnelles (partiel)

Le passage d'une onde gravitationnelle induit une déformation différentielle entre les deux bras de l'interféromètre qui va changer l'état d'interférence au niveau du port de sortie. En théorie un interféromètre parfaitement équilibré sera insensible aux fluctuations de puissance et de fréquence du laser. En pratique l'interféromètre est "pétri" d'imperfections et d'asymétries liées aux limitations technologiques ainsi qu'au choix de stratégie de détection.

En parallèle la nature quantique de la lumière impose une limite fondamentale, à savoir, le bruit de grenaille. La présence conjointe du bruit de grenaille et de la pression de radiation définit la limite quantique standard pour les mesures de type interférométrique. [30, 37, 38]

Le bruit de grenaille limite la sensibilité en haute fréquence. Bien qu'il ait été démontré que l'injection de lumière comprimée puisse augmenter la sensibilité de 3.7 dB [39], l'augmentation de la puissance intra-cavité reste un moyen efficace pour réduire les limitations dues au bruit de grenaille.

La figure 2.1 est un schéma de principe d'Advanced Virgo, où l'on voit que la puissance optique dans l'interféromètre sera augmentée grâce à un laser plus puissant et l'optimisation du recyclage de puissance [40, 41].

Le port de sortie étant réglé sur une frange noire, la conservation de l'énergie impose que la lumière soit réfléchie par l'interféromètre vers le port d'entrée, tel un miroir. L'ajout d'un miroir, dit de recyclage de puissance, permet ainsi d'augmenter la puissance dans cette nouvelle cavité sans besoin d'agir sur la source laser.

Pour l'ensemble des cavités de l'interféromètre, un gain important induit une largeur de raie étroite qui limite la bande passante de détection associée. La technique de recyclage de puissance est donc un compromis entre gain optique et bande de détection.

Sur la base de toutes ces considérations on obtient les spécifications sur le laser, à savoir, une puissance de 175 W, un bruit relatif de puissance de $2.35 \times 10^{-9} \sqrt{\text{Hz}}^{-1}$ à 30 Hz, un bruit de fréquence de $4.00 \times 10^{-7} \sqrt{\text{Hz}}^{-1}$ à 55 Hz. Ce chapitre décrit la

stratégie prévue pour atteindre ces performances.

◇ ◇ ◇

Ci-dessus sont les titres des sections et des sous-sections de ce chapitre.

2.1) Source laser ultra-stable: *Non-Planar Ring Oscillator*

2.2) Système laser de haute-puissance et de bas-bruit

- Oscillateur laser verrouillé par l'injection
- Oscillateur laser maître amplifié

2.3) Amplificateurs laser mono-fréquence à fibre

- Diffusion Brillouin stimulée
- Fibres de grande surface de mode
- Suppression de la diffusion Brillouin stimulée
- Augmentation de puissance d'amplificateurs laser mono-fréquence à fibre
- Instabilité de mode transverse
- Photo-noircissement
- Émission stimulée amplifiée
- Luminance des laser pompe et combineur de faisceaux signal/pompe

2.4) Combinaison cohérente de faisceaux laser

2.5) Stabilisation de laser

- Stabilisation de puissance
- Stabilisation de fréquence

2.6) Cavité optique comme *Mode Cleaner* (pour la filtrage des modes transverses)

2.7) Laser pré-stabilisé pour le projet Advanced Virgo: les spécifications et une conception

- La cavité *Input Mode Cleaner* d'Advanced Virgo
- Spécifications du laser à l'entrée de l'interféromètre
- Spécifications du laser à l'entrée du sous-système d'injection
- Schéma du sous-système de laser pré-stabilisé d'Advanced Virgo
- La cavité *Pre Mode Cleaner* d'Advanced Virgo
- Stabilisation du laser d'Advanced Virgo
- Spécifications du laser libre d'Advanced Virgo

Chapitre 3 Caractérisation de laser (partiel)

Imposer des spécifications nécessite d'être capable de mesurer les performances du système. Ce chapitre décrit les techniques utilisées pour parvenir à ces mesures.

Je présente notre technique pour une mesure absolue de la puissance continue de nos lasers.

Je décrirai les techniques utilisées et leur limitations pour la mesure des fluctuations de puissance, en particulier l'effet d'une ouverture finie sur nos faisceaux ainsi que les défauts d'homogénéité des photodiodes utilisées seront précisés.

Je décrirai la technique utilisée pour la mesure du bruit de phase/fréquence.

Je décrirai la technique utilisée pour la mesure du bruit de pointé de faisceau; basée sur l'utilisation de photodiodes à quadrant, je démontrerai l'invariance, au travers d'un système optique, de la variable utilisée pour décrire le bruit de pointé.

Je décrirai la technique utilisée pour quantifier la "qualité" du faisceau, basée sur le couplage dans une fibre mono-mode transverse.

Enfin je présenterai quelques considérations utiles sur la mesure des fonctions de transfert électrique de nos systèmes.

◇ ◇ ◇

Ci-dessus sont les titres des sections et des sous-sections de ce chapitre.

- 3.1) Mesure de puissance optique
- 3.2) Bande de fréquence d'intérêts d'Advanced Virgo
- 3.3) Mesure de bruit de puissance d'un laser
- 3.4) Effet d'apodization d'un faisceau sur la mesure de bruit de puissance d'un laser
- 3.5) Inhomogénéité spatiale de la réponse des photodiodes
- 3.6) Mesure de bruit de fréquence/phase de laser
 - Mesure de bruit de fréquence de laser en utilisant une cavité optique
 - Interférométrie de Mach-Zehnder
 - Un interféromètre hétérodyne de Mach-Zehnder
 - Technique perturbative pour la verrouillage d'un interféromètre de Mach-Zehnder
 - Plancher de bruit de mesure de phase par interférométrie de Mach-Zehnder
 - Modulation frontale de phase pour la verrouillage d'un interféromètre de Mach-Zehnder asymétrique
- 3.7) Mesure de stabilité de pointé d'un faisceau laser
- 3.8) Invariance de stabilité de pointé d'un faisceau Gaussien

- 3.9) Mesure de profil d'un faisceau
- 3.10) Modes transversales: LP_{01} dans un fibre vs. Gaussien TEM_{00} en espace libre
- 3.11) Mesure de densité spectrale de puissance
- 3.12) Mesure de fonction transfert
- 3.13) Acquisition de données automatisé

Chapitre 4 Laser à fibre en amplifiant un oscillateur maître (partiel)

Ce chapitre fait l'historique du laboratoire en matière d'amplificateurs à fibre de haute-puissance, possibles candidats pour Advanced Virgo. Je m'attacherai ensuite à présenter les tests du dernier candidat prometteur, à savoir un amplificateur à fibre commercial alimenté par un laser de type NPRO.

Ce dernier candidat a été testé sur plusieurs milliers d'heures et on démontre que le système atteint les spécifications de Advanced Virgo en tous points mais montre un "léger" déficit de puissance. Ensuite on aborde la problématique d'un laser source fibré pour Advanced Virgo. L'accent étant mis sur les limitations des composants fibrés, des problèmes liés à la diffusion Brillouin stimulée, ainsi que des contraintes imposées par les spécificités du site de Advanced Virgo. Je présente les résultats de nos investigations et mesures.

Je présente ensuite les résultats obtenus avec les amplificateurs à fibre provenant des compagnies Nufern, Eolite et Azur Light Systems.

◇ ◇ ◇

Ci-dessus sont les titres des sections et des sous-sections de ce chapitre.

- 4.1) Lasers maîtres pour les amplificateurs laser à fibre
- 4.2) Couplage à fibre de laser NPRO
 - Fibre d'intérêt
 - Perte et bruit de la couplage à fibre
 - NPRO-400
 - NPRO-900
 - NPRO-800
 - Sommaire sur la couplage à fibre du laser NPRO
- 4.3) Couplage dans une fibre pour le transport d'un faisceau laser
- 4.4) Amplificateurs laser à fibre de Nufern
- 4.5) Amplificateurs laser à fibre de Eolite

4.6) Amplificateurs laser à fibre d'Azur Light Systems

- Puissance optique
- Analyse de stabilité dans la domaine temporel de l'amplificateur laser à fibre ALS 2 de $t = 0$ h à $t = 650$ h
- Qualité de faisceau
- Bruit de puissance
- Bruit de fréquence
- Stabilité de pointé de faisceau

4.7) Chemins d'actuation pour la stabilisation de puissance

Chapitre 5 Combinaison cohérente de faisceaux laser (partiel)

Pour l'obtention de fortes puissances la combinaison cohérente est une des solutions offertes pour l'augmentation d'échelle. Jusqu'à présent de nombreuses configurations ont été proposées [109], en particulier, celles mettant en jeux des amplificateurs ytterbium [110, 165]. Dans notre cas nous avons retenu le schéma d'un interféromètre de Mach-Zehnder [166].

Dans ce chapitre nous décrivons certaines des techniques de génération d'un signal d'erreur pour l'asservissement de l'interféromètre de Mach-Zehnder qui sera utilisé pour la combinaison cohérente de nos systèmes. Nous présentons la technique d'hétérodynage, la technique perturbative de phase et la technique de modulation frontale.

Finalement nous présentons les performances du système retenu, soit un interféromètre de Mach-Zehnder asservi par la technique perturbative de phase. Je démontre que ce système remplit les spécifications pour Advanced Virgo.

◇ ◇ ◇

Ci-dessus sont les titres des sections et des sous-sections de ce chapitre.

- 5.1) Interférométrie de Mach-Zehnder en espace libre verrouillée par la technique perturbative pour la combinaison cohérente de faisceaux laser
- 5.2) Dynamique de phase des amplificateurs laser à fibre d'Azur Light Systems
- 5.3) Efficace et pénalité de puissance
- 5.4) Bruit de puissance
- 5.5) Bruit de fréquence et qualité de faisceau
- 5.6) Stabilité de pointé de faisceau

5.7) Résultats sur le suivi long-terme

5.8) Stabilisation de puissance sur la combinaison cohérente de faisceaux laser

5.9) Combinaison de plus de deux faisceaux laser

Chapitre 6 Conclusions et perspectives (intégral)

6.1 Amplificateurs laser à fibre de haute-puissance

Les résultats des tests du chapitre 4 ont montré que l’amplificateur de puissance à fibre associé à un oscillateur laser maître (acronyme répandu “MOFPA” en anglais) peut délivrer 42W de puissance stable et à très bas bruit pendant des durées de temps de l’ordre de plusieurs mois. Ainsi démontré, le système répond aux spécifications de Advanced Virgo en terme de bruits.

Ce qui n’est à priori pas démontré pour l’instant est un niveau de puissance suffisamment élevé tout en respectant les spécifications imposées par Advanced Virgo. Bien que la puissance de l’amplificateur testé ne soit pas celui demandé dans la description de référence de la figure 2.15, les caractéristiques de fonctionnement sur le long terme justifient cette étude, qui, d’après nous n’a jamais été menée de façon systématique jusqu’à présent et démontre son intérêt pour les détecteurs à interférométrie laser d’ondes gravitationnelles (DILOG).

En terme de la recherche et développement, comme décrit dans la section 2.3, dans les années récentes il y a eu des recherches systématiques sur les stabilités des modes transverses et le photo-noircissement qui représentent les deux facteurs limitants de la technologies des amplificateurs à fibre. La recherche de solutions est toujours en cours et va sans aucun doute converger vers des solutions performantes en terme de structure et conception de fibres spécifiques et l’utilisation de composants fibrés critiques.

Au niveau des systèmes pour une application dans les DILOG et dans la perspective du contrôle long terme des amplificateurs à fibre il sera utile de mettre en œuvre de sondes pour différencier l’effet du photo-noircissement et du vieillissement des composants fibrés critiques. Ceci peut être fait en co-injectant un faisceau laser aux longueurs d’onde visible. L’avantage est double. D’une part on a démontré que le taux de photo-noircissement était plus important aux longueurs d’onde courtes [104, 106]; ainsi la co-injection dans le visible permet d’être plus sensible qu’à la longueur d’onde d’utilisation de 1064 nm. D’autre part il a été démontré que la co-injection de lumière visible permet de réduire les pertes induites par le photo-noircissement [178, 179], un tel “blanchiment” a aussi été démontré pour des expositions à la lumière ultraviolet [106].

D’autre part ces sondes pourraient être introduites au niveau du combineur pompe-signal afin d’évaluer le vieillissement de ces composants optiques fibrés. L’introduction de ces sondes amènera une meilleure compréhension dans les prochains tests des amplificateurs à fibre et permettra aussi une planification de leur utilisation dans les DILOGs.

On pourra aussi prendre en considération le contrôle de puissance pour la stabilisation de puissance pour Advanced Virgo. Comme l’équation 4.6 le suggère la

fréquence de coupure est dépendante de la configuration de les amplificateurs, en particulier le rapport entre signal et pompe. Si on considère étendre la technique de shunt utilisée jusqu'à présent pour Virgo à Advanced Virgo, il sera utile de prendre en compte ce paramètre lors de la définition du MOFPA.

6.2 Combinaison cohérente de faisceaux laser

Dans le chapitre 5 nous avons montré que si on considère des lasers mono-fréquence, alors la combinaison cohérente remplit les spécifications d'Advanced Virgo. La technique est modulable mais au prix d'une complexité accrue.

Aussi, en prenant en compte le taux de panne par système il n'est peut être pas judicieux de multiplier le nombre d'unités dans le cadre d'une utilisation continue. Considérant toutes ces remarques et compte tenu des puissances obtenues actuellement, il semble que l'utilisation de 3 ou 4 unités soit un compromis raisonnable pour Advanced Virgo. Ceci implique la mise à disposition d'amplificateurs à fibre de 50 W à 70 W. Des amplificateurs à fibre des 100 W seraient sans doute un plus mais ne peuvent pas être considérés suffisamment mûres au vu du planning prévu pour Advanced Virgo.

6.3 Outre de laser de haute-puissance

Les lasers de haute puissance ne sont pas le seul moyen de remplir les spécifications fixées par la limite quantique à la sensibilité du détecteur. De plus la pression de radiation augmente avec la puissance des faisceaux; de plus fortes puissance implique d'utiliser des masses plus lourdes afin de contrer la limite quantique standard [30, 37, 38]. Une puissance intra-cavité extrême provoque aussi des instabilités paramétriques dans les cavités résonnantes [180–183], déjà observées dans Advanced LIGO [184].

Comme indiqué au chapitre 2, l'utilisation de lumière comprimée peut aussi améliorer la sensibilité des DILOGs. Le projet GEO-HF a déjà démontré plus de 3.7 dB de gain sur la sensibilité [39, 185, 186] et jusqu'à 2.15 dB pour LIGO [187]. L'amélioration par l'usage de la lumière comprimée est inversement proportionnel aux pertes optiques. Par exemple 10 % de pertes limiteront le gain à 10 dB. Pour Advanced LIGO les pertes sont estimées de 20 % à 32 % ce qui permet une compression de 5 dB à 7 dB, et la perte totale prévue après optimisation, soit de 9 % à 17 %, permettrait une compression de 8 dB à 10 dB au maximum [188]. Une compression de 10 dB est équivalente à une augmentation de la puissance optique d'un facteur 10 et représente donc une alternative efficace pour repousser la sensibilité des futurs DILOGs.

Après un examen attentif de la figure 1.5, on voit que le bruit des traitements des miroirs domine pour les fréquences intermédiaires. Dans ces conditions la recherche de meilleures techniques de traitement doit être aussi considérée pour repousser la limite quantique standard.

Enfin, des configurations optiques différentes, l'interféromètre de Sagnac qui a une meilleure sensibilité à basse fréquence, ont aussi été proposées [189].

6.4 Au-delà des détecteurs avancé d'ondes gravitationnelles

La construction des deux détecteurs d'Advanced LIGO a été terminée en mars 2015 et la première observation a commencé le 18 septembre 2015 lançant ainsi le début de la recherche d'ondes gravitationnelles avec des détecteurs avancés, soit presque un siècle après la prédiction de leur existence par Albert Einstein en 1916.

Pendant ce temps la construction d'Advanced Virgo est en cours et est prévu d'être terminée en 2016. Le lancement de LISA pathfinder⁸, dont l'objectif est de tester les technologies nécessaire pour le projet eLISA⁹ est prévu pour fin 2015. Tous ces efforts scientifiques apporteront des données expérimentales utiles à la physique fondamentale et ouvriront une nouvelle fenêtre sur l'univers.

Si la détection des ondes gravitationnelles a été possible avec la première génération des détecteurs et sera probable avec la seconde génération, il est naturel de se demander quel sera l'objectif pour les détecteurs futurs.

Une étude conceptuelle d'un détecteur avancé basé sur des technologies validées envisage une base de 40 km grâce à laquelle des distances cosmologiques seront appréhendées [190]. D'autre part il a été estimé que la sensibilité des détecteurs avancés pourrait être améliorée d'un facteur 2 en réduisant les sources de bruit limitantes [191].

Comme le montre la figure 1.3 l'Einstein Telescope (ET), un DILOG de troisième génération, sur une base de 10 km, a été proposé et sa conception bien étudiée avec une amélioration de la sensibilité de détection de plusieurs ordre de grandeur. Le schéma d'ET prévoit un laser de 500W soit 4 fois plus que ce qui est prévu pour les détecteurs avancés [192].

Le développement de lasers ultra stable de haute puissance sera donc toujours un besoin pour des performances de plus en plus élevées en interférométrie de précision, dont la recherche d'ondes gravitationnelles et finalement l'astronomie des ondes gravitationnelles est la partie la plus excitante.

La découverte accidentelle du fond cosmique de micro-ondes a apporté en 1978 le prix Nobel de physique à Arno A. Penzias et Robert W. Wilson [193] et une description d'un univers *jeune* à $\sim 380\,000$ années après le Big Bang, soit l'instant où la première lumière a émergé. Ainsi, même une vision sans limite via les ondes électromagnétiques ne permet de voir que jusqu'à $\sim 380\,000$ années après le Big Bang.

Le modèle cosmologique lambda matière noire froide (lambda cold dark matter, Λ -CDM) ainsi que les résultats récents de la mission Planck suggère que l'univers se compose de 4.9 % de matière classique, 26.8 % de matière noire, 68.3 % d'énergie noire¹⁰. Ainsi, même avec une vision sans limite via les ondes électromagnétiques, on n'accède qu'à 4.9 % de l'univers.

Ce qui reste, en espace et en temps, est constitués d'inconnues identifiées, ou d'inconnues non identifiées, qui seront partiellement dévoilées grâce à l'écoute des interféromètres laser.

⁸<http://sci.esa.int/lisa-pathfinder/>

⁹Evolved Laser Interferometer Space Antenna

¹⁰<http://sci.esa.int/planck/51557-planck-new-cosmic-recipe/>

Appendices

Appendix A

Test Results of the 50 W Demo Fiber Amplifier from Nufern

This is the test report of the 50 W demo fiber amplifier from Nufern (cf. Section 4.4) archived in the Technical Documentation System (TDS) of Virgo (<https://tds.ego-gw.it/itf/tds/>). Although the report is titled with *first part*, so far there is no *second part* or so. After the failure of the fiber amplifier due to the lack of the seed laser signal, there was the intention to have it repaired and continue on with the characterization to better understand the causes of the constant loss of output power and the excessive power noise in the MHz frequency range.

Title	Nufern 50W fiber amplifier test - first part
Author(s)	F. Cleva, Li-Wei Wei
Document type	Advanced Virgo R&D document
Code	VIR-0102B-13
Referral URI	https://tds.ego-gw.it/ql/?c=9447




Nufern 50W fiber amplifier test – first part

VIR-0102B-13

F. Cleva, L.-W. Wei for PSL @ ARTEMIS (J.P. Coulon, F. Kéfélian, N. Man , M. Merzougui)

15/04/2013

V1.0


	Title	Date 15/04/2013 VIR-0102B-13 Page 2 of 11
---	-------	---

CHANGE RECORD

Version	Date	Section affected	Reason/ remarks
1.0	15/04/2013	- Figures 5 and 6 - Proposal “3)” on page 9 - PMC pole and power density on page 9, item “2)”	First official release

Table of contents

1. Introduction	3
2. Experimental setup	3
3. Long term test on output power stability	4
4. Master failure led to amplifier breakdown	7
5. Relative intensity noise (RIN)	7
6. Beam jitter and drift	9
7. Conclusion	11

	Title	Date 15/04/2013 VIR-0102B-13 Page 3 of 11
---	-------	---

1. Introduction

In order to find another vendor of fiber amplifier, we have approached Nufern, a US company producing fibers and we have got a 2 weeks loan of their commercial 50W fiber amplifier. The product has been shipped to Nice for product demonstration: it is an engineering version (ie devoted for testing) of the commercial 50-Watt, polarization-maintaining (PM) fiber amplifier of the NuAMP product series. The operational input power of the Master laser is in the range of 50 to 200 mW, and the output is delivered through a 1.5 m-long PM fiber, which is spliced to a free space Faraday isolator. The reference number of the unit is NUA-1064-PD-005-C0.

Depending on the availability of the EOLITE prototype at the delivery time of end of 2013 (cf planning of AdV), the NuAMP 50 W is a potential candidate for fulfilling this request.

We present herewith the noise measurements and some preliminary conclusions based on these few days tests.

Unfortunately, a failure of the Innolight Master laser induces some damage in the fiber amplifier (see Section Master failure) and we have not undergone all the tests planned for the moment.

2. Experimental setup

The unit arrived on Mar. 6th 2013, and was scheduled to undergo two weeks of test at Artemis. The unit comprises a Yb doped fiber pumped by one or two laser diodes in order to amplify in a few hundred times any input signal coming from a Master laser. For the tests, we have mounted an experimental setup shown in **Figure 1**. An NPRO laser, identical to the one used in the Virgo+ operations, was borrowed from EGO and served as the Master laser. It is coupled into a 3 m-long PM fiber connected to the fibered input port of the amplifier. A fiber beam-splitter is inserted in order to monitor the master laser power during the tests.

The amplifier was cooled using a Virgo-like water chiller; the water temperature was set to 23 degrees Celsius.

The output of the amplifier was monitored with a quadrant photodiode for beam-jitter measurement, two photodiodes and a calorimeter for absolute power and relative intensity noise (RIN) measurements, as well as a Fabry-Perot cavity for spatial mode content measurement.

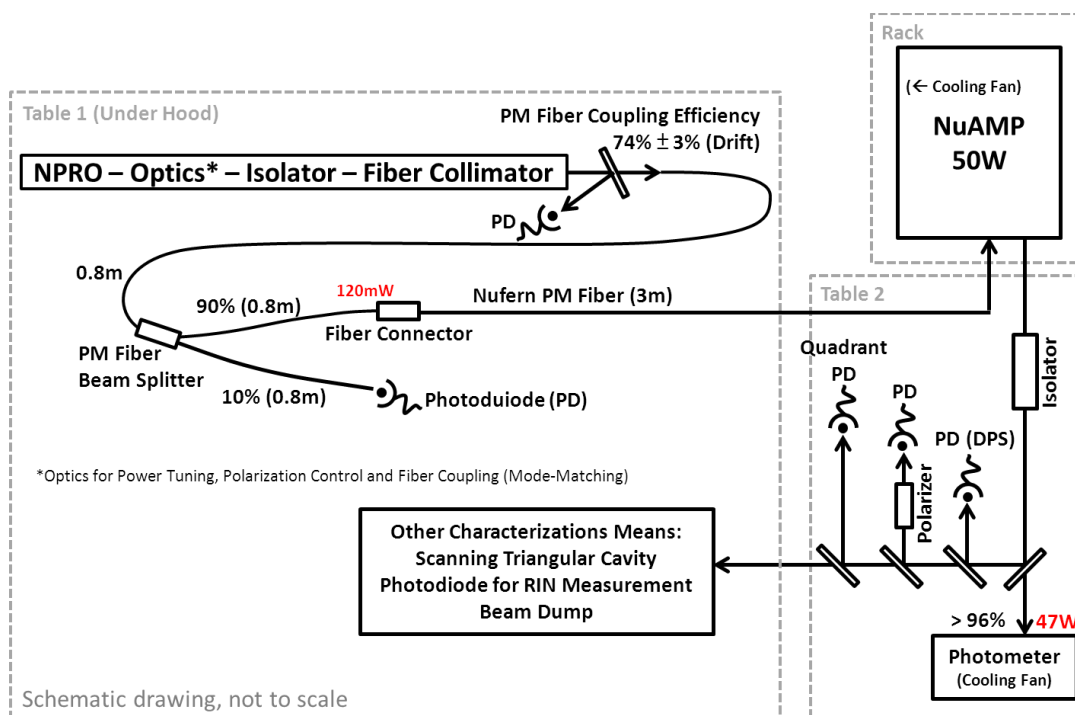


Figure 1: Schematic drawing of the experimental setup

1. Long term test on output power stability

At first start-up 49-Watt output power was obtained with 120 mW of input laser. Two continuous runs were conducted; the first lasted 62 hours and the second lasted 57 hours. During the first run a 4.5% continuous drop in output power was observed [Figure 2]. Following the response from Nufern regarding the power drop, the unit was turned off temporarily for some 15 minutes before the restart for the second run. No obvious recovery was observed. The second run was terminated on Mar. 18th owing to a stop of the master NPRO laser. A continuous drop in output power was also observed during the second run, but the rate was reduced to 1.5% [Figure 2]. The long term test has been done during 5 days.

- We have checked experimentally that the amplifier output power is independent of the input Master power. The output power of the amplifier oscillated around a more or less constant value even when up to 30% variation in the Master power was applied [Figure 3]. This clearly shows that input power fluctuations from the NPRO laser and the fiber-coupling optics do not match the long-term power drop observed.
- We have measured the temperature dependency of the amplifier output power, and observed that a 2-degrees-Celsius variation of the chiller leads to a 6% variation of the amplifier output power [Figure 4]. Since the chiller temperature was regulated within 0.2 degree Celsius peak-to-peak, the corresponding temperature fluctuation could not match the power drop observed. Moreover the time constant of temperature variation is few minutes rather than tens of hours.

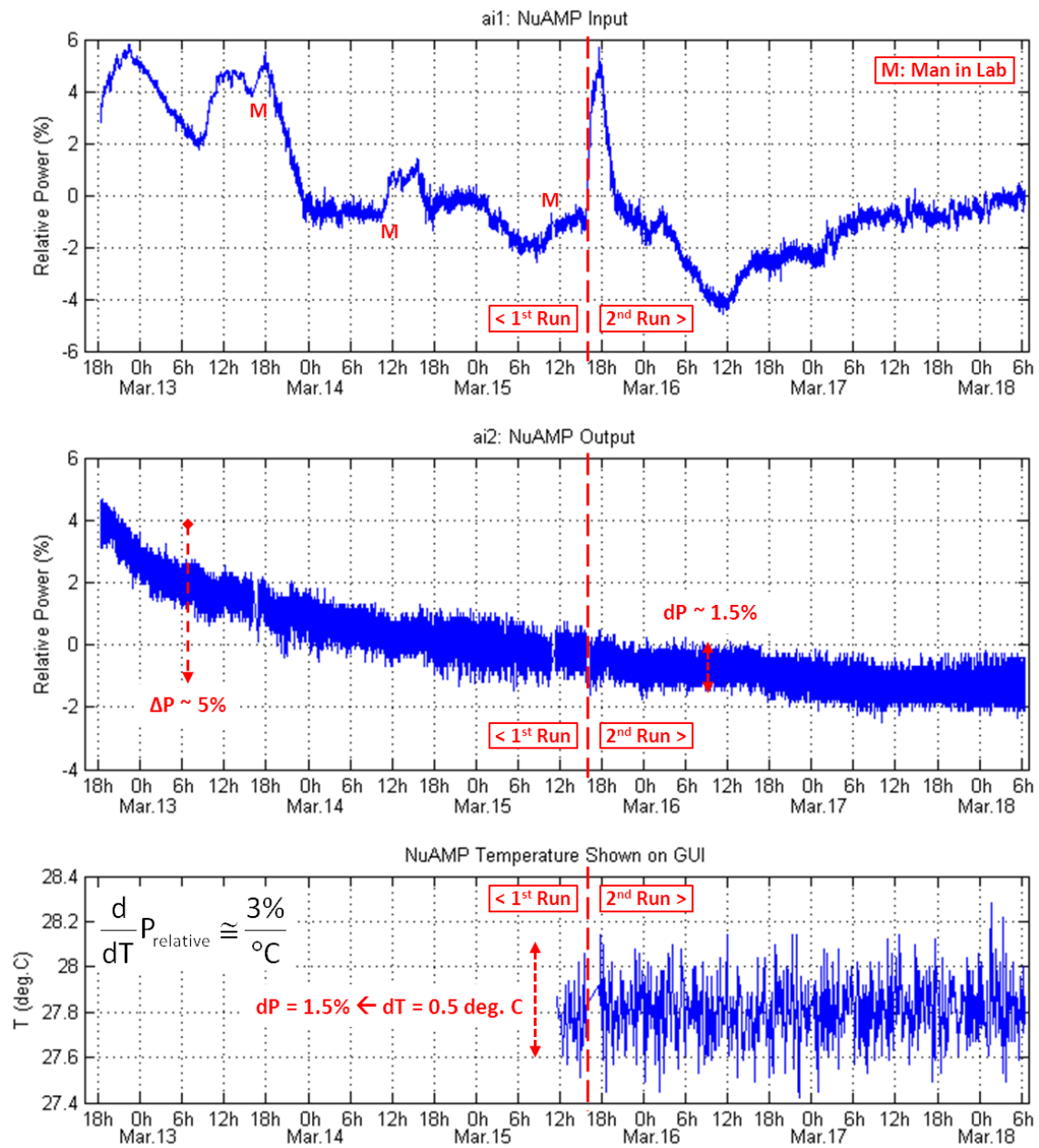


Figure 2: Amplifier input/output and temperature curves vs time. Top curve: Relative power fluctuations of the Master laser read on the input fiber beam-splitter 10% port; Middle curve: Relative output power fluctuations of the amplifier; Bottom curve: Temperature of the amplifier unit shown on its Nufern GUI. M, which is a human presence in the lab induces small perturbations in the relative power.

- In addition to the power drop, the amplifier output power also oscillated with a magnitude of 1.5% peak-to-peak [Figure 2, Figure 3, Figure 4]. This is very likely because of the temperature fluctuation of the amplifier itself, which is about 0.5 degree Celsius peak-to-peak [Figure 2] and corresponds to 1.5% of output power fluctuation.

Accordingly, the long term power drop is considered as an intrinsic property of the amplifier unit and the attached isolator.

Nufern has provided us some long term measurements made over 500 hours, where they have observed less than 3% drop over 1000 hours. Since the unit we received was dedicated for the isolator qualification, Nufern claimed that the power drop might come from the Faraday isolator spliced to the output fiber and is likely to be not relevant of standard units.

Meanwhile, it should be noted that Nufern guarantees against drifts of output power down to 3% over 1/2/3 years according to the warranty chosen by customers. Last, we have contacted two laboratories in Germany, Max-Planck Institute of Quantum Optics, Munich and Heidelberg University, to inquire about the reliability of such unit: the feedback was quite positive regarding the reliability, see below: e-mail discussion between Max-Planck Institute of Quantum Optics (MP) and F. Cleva (FC):

MP: “after fixing some bugs together with Nufern, the long term reliability now seems good. We have systems running for over a year now without a problem.”

FC: “Do you mean continuous running at full power?”

MP: “about 6-10 hours 5 days a week.”

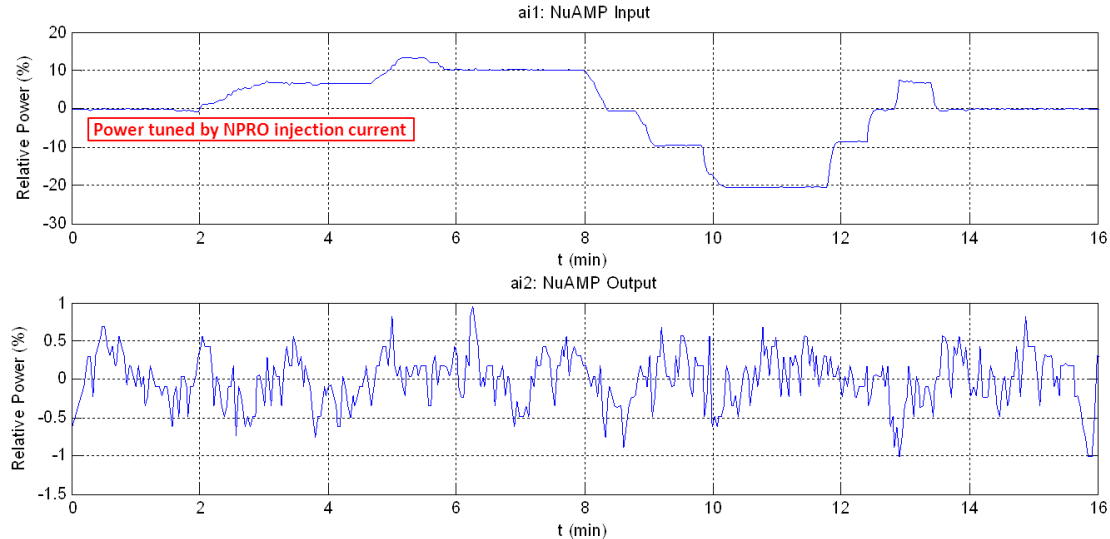


Figure 3: Input Master level (in)dependency of the amplifier output power. We changed in steps the Master power (upper plot) and measured the effect on the amplifier output power (lower plot) and observed no changes.

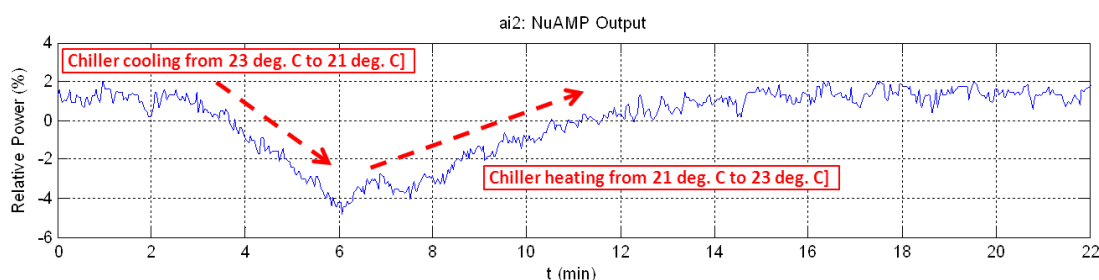


Figure 4: Temperature dependency of the amplifier output power. We changed the chiller temperature setting and measured its effect on the amplifier output power.

2. Master laser failure led to amplifier breakdown

After 120 hours (5 days and ½) of operation the Master laser switched off for some unknown reason (the laser driver was plugged in to an uninterruptible power supply) without any failure. The NuAMP 50W unit came with a protection against the absence of input signal and shuts down the pumping diodes as fast as possible to avoid any Q-switch behaviour of the amplifier that might destroy the fiber facets. When the master stopped, the amplifier went on safety mode triggered by the “Back Reflection” (BR) level which monitors the amount of light back-reflected to the amplifier. After checking that no optical part of the amplifier has been damaged, we were unable to restart it again as of the BR level has been set itself above some safety threshold. Even a cold restart from scratch of the amplifier was not able to reset such safety level, whatever the presence or absence of the input master signal.

Nuferm has then suspected a damage of the BR probe, and proposed to retrieve the unit for repair and they would send it back again to us for further tests. After agreements, the unit was shipped back to Nuferm on Mar. 20th.

3. Relative intensity noise (RIN)

Figure 5 shows the Nuferm RIN from DC to 100. If we compare it to the RIN level of the Eolite rod fiber at 55W displayed in the TDR (see TDR, §3.6.2.1, page 105, figure 3.5, recalled here in figure 5bis), we can see that it is comparable or even better above 500 Hz then we can confirm that it is fully managed by our power stabilization loop.

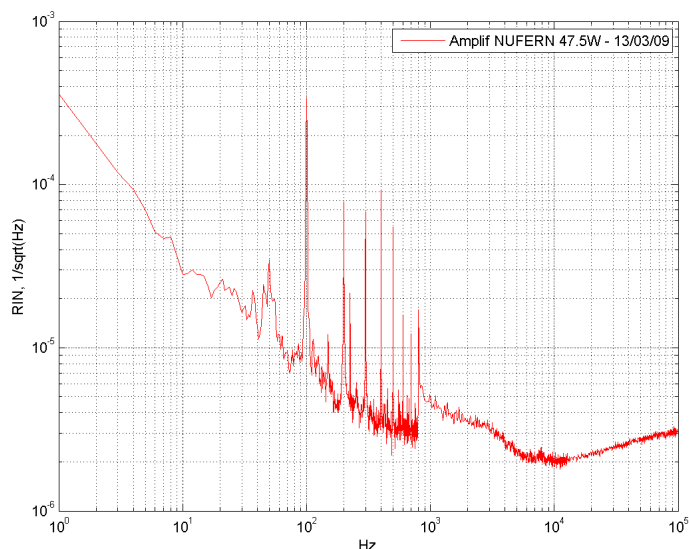


Figure 5: RIN at 48W output power, low frequency

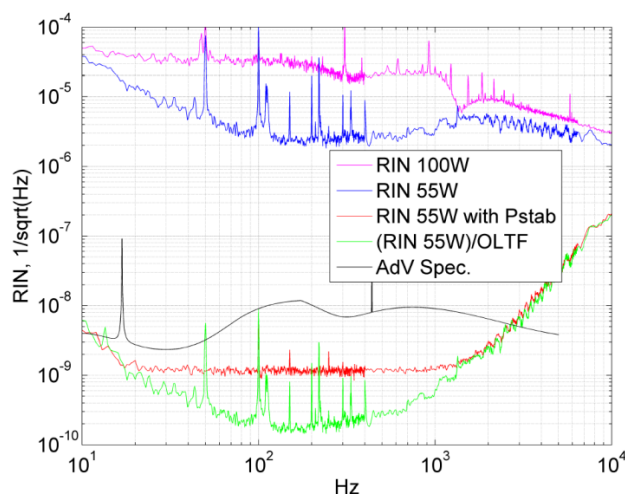


Figure 3.5: The magenta curve is the RIN of 100 W HP amplifier. Blue curve: RIN of the 55 W amplifier. Red curve: RIN of the 55 W amplifier after stabilization. Green curve: 55 W RIN divided by the open loop transfer function of the servo loop. Black curve: AdV specification.

Figure 5bis : RIN specifications and performances of the Eolite fiber rod amplifier as presented in the TDR.

Figure 6 shows the RIN above 100 kHz. At the RF frequencies of a few MHz, the noise shows 3 orders of magnitude more than what is requested. So far we had no time to investigate this feature further. Such a noise was not observed with the Virgo+ solid state laser and amplifiers (20W and 60W), nor the rod fiber amplifier prototype of EOLITE we tested in January, 2010 (50W). On the other hand, we have already observed such feature with the previous 100W Nufern amplifier prototype we tested in 2009, but with a rather smaller amplitude ($2e-7/\text{sqrt}(\text{Hz})$ @ 6MHz).

Several solutions could be considered to overcome this situation:

- 1) If the extra noise comes from amplified spontaneous emission (ASE) beatings, using

therefore some ASE filtering could improve things.

- 2) On the other hand we can filter that RF noise by using a combination of 2 pre-mode-cleaners (PMCs) in series, each providing more than $1/\sqrt{1000}$ attenuation factor at 6MHz. It means a cavity pole of 190kHz, assuming a finesse of 2000 and a half length of 20cm; this implies 114kW in the cavities (for 180W incident power), and 29MW/cm² flux on the mirrors.
- 3) Another solution could be to act on the Master input power (through a fibered amplitude modulator) at 6MHz, relying on the fact that the amplifier transmits enough amount of the 6MHz “perturbation”. We would then complete some fast power stabilization.

The options 1 and 3 can be tested as soon as we get the amplifier back after repair.

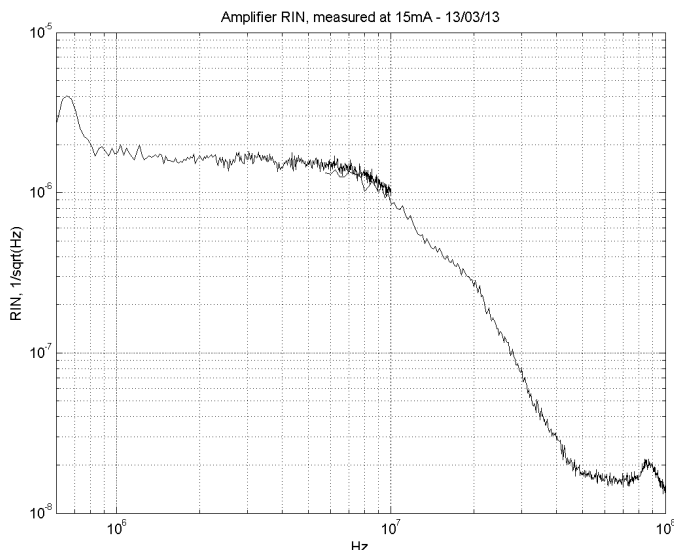


Figure 6: RIN at 48W output power, high frequency. The peak near 700 kHz refers to the Master laser oscillation relaxation. The shot noise limited RIN at 0.1A is $1.79e-9/\sqrt{\text{Hz}}$.

4. Beam jitter and drifts

Figure 7 and **Figure 8** give the angular beam-jitter (BJ) measured 1.28m away from the amplifier output. No attempt has been made yet to measure the BJ shift.

The measured BJ match the AdVirgo specifications (see TDR p109, figure 3.8), and hence, from that specific point of view, one single PMC would be enough. Moreover, part of the noise in the range from 100 Hz to 1 kHz comes from the fan used to cool down the calorimeter we use for the overall power measurement. Therefore the amplifier intrinsic BJ noise should be lower by a factor 2 in this region than what is displayed herewith.

Figure 9 displays the beam drift at 1.28m from the fiber output. We guess the large vertical drift (350 μm) comes from some tilt drift. So far we don't know whether it comes from the spliced output Faraday isolator or from some thermalisation of the test bench. On March the 15th, at 16 o' clock we proceed with a centering of the quadrants photodiode position, which explains the large gap on the vertical direction. Assuming the drift comes from a beam tilt one has to compare the associated tilt (273 μrad) with the beam divergence (1513 μrad).

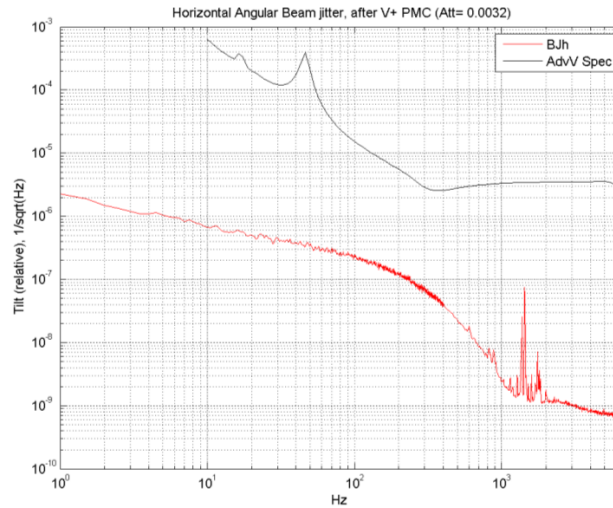


Figure 7: Horizontal angular beam jitter together with the AdVirgo specifications at IMC input (after PMC). The red curve is the BJ measured at the amplifier output and multiplied by the Virgo+ like PMC attenuation factor (1/312). Beam-jitter is overestimated since part of the noise from 100 Hz to 1 kHz comes from the fan of the calorimeter used to measure the output power.

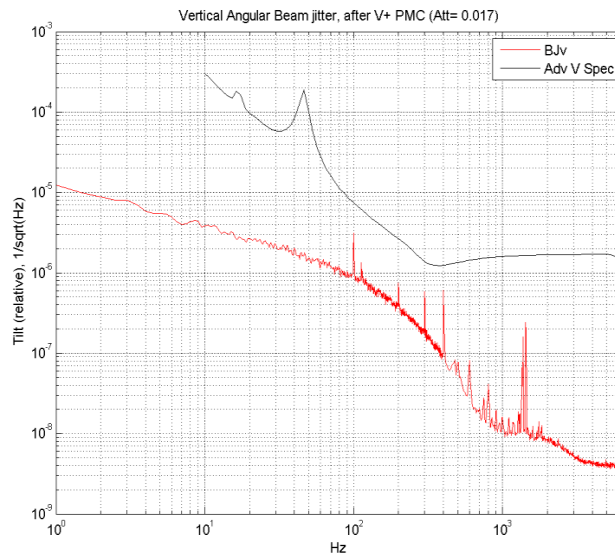


Figure 8: Vertical angular beam jitter together with the AdVirgo specifications at IMC input (after PMC). The red curve is the BJ measured at the amplifier output and multiplied by the Virgo+ like PMC attenuation factor (1/59). Beam-jitter is overestimated since part of the noise from 100 Hz to 1 kHz comes from the fan of the calorimeter used to measure the output power.

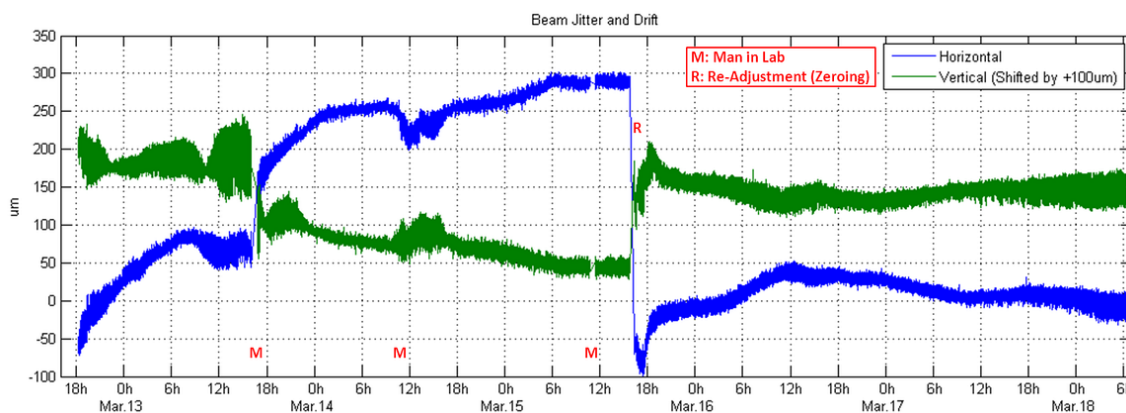


Figure 9 Beam jitter and drift after the amplifier

5. Conclusion

These first tests have been conducted with a Nufern amplifier (demonstration model) during 120 hours. We can give some preliminary conclusion about the noises, which are manageable with the usual controls, passive for beam jitters, active for RIN. High frequency RIN deserves a deeper understanding in relation with the manufacturer and probably an extra servo or an extra PMC to kill the noise at the 6 MHz modulation frequency. As far as long-term tests are concerned, the 120 hours of operation are not enough as we have not reached the Nufern guarantee of 3% power drop after 1000 h.

The impossible restart and power drop we have encountered with this demo unit is actually linked to that specific engineering unit and should be corrected.

Up to now none of the performances we have measured have excluded Nufern as a possible amplifier option for the end of 2013 and we expect the return of the unit to conduct further tests in the lab.

Appendix B

Test Results of the 30 W Demo Fiber Amplifier from Azur Light Systems

These are the summarizing slides on the test results of the 30 W demo fiber amplifier from Azur Light Systems (ALS) performed in July, 2013. The measurements were made at ALS in Pessac, Bordeaux. We acknowledge the kind assistance of Johan Boulet and Nicholas Traynor from ALS. We also acknowledge the assistance of Walid Chaibi from ARTEMIS.

As far as we know, the main difference between this demo unit and the two fiber amplifiers described in Section 4.6 lies in the number of pumping laser diodes. Having only one pumping laser diode, the output power of the demo unit was limited to ~ 30 W. Fluctuations in the output power noise level were also observed with the demo unit at ~ 30 W output power.

ALS 30W Fiber Amplifier Demo Performance

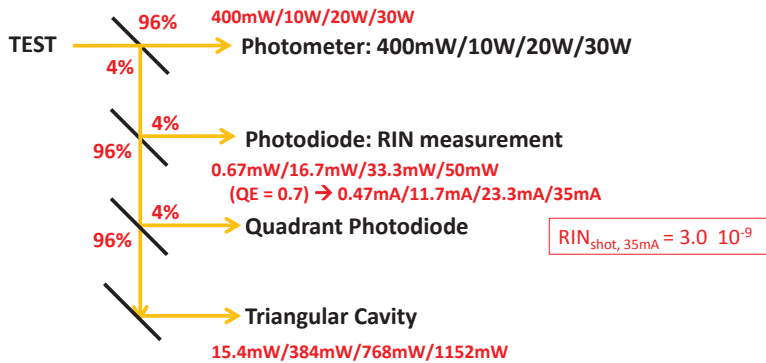
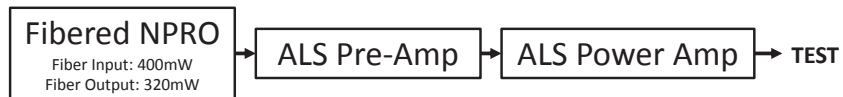
Version PSL

1

A) RIN MEASUREMENTS

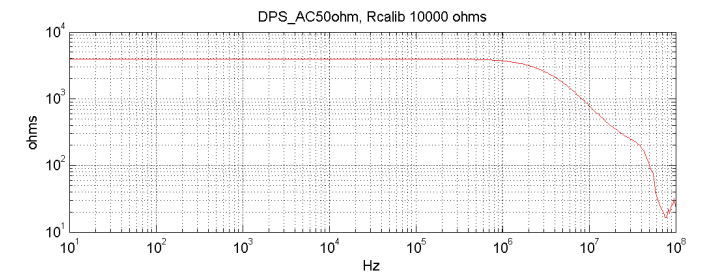
3

Test Setup

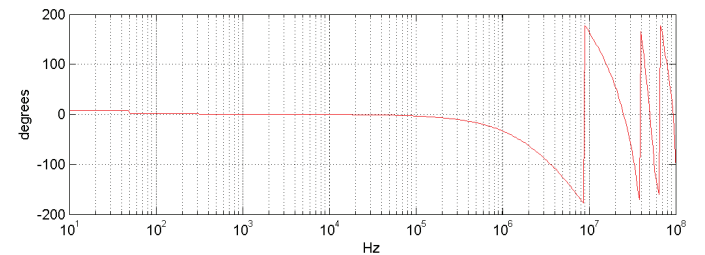


2

Transfer Function of RIN Photodiode, AC

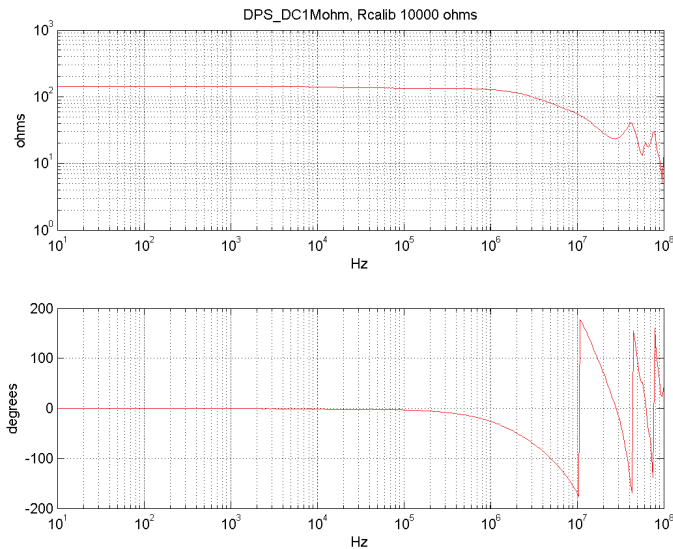


* Already takes into account the factor 2 of the 50 Ohm – 50 Ohm input connection *



4

Transfer Function of RIN Photodiode, DC



5

RIN Data Flow – Deriving RIN

- Low-F ASD is further processed in the following manner to derive RIN:

$$\text{rin_lf} = \text{asd_lf} / \text{dps_R_ac} / (\text{dps_dc} / \text{dps_R_dc});$$
 Where: $\text{dps_R_dc} = 136$; $\text{dps_R_ac} = 4\text{e}3$;
 And dps_dc is the DC value read by the RIN photodiode;
- High-F ASD is processed with an eye on the non-uniform transfer magnitude of the RIN photodiode:

$$\text{rin_hf} = \text{asd_hf} / \text{dps_R_ac} / (\text{dps_dc} / \text{dps_R_dc});$$

7

RIN Data Flow - Instrumental

- SR780
 - 800Hz/12.8kHz/102.4kHz, all in ASD units (Vrms/rtHz), SRTRANS v3.0 data conversion, without additional correction
- HP8591A
 - $\text{dBm}_{\text{Noise Marker}} = 10 \log(\text{PSD}/1\text{mW}/1.12/\text{RBW}) + 2.5\text{dB}$
 - $\text{dBm} = 10 \log(\text{PSD}/1\text{mW})$
 - 20kHz – 200kHz, RBW: 3kHz VBW: 3kHz
 - 100kHz – 1MHz, RBW: 10kHz VBW: 10kHz
 - 1MHz – 10MHz, RBW: 100kHz VBW: 30kHz
 - 10MHz – 100MHz, RBW: 1MHz VBW: 300kHz
 - All in Sample Mode (i.e., Noise Marker ON)
 - All in power units dBm, and converted to ASD with

$$\text{ASD} = \sqrt{10^{(\text{dBm}/10)} * 1\text{e-}3 * 50 / 1.12 / \text{RBW} * 1.7783};$$
 Where 1.12 is the correction for noise/resolution bandwidths, and 2.5dB (1.7783) for log detection mode

6

Some notes on RIN derivation

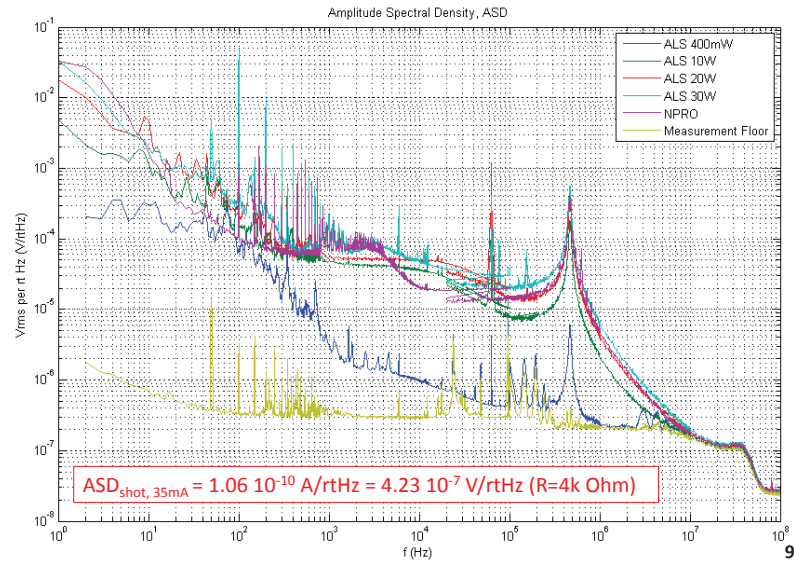
$$\text{RIN} = dP/P \sim dI_{\text{ph}}/I_{\text{ph}} = (dV_{\text{meas}}/R_{\text{AC}}) / (V_{\text{meas}}/R_{\text{DC}}) \rightarrow$$

$$\text{RIN} = \text{ASD} / R_{\text{AC}} / (V_{\text{DC}} / R_{\text{DC}})$$

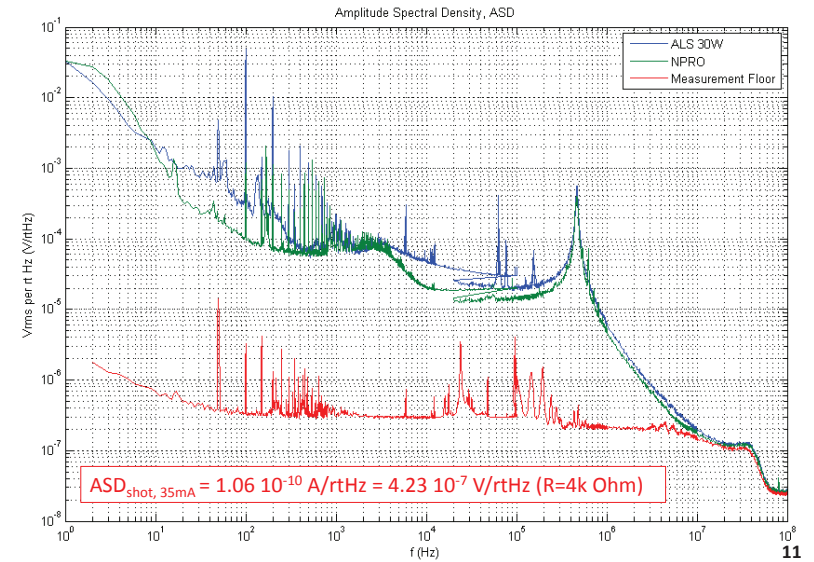
The magnitude transfer from dP/P to $dI_{\text{ph}}/I_{\text{ph}}$ is assumed to be uniform within the frequency range of interest.

8

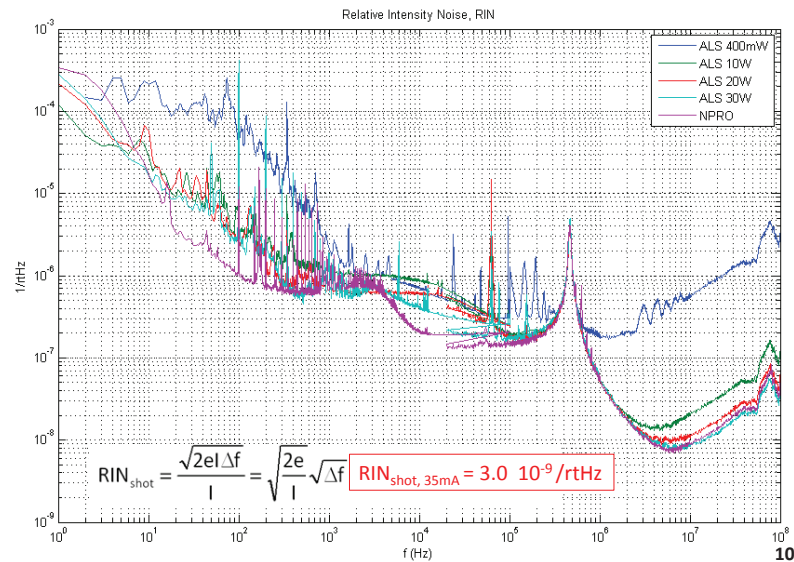
ASD Results, Noise Eater OFF



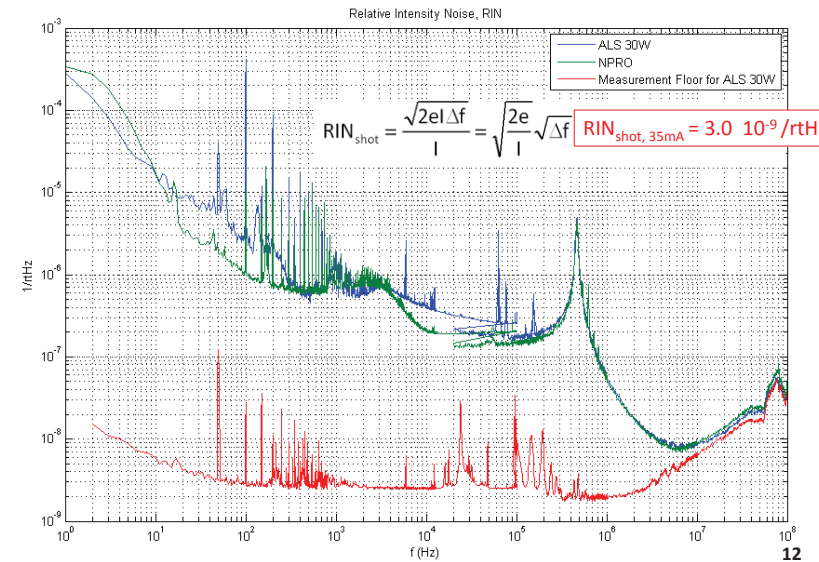
ASD Results at P=30W, Noise Eater OFF



RIN Results, Noise Eater OFF



RIN Results at P=30W, Noise Eater OFF

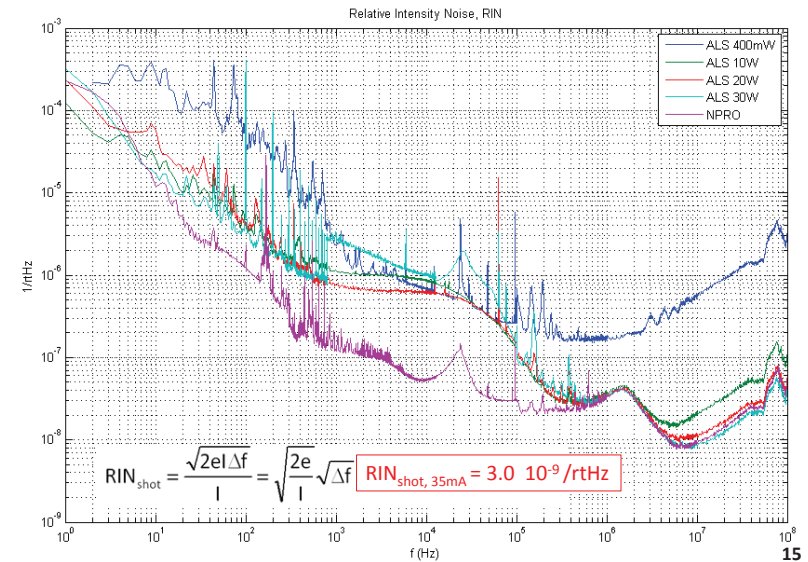


ASD/RIN Remarks, without Noise Eater

- The sensitivity of the RIN photodiode used was quite limited at $f > 10\text{MHz}$
- When the Noise Eater was OFF, no significant RIN increase in comparison with NPRO was observed at $f > 100\text{kHz}$
- Relaxation peak of NPRO-Artemis was seen at $\sim 450\text{kHz}$, which is different from the $\sim 650\text{kHz}$ of NPRO-EGO
- In general the ALS fiber amplifier possesses similar RIN performance to that of the Eolite fiber amplifier
- Unlike Nufern fiber amplifier, no excess 1-30MHz RIN was observed

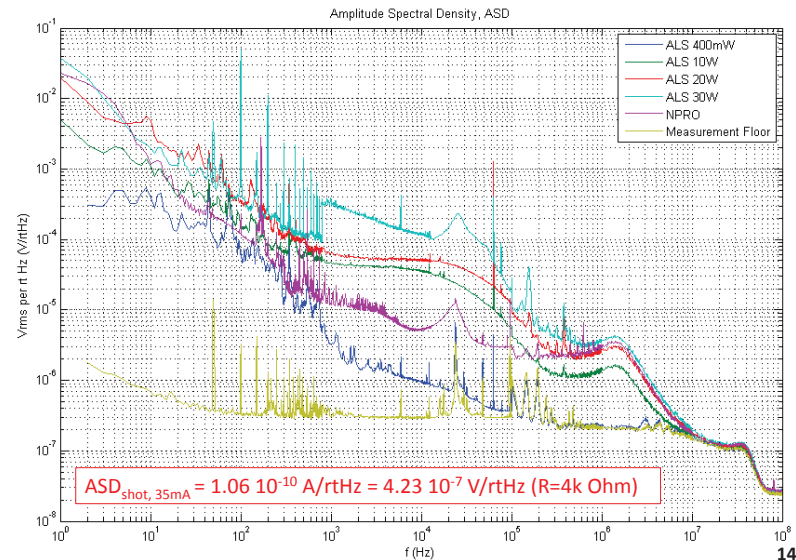
13

RIN Results, Noise Eater ON



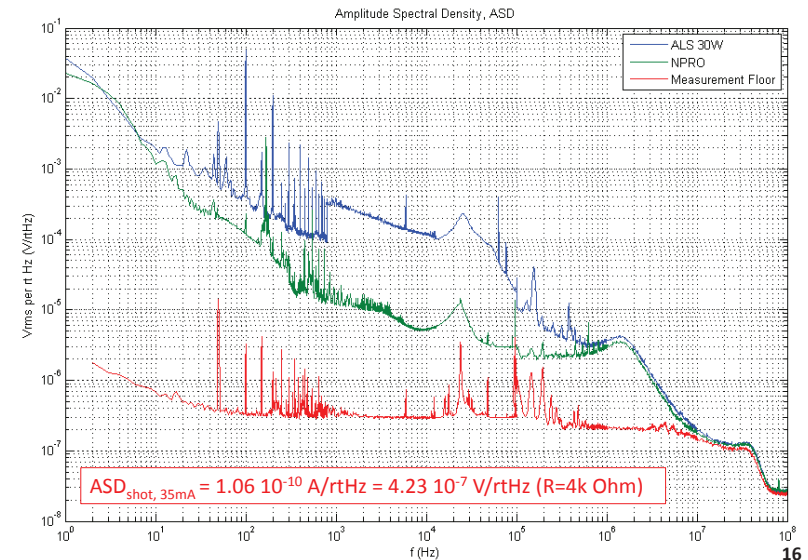
15

ASD Results, Noise Eater ON



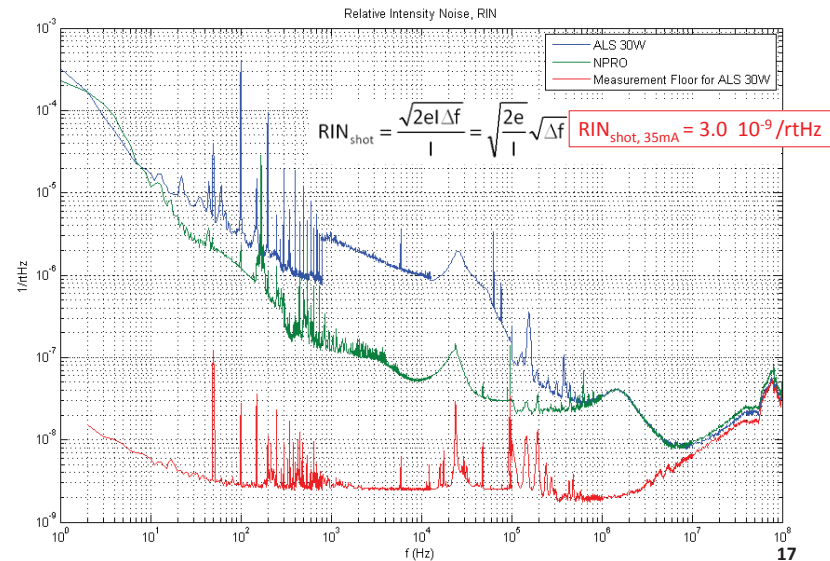
14

ASD Results at P=30W, Noise Eater ON



16

RIN Results at P=30W, Noise Eater ON



B) BEAM POINTING

19

ASD/RIN Remarks, with Noise Eater

- When the Noise Eater is switched on, more than ten times of excess RIN is observed at $f \sim 2\text{kHz}$
- The RIN level jump at $f = 800\text{Hz}$ is not a bug; it's physical
 - The RIN level for $f = [100\text{Hz}, 10\text{kHz}]$ at $P=30\text{W}$, with Noise Eater ON, fluctuate to up to a factor of about 5
 - The evolution was quite irregular. The RIN measurements shown here are all averaged results, but still, such a fluctuation can also be observed
- With Noise Eater ON, the RIN performance of the fiber amplifier is deteriorated

18

Beam Pointing Data Flow - Instrumental

- SR780
 - 800Hz/6.4kHz/102.4kHz, all in ASD units ($V_{\text{rms}}/\text{rtHz}$), SRTRANS v3.0 data conversion, without additional correction

20

Beam Pointing Data Flow – Derivation

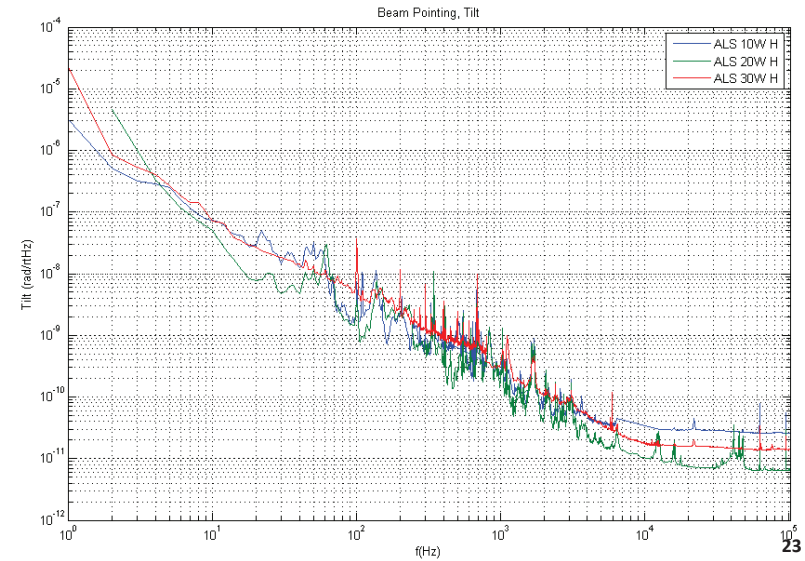
- H/V 1** The ASD data are converted into Meters with the following equation:

$$Tr: \text{Translation (m)} = ASD ./ (2 .* \text{sqrt}(2/pi) .* QPD_DC ./ \text{beamsize});$$
- H/V 2** Translation can be normalized with respect to laser beam size (λ). This results in the dimensionless beam pointing invariant, at least to the first order, of an optical system of lenses. (Frederic)
- H/V 3** By measuring the distance ($d=0.6\text{m}$) between the beam waist and the Quadrant Photodiode (QPD), the jitter can also be seen as

$$Ti: \text{Tilt (rad)} = Tr / d$$
- H/V 4** Tilt can further be normalized with respect to laser beam divergence. This results in the dimensionless beam pointing invariant, at least to the first order, of an optical system of lenses. (Frederic)
- H/V 5** Last, to be comparable with previous data, the V+ PMC tilt attenuation maybe introduced: $Att_H=0.0032, Att_V=0.017$

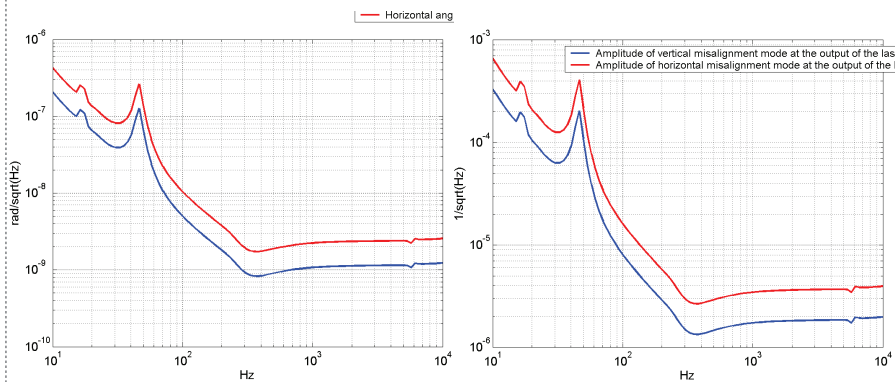
21

Beam Pointing Results – H3



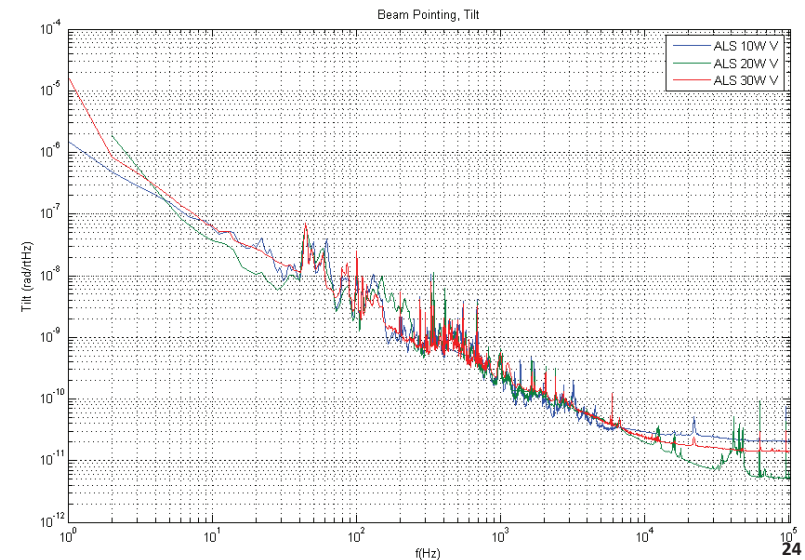
23

Beam Pointing – Adv Specs



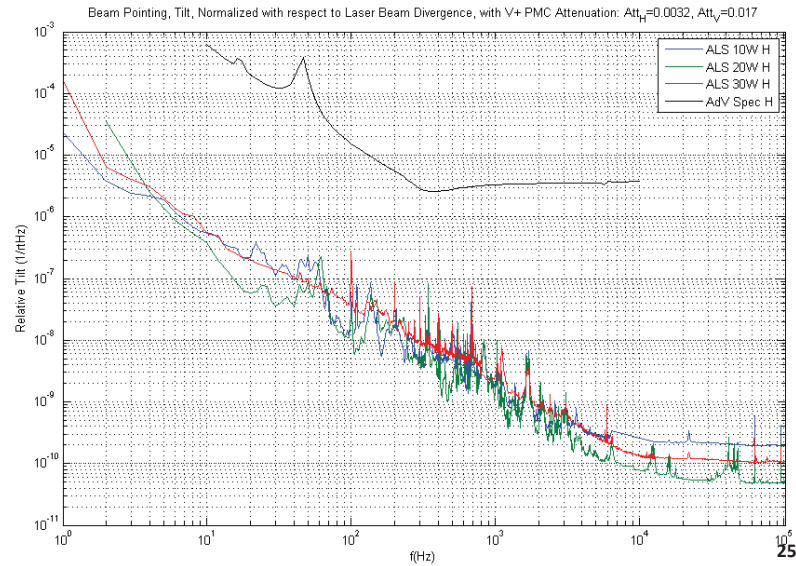
22

Beam Pointing Results – V3



24

Beam Pointing Results – H5



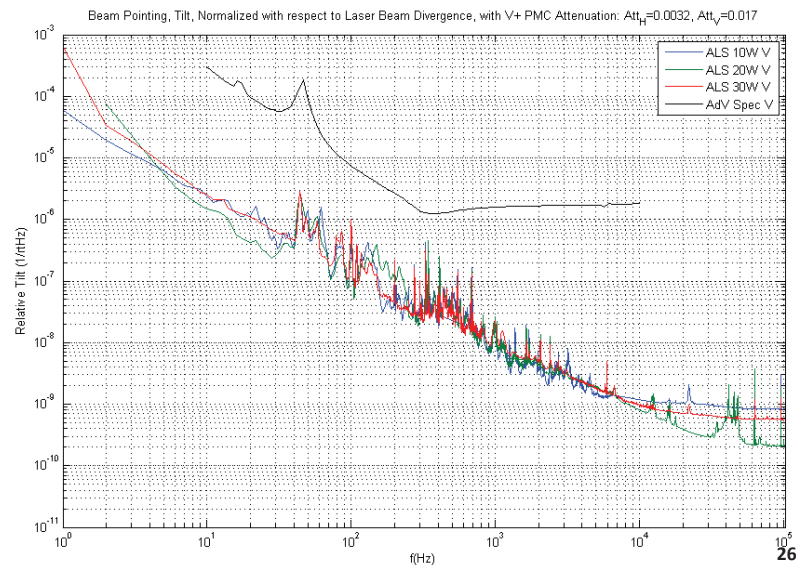
25

Beam Pointing Remarks

- Owing to the fact that only one quadrant photodiode was used, it is not possible to decouple translation and tilt beam jittering; here it is assumed that tilt is the dominating degree of freedom
- Laser beam waist after the fiber amplifier was measured by ALS to be 800um; this value, although might have changed during some adjustments of the output optics, is used in deriving beam jittering performance

27

Beam Pointing Results – V5

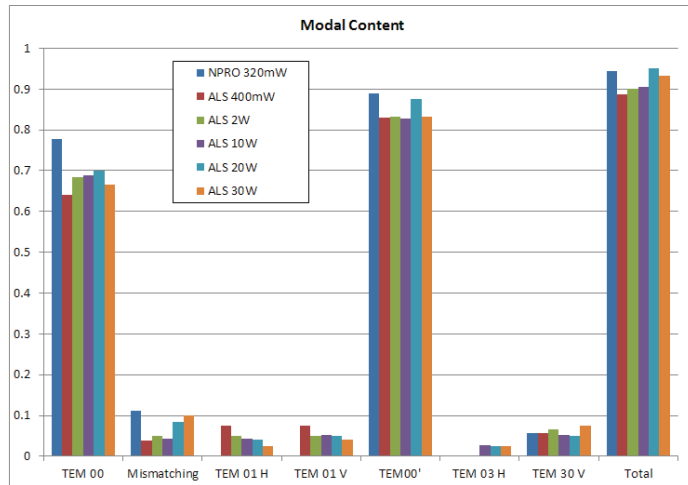


26

C) MODAL CONTENT ANALYSIS

28

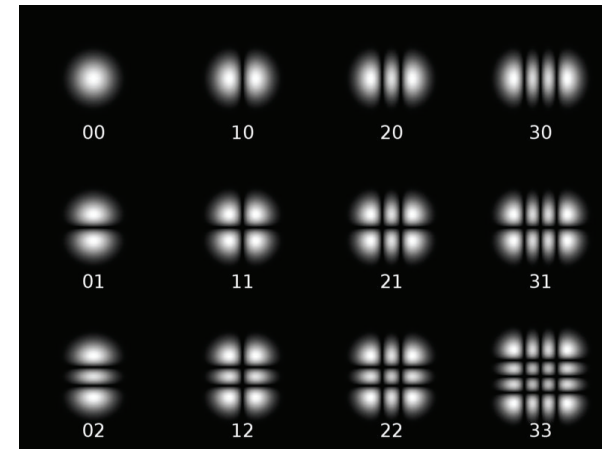
Modal Analysis



* TEM00' = TEM00 + Mismatching + TEM01 + TEM10

29

Modal Analysis



31

Modal Analysis

	TEM 00	Mismatching	TEM 01 H	TEM 01 V	TEM00'	TEM 03 H	TEM 30 V	Total	TEM00'/Total
NPRO 320mW	0.7778	0.1111	0	0	0.8889	0	0.0556	0.9445	0.9411
ALS 400mW	0.6415	0.0377	0.0755	0.0755	0.8302	0	0.0566	0.8868	0.9362
ALS 2W	0.6833	0.05	0.05	0.05	0.8333	0	0.0667	0.9	0.9259
ALS 10W	0.6897	0.0431	0.0431	0.0517	0.8276	0.0259	0.0517	0.9052	0.9143
ALS 20W	0.7	0.0833	0.0417	0.05	0.875	0.025	0.05	0.95	0.9211
ALS 30W	0.6667	0.1	0.025	0.0417	0.8334	0.025	0.075	0.9334	0.8929

* TEM00' = TEM00 + Mismatching + TEM01 + TEM10

- Measurement resolution is about 1.7% (0.1 div/6 div)
- Close to or more than 90% of accounted power falls into TEM00'
- Limited accounted power less than 100% might have come from cavity loss and spreading into negligible high order modes
- At high power, thermal lensing resulted in higher mismatching

30

32

Appendix C

Responsivity Maps of Excelitas C30665GH Photodiodes

The responsivity of a handful of 3 mm diameter photodiodes, C30665GH from Excelitas (formerly PerkinElmer), were mapped using the scanning setup driven by stepper motors described in Section 3.5 and Appendix D.

These photodiodes were delivered with protective glass windows. The glass windows were then removed with a can opener¹ under a high-efficiency particulate arrestance (HEPA) hood. Caution was taken to avoid dust contamination onto the photodiode surface, however, as seen in the following responsivity maps the dust particles are clearly present. The dust contamination most likely comes from the removal of the protective glass window.

There was no attempt in removing the dusts from these photodiodes as the wiring was so delicate that cleaning with pressurized air might cause damages. A previous attempt with First ContactTM damaged one of the two metallic wires and led to increased dark noise of the photodiode. Since the scanning setup would be too slow to make any cleaning attempt efficient, microscope objectives are used for more efficient inspections of the dust particles.

Two of the these photodiodes were integrated into the photodiode array for laser power stabilization in Advanced Virgo [116]. A mirror mounted on a piezoelectric actuator was used to induce beam displacements on the photodiode surface, calibrated with a quadrant photodiode, to measure the coupling factor κ at the center. The results are shown below for comparison:

Serial Number	2205	2621
κ_x	5.4	1.3
κ_y	6.8	2.0

We see that the results with the photodiode 2621 are more or less consistent, while those with the photodiode 2205 show considerable discrepancy. The reason for the discrepancy is unclear and requires further investigation.

¹Thorlabs, WR1, Laser Diode, Photodiode, and LED Can Opener, https://www.thorlabs.com/newgrouppage9.cfm?objectgroup_id=1830

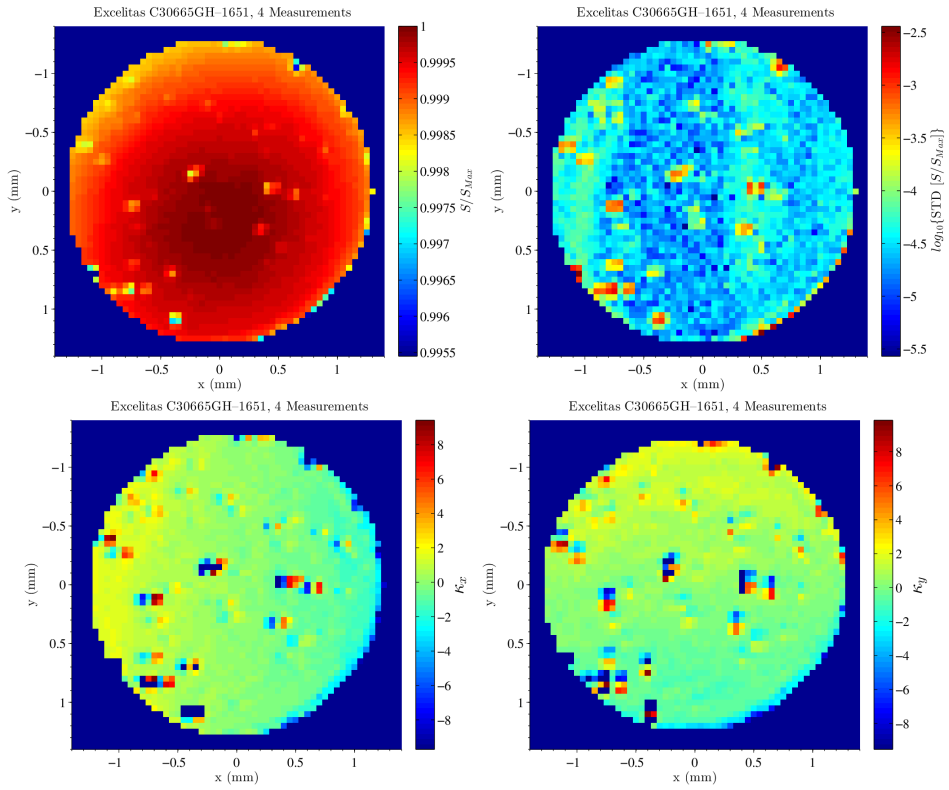


Figure C.1: Serial Number: 1651.

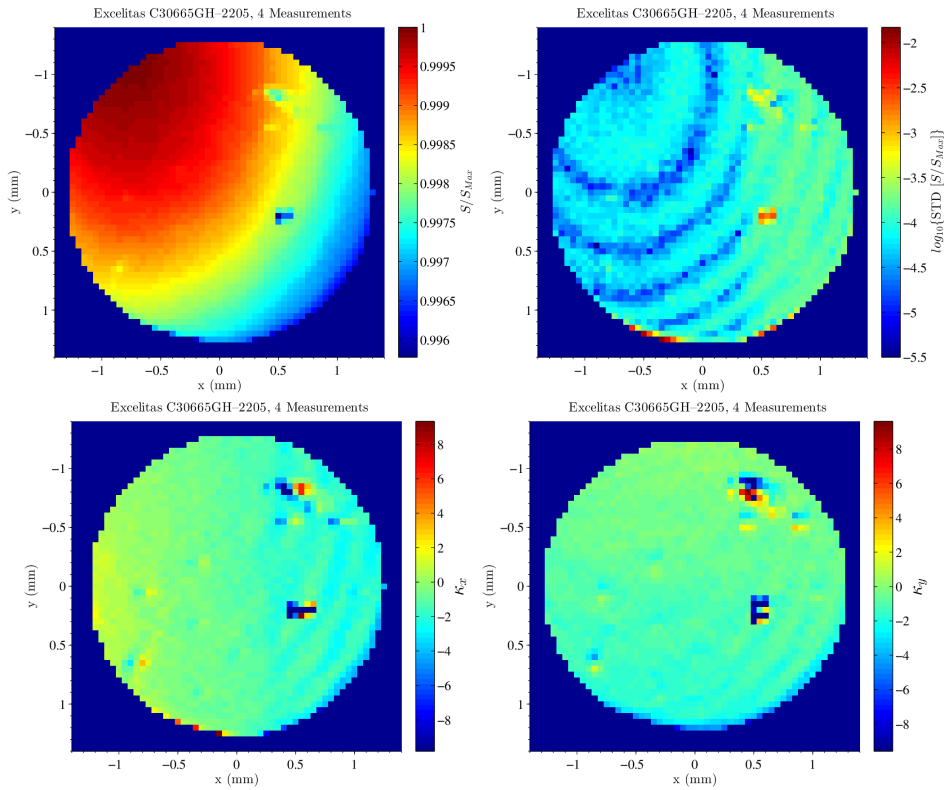


Figure C.2: Serial Number: 2205.

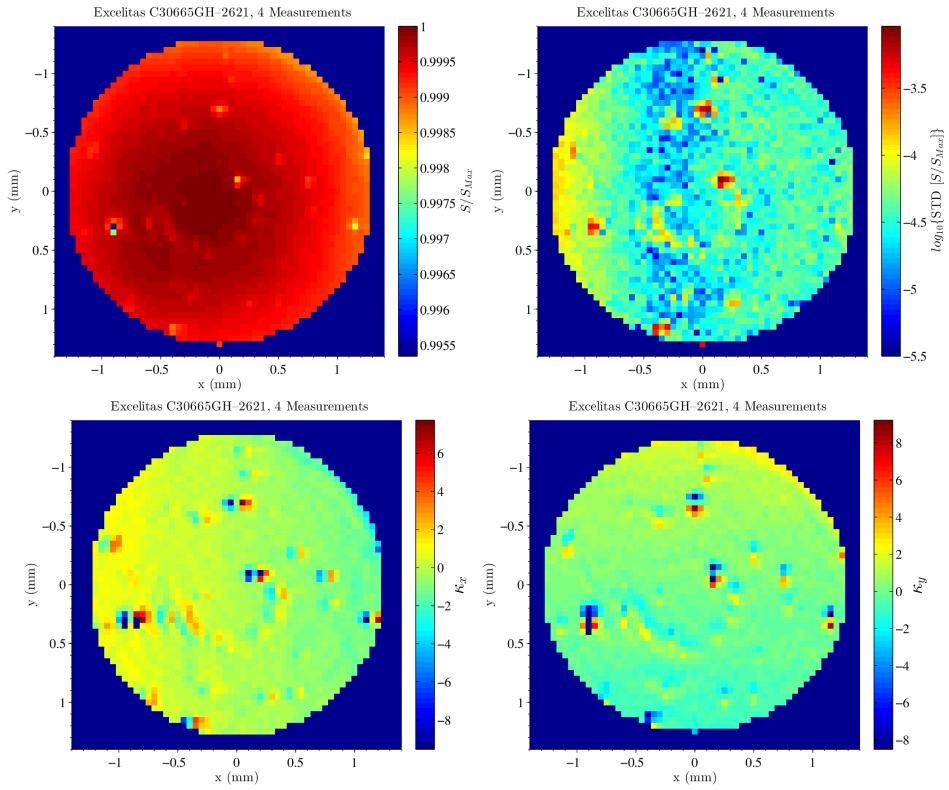


Figure C.3: Serial Number: 2621.

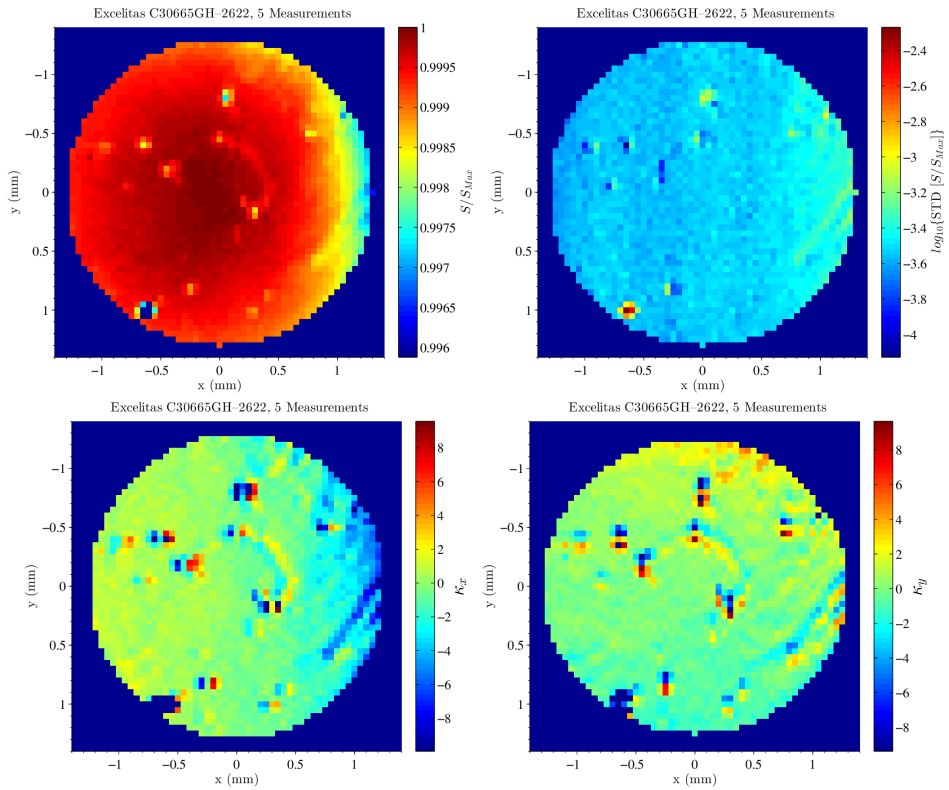


Figure C.4: Serial Number: 2622.

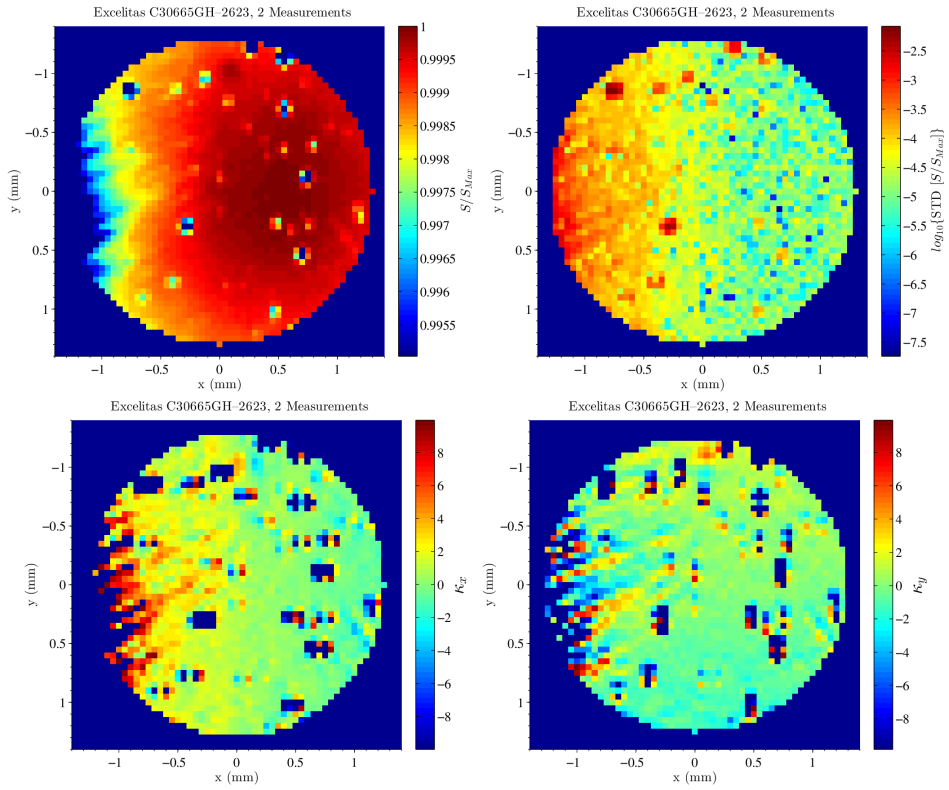


Figure C.5: Serial Number: 2623.

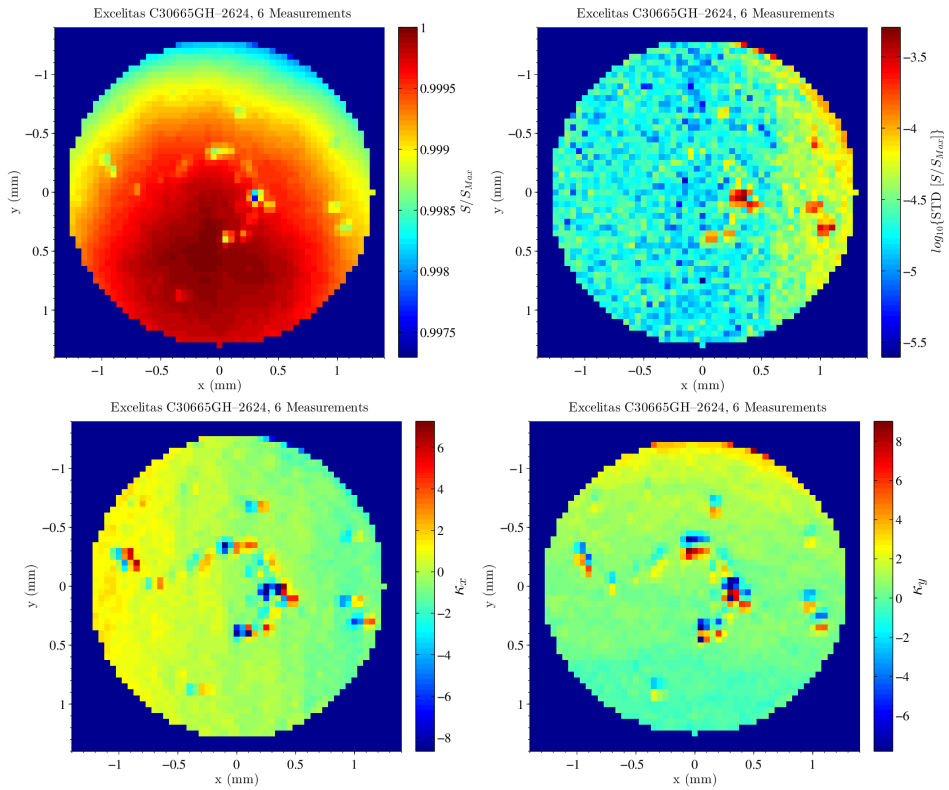


Figure C.6: Serial Number: 2624.

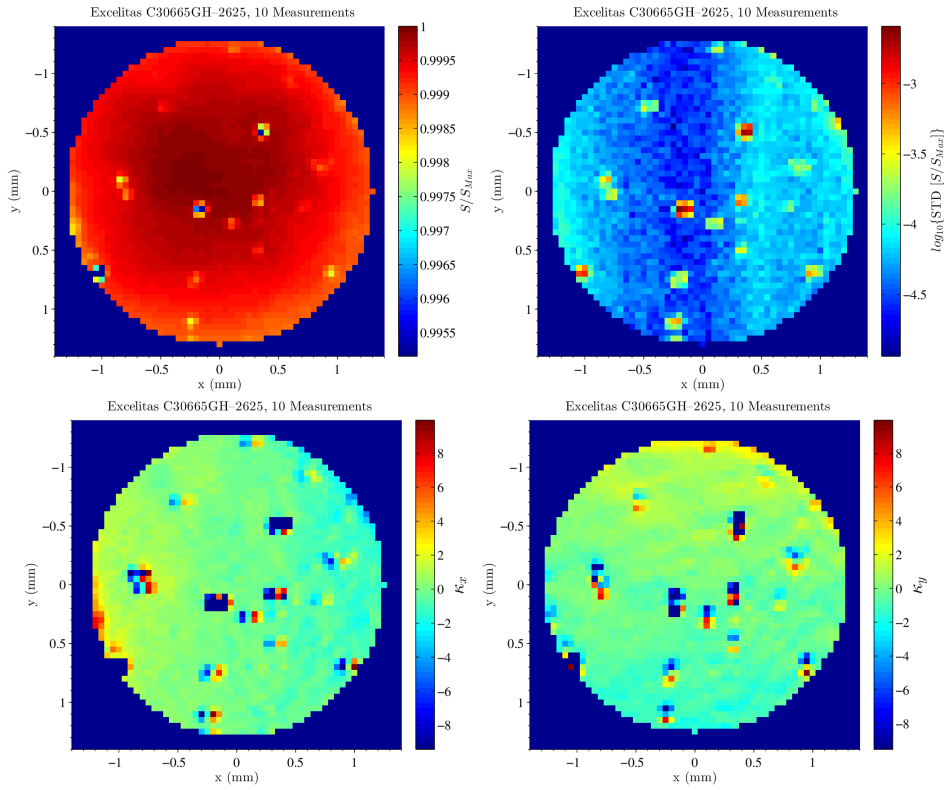


Figure C.7: Serial Number: 2625.

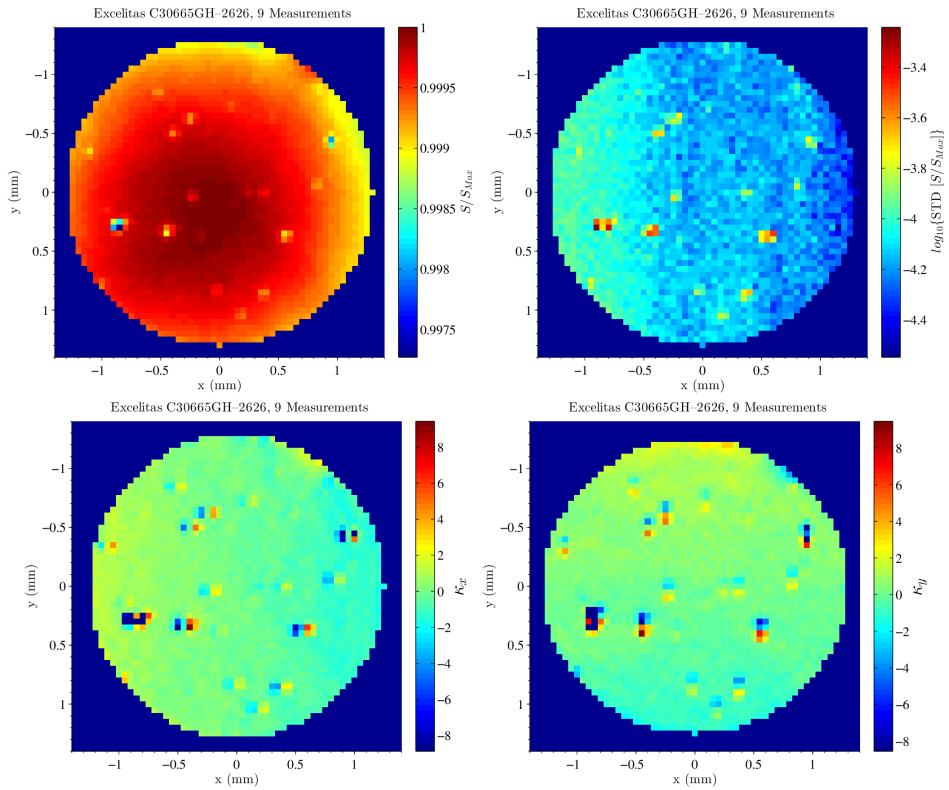


Figure C.8: Serial Number: 2626.

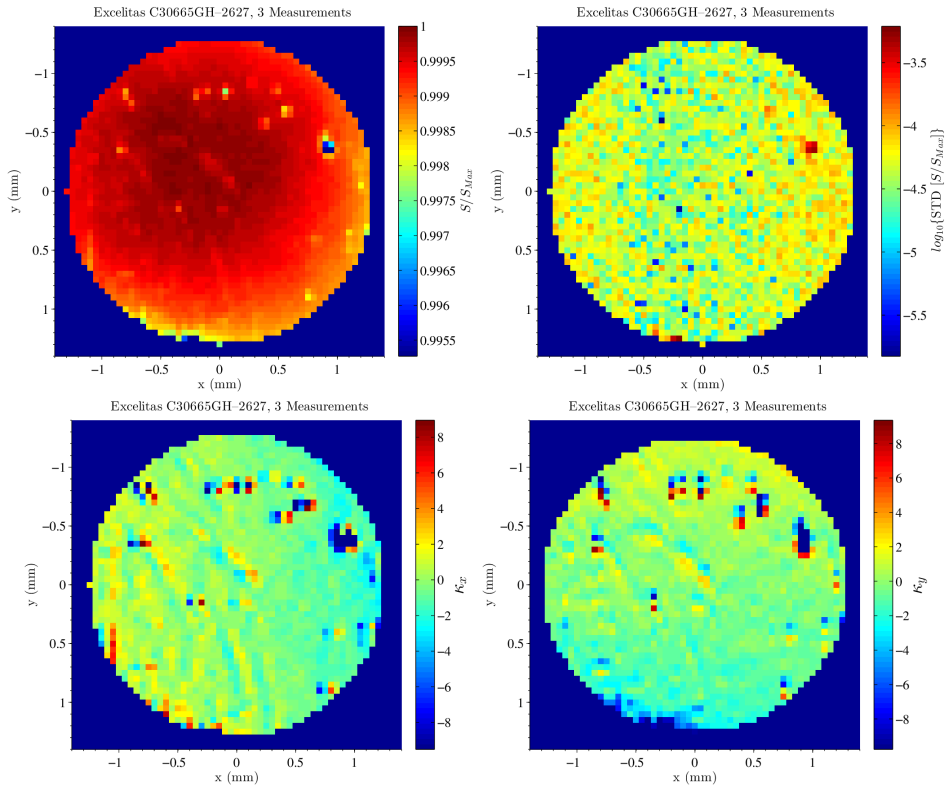


Figure C.9: Serial Number: 2627.

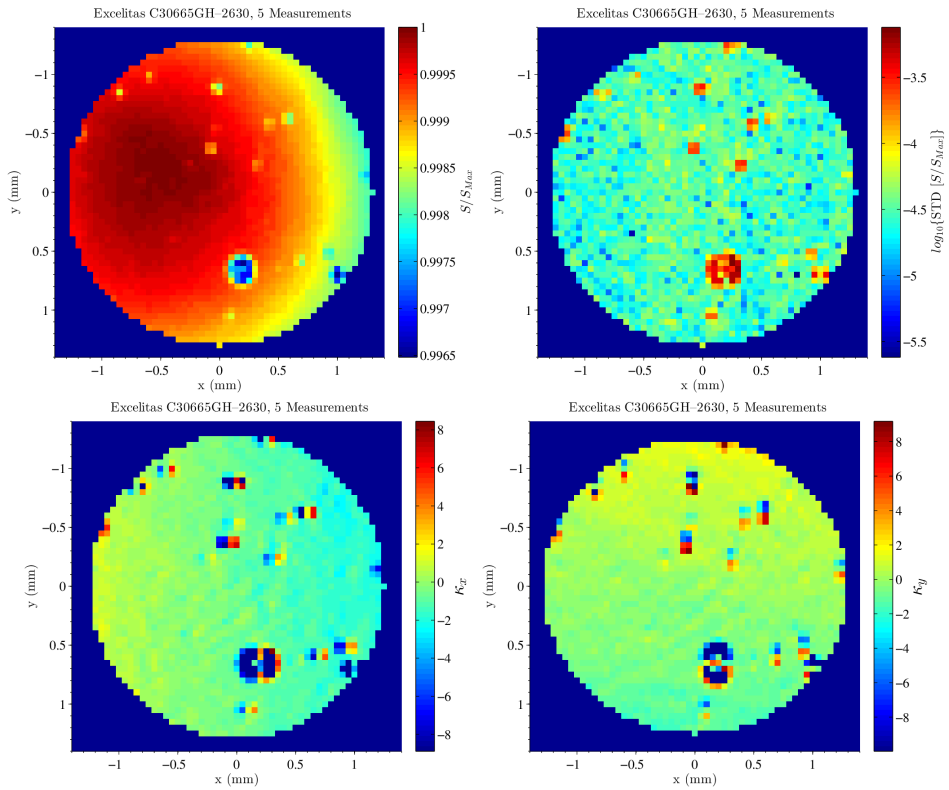


Figure C.10: Serial Number: 2630.

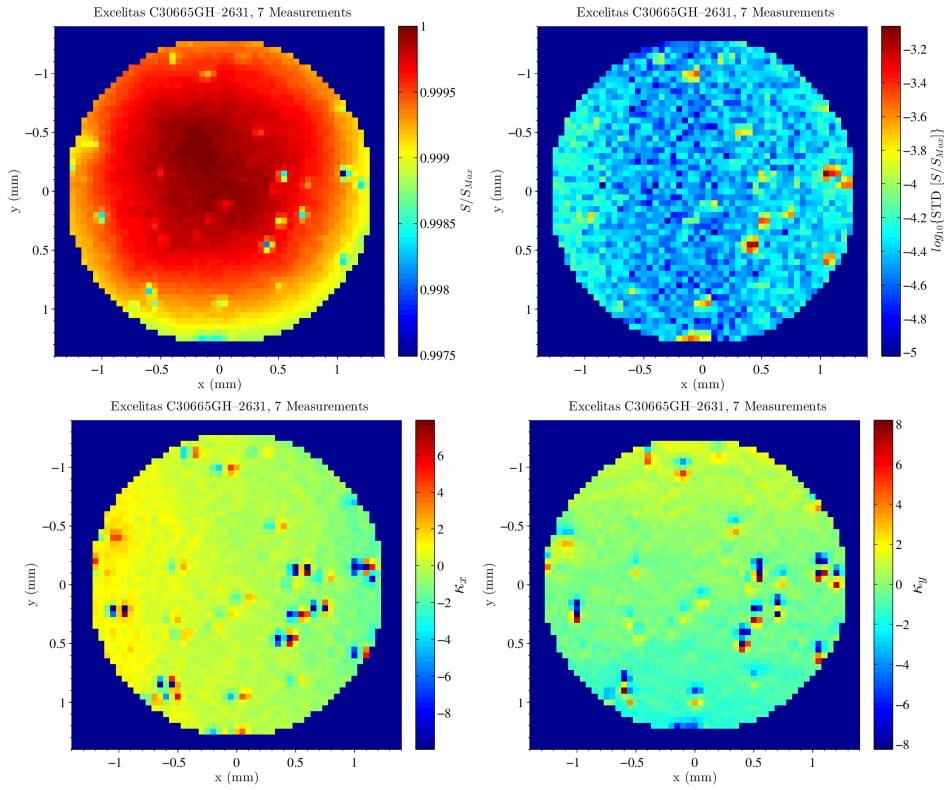


Figure C.11: Serial Number: 2631.

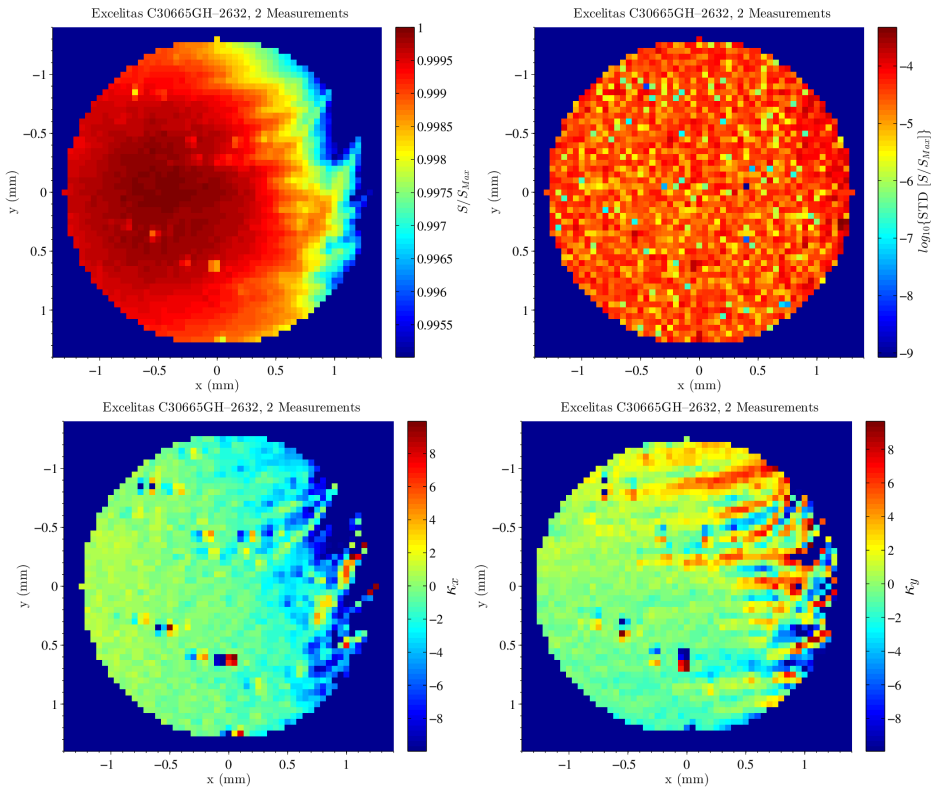


Figure C.12: Serial Number: 2632.

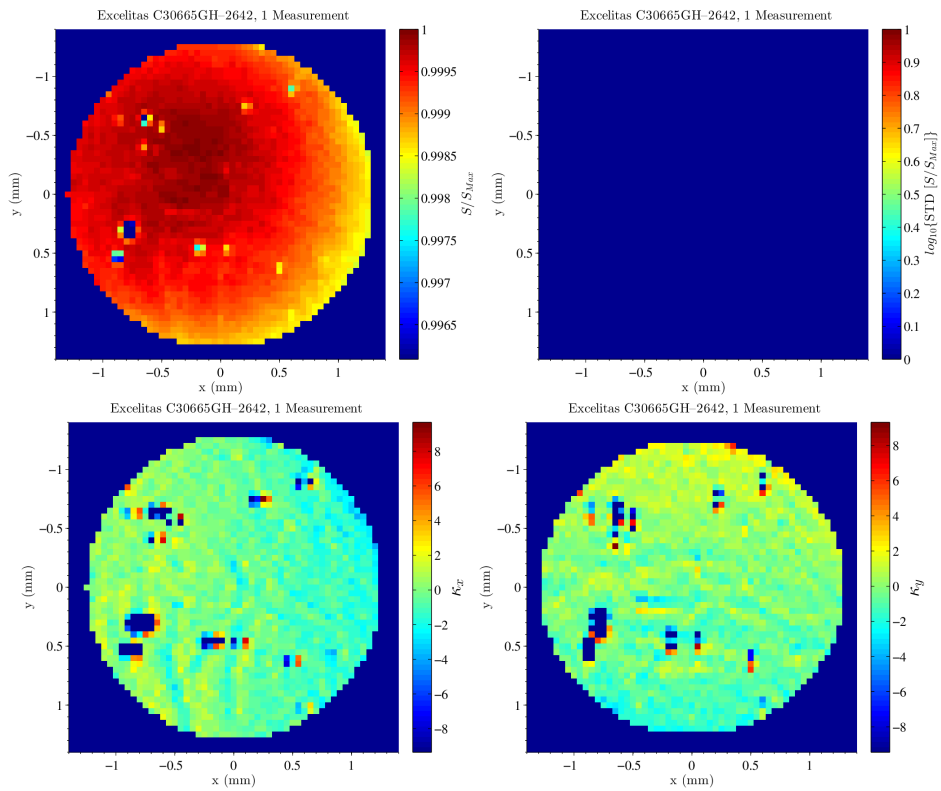


Figure C.13: Serial Number: 2642.

Appendix D

Mapping Photodiode Responsivity

The scanning setup was developed during a summer internship in 2010. The same setup, with subsequent adjustments and optimizations, was used to measure the spatially inhomogeneous responsivity of the photodiodes shown in Section 3.5. The internship report is attached for reference. Although the definition of κ is not strictly correct (should be normalized by R to result in unit m^{-1}) and the statistical analysis does not take into account the bias of the number of samples, the report should provide some additional information on the characteristics of the measurement setup.

Title

**Compensation of inhomogeneous responsivity
of the photodiodes used in the Virgo project**

Intern Student

WEI Li-Wei
aelo.tw@gmail.com

Supervisor

CLEVA Frédéric
cleva@oca.eu
+33 (0)4 92 00 31 97

Location

Observatoire de la Côte d'Azur
Département ARTEMIS
BP 4229
06304 NICE Cedex 4

Duration

May 24th – August 6th, 2010

Contents

- 1) Description of the internship
- 2) Experimental scheme
- 3) Progress and results
- 4) Discussions

1) Description of the internship

Please see Appendix A for general description (French).

The Virgo Project

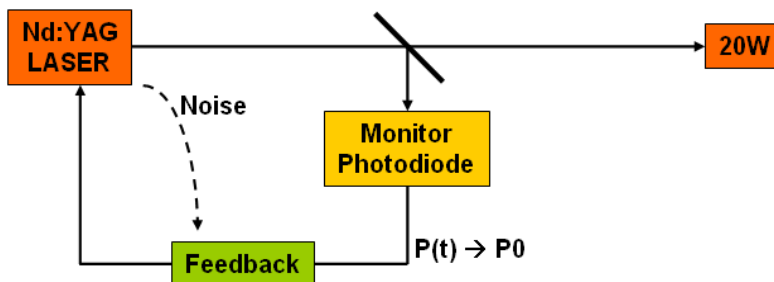
VIRGO is a Michelson interferometer built for the detection of gravitational waves. Its operation started in 2007 on the site of Pisa, Italy, and has reached nominal sensitivity of some $10^{-17}\text{m}/\sqrt{\text{Hz}}$ at 10Hz.

Advanced Virgo, an upgraded version of VIRGO to be operational from 2014, will impose improved sensitivity and increased stability of the power of the laser source, dP/P about few $10^{-9}/\sqrt{\text{Hz}}$ at 10Hz. Artemis works on the stabilized laser source, which is a injection-locked 20W YAG laser.

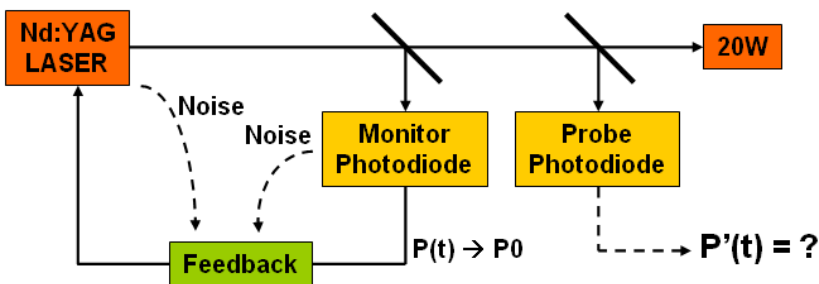
Reference: The Virgo Homepage - <http://www.virgo.infn.it/>

Issue

The power of the laser is stabilized through a feedback control loop.



With properly designed control circuit, the system can provide noise stabilization for frequencies up to 100 kHz. In addition to the intrinsic noise of the laser, an additional noise comes from the coupling between inhomogeneous responsivity of the monitor photodiode and the beam jittering of the laser beam; although this coupling is small, it is a concern for Advanced Virgo.



In the figure above, $P(t)$ read by the monitor photodiode (PHD1) can be made as stable as required assuming feedback is enough. But it is reported that by adding another probe photodiode (PHD2) to measure the power of the laser, one can find that $P'(t)$ is not as stable as expected from PHD1. This infers that some extra noise is introduced either at PHD1 or PHD2 level. For sure beam-jitter-to-inhomogeneity of the photodiode responsivity introduces noise at both photodiode levels. To overcome this

issue the possible solutions are either to find photodiodes with good homogeneity or to have a laser beam which shows low beam jitter. In Virgo, both methods are considered.

Photodiode Responsivity

By definition, the responsivity* of photodiode

$$R = \eta \frac{e}{E_{\text{photon}}} = \eta \frac{e}{h \cdot \nu} = \eta \frac{e}{h \cdot c} \lambda$$

η : quantum efficiency

e : charge of an electron

E : energy of photon

h : Planck's constant

ν : frequency of photon

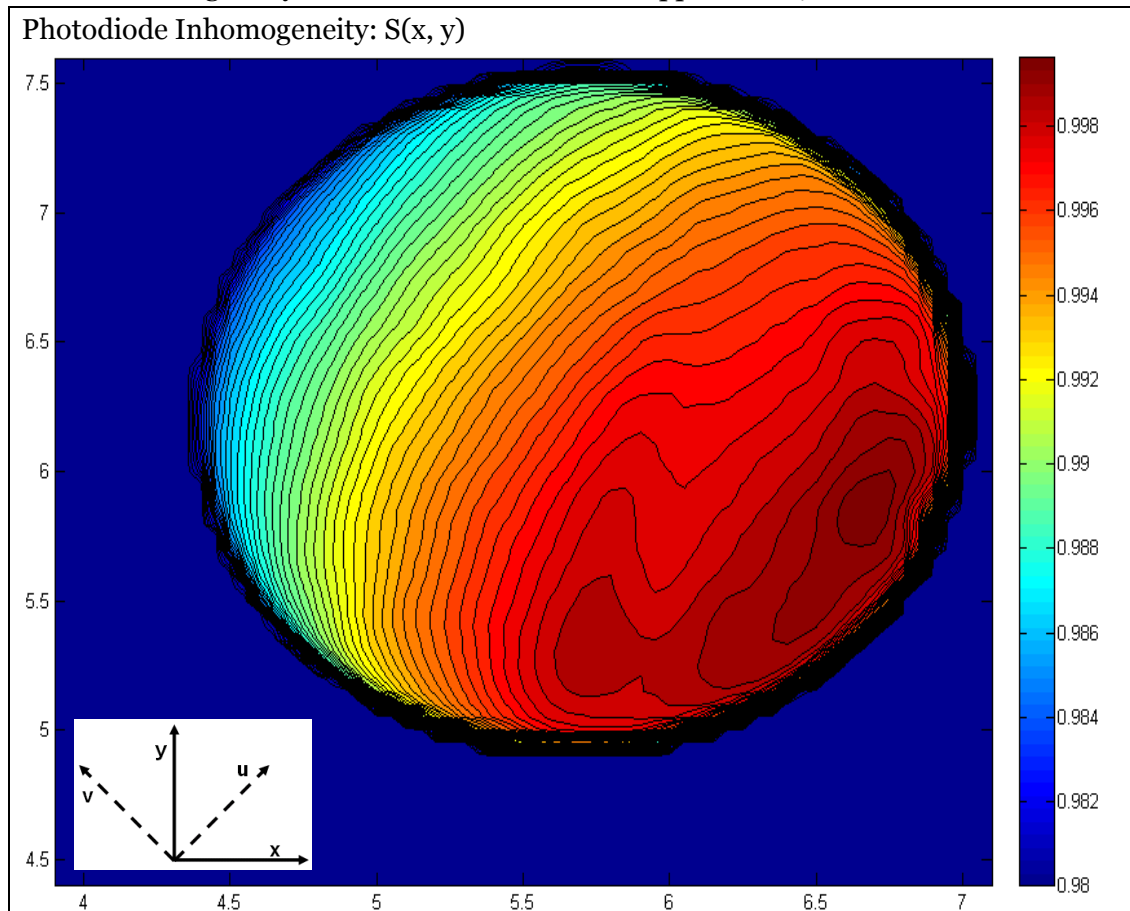
λ : wavelength of photon

**Responsivity* is sometimes expressed by the deprecated synonym *sensitivity*.

By nature, R is related to both properties of light, λ , and material, η . Moreover, resulting from the device design, the responsivity R can vary over the surface of the photodiode by a factor $S(x, y)$. Hence, one can write the responsivity as

$$R(\lambda, x, y) = S(x, y) \cdot \eta \frac{e}{h \cdot c} \lambda$$

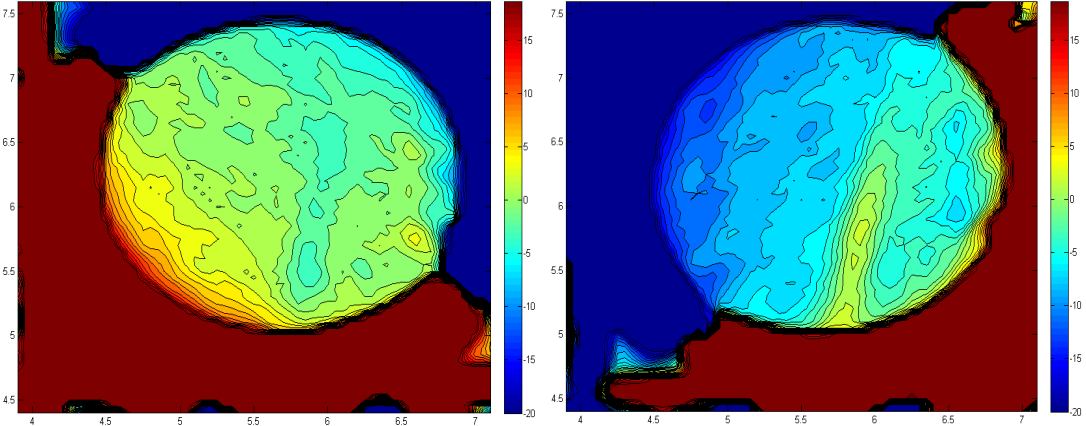
In which $S(x, y)$ denotes the inhomogeneity of the photodiode. Following is an example of such inhomogeneity from our measurements (clipped to [0.98 1]):



2D scan: Coordinates in mm
 Color map: Inhomogeneity S, normalized to [0, 1] then clipped to [0.98, 1]

We define the coupling factor $\kappa = \frac{\partial R}{\partial(x,y)}$, it has dimension m^{-1} ; κ is such that $dP/P = \kappa * \Delta$, where Δ is the beam displacement on the photodiode surface, dP/P is the relative power fluctuation induced by beam displacement Δ . We try to characterize the map by rotating (x, y) into another set of orthogonal axes (u, v) ; in the above example, u represents the axis for which $\kappa(u)$ is minimum and forms a set of orthogonal axes (u, v) together with v . This is useful since we know that in Virgo, beam jitter has two "natural", i.e. horizontal and vertical, components, with one of the two significantly less noisy. What might be interesting is to adjust the photodiode orientation to the "natural" axis of the beam jitter to minimize the coupling effect.

For example, $\kappa(u)$ and $\kappa(v)$ of the above map are (clipped to [-20 20] in m^{-1})



Legends: x, y coordinates in mm, z expressed in m^{-1}):

Beam Jitter

Both beam jitter and beam wander are related to the movement of the laser beam. Beam jitter accounts for faster varying movements. The frequency of interest in the Virgo project ranges from 10Hz to 10000Hz. Beam jitter caused by mechanical and seismic vibrations also lies in this range. In the Virgo setup, a mode cleaner (140m long plano-concave Fabry-Perot resonator) is used to provide pure TEM00 Gaussian mode at the output. It also reduces the magnitude of beam jitter by a factor of about 100. Before the mode cleaner, specifications on beam jitter are given that the shift is $1*10^{-7}m/\sqrt{Hz}$ and the tilt is $1*10^{-9}m/\sqrt{Hz}$.

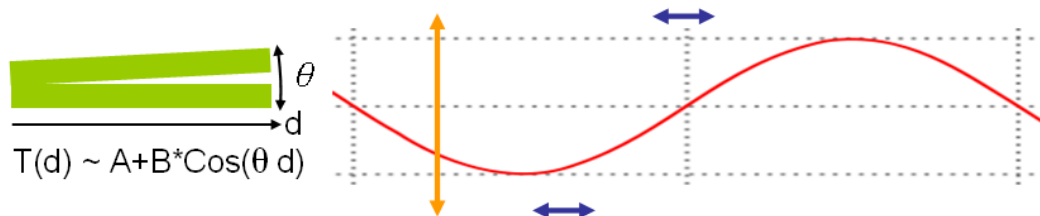
It is shown that the magnitude of beam agitation differs in two orthogonal axes as well (due to mechanical structure of the mount, seismic wave amplitude direction), which provides us some degrees of freedom in reducing the noise to the specification required as we can adjust the photodiode orientation such that the photodiode-axis along which

the photodiode responsivity varies less (minimum κ factor) is aligned with the beam-jitter-axis along which the beam jitter magnitude is the largest.

Possible Solutions

To obtain a truly-stabilized laser source, in view of the issue discussed above, we can work either to reduce the inhomogeneity of photodiode or to stabilize the laser beam. This internship sets its focus on the former. The task is to characterize the commercially available photodiodes of interest in Virgo's laser source stabilization, build a bank of data, analysis.

The second part of the internship is to compensate and reduce the inhomogeneity possibly by designing a so-called optical 'compensators' described below: Provided that the inhomogeneity was in the form of simple curves (i.e. $\kappa \sim \text{constant}$), one proposed compensator is to take advantage of the interference between wedged glasses.

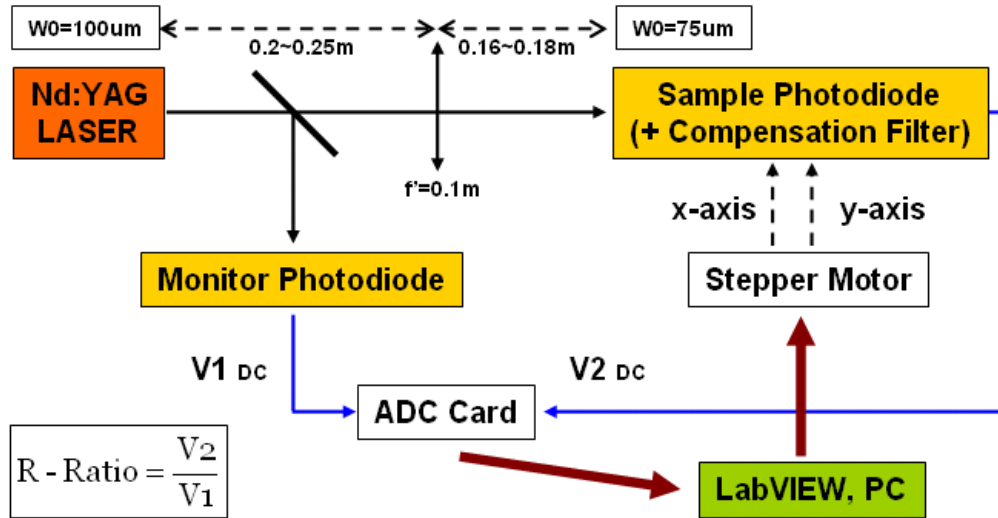


By tuning θ and the reflectance of the surfaces, we can modulate the transmittance in the form of $A+B*\cosine$, and then choose the proper region that best fit the inhomogeneity such that $T(x, y) * R(x, y) = \text{Constant}$.

We set the goal to compensate the photodiode inhomogeneity to $\kappa' < 1 \text{ m}^{-1}$, which is compatible with the laser stability requirement:

$$\begin{array}{lcl} \text{Laser Stability} & = & \text{Beam Jitter} \quad / \quad \text{Attenuation by the mode cleaner} \quad * \quad \kappa' \\ 1*10^{-9} / \sqrt{\text{Hz}} & = & 1*10^{-7} \text{m} / \sqrt{\text{Hz}} \quad / \quad 100 \quad * \quad 1 \text{ m}^{-1} \end{array}$$

2) Experimental scheme



We use a beam-splitting scheme. The monitor photodiode is kept constant while the sample photodiode is being translated.

The R-Ratio between V2 and V1 gives a relative responsivity map (inhomogeneity) of the sample photodiode. We test the temporal stability of the system by keeping both photodiodes static.

Instrumentation

Stepper Motor: Newport TRA12PP x2 driven by SMC100PP

Specifications	
Resolution	0.0977 μm
Minimum Incremental Motion	0.1 μm
Unidirectional Repeatability	2 μm
Hysteresis	12 μm
On-Axis Accuracy	6 μm

The main concern here is the repeatability of about 2 μm , which is about 2% when compared with the 100 μm -step scan resolution we foresee.

ADC Card: Measurement Computing PCI-DAS1000 (12-bit)

Specifications	
Resolution	12 bits
Input Ranges	$\pm 10, \pm 5, \pm 2.5, \pm 1.25$ $0 \sim 10, 5, 2.5, 1.25 \text{ V}$
Relative Accuracy	$\pm 1.5 \text{ LSB}$
Rate	1 - 250 kHz
CMRR @ 60 Hz	70 dB

Target Resolution: 10^{-5}

The compensation on inhomogeneity is targeted at $\kappa' < 1 \text{ m}^{-1}$. The photodiodes of interest have circular areas with 3mm diameter. We wish to obtain 2-D responsivity maps in steps of $\delta = \delta x = \delta y = 100\mu\text{m}$, which is compatible with the focused laser beam width.

$\kappa' (=1 \text{ m}^{-1}) * \delta (=100\mu\text{m}) = 1*10^{-4}$ gives the required relative resolution for our scheme. For an SNR of 10, $1*10^{-5}$ relative resolution is targeted on the R-Ratio measurement.

Concerns

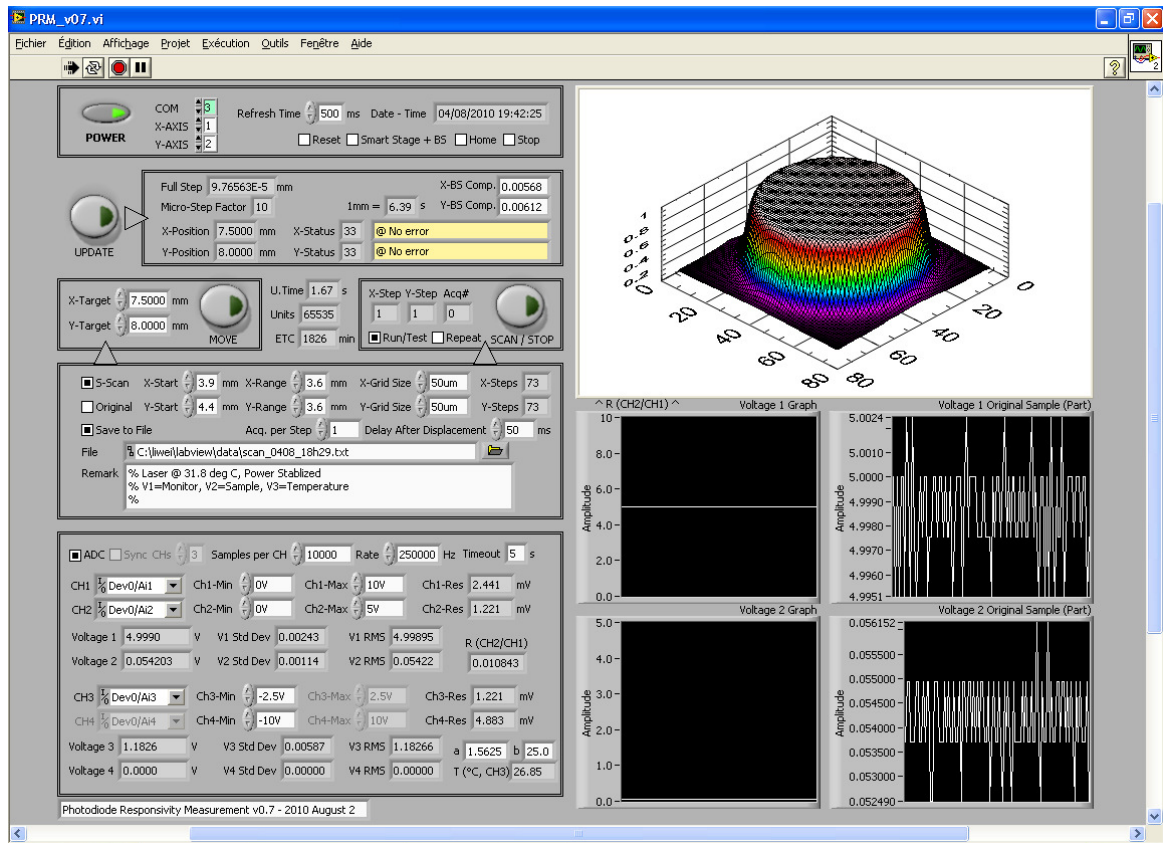
The relative resolution of the 12-bit ADC card (best case) is $1/4096 = 2.44*10^{-4}$. We use over-sampling to increase the resolution. Amplifiers are considered when further resolution is required.

Estimated scanning time for a responsivity map is around 2 hours. Temporal stability of the system with a span of 2 hours is taken into account.

3) Progress and results

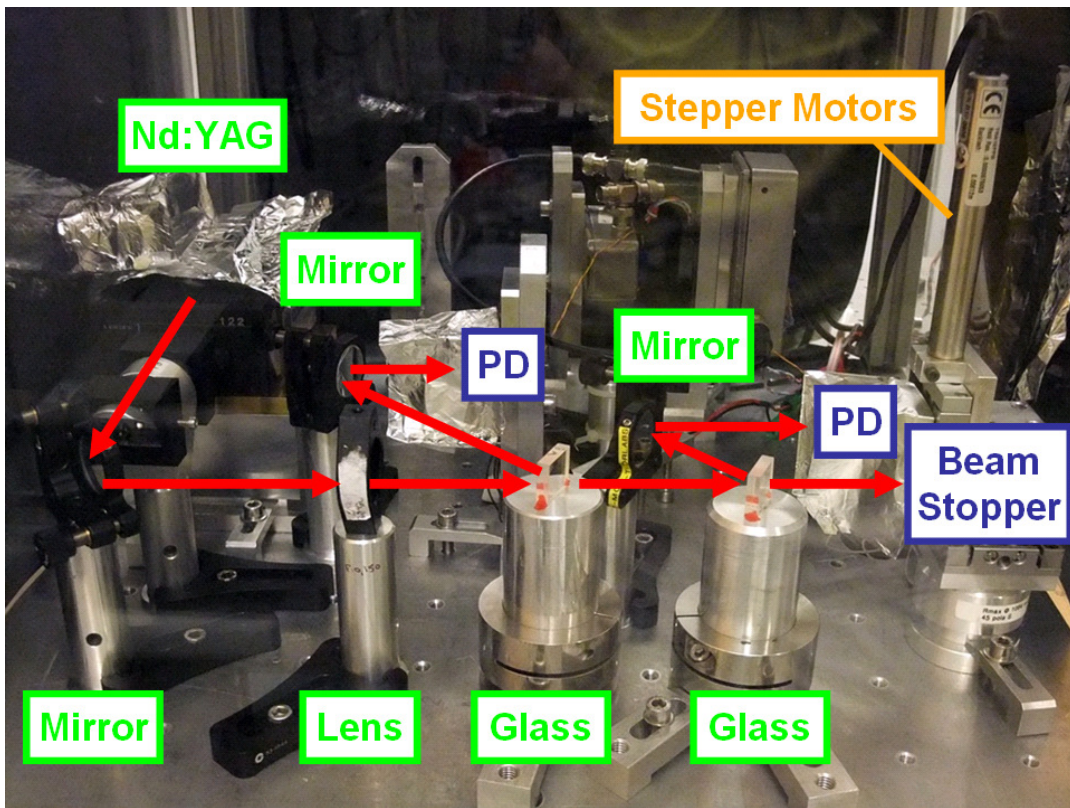
First of all I spent my time on getting familiar with the stepper motors and the ADC card and bringing them to LabVIEW's VI interface through the libraries provided by the manufacturers. One notable problem I had was the different decimal point notations between US and Europe, which was trivia but stuck me until I looked into the libraries themselves.

The final version of the VI looks like this (Front panel, August 2nd):

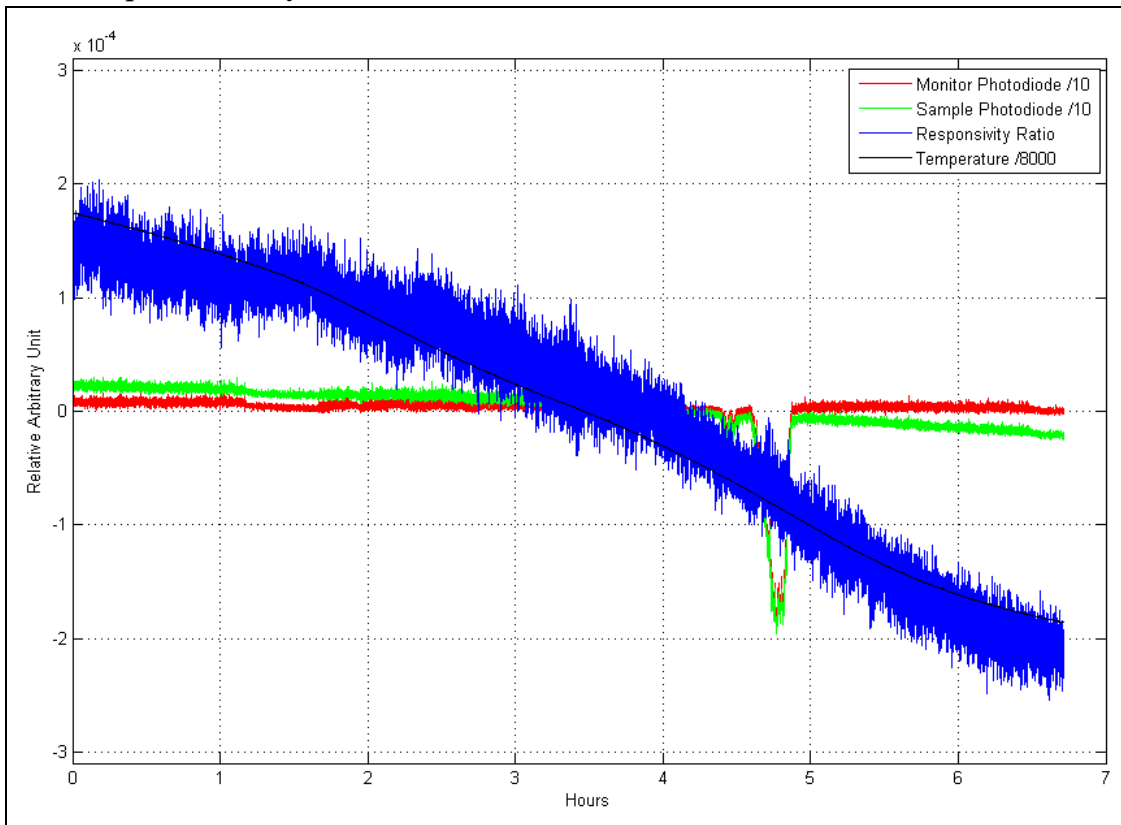


After prototyping the VI (around June 16th), I installed the proposed optical setup. The system was thus ready, but before going onto real measurements we first tried to characterize the performance/stability of our system. Indeed we faced some difficulties in stabilizing the optical beam-splitting setup. We changed the optical setup a few times trying to improve (mostly the supervisor's effort). Changes included the stabilization of the laser, the beam-splitting components (in the end simply glass plates were used), balancing the power of each beam, the type of photodiode material, taking off the protective windows of the photodiodes, thermal/ventilation isolation of the system with a darkened plastic cover, etc.

During this period of time some parameters of the system such as ADC crosstalk, common-mode rejection ratio, coupling factor of laser power/polarization to the signal were also studied. The final real setup is as follows:



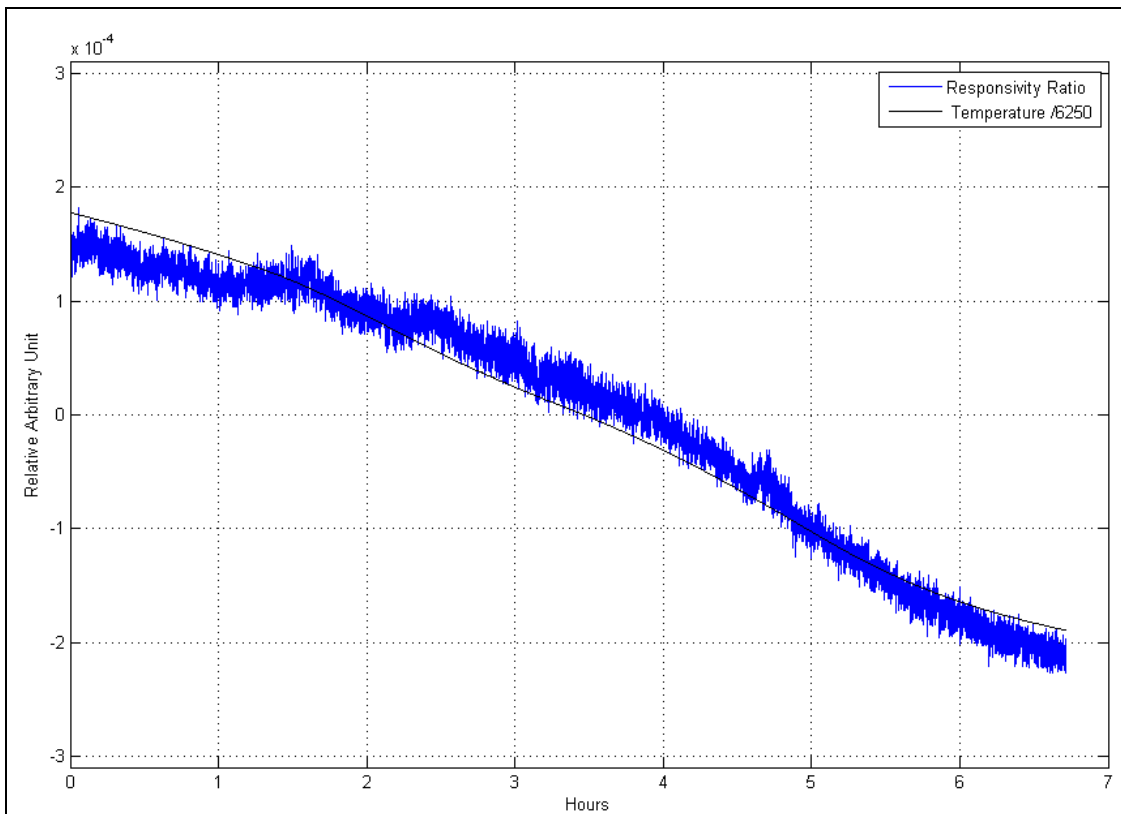
With temporal stability shown as follows (Plot1 & Plot2):



-- Plot1, Legends --
 RED: Monitor Photodiode (laser feedback control)
 GREEN: Sample Photodiode
 BLUE: Responsivity Ratio (Sample/Monitor)
 Timeline in hours

We can see that in this measurement (Plot1) the laser power is stabilized within 1×10^{-4} . In principle, since we are measuring the ratio between the voltages of the photodiodes, laser power fluctuation will not influence the results, but we have seen it is safer to deal always with the same working point at each level of the monitoring chain to improve stability.

The stability of the system is within 1×10^{-4} within 2 hours. We note that apart from the slow varying fluctuations, fast varying fluctuations have a magnitude of 7×10^{-5} , but in this particular case, averaging over more samples will improve resolution following a $1/\sqrt{\text{Number of Samples}}$ law, as seen in Plot2, at the expense of a longer measurement.



-- Plot2 --
 Plot2 gives responsivity ratio (plotted in Plot1) with a sweeping average on 4 samples.

In Plot2, the average over 4 times more samples than in Plot 1 reduces fast signal fluctuation by a factor of 2, and we get a responsivity ratio with root-mean-square value of about 3×10^{-5} (as far as fast fluctuations are concerned). That means a resolution of about 0.6 m^{-1} for $50 \mu\text{m}$ steps.

If we consider longer time period, fluctuations on responsivity ratio are about $1 \cdot 10^{-4}$ over a couple of hours; assuming that the "xy" scan of the beam onto the photodiode is of "S" shape, lasts about 2 hours for a 3mm-side square map, and $60 \cdot 60$ measurement points, it means that, between 2 adjacent measurements (step of $50\mu\text{m}$), it lasts either $2\text{hr}/(60 \cdot 60) = 2\text{sec}$ (from step "i" to step "i+1"), or (less than) $2\text{h}/60 = 120\text{sec}$ (from step "i" to step "i+61": due to "S" shape scanning).

RMS fluctuations over 2 seconds stay within $3 \cdot 10^{-5}$; RMS fluctuations over 120 seconds also stay within $3 \cdot 10^{-5}$, to which we have to add a deterministic fluctuation of $1 \cdot 10^{-4} / 2\text{hr} \cdot 120\text{sec} / 50\mu\text{m} = 0.033 \text{ m}^{-1}$, due to the overall trend of the Sratio signal; the residual K obtained (0.033 m^{-1}) is quite negligible compared to noise induced by fast fluctuations.

As a preliminary conclusion, we reached a resolution of about 6 m^{-1} (SNR=10), for typical measurements lasting 2hours, on $60 \cdot 60$ steps of $50\mu\text{m}$. Increasing further the resolution would be possible at the expense of longer measurement. We decided to go on to real measurements for that the inhomogeneity of photodiodes ($\kappa \sim 6$) will still be measurable (SNR~10) with our setup. The first scan took place on July 22nd.

With the data, some MATLAB codes were developed to visualize/analyze/process the data, and also to simulate the effect of possible tunings. Optimization of the compensator configuration was also undertaken but yet not thoroughly studied. After accumulating some sets of data, we tried to evaluate the performance (repeatability) of our system. To quantify the results, we calculate the standard deviation according to the following formula:

$$\sigma = \left(\frac{1}{m} \sum_i \frac{1}{n^2} \sum_{x,y} [R_i(x,y) - \overline{R}_i(x,y)]^2 \right)^{\frac{1}{2}}$$

m: number of responsivity maps $R(x, y)$
 n: number of steps in x and y
 Average(R) is the average on parameter i:
 same point (x, y) on surfaces 1 to m.

We have 9 sets of data which were taken consecutively in 3- 2- 4- sets:

C1	C2	C3
06_scan_0308_19h39.txt	09_scan_0408_09h30.txt	11_scan_0508_08h55.txt
07_scan_0308_21h44.txt	10_scan_0408_11h35.txt	12_scan_0508_10h55.txt
08_scan_0308_23h43.txt		13_scan_0508_12h55.txt
		14_scan_0508_14h54.txt

We also have 4 sets of data taken individually:

Co	I1: 01_scan_3007_08h18.txt	I2: 02_scan_3007_11h50.txt
	I3: 03_scan_3007_15h54.txt	I4: 04_scan_0308_10h40.txt

The scans and acquisitions were performed with the following parameters. Stepper motors: S-Scan (motor scans forth and backward in vertical axis); Area = 3.2mm * 3.2mm; Step size = 50 μ m; Motor speed = 6.39 seconds/mm (0.156mm/s). ADC card: 10000 sample acquired at each point (x, y) @ rate = 250 kHz; Time delay after displacement = 50 ms; Dynamic range/Resolution = 0-10V/2.44mV for monitor photodiode and 0-5V/1.22mV for sample (probe) photodiode. Each scan took two hours.

We note that 50- μ m step size was used instead of the original 100- μ m framework. This is because we found that 100- μ m was not sufficient to characterize the surface details of the map.

Each set of data is normalized to [0, 1] with respect to its own maximum and minimum. To focus on the region of interest, we apply concentric circular masks with different sizes (points outside the masks are not taken into calculation of σ).

The results are:

Mask radius/ σ	σ_R (C0)	σ_R (C1)	σ_R (C2)	σ_R (C3)	σ_R (C1+C2+C3)	σ_R (C0+C1+C2+C3)
No Mask	0.0060	0.0012	0.0027	0.0033	0.0045	0.0057
1.5 mm	0.0049	9.8074E-4	0.0024	0.0030	0.0039	0.0048
1.4 mm	0.0014	2.8682E-4	7.9402E-4	0.0010	0.0012	0.0014
1.3 mm	1.6686E-4	3.5108E-5	7.7474E-5	1.0797E-4	1.2709E-4	1.4862E-4
1.2 mm	1.2554E-4	2.0964E-5	2.2114E-5	4.7450E-5	5.9054E-5	8.9292E-5
1.1 mm	1.1656E-4	2.0440E-5	1.6642E-5	4.7215E-5	6.1600E-5	8.6459E-5
1.0 mm	1.1070E-4	1.7952E-5	1.5524E-5	4.7190E-5	5.6379E-5	8.1438E-5

We take the uncertainty of our measurement as 2σ at 80% of the radius of the photodiode to avoid possible edge effects, and with the sets C1+C2+C3 which were measured in a more systematic way. In this case, the uncertainty in R is $1.2 \cdot 10^{-4}$.

However, since the specification required is given in κ ($< 1m^{-1}$), it is more practical to convert our results from R to κ (in two orthogonal directions x-horizontal and y-vertical).

K for x - Horizontal Axis

Mask radius/ σ	$\sigma_{\kappa x}$ (C0)	$\sigma_{\kappa x}$ (C1)	$\sigma_{\kappa x}$ (C2)	$\sigma_{\kappa x}$ (C3)	$\sigma_{\kappa x}$ (C1+C2+C3)	$\sigma_{\kappa x}$ (C0+C1+C2+C3)
No Mask	44.2086	10.5914	19.6964	24.9559	35.7014	42.9286
1.5 mm	60.3355	12.2422	26.6626	34.2958	47.9448	57.6650
1.4 mm	18.3963	3.7798	10.3709	13.3415	16.2844	18.2590
1.3 mm	1.4233	0.4409	0.9993	1.3683	1.5916	1.6305
1.2 mm	0.5558	0.2240	0.2266	0.2961	0.3306	0.4342
1.1 mm	0.5404	0.2165	0.1939	0.2952	0.3282	0.4260
1.0 mm	0.5337	0.2088	0.1934	0.3023	0.3280	0.4272

K for y - Vertical Axis

Mask radius/ σ	$\sigma_{\kappa y}$ (C0)	$\sigma_{\kappa y}$ (C1)	$\sigma_{\kappa y}$ (C2)	$\sigma_{\kappa y}$ (C3)	$\sigma_{\kappa y}$ (C1+C2+C3)	$\sigma_{\kappa y}$ (C0+C1+C2+C3)
No Mask	28.6168	6.3474	13.0050	14.0162	19.5996	28.1715
1.5 mm	43.1980	9.3600	20.8523	23.5193	32.5558	42.4717
1.4 mm	16.0545	3.4053	8.6015	10.6643	12.9445	16.0681
1.3 mm	1.3250	0.3819	0.8485	1.1424	1.3095	1.4199
1.2 mm	0.6399	0.2076	0.1993	0.2563	0.2937	0.4546
1.1 mm	0.6057	0.2068	0.1743	0.2558	0.2986	0.4401
1.0 mm	0.5684	0.2029	0.1736	0.2672	0.2980	0.4239

In the same manner we have the uncertainty in $\kappa-x = 0.66$ and the uncertainty in $\kappa-y = 0.58$. We took the largest number of measurement (C1+C2+C3 sets) in order to get a larger population on which the statistics were made.

The minimum signal to be measured is $\kappa' = 1 \text{ m}^{-1}$, which is our goal on compensation. With the above repeatability statistics, our setup reaches an SNR = 1.5; this is more or less compatible with our temporal stability test (without further averaging) where SNR = 1. This implies that no significant perturbations were introduced by the scanning displacements and the performance of the system shall depend mostly on the temporal stability of the system. This must be extended to a larger set of data to increase the population on which we make our statistics; however, at this point we are confident that the performance is limited by temporal stability rather than positioning error of the beam onto the photodiode.

Owing to limited time, by the end of my internship, we have only reached the beginning of the characterization of photodiode inhomogeneity, which is only the first part of the internship. (The internship was proposed for M2 studies with 4-5 months.)

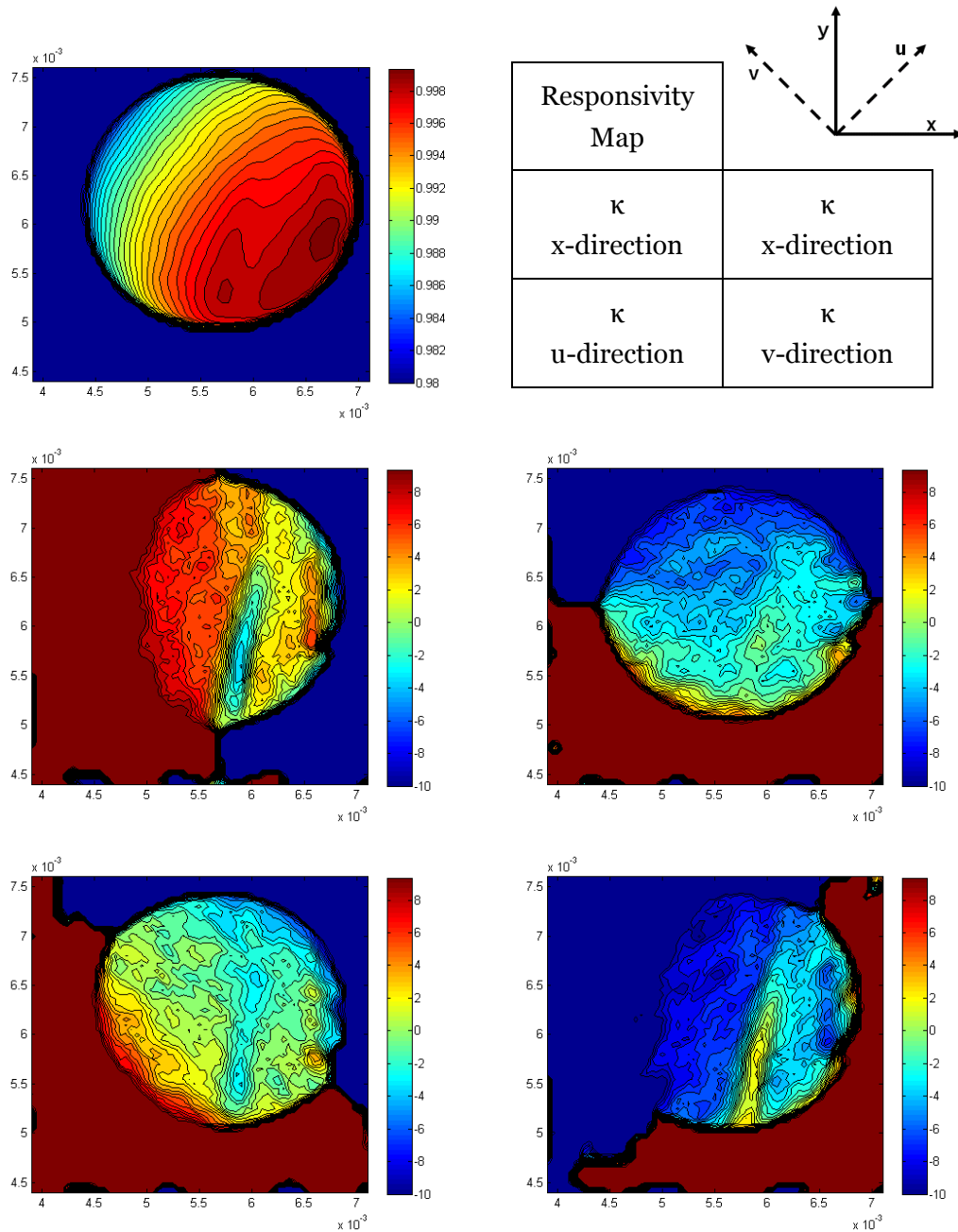
4) Discussions

During the internship, despite the fact that there are still many issues to be studied to further increase performance, we have nevertheless built a system that is able to characterize the responsivity inhomogeneity of photodiodes with a resolution $\sim 3 \cdot 10^{-5}$; this allows measurements of κ down to 6 m^{-1} with an SNR of 10 (assuming $50 \mu\text{m}$ steps).

Effect on the coupling factor κ by tuning beam waist (MATLAB Simulation)

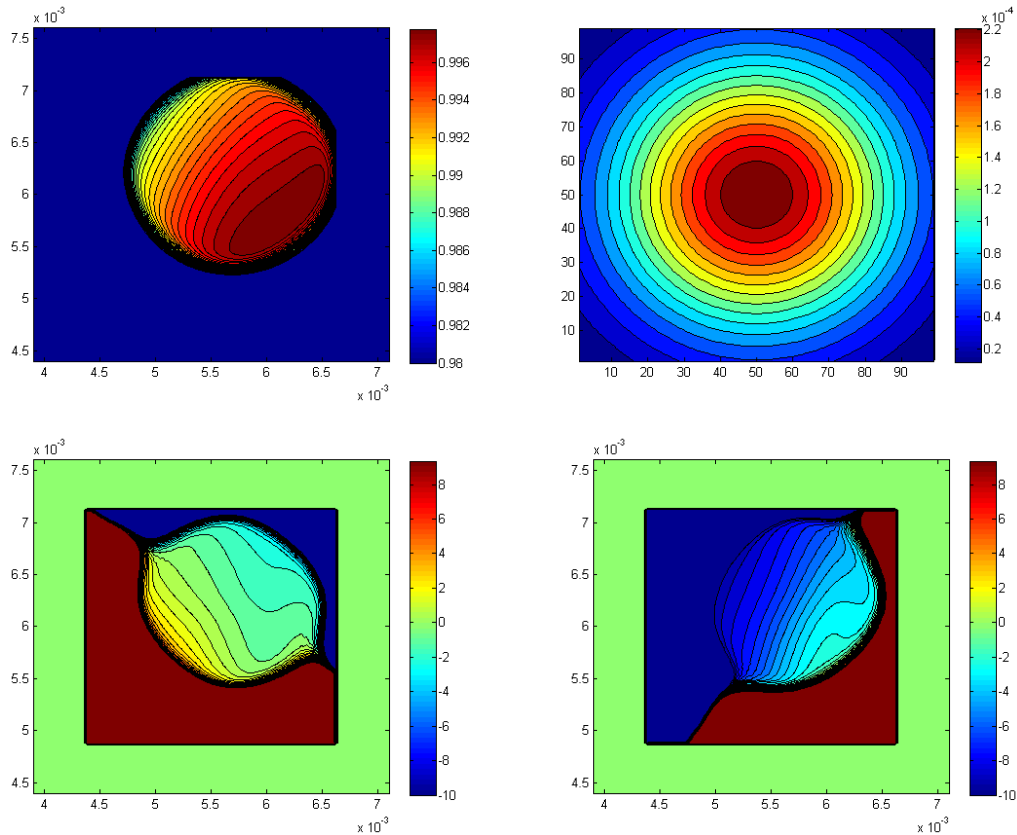
The original data were measured with $50 \mu\text{m}$ steps. We try to simulate the effect of the width of the laser waist (FWHM). The original were interpolated into $10 \mu\text{m}$ steps. A Gaussian filter with $99 \cdot 99$ steps was used. Axis u and axis x form an angle of 55 degrees.

◆ Original Data (Beam Waist = 100 μm @ $1/e^2$ or 118 μm @ FWHM)



In the following, we simulated the effect of a 400 μm beam waist and focused on the κ maps in the u direction (minimum coupling). Top-left represents the R map; top-right represents the Gaussian filter (coordinates in steps); bottom-left is the κ map in u-direction; bottom right is the κ map in v-direction. We note that the 50-step (0.5-mm) margin is due to the correlation between the Gaussian filter and the map.

◆ Beam Waist = 400 μ m



It is clear that for this specific photodiode the κ map smoothens with larger beam waist, which is advantageous for the compensation task. On the other hand, increasing the spot size also means that larger ‘flat’ areas are needed, which in turn limits the benefit of increased spot size (the useful surface is smaller). In any case, the benefit is by some units rather than by orders of magnitude and thus cannot be considered as the only improvement.

Scanning Procedure / Time

In view of the long-term fluctuation of the system, we have always tried to reduce the time required for each scan. The time consumed can be separated into several parts:

1	Motor Control / Response	??		
2	Displacement	18.8%	0.32 s	= 0.05 mm / 0.156 mm/s
3	ADC Acquisition	7.2%	0.12 s	= 10 k samples / 250 kHz * 3 channels
4	ADC Post-Processing	??		
5	LabVIEW & Write to File	??		
Time per Step		100%	1.70 s	= 7200 s (2 hr) / 4225 steps

We see that both the 2) Displacement and 3) ADC Acquisition parts account for very small portions of time. On the other hand, 1), 4) and 5) account for almost 74% of the

time. The possibilities in each part to reduce the scanning time are:

- 1) Motor Control / Response: The LabVIEW VI synchronizes with the motors in active mode, so there is not much room to shorten the response.
- 2) Displacement: If we increase the speed of the motors by a factor of 2.56 to the maximum, 0.4 mm/s, we can reduce the scanning time by 11.4%.
- 3) ADC Acquisition: The number of samples depends on the resolution we needed by over-sampling. Reducing the number of samples will not effect much the scanning time. Taking 10 times more samples will result in 22% more scanning time, and a gain of 3 on the resolution
- 4) ADC Post-Processing: We assume the time required for this part is fixed (hardware dependent).
- 5) LabVIEW & Write to File: Although there is no exact time duration for this part, but I think this is most likely the part we can work on to reduce the scanning time without introducing additional issues. Assuming this part accounts for 30% of the time per step, by removing unnecessary functionalities and displays, we can expect to shorten the time by $1/3 \sim 1/2$, which will reduce the scanning time by 10%~15%.

Temporal Stability of the System: Long-Term & Fast-Varying Fluctuations

In order to increase performance, apart from reducing scanning time, what might be more straightforward is to increase the temporal stability of the setup. We note that all the measurements we had based on the use of an ADC card with insufficient native resolution. We expect to increase the resolution by over-sampling, but have not yet verified and quantified the performance (crosstalk, common mode rejection ratio, etc) with systematic studies. We have made quite an effort to stabilize the system, but the effect of temperature fluctuation on the stability is yet unclear and awaits further study, although we saw that it is not the limiting factor regarding the resolution

In addition to the previous discussions where future work may first apply, there are other remaining steps to make the internship subject complete. For example, to compensate such inhomogeneity into required specifications, we can:

1. Find a photodiode model that is easier to compensate which means building a bank of inhomogeneity data of photodiodes of interest.
2. Evaluate and optimize the possible optical compensators (simulation).
3. Fabricate and characterize the optical compensators, which will require additional test benches.
4. Finally to characterize the compensated photodiodes.

From the first results on " κ " we see that " κ " does not behave in a simple manner (neither constant nor linear) with respect to x, y dimensions) which means that simple compensation might be tricky for a poor result (one may expect few units in " κ " reduction). More delicate spatial filters might be needed for good compensation.

Compensation des défauts de sensibilité des photodiodes de Virgo

Virgo est un interféromètre de Michelson utilisé pour la détection des ondes de gravitation. Il est opérationnel sur le site de Pise (Italie) et a atteint sa sensibilité nominale de quelques $10^{-17} \text{m}/\sqrt{\text{Hz}}$ à 10Hz.

La version avancée de ce détecteur (Advanced Virgo, 2014) aura une sensibilité améliorée et impose une stabilité accrue de la puissance de la source laser, soit $10^{-9}/\sqrt{\text{Hz}}$ à 10Hz.

A ce niveau de performances un des problèmes récurrent est le couplage "K" entre les inhomogénéités résiduelles de la sensibilité (S_{PHD}) de la photodiode utilisée pour la détection et le bruit de pointé de faisceau; ce couplage sera interprété par la photodiode comme un bruit de puissance et attribué, à tort, au laser.

On désire donc minimiser le plus possible cet effet.

On a mis en évidence que ces inhomogénéités ont au premier ordre une dépendance linéaire selon une direction (Oy) dans le plan de la photodiode (et un résidu quadratique); on pense pouvoir réduire cette dépendance par l'adjonction d'une optique "compensatrice", placée en amont de la photodiode, et dont la transmission, $T(y)$, selon (oy) affichera une dépendance inverse à celle de la photodiode; ainsi $T(y).S_{\text{PHD}}(y) = \text{Cste}$.

L'enjeu, ici, est de développer ce système compensateur pour une photodiode donnée: on envisage un système intégrant 2 lames formant un coin d'air; la transmission de cet ensemble sera modulée pour un faisceau se déplaçant normalement à la "charnière" du coin d'air (du fait des interférences entre les deux faces du coin d'air). Le pas et l'amplitude de cette modulation dépendront de l'angle du coin d'air et de la réflectivité des faces des lames; on ajustera ces paramètres pour compenser les défauts de la photodiode.

Durant ce stage, le travail consistera (entre autres) à :

- 1- caractériser la sensibilité de la photodiode en "tous" points de sa surface : on développera un banc de mesure spécifique et l'interfaçage de ce banc, à l'aide de platines motorisées pilotées sous labview.
- 2- définir et réaliser le montage du "compensateur", on envisage de coller 2 lames en maintenant un coin d'air entre ces lames grâce à des cales micrométriques.
- 3- caractériser le compensateur, soit en utilisant le montage décrit au §1, soit par l'utilisation d'une caméra et de l'interprétation des franges transmises par ce compensateur.
- 4- associer photodiode et compensateur, et vérifier l'efficacité de la compensation ; on sera amené à utiliser matlab pour obtenir fits et optimisations des différents paramètres.

Mots clefs : interfaçage expérience (moteur pas à pas, Labview, carte ADC/DAC)
interférences et imagerie, simulation (zemax, matlab)

Niveau: master 2^{ème} année ou école d'ingénieur 3^{ème} année

Laboratoire d'accueil : Observatoire de la Côte d'Azur, Nice,
Boulevard de l'Observatoire
B.P. 4229

F-06304 NICE Cedex 4

Contact et Encadrant : Frédéric Cleva, Ingénieur de recherche
04 92 00 31 97 / cleva@oca.eu

Appendix E

Numerical Calculation on Gaussian Beam Clipping Effects

As presented in Section 3.4, the beam clipping effect due to the finite diameter of photodiodes introduces certain coupling κ to the measured optical power value.

This appendix shows the 2-dimensional numerical calculation which takes into account the geometry of the photodiode and compares the results with the 1-dimensional analytical derivation in Section 3.4. As we will see, the coupling factor κ is slightly higher when the geometry is taken into account. This is because the waist of the slice of a 2-dimensional Gaussian beam decreases over the radial distance, and therefore a given on-axis displacement introduces larger effect off-axis than on-axis.

The difference is nevertheless subtle, so in general the 1-dimensional analysis is sufficient, while 2-dimensional numerical calculations may be useful when implementing some exotic ideas. For example, we can consider a realistic photodiode responsivity map and certain impinging beam radius. The 2-dimensional calculation can then give us information on the *sweet* spots where the coupling factor κ is minimum. An illustrative case is to locate the beam on the high edge of a photodiode with a linear slope in responsivity. When the position of the beam is just right, the loss of received power due to clipping may be compensated by increased responsivity, and vice versa.

Calculation on Photodiode Gaussian Beam Clipping Effect

Li-Wei Wei
2014-5-13

1

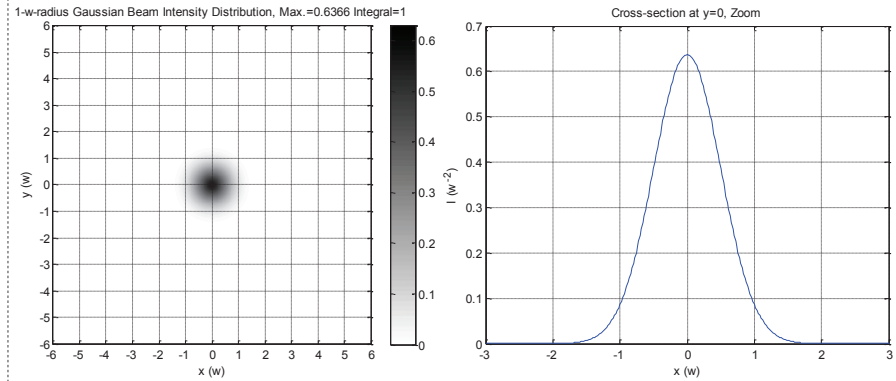
Calculation Parameters

- TEM₀₀ Gaussian Beam
- Beam Radius (e^{-2}) on Photodiode: w
- Photodiode Diameter: $3.5w$
- Calculation Window: $6w$ -by- $6w$
- Grid Size: $0.02w$
- Intensity Normalization: $0.6366/w^2$, so that the whole integral equals to 1

2

Step 1

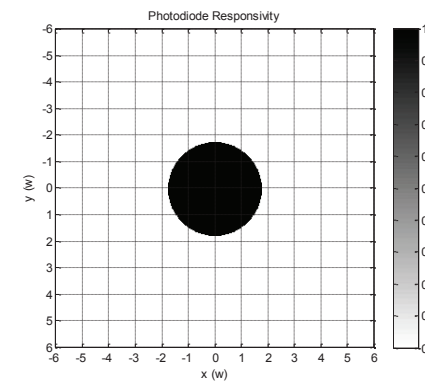
- Generate TEM₀₀ Beam Profile



3

Step 2

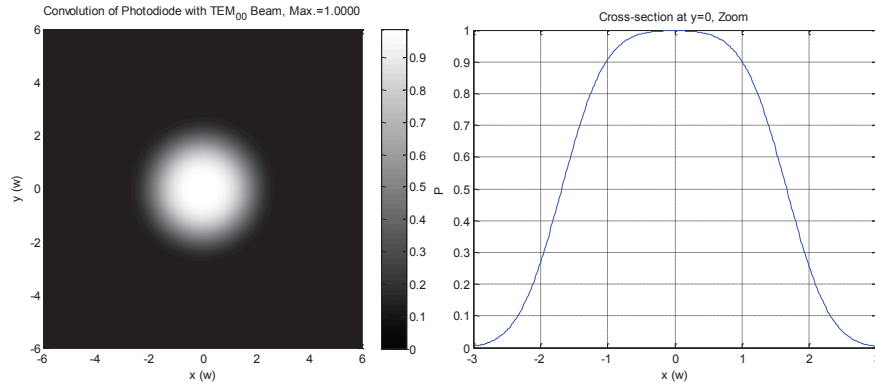
- Generate Photodiode Profile



4

Step 3

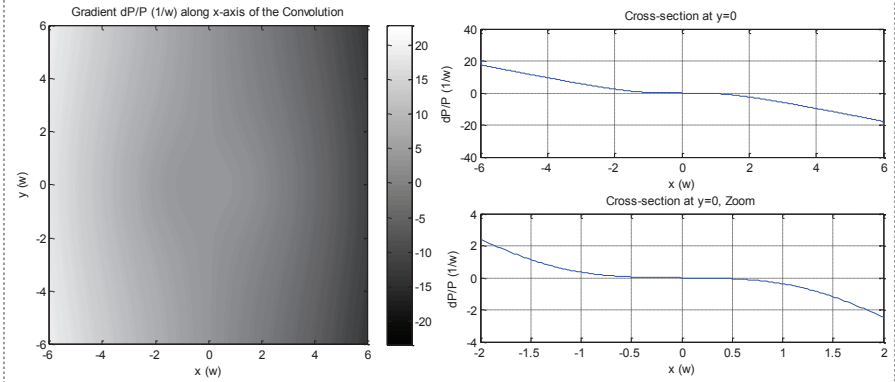
- Convolute the Photodiode and the TEM₀₀ Profiles



5

Step 5

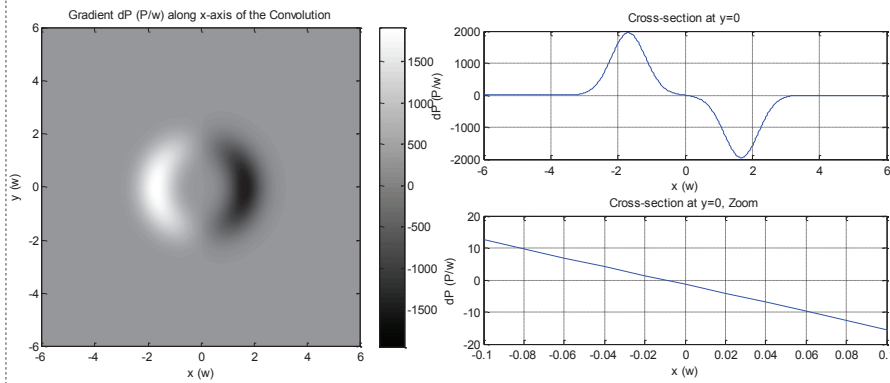
- Normalize the Gradient with respect to P to get RIN, i.e., divide Step 4 by Step 3



7

Step 4

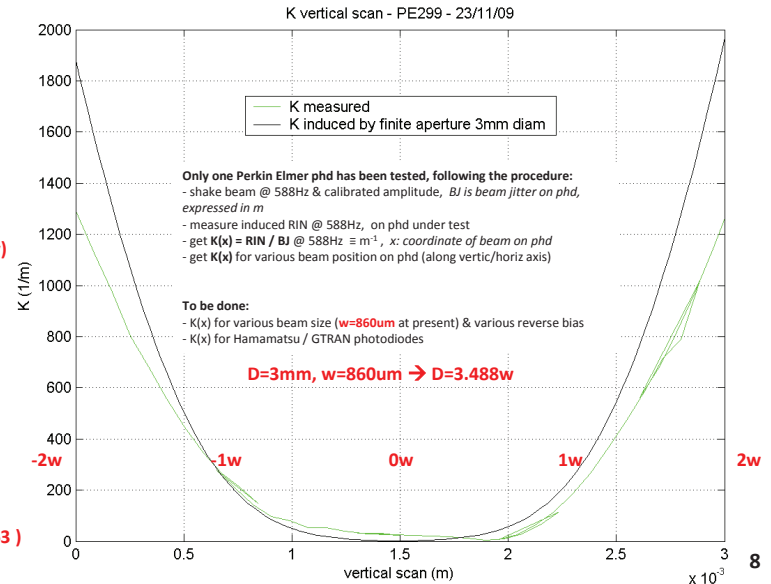
- Calculate the Gradient of the Convolution Map



6

2 (1/w)

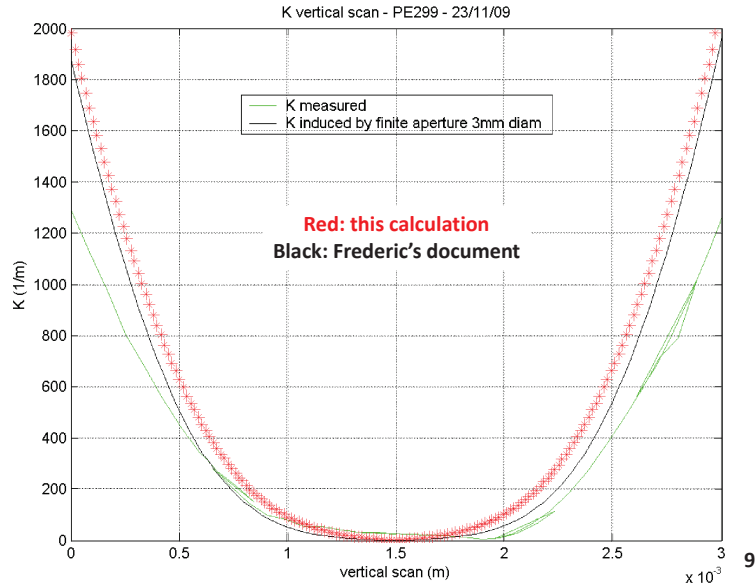
Compare to Frederic's document - 1



1 (1/w)

8

Compare to Frederic's document - 2



Calculation using erf: Gauss Error Function

2D Gaussian Integral

$$P = I_0 \int_{-\infty}^{\infty} \int_{-\infty}^{\infty} \exp\left(\frac{-2x^2}{\omega_x^2}\right) \exp\left(\frac{-2y^2}{\omega_y^2}\right) dx dy = I_0 \cdot \frac{\pi}{2} \cdot \omega_x \cdot \omega_y \quad I_0 = \frac{2}{\pi} \cdot \frac{1}{\omega_x} \cdot \frac{1}{\omega_y} \cdot P \quad \frac{2}{\pi} \cong 0.637$$

Assuming finite x-aperture and infinite y-aperture

$$P = I_0 \int_{-\infty}^{\infty} \exp\left(\frac{-2y^2}{\omega_y^2}\right) dy \cdot \int_{-\infty}^{\infty} \exp\left(\frac{-2x^2}{\omega_x^2}\right) dx = I_0 \cdot \sqrt{\frac{\pi}{2}} \cdot \omega_y \cdot \int_{-\infty}^{\infty} \exp\left(\frac{-2x^2}{\omega_x^2}\right) dx \quad I_0' \equiv I_0 \cdot \sqrt{\frac{\pi}{2}} \cdot \omega_y$$

x': center of the photodiode, r: photodiode radius; the beam is centered at x=0

$$P(x', r) = I_0' \int_{x'-r}^{x'+r} \exp\left(\frac{-2x^2}{\omega_x^2}\right) dx = I_0' \left[\int_0^{x'+r} \exp\left(\frac{-2x^2}{\omega_x^2}\right) dx - \int_0^{x'-r} \exp\left(\frac{-2x^2}{\omega_x^2}\right) dx \right]$$

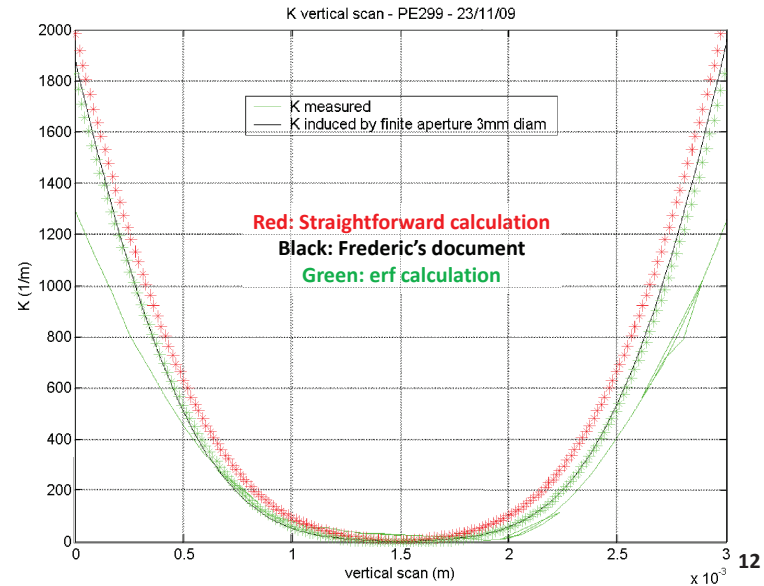
$$= I_0' \cdot \frac{\omega_x}{\sqrt{2}} \cdot \frac{\sqrt{\pi}}{2} \left[\frac{2}{\sqrt{\pi}} \int_0^{a_2(x'+r)} \exp(-t^2) dt - \frac{2}{\sqrt{\pi}} \int_0^{a_2(x'-r)} \exp(-t^2) dt \right] \quad t = \frac{\sqrt{2}}{\omega_x} x \equiv a_2 x$$

$$= I_0' \cdot \frac{\omega_x}{\sqrt{2}} \cdot \frac{\sqrt{\pi}}{2} [\text{erf}(a_2(x'+r)) - \text{erf}(a_2(x'-r))]$$

$$= I_0' \cdot a_1 \cdot [\text{erf}(a_2(x'+r)) - \text{erf}(a_2(x'-r))] \quad \text{Eq. 1} \rightarrow \text{Corresponds to Step 3} \quad a_1 \equiv \frac{\omega_x}{\sqrt{2}} \cdot \frac{\sqrt{\pi}}{2}$$

- The calculation here agrees in general with that of Frederic, with some discrepancy
- The discrepancy may have come from:
 - Slightly different D/w ratios (3.5 vs 3.488)
 - Finite calculation window and grid size of my calculation
- The clipping can also be calculated in a more analytical way, while the previous calculation should be more straightforward.

Eq. 1



Appendix F

MATLAB m-files for Gaussian Beam Waist Calculation

Initially, these MATLAB m-files were written to replace an older code written with Eureka¹ in which only two beam cross-section measurements could be considered. The measurements on the beam cross-section profile were made by a rotating slit².

A subsequent effort was made to extend the calculation to more general situations with multiple measurements to reduce uncertainties. There probably are many known Gaussian fitting tools (we have never checked though), but due to the historical reason above we generally use these m-files to fit our beam propagation measurements. A future possible improvement could be to introduce a weighting function on the significance of the measurements, i.e., to credit more the measurements made farther away from the beam waist.

The source codes of the console m-file (`beam_scan_example.m`) as well as the function m-files (`solve_beam_waist.m`, `err_func_gen.m`, `beam_waist_2d.m`) are attached below, followed by some slides explaining the basis of the calculation process.

¹Eureka: the Solver, <http://www.spinstop.com/roger/eureka.htm>

²Photon, Inc., BeamScan, Model 1080 Slit Scan.

beam_scan_example.m

```

% an exemplary console m-file for the calculations

lambda = 1064e-9; % wavelength, in meter

% h for horizontal, v for vertical
h_z_array = [0.097 0.110 0.122 0.139]; % z, in meter
v_z_array = h_z_array;
h_z_sign = [1 1 1 1]; % slope of waist size at z
v_z_sign = [1 1 1 1]; % increasing: 1; decreasing: -1
h_w_array = [861 930 982 1042]./2.*1e-6; % measured waist size at z, in meter
v_w_array = [818 864 902 980]./2.*1e-6;

% set root-seeking step size, in meter, for solve_beam_waist function
stepsize = 1e-7;

% pass the parameters to solve_beam_waist function
[h_w0, h_z0, h_z0_err_abs_avg] = ...
solve_beam_waist (lambda, stepsize, h_z_array, h_z_sign, h_w_array);
[v_w0, v_z0, v_z0_err_abs_avg] = ...
solve_beam_waist (lambda, stepsize, v_z_array, v_z_sign, v_w_array);

% calculate fitting error pointwise
h_w_err = h_w_array - beam_waist_2d(lambda, h_w0, h_z_array, h_z0);
v_w_err = v_w_array - beam_waist_2d(lambda, v_w0, v_z_array, v_z0);

% set up the range for the Gaussian fitting
z_step = 0.002;
z_all = [h_z_array v_z_array h_z0 v_z0];
z_span = max(z_all) - min(z_all);
z = min(z_all) - 0.2*z_span : z_step : max(z_all) + 0.2*z_span;

% pass the parameters to beam_waist_2d.m
h_w_z = beam_waist_2d(lambda, h_w0, z, h_z0);
v_w_z = beam_waist_2d(lambda, v_w0, z, v_z0);

% plot the results
figure;
plot( h_z0, h_w0*1e6, 'rs', ...
      v_z0, v_w0*1e6, 'bs', ...
      z, h_w_z*1e6, 'r-', ...
      z, v_w_z*1e6, 'b-', ...
      h_z_array, h_w_array*1e6, 'ro', ...
      v_z_array, v_w_array*1e6, 'bv', ...
      'LineWidth', 2);
title(sprintf('Beam Propagation: z_0_h_Error=%0.5gm, z_0_v_Error=%0.5gm', ...
             h_z0_err_abs_avg, v_z0_err_abs_avg));
xlabel('z_(m);_Laser_Aperture@z_0=0m');
ylabel('w_(um)'); grid on;
legend( sprintf('w_0h:%0.5gum,%0.2gm', h_w0*1e6, h_z0), ...
        sprintf('w_0v:%0.5gum,%0.2gm', v_w0*1e6, v_z0), ...
        sprintf('h-fit;_RMS_Error=%0.5gum', sqrt(mean(h_w_err.^2))*1e6), ...
        sprintf('v-fit;_RMS_Error=%0.5gum', sqrt(mean(v_w_err.^2))*1e6), ...
        'horizontal', 'vertical', ...
        'location', 'NorthWest');

```

solve_beam_waist.m

```

% solves for the size and location of the beam waist

function [w0, z0, z0_err_abs_avg] = ...
solve_beam_waist (lambda, stepsize, z_array, z_sign, w_array)

% Input >>
% lambda: wavelength
% stepsize: root-seeking step size
% z_array: position z of measurements
% z_sign: the slope of beam radius at z; increasing: 1; decreasing: -1
% w_array: measured waist size at z
% Output >>
% w0: beam waist size
% z0: beam waist location
% z0_err_abs_avg: finite (non-zero) minimum value of error function, averaged

if stepsize<=min(w_array)
% define the guesses on w0
w0_guess_1 = stepsize:stepsize:min(w_array);

% number of input (measurement) data -> for meshgrid
n_input = size(z_array, 2);
% number of w0 guesses made -> for meshgrid
n_step = size(w0_guess_1, 2);
% create the meshgrids for matrix calculation
[w0_guess_2, ~] = meshgrid(w0_guess_1, ones(1,n_input));
[~, z_array_2] = meshgrid(ones(1,n_step), z_array);
[~, z_sign_2] = meshgrid(ones(1,n_step), z_sign);
[~, w_array_2] = meshgrid(ones(1,n_step), w_array);

% calculate zR(w0)
zR_guess_2 = pi.*w0_guess_2.^2./lambda;
% calculate z0(w0, zR(w0))
z0_guess_2 = z_array_2 ...

```

```

- z_sign_2.*sqrt(zR_guess_2.^2.*(w_array_2.^2./w0_guess_2.^2-1));

% generate error function
z0_guess_diff_1 = err_func_gen(z0_guess_2);
% look for error function minimum
z0_err_abs = min(min(abs(z0_guess_diff_1)));
% calculation benchmarking by calculating the averaged minimum
z0_err_abs_avg = z0_err_abs./n_input./(n_input-1).*2;
% w0's that correspond to the minimum; take the average as the best guess
w0_2 = w0_guess_2(:, abs(z0_guess_diff_1)==z0_err_abs);
w0 = mean(mean(w0_2));
% z0's that correspond to the minimum; take the average as the best guess
z0_2 = z0_guess_2(:, abs(z0_guess_diff_1)==z0_err_abs);
z0 = mean(mean(z0_2));

else
% if stepsize is too big than no calculation is done
disp('Error: Step size is larger than smallest input beam radius. ');
w0 = NaN;
z0 = NaN;
z0_err_abs_avg = NaN;
end
end

```

err_func_gen.m

```

% generates the defined error function

function err_func = err_func_gen(z0_guess)
n_input = size(z0_guess,1);
n_step = size(z0_guess,2);
err_func = zeros(1,n_step);
for i = 1:n_input-1
for j = i+1:n_input
err_func = err_func + abs(z0_guess(i,:)-z0_guess(j,:));
end
end
end

```

beam_waist_2d.m

```

% generates a Gaussian beam propagation

function w_z = beam_waist_2d(lambda, w0, z, z0)
zR = pi.*w0.^2./lambda;
w_z = w0.*sqrt(1+(z-z0).^2./zR^2);
end

```

MATLAB: Gaussian Optics Solve Beam Waist

2013-3-4

1

THE PROPAGATION CONSTANT

The propagation of a pure Gaussian beam can be fully specified by either its beam waist diameter or its far-field divergence. In principle, full characterization of a beam can be made by simply measuring the waist diameter, $2w_0$, or by measuring the diameter, $2w(z)$, at a known and specified distance (z) from the beam waist, using the equations

$$w(z) = w_0 \left[1 + \left(\frac{\lambda z}{\pi w_0^2} \right)^2 \right]^{1/2}$$

and

$$R(z) = z \left[1 + \left(\frac{\pi w_0^2}{\lambda z} \right)^2 \right]$$

$$z_R = \frac{\pi w_0^2}{\lambda}$$

Simultaneously, as $R(z)$ asymptotically approaches z for large z , $w(z)$ asymptotically approaches the value

$$w(z) = \frac{\lambda z}{\pi w_0}$$

where z is presumed to be much larger than $\pi w_0 / \lambda$ so that the $1/e^2$ irradiance contours asymptotically approach a cone of angular radius

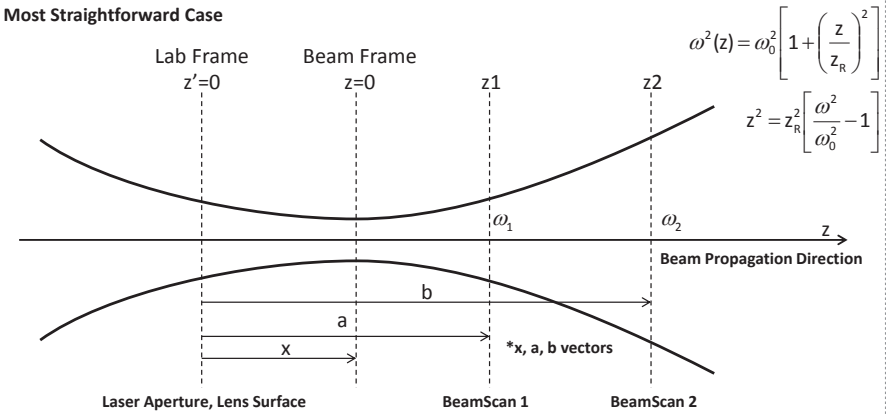
$$\theta = \frac{w(z)}{z} = \frac{\lambda}{\pi w_0}$$

Formulae

$$\omega^2(z) = \omega_0^2 \left[1 + \left(\frac{z}{z_R} \right)^2 \right]$$

2 (2.8)

Most Straightforward Case

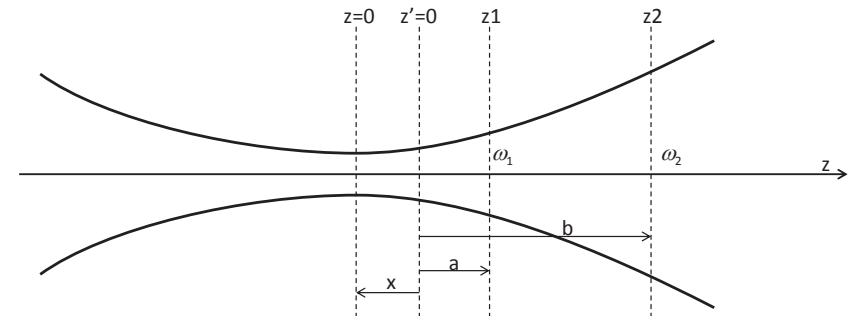


$$z_1^2 = z_R^2 \left[\frac{\omega_1^2}{\omega_0^2} - 1 \right] \quad (x-a)^2 = z_R^2 \left[\frac{\omega_1^2}{\omega_0^2} - 1 \right] \quad |a-x| = z_R \sqrt{\frac{\omega_1^2}{\omega_0^2} - 1} \quad x = a - z_R \sqrt{\frac{\omega_1^2}{\omega_0^2} - 1}$$

$$z_2^2 = z_R^2 \left[\frac{\omega_2^2}{\omega_0^2} - 1 \right] \quad (x-b)^2 = z_R^2 \left[\frac{\omega_2^2}{\omega_0^2} - 1 \right] \quad |b-x| = z_R \sqrt{\frac{\omega_1^2}{\omega_0^2} - 1} \quad x = b - z_R \sqrt{\frac{\omega_1^2}{\omega_0^2} - 1}$$

Here $x > 0, a > 0, b > 0$ 3

Even More Straightforward?

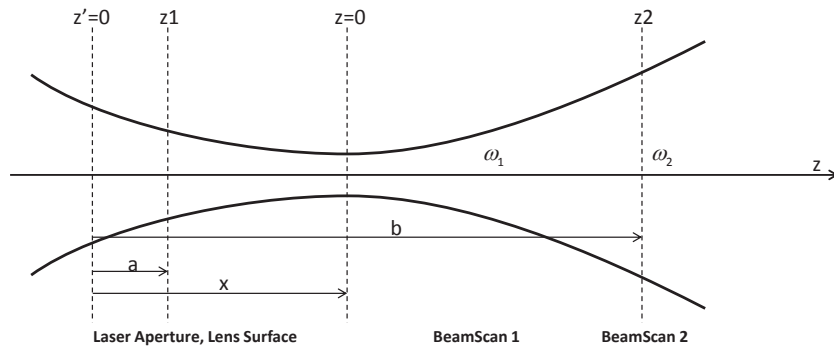


$$|a-x| = z_R \sqrt{\frac{\omega_1^2}{\omega_0^2} - 1} \quad x = a - z_R \sqrt{\frac{\omega_1^2}{\omega_0^2} - 1}$$

$$|b-x| = z_R \sqrt{\frac{\omega_1^2}{\omega_0^2} - 1} \quad x = b - z_R \sqrt{\frac{\omega_1^2}{\omega_0^2} - 1}$$

Here $x < 0, a > 0, b > 0$ 4

Other Cases - I



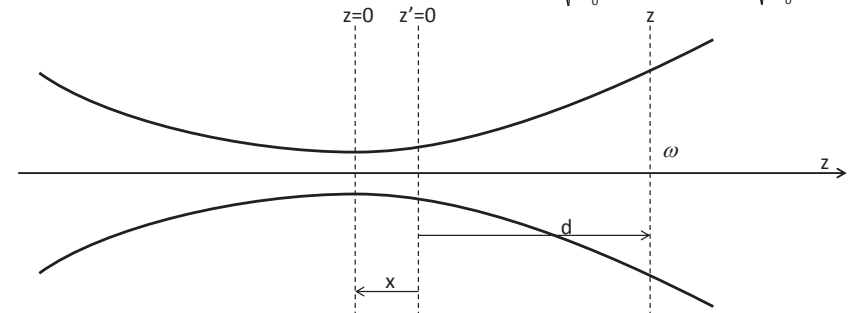
$$|a-x| = z_R \sqrt{\frac{\omega_1^2}{\omega_0^2} - 1} \quad x = a + z_R \sqrt{\frac{\omega_1^2}{\omega_0^2} - 1}$$

$$|b-x| = z_R \sqrt{\frac{\omega_2^2}{\omega_0^2} - 1} \quad x = b - z_R \sqrt{\frac{\omega_2^2}{\omega_0^2} - 1}$$

Here $x > 0, a > 0, b > 0$ 5

Summary

Assuming $d > 0$ (reasonable for real measurements) $|d-x| = z_R \sqrt{\frac{\omega^2}{\omega_0^2} - 1} \rightarrow x = d \pm z_R \sqrt{\frac{\omega^2}{\omega_0^2} - 1}$



if $|d| \geq |x| \rightarrow x = d - z_R \sqrt{\frac{\omega^2}{\omega_0^2} - 1}$

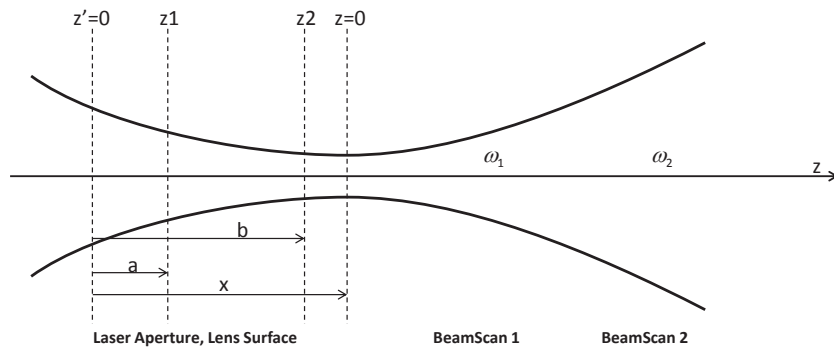
if $|d| \leq |x| \rightarrow x = d + z_R \sqrt{\frac{\omega^2}{\omega_0^2} - 1}$

- Happens when the measurement is taken @ z_0+
- i.e., Beam Diverging, derivative of waist size > 0

- Happens when the measurement is taken @ z_0-
- i.e., Beam Converges, derivative of waist size < 0

7

Other Cases - II



$$|a-x| = z_R \sqrt{\frac{\omega_1^2}{\omega_0^2} - 1} \quad x = a + z_R \sqrt{\frac{\omega_1^2}{\omega_0^2} - 1}$$

$$|b-x| = z_R \sqrt{\frac{\omega_2^2}{\omega_0^2} - 1} \quad x = b + z_R \sqrt{\frac{\omega_2^2}{\omega_0^2} - 1}$$

6

MATLAB Implementation - Idea

$$x = d \pm z_R \sqrt{\frac{\omega^2}{\omega_0^2} - 1} \quad z_R = \frac{\pi \omega_0^2}{\lambda}$$

- Unknowns: $w(0), x$
- Make guesses on $w(0)$ from 0 to $\min[w(d)]$ with certain step size (e.g. 1E-7m)
- Calculate the corresponding possible x 's
- With 2+ measurement data ($d, w(d)$), find the cross-section of (ideal) or the closest (in practice) between these two x curves
- This can be defined into an error function \rightarrow seek minimum

8

solve_beam_waist.m

```
function [w0, z0, z0_err_abs_avg] = solve_beam_waist(lambda, stepsize, z_array, z_sign, w_array)
% w0 = beam waist size
% z0 = beam waist location
% z0_err_abs_avg = finite (non-zero) minimum value of error function, averaged
if stepsize <= min(w_array)
    w0_guess_1 = stepsize:stepsize:min(w_array); % guesses on w0
    n_input = size(z_array, 2); % number of input (measurement) data -> for meshgrid
    n_step = size(w0_guess_1, 2); % number of w0 guesses made -> for meshgrid
    [w0_guess_2, null] = meshgrid(w0_guess_1, ones(1, n_input));
    [null, z_array_2] = meshgrid(ones(1, n_step), z_array);
    [null, z_sign_2] = meshgrid(ones(1, n_step), z_sign);
    [null, w_array_2] = meshgrid(ones(1, n_step), w_array);
    zR_guess_2 = pi.*w0_guess_2.^2./lambda; % calculate zR(w0)
    → z0_guess_2 = z_array_2-z_sign_2.*sqrt(zR_guess_2.^2.*(w_array_2.^2./w0_guess_2.^2-1)); % calculate z0(w0, zR(w0)) --- x
    z0_guess_diff_1 = err_func_gen(z0_guess_2); % generate error function
    z0_err_abs = min(min(abs(z0_guess_diff_1))); % look for error function minimum
    z0_err_abs_avg = z0_err_abs./n_input./(n_input-1).*2; % calculation benchmarking by calculating the averaged minimum
    w0_2 = w0_guess_2(:, abs(z0_guess_diff_1)==z0_err_abs); % w0's that correspond to the minimum
    z0_2 = z0_guess_2(:, abs(z0_guess_diff_1)==z0_err_abs); % z0's that correspond to the minimum
    w0 = mean(mean(w0_2));
    z0 = mean(mean(z0_2));
else
    disp('Error: Stepsize is larger than smallest beam radius inputed. ');
    w0 = NaN;
    z0 = NaN;
    z0_err_abs_avg = NaN;
end
end
```

9

MATLAB Implementation - Error Function

Definition: Err. Func. = $\sum_{i=1}^{n-1} \sum_{j=i+1}^n |x_{0,i} - x_{0,j}|$

where n = number of inputs

For n inputs, there are n*(n-1)/2 combinations.

This is averaged to get a general idea of the quality of the beam waist solver together with that of the measurements.

```
function err_func = err_func_gen(z0_guess)
n_input = size(z0_guess, 1);
n_step = size(z0_guess, 2);
err_func = zeros(1, n_step);
for i = 1:1:n_input-1
    for j = i+1:1:n_input
        err_func = err_func + abs(z0_guess(i,:) - z0_guess(j,:));
    end
end
end
```

10

Example

$$\rightarrow x = d \pm z_R \sqrt{\frac{\omega^2}{\omega_0^2} - 1}$$

```
lambda = 1064e-9;
h_z_array = [0.03 0.41 0.68]; % h for horizontal
→ h_z_sign = [-1 -1 -1]; % increasing: 1; decreasing: -1
h_w_array = [2255.2 2240.7 2236.2]/2.*1e-6;
v_z_array = h_z_array; % v for vertical
→ v_z_sign = [1 1 1]; % increasing: 1; decreasing: -1
v_w_array = [2198.7 2218.5 2238.3]/2.*1e-6;
stepsize = 1e-7; % root-seeking step size
[h_w0, h_z0, h_z0_err_abs_avg] = ...
solve_beam_waist(lambda, stepsize, h_z_array, h_z_sign, h_w_array);
h_w_err = h_w_array - beam_waist_2d(lambda, h_w0, h_z_array, h_z0); % calculate fitting error pointwise
[v_w0, v_z0, v_z0_err_abs_avg] = ...
solve_beam_waist(lambda, stepsize, v_z_array, v_z_sign, v_w_array);
v_w_err = v_w_array - beam_waist_2d(lambda, v_w0, v_z_array, v_z0); % calculate fitting error pointwise
```

Results: w0, z0, solver error, fitting error

11

beam_waist_2d.m

```
function w_z = beam_waist_2d(lambda, w0, z, z0)
zR = pi.*w0.^2./lambda;
w_z = w0.*sqrt(1+(z-z0).^2./zR.^2);
end
```

12

Appendix G

GPIB Commands Wrapped with Perl

Some efforts were made to standardize power spectral density (PSD) measurements with the fast Fourier transform (FFT) based and the swept-tuned super-heterodyne spectrum analyzers. Since they both have the IEEE 488 General Purpose Interface Bus (GPIB) interface, measurements can be done remotely and automatically with pre-defined commands.

The following configuration is chosen for the fast FFT based spectrum analyzer SR780:

Span (Hz)	RBW♣ (Hz)	Averaging
102400	128	500
25600	32	200
6400	8	50
1600	2	20
400	0.5	10

* Hann Window, Linear Root-Mean-Square Averaging

♣ Resolution Bandwidth

And the following for the swept-tuned spectrum analyzer HP8591A:

Start Freq.	Stop Freq.	RBW	VBW♠	Averaging
10 kHz	100 kHz	1 kHz	100 Hz	5
100 kHz	300 kHz	3 kHz	300 Hz	15
300 kHz	1 MHz	10 kHz	1 kHz	25
1 MHz	3 MHz	30 kHz	3 kHz	50
3 MHz	10 MHz	100 kHz	10 kHz	50
10 MHz	30 MHz	300 kHz	30 kHz	100
30 MHz	100 MHz	1 MHz	100 kHz	100

* Detector Mode: Sample

♠ Video Bandwidth

The Perl programming language¹ is used to wrap up these GPIB commands with the use of the driver library of the Virtual Instrument Software Architecture (VISA). The PGPLOT² library is used to generate plots. The source codes are attached. We

¹<https://www.perl.org/>

²PGPLOT Graphics Subroutine Library <http://www.astro.caltech.edu/~tjp/pgplot/>

note that the coding is not optimized and lacks arrangements, but should nevertheless provide some information for possible future developments. LabVIEW was also used for some early implementations, but eventually for more flexibility, easier code maintenance and the free software concept, the migration towards Perl took place.

We also note the related software resources:

- KE5FX GPIB Toolkit
<http://www.ke5fx.com/gpib/readme.htm>,
in particular the *Win32-based emulator for the HP 7470A plotter*.
- Lab-Measurement, Perl Module
<http://search.cpan.org/dist/Lab-Measurement/>
- Stanford Research Systems, SR780 User's Manual
<http://www.thinksrs.com/downloads/PDFs/Manuals/SR780m.pdf>
Chapter 5 Programming
- Programmer's Guide, HP 8590 E-Series and L-Series Spectrum Analyzers and HP 8591C Cable TV Analyzer
ftp://ftp.agilent.com/manuals/08590-90235_8590E_90L_91C_Prog_Guide_Jun95.pdf
- Agilent Spectrum Analysis Basics, Application Note 150
<http://www.keysight.com/find/AppNote150>
- LabVIEW Driver Library for Agilent / Keysight Technologies 8591A
http://sine.ni.com/apps/utf8/niid_web_display.model_page?p_model_id=393

G.1 For Stanford Research Systems SR780 Network Signal Analyzer

```
#!/usr/bin/perl -w
use strict;
use Win32::API;
use POSIX qw(floor ceil);
use Time::HiRes qw(usleep);
use PGPLOT;
use List::Util qw(min max);

##### This Perl script configures Stanford SR780 to a given state #####

# Data/Plot Settings >> #
my $data_dir_path = 'C:\pl_data\sr780';
my $gsview = q/"C:\Program_Files\Ghostgum\gsview\gsview32.exe"/;
# << Data/Plot Settings #

# Scan Parameters >> #
my $n_span = 5;
my @scan_param = (
    # 0,      1,
    # F SPAN,  n_VAVG
    # Respect the descending order for better auto plot
    [ 102_400, 500],
    [ 25_600, 200],
    [ 6_400, 50],
    [ 1_600, 20],
    [ 400, 10],
);
my $smart_auto_preview = 1;
my $preview_x_min = 1;      # log scale
my $preview_x_max = 5;     # log scale
my $preview_y_min = -9;    # log scale
my $preview_y_max = -4;    # log scale

# << Scan Parameters #
```

```

# SR780 Configuration >> #
my @sr780_config = (

    # Alarm? 0: Off; 1: On
    'ALRM_0',
    'ALRT_0',
    'ADON_0',

    # Source? 1: On; 0: Off
    'SRCO_0',

    # Ch1/Ch2 Input Mode? 0: A, Single-Ended; 1: A-B, Differential
    'I1MD_0',
    'I2MD_0',

    # Ch1/Ch2 Grounding? 0: Float, Connects the shields to chassis ground through 1MOhm+0.01uF;
    # 1: Ground, Connects the shields to chassis ground with 50 Ohm.
    # In this mode, do not exceed 3V on the shields.
    'I1GD_0',
    'I2GD_0',

    # Ch1/Ch2 Coupling? 0: DC; 1: AC, The 3 dB bandwidth of the AC coupling is 0.16 Hz;
    # 2: ICP, ICP coupling connects a 5 mA current source (26 VDC open circuit) to the center
    # conductor of the A input connector. This supply powers ICP accelerometers. The signal
    # is AC coupled from the center conductor. Set the Input Mode to A (not A-B).
    'I1CP_0',
    'I2CP_0',

    # Ch1/Ch2 Anti-Aliasing Filter? 1: On; 0: Off
    'I1AF_1',
    'I2AF_1',

    # Auto Offsetting? (Internally ground both inputs and correct their DC offsets.
    # This only takes a second.) 0: Off; 1: On
    'IAOM_0',

    # Measurement Group? [s] 0: FFT; 1: Octave; 2: Swept Sine
    # [d][s] [d] 0: Display A; 1: Display B
    'MGRP_0_0',
    'MGRP_1_0',

    # FFT Base Frequency? 0: 100.0 kHz; 1: 102.4 kHz
    'FBAS_2_1',

    # Measurement of Display
    'MEAS_0_0', # 0: FFT Ch1
    'MEAS_1_1', # 1: FFT Ch2

    # FFT Resolution? 0: 100; 1: 200; 2:400; 3:800
    'FLIN_0_3',
    'FLIN_1_3',

    # FFT Window? 0: Uniform; 1: Flattop; 2: Hanning; 3: BMH... (note the mistake in manual?)
    'FWIN_0_2',
    'FWIN_1_2',

    # X Axis Scale Type? 0: Linear; 1: Logarithmic
    'XAXS_0_0',
    'XAXS_1_0',

    # View of Display? 0: Log Magnitude; 1: Linear Magnitude...
    'VIEW_0_0',
    'VIEW_1_0',

    # Unit of Display? 0: Vpk; 1: Vrms; 2: Vpk square; 3: Vrms square...
    'UNIT_0_1',
    'UNIT_1_1',

    # Show PSD Units? 0: Off; 1: On
    'PSDU_0_1',
    'PSDU_1_1',

    # Full Span
    'FSPN_0_102400',
    'FSPN_1_102400',

    # Turn off averaging
    'FAVG_0_0',
    'FAVG_1_0'
);

# << SR780 Configuration #

# GPIB Setting >> #
my $resource_name = "GPIB1::10::INSTR";
my $timeout = 20000; # ms
# >> c.f. VISA C Reference Help for VISA32 function prototypes
my $FViOpenDefaultRM = Win32::API->new('visa32','viOpenDefaultRM','P','I'); # RM: Resource Manager
my $FViOpen = Win32::API->new('visa32','viOpen','IPIP','I');
my $FViSetAttribute = Win32::API->new('visa32','viSetAttribute','III','I');
my $FViWrite = Win32::API->new('visa32','viWrite','IPIP','I');
my $FViRead = Win32::API->new('visa32','viRead','IPIP','I');
my $FViBufRead = Win32::API->new('visa32','viBufRead','IPIP','I');
my $FViClose = Win32::API->new('visa32','viClose','I','I');
my $FViReadAsync = Win32::API->new('visa32','viRead','IPIP','I');
my $FViReadSTB = Win32::API->new('visa32','viReadSTB','IP','I');

```

```

my $fViClear = Win32::API->new('visa32', 'viClear', 'I', 'I');
# >> c.f. visa.h for VISA32 constants
my $cVI_NULL = 0; # VI_NULL constant from visa.h
my $cVI_ATTR_TMO_VALUE = 1073676314; # Timeout Attribute Constant from visa.h
# >> Initialize Variables
my $bytes_written = 0;
my $bytes_read = 0;
my $vi_return = 0;
# << GPIB Setting #

##### Main #####

system("cls");

## Header >>
my $buf_bytes = 80;
my $msg = '';
my $cmd = '';
my $ans_GPIB = '';

# Start GPIB communication
my ($manager_handle, $session_handle) = &vi_initialize($resource_name, 0, 0);
$msg = ">_GPIB_Connection_Started.\n\n";
print $msg;

# # Configure SR780?
# my $conf = &ui_getkey("Do you want to configure SR780? (Y/N) ", 'NY');
# goto SCAN unless $conf;

# Let user decide SR780 reset
my $reset = &ui_getkey("Reset_Stanford_SR780?(Y/N) ", 'NY');
# Reset SR780 if requested
if ($reset){
    &vi_write($session_handle, '*RST');
    $msg = ">_Resetting_Device:_Takes_about_15_seconds._Press_any_key_when_ready.\n\n";
    print $msg;
    system("pause");
}

# Clear all status registers. (The enable registers are not changed.)
&vi_write($session_handle, 'CLS');

# Set the output interface to GPIB
&vi_write($session_handle, 'OUTX_0');

# Device Identification String
&vi_write($session_handle, '*IDN?');
$msg = '>_Device:' . &vi_read($session_handle, $buf_bytes) . "\n";
print $msg;

&vi_debug($session_handle);
print STDOUT "\n";
## << Header

SCAN:

# Write Configuration to Device?
my $re_conf = &ui_getkey("Write_Configuration_to_Device?(Y/N) ", 'NY');
# Write Configuration to Device if requested
if ($re_conf){
    $msg = ">_Writing_Configuration_to_Device...\n";
    print $msg;
    foreach(@sr780_config){
        &vi_write($session_handle, $_);
        print STDOUT $_ . ";_";
    }
    print STDOUT "\n\n";
}

# Auto Range?
my $auto_range = &ui_getkey("Auto_Range?(Y/N) ", 'NY');
if ($auto_range){
    my $ar_timeout = 15;
    my $ar_counter_1 = 0;
    my $ar_ready_ch1 = 0;
    &vi_write($session_handle, 'A1RG_1');
    until ($ar_ready_ch1){
        &vi_write($session_handle, 'INPS?_4');
        &usleep(1.0*1_000_000);
        $ar_ready_ch1 = &vi_read($session_handle, $buf_bytes);
        $ar_counter_1++;
        unless($ar_counter_1 < $ar_timeout){
            $ar_ready_ch1 = 1;
        }
    }
    &vi_write($session_handle, 'A1RG_0');

    my $ar_counter_2 = 0;
    my $ar_ready_ch2 = 0;
    &vi_write($session_handle, 'A2RG_1');
}

```

```

until ($ar_ready_ch2){
    &vi_write($session_handle, 'INPS?_12');
    &usleep(1.0*1_000_000);
    $ar_ready_ch2 = &vi_read($session_handle, $buf_bytes);
    $ar_counter_2++;
    unless($ar_counter_2 < $ar_timeout){
        $ar_ready_ch2 = 1;
    }
}
&vi_write($session_handle, 'A2RG_0');

print ">_Auto_Range_Done.\n\n";
}

# Auto Scale?
my $auto_scale = &ui_getkey("Auto_Scale?_(Y/N)_", 'NY');
if ($auto_scale){
    &vi_write($session_handle, 'ASCL_0');
    &vi_write($session_handle, 'ASCL_1');
    $msg = ">_Auto_Scale_Done.\n\n";
    print $msg;
}

my $scan_done = 0;
my $span_index = 0;

# Start Scan?
my $start_scan = &ui_getkey("Start_Scan?_(Y/N)_", 'NY');

unless($start_scan){
    goto FINE;
}

my $remark = '';
if ($start_scan){
    print "Scan_Remark?_";
    $remark = <STDIN>;
    chomp $remark;
}

# Auto or Manual Scan?
my $auto_scan = -1;
if ($start_scan){
    $auto_scan = &ui_getkey("Manual_or_Auto?_(M/A)_", 'MA');
}

# Which Display(s) to Scan?
my $display = -1;
if ($auto_scan >= 0){
    $display = &ui_getkey("Display_A,_B,_or_Both?_(A/B/O)_", 'ABO');
}

# Use PGPLOT for Preview?
my $preview = -1;
if ($auto_scan >= 0){
    $preview = &ui_getkey("Plot_preview_after_scan?_(Y/N)_", 'NY');
}

print "\n";

### Get the job done >> ###
# Define default file name by time
my $start_time = &get_time(Time::HiRes::time);
my $data_file_A = $data_dir_path . '\SR780_' . $start_time . '_A.txt';
my $data_file_B = $data_dir_path . '\SR780_' . $start_time . '_B.txt';
my $plot_file = $data_dir_path . '\SR780_' . $start_time . '.ps';

# Open File(s) to Save Scan
if ($display != 1){ # Save Display A
    open DAT_A, ">>$data_file_A";
}
if ($display != 0){ # Save Display B
    open DAT_B, ">>$data_file_B";
}

# Open PGPLOT if preview is requested
if ($preview){
    &pgopen("$plot_file/ps");
    &pgenv($preview_x_min, $preview_x_max, $preview_y_min, $preview_y_max, 0, 30);
    &pglabel('Frequency_(Hz)', "PSD", '[SR780:_]' . $start_time . ']' . $remark);
}

# Start Manual Scan
$span_index = 1;
until ($scan_done){

    if ($auto_scan == 0){ # Manual Scan Mode
        print ">_Manual_Scan:_Adjust_SR780_and_take_acquisition.\n\n_When_ready,_come_back_to_
        ~~~~~
        program_to_download_data.\n\n";
        $scan_done = &ui_getkey("Download_Data_or_Finish_Scan?_(D/F)_", 'DF');
    }

    if ($auto_scan == 1){ # Auto Scan Mode

        $msg = ">_Acquiring_Span_#" . $span_index . "... \n";
    }
}

```

```

print $msg;

if ($span_index <= $n_span){

    if ($display != 1){ # Display A
        &vi_write($session_handle, 'FAVG_0,_1');
        &vi_write($session_handle, 'FAVM_0,_1'); # RMS Averaging
        &vi_write($session_handle, 'FAVT_0,_0'); # Linear Averaging Type
    }
    if ($display != 0){ # Display B
        &vi_write($session_handle, 'FAVG_1,_1');
        &vi_write($session_handle, 'FAVM_1,_1'); # RMS Averaging
        &vi_write($session_handle, 'FAVT_1,_0'); # Linear Averaging Type
    }
    $cmd = 'FREJ_2,_1';
    &vi_write($session_handle, $cmd);

    $msg = ">_Span_set._Start_Averaging...\n";
    print $msg;

    if ($display != 1){ # Display A
        &vi_write($session_handle, 'FSPN_0,_1' . $scan_param[$span_index-1][0]);
        &vi_write($session_handle, 'FAVN_0,_1' . $scan_param[$span_index-1][1]);
    }
    if ($display != 0){ # Display B
        &vi_write($session_handle, 'FSPN_1,_1' . $scan_param[$span_index-1][0]);
        &vi_write($session_handle, 'FAVN_1,_1' . $scan_param[$span_index-1][1]);
    }

    &vi_write($session_handle, 'DSPS?');
    &vi_read($session_handle, $buf_bytes);

    &vi_write($session_handle, 'STRT');

    if ($display != 1){ # Display A
        &vi_wait_AVGA($session_handle, 0, 60);
        &vi_write($session_handle, 'ASCL_0');
    }
    if ($display != 0){ # Display B
        &vi_wait_AVGA($session_handle, 1, 60);
        &vi_write($session_handle, 'ASCL_1');
    }
}

}

unless ($scan_done) {
    if ($display != 1){ # Download Display A
        $msg = ">_Reading_X_Data_of_Display_A...\n";
        print $msg;
        &vi_write($session_handle, 'FSTR?_0');
        my $f_a = &vi_read($session_handle, $buf_bytes);
        &vi_write($session_handle, 'FEND?_0');
        my $f_b = &vi_read($session_handle, $buf_bytes);
        &vi_write($session_handle, 'FLIN?_0');
        my $n_bin = 100*(2**&vi_read($session_handle, $buf_bytes)) + 1;

        my @data_x = ();
        my @data_y = ();
        &freq_axis_lin($f_a, $f_b, $n_bin, \@data_x);
        &vi_write($session_handle, 'DSPY?_0');

        $msg = ">_Reading_Y_Data_of_Display_A...\n";
        print $msg;
        &psd_parse(&vi_read($session_handle, 14000), \@data_y);

        print DAT_A '%_Span#' . $span_index . "\n";
        for (my $j = 0; $j < $n_bin; $j++){
            print DAT_A $j+1, "\t", $data_x[$j], "\t", $data_y[$j], "\n";
        }

        if ($preview){
            shift @data_x;
            shift @data_y;

            if ($auto_scan && $smart_auto_preview){
                if ($span_index < $n_span){
                    splice(@data_x, 0, 200);
                    splice(@data_y, 0, 200);
                }
            }

            foreach(@data_x){$_ = log($_)/log(10)};
            foreach(@data_y){$_ = log($_)/log(10)};

            # &pgsci($span_index);
            if ($auto_scan && $smart_auto_preview && ($span_index < $n_span)){
                &pgline($n_bin-1-200, \@data_x, \@data_y);
            }
            else{
                &pgline($n_bin-1, \@data_x, \@data_y);
            }
        }
    }
}

```

```

}
if ($display != 0){ # Download Display B
$msg = ">_Reading_X_Data_of_Display_B...\n";
print $msg;
&vi_write($session_handle, 'FSTR?_1');
my $f_a = &vi_read($session_handle, $buf_bytes);
&vi_write($session_handle, 'FEND?_1');
my $f_b = &vi_read($session_handle, $buf_bytes);
&vi_write($session_handle, 'FLIN?_1');
my $n_bin = 100*(2**&vi_read($session_handle, $buf_bytes)) + 1;

my @data_x = ();
my @data_y = ();
&freq_axis_lin($f_a, $f_b, $n_bin, \@data_x);
&vi_write($session_handle, 'DSPY?_1');

$msg = ">_Reading_Y_Data_of_Display_B...\n";
print $msg;
&psd_parse(&vi_read($session_handle, 14000), \@data_y);

&usleep(1.0*1_000_000);

print DAT_B '%_Span_#' . $span_index . "\n";
for (my $j = 0; $j < $n_bin; $j++){
print DAT_B $j+1, "\t", $data_x[$j], "\t", $data_y[$j], "\n";
}

if ($preview){
shift @data_x;
shift @data_y;

if ($auto_scan && $smart_auto_preview){
if ($span_index < $n_span){
splice(@data_x, 0, 200);
splice(@data_y, 0, 200);
}
}

foreach(@data_x){$_ = log($_)/log(10);}
foreach(@data_y){$_ = log($_)/log(10);}

# &pgsci($span_index);
if ($auto_scan && $smart_auto_preview && ($span_index < $n_span)){
&pgline($n_bin-1-200, \@data_x, \@data_y);
}
else{
&pgline($n_bin-1, \@data_x, \@data_y);
}
}
}

if (($auto_scan == 1) && ($span_index == $n_span)){
$scan_done = 1;
}

$msg = ">_Span_#" . $span_index . "_Done.\n\n";
print $msg;

$span_index++;
}

# Close Files
close DAT_A;
close DAT_B;

if ($display != 1){ # Save Display A
print "Data_file_created_(A):_" . $data_file_A . "\n";
}
if ($display != 0){ # Save Display A
print "Data_file_created_(B):_" . $data_file_B . "\n";
}

# Close Preview
if ($preview){
&pgclos;
print "Plot_file_created:_" . $plot_file . "\n";
print "\n(Close_preview_to_return_to_program...)\n\n";
system("$gsview_$plot_file");
}

# Another Scan?
if (&ui_getkey("Scan_Finished._Take_another_Scan?(Y/N)_", 'NY')){
$scan_done = 0;
goto SCAN;
}

FINE:

## Footer >>
&vi_close($manager_handle, $session_handle);
$msg = ">_GPIB_Connection_Closed.\n\n";
print $msg;
$msg = "End_of_Perl_script:_sr780_v302.pl_by_Li-Wei_Wei\n";

```



```

print $msg;
## << Footer

##### Subroutines / Functions #####

# Data Processing >> #
sub freq_axis_lin{
my $f_a = shift;
my $f_b = shift;
my $n_bin = shift;
my $ptr_array = shift;
for (my $i = 0; $i < $n_bin; $i++){
    $$ptr_array[$i] = $f_a + ($f_b-$f_a)/($n_bin-1)*$i;
}
}

sub psd_parse{
my $data_str = shift;
my $ptr_array = shift;
@$ptr_array = split(/,/ , $data_str);
}
# << Data Processing #

# UI >> #
sub ui_getkey{
my $msg = shift;
my @ans_array = split(/, / , shift);
my $key = '';
my $key_index = 0;
my $match = 0;

while ($key eq ''){
print STDOUT $msg;
$key_index = 0;
$key = <STDIN>;
$key = uc(substr($key, 0, 1));

foreach (@ans_array){
if ($key eq $_){
$match = 1;
last;
}
}
$key_index++;
}
unless ($match){
$key = '';
}
}
return $key_index;
}
# << UI #

# GPIB >> #

sub vi_initialize{
my $resource_name = shift;
my $manager_handle = shift;
my $session_handle = shift;

$manager_handle = pack('i', $manager_handle); # Resource Manager Handle
$vi_return = $fViOpenDefaultRM->Call($manager_handle);
die ("Could_not_open_Resource_Manager._Error:_", $vi_return, "\n" ) unless ($vi_return == 0);
$manager_handle = unpack('i', $manager_handle);

$session_handle = pack('i', $session_handle); # Instrument Handle
$vi_return = $fViOpen->Call($manager_handle, $resource_name, $cVI_NULL, $cVI_NULL, $session_handle);
die ("Could_not_open_Resource_Session._Error:_", $vi_return, "\n" ) unless ($vi_return == 0);
$session_handle = unpack('i', $session_handle);

$vi_return = $fViSetAttribute->Call($session_handle, $cVI_ATTR_TMO_VALUE, $timeout);
die ("Could_not_set_Timeout_Attribute._Error:_", $vi_return, "\n" ) unless ($vi_return == 0);

print "\nConnection_Established_at_" . $resource_name . "\n\n";

return ($manager_handle, $session_handle);
}

sub vi_write{
my $session_handle = shift;
my $bufferToWrite = shift;

my $bytesToWrite = length($bufferToWrite);
$bytes_written = pack('i', 0);
$vi_return = $fViWrite->Call($session_handle, $bufferToWrite, $bytesToWrite, $bytes_written);
unless ($vi_return == 0){
print STDOUT "Could_not_write_" . $bufferToWrite . "_to_Device._Error:_", $vi_return, "\n" ;
my $debug = &ui_getkey("Ignore,_Debug,_or_Abort_(I/D/A)_", 'IDA');
if ($debug == 0){
# Clear all status registers. (The enable registers are not changed.)
&vi_write($session_handle, '*CLS');
}
}
elseif ($debug == 1){

```

```

        &vi_debug($session_handle);
        &vi_write($session_handle, '*CLS');
    }
    else{
        die;
    }
}
$bytes_written = unpack('i', $bytes_written);
&usleep(0.1*1_000_000);
# system("pause");
}

sub vi_read{
my $session_handle = shift;
my $bytesToRead = shift;
my $response = "\0" x $bytesToRead;
$bytes_read = pack('i', 0);
$vi_return = $fViRead->Call($session_handle, $response, $bytesToRead, $bytes_read);
unless ($vi_return == 0){
    print STDOUT "Could_not_Read_Response_from_Device_Error:\n", $vi_return, "\n" ;
    my $debug = &ui_getkey("Ignore,_Debug,_or_Abort_(I/D/A)\n", 'IDA');
    if ($debug == 0){
        # Clear all status registers. (The enable registers are not changed.)
        &vi_write($session_handle, '*CLS');
    }
    elsif($debug == 1){
        &vi_debug($session_handle);
        &vi_write($session_handle, '*CLS');
    }
    else{
        die;
    }
}

$bytes_read = unpack('i', $bytes_read);
$response =~ s/\n.*$//;
return $response;
}

sub vi_close{
$manager_handle = shift;
$session_handle = shift;
$vi_return = $fViClose->Call($session_handle);
die ("Could_not_close_Resource_Session_Error:\n", $vi_return, "\n" ) unless ($vi_return == 0);
$vi_return = $fViClose->Call($manager_handle);
die ("Could_not_close_Resource_Manager_Error:\n", $vi_return, "\n" ) unless ($vi_return == 0);

print "\nConnection_Closed.\n\n";
}

sub vi_debug{
my $session_handle = shift;
my $response = "\0" x 1;

print STDOUT ">_-----_FEDCBA9876543210\n";

$response = "\0" x 1;
&vi_write($session_handle, '*STB?');
$response = &vi_read($session_handle, $buf_bytes);
chomp($response);
print STDOUT ">_STB_ " . sprintf("%18.08b", $response) . "\n";

$response = "\0" x 2;
&vi_write($session_handle, 'INST?');
$response = &vi_read($session_handle, $buf_bytes);
chomp($response);
print STDOUT ">_0_INST" . sprintf("%18.016b", $response) . "\n";

$response = "\0" x 2;
&vi_write($session_handle, 'DSPS?');
$response = &vi_read($session_handle, $buf_bytes);
chomp($response);
print STDOUT ">_1_DSPS" . sprintf("%18.016b", $response) . "\n";

$response = "\0" x 2;
&vi_write($session_handle, 'INPS?');
$response = &vi_read($session_handle, $buf_bytes);
chomp($response);
print STDOUT ">_2_INPS" . sprintf("%18.016b", $response) . "\n";

$response = "\0" x 2;
&vi_write($session_handle, 'ERRS?');
$response = &vi_read($session_handle, $buf_bytes);
chomp($response);
print STDOUT ">_3_ERRS" . sprintf("%18.016b", $response) . "\n";

$response = "\0" x 1;
&vi_write($session_handle, '*ESR?');
$response = &vi_read($session_handle, $buf_bytes);
chomp($response);
print STDOUT ">_5_ESR_ " . sprintf("%18.08b", $response) . "\n";
}
}

```

```

sub vi_wait_AVGA{
my $session_handle = shift;
my $display = shift;
my $timeout = shift;
my $avg_done = 0;
my $counter = 0;

until ($avg_done){
if ($display == 0){
&vi_write($session_handle, 'DSPS?_1'); # Bit 1: AVGA, DisplayA linear average has completed
}
if ($display == 1){
&vi_write($session_handle, 'DSPS?_9'); # Bit 9: AVGB, DisplayB linear average has completed
}
&usleep(1.0*1_000_000);
$avg_done = &vi_read($session_handle, $buf_bytes);

$counter++;
unless($counter < $timeout){
$avg_done = 1;
}
}
}

# << GPIB #

# AUX >> #
sub get_time{
my $time_hi_res = shift;
my $time = floor($time_hi_res);
my $sec_fraction = floor(($time_hi_res - $time)*1000);
my ($sec,$min,$hour,$mday,$mon,$year,$yday,$isdst) = localtime($time);
$year -= 100;
$mon += 1;
return (sprintf("%02d%02d%02d_%02dh%02dm%02ds%03d", $year, $mon, $mday, $hour, $min, $sec, $sec_fraction));
}

# << AUX #

```

G.2 For Hewlett-Packard HP8591A Spectrum Analyzer

```

#!/usr/bin/perl -w
use strict;
use POSIX qw(floor ceil);
use Time::HiRes qw(usleep);
use Win32::API;
use PGPLOT;
use Net::SMTP::SSL;
use MIME::Base64;
use List::Util qw(min max);

##### Scan Parameters #####

my $remark = '';

# Instrument Settings
my $resource_name = "GPIB1::13::INSTR"; # Resource: GPIB Device 0, Primary Address 2
my $timeout = 50000; # Timeout: 50000ms
my $n_span = 7;
my $amp_unit = 'V';
my $det_mode = 'SMP';
my $input_z = '50';
my $ref_lvl = '10E-3';
my @scan_param = (
# 0, 1, 2, 3, 4, 5, 6
# ref_lvl, Attenu, Freq_a, Freq_b, RBW, VBW, n_VAVG
[$ref_lvl, '0_DB', '10kHz', '100kHz', '1kHz', '100Hz', '5'],
[$ref_lvl, '0_DB', '100kHz', '300kHz', '3kHz', '300Hz', '15'],
[$ref_lvl, '0_DB', '300kHz', '1MHz', '10kHz', '1kHz', '25'],
[$ref_lvl, '0_DB', '1MHz', '3MHz', '30kHz', '3kHz', '50'],
[$ref_lvl, '0_DB', '3MHz', '10MHz', '100kHz', '10kHz', '50'],
[$ref_lvl, '0_DB', '10MHz', '30MHz', '300kHz', '30kHz', '100'],
[$ref_lvl, '0_DB', '30MHz', '100MHz', '1MHz', '100kHz', '100']
);

# Data Settings
my $data_dir_path = 'C:\pl_data\hp8591a';
my $debug_on = 1;
my $send_by_email = 0;
my $email_recipients = 'aelo.tw@gmail.com';
# &GMail_Send($gmail_acc, $gmail_pwd, $from, $to, $subject, $body);

#####

```

```

# Plot Settings
my $plot = 'loglog';
my $axes = 'arbitrary';
my $gsview = q/"C:\Program Files\Ghostgum\gsview\gsview32.exe"/;

# Define default file name by time
my $start_time = &get_time(Time::HiRes::time);
my $data_dir_path = "\HP8591A\_";
my $data_file = $data_dir_path . $start_time . '.txt';
my $plot_file = $data_dir_path . "\HP8591A\_";
my $debug_file = $data_dir_path . "\debug\HP8591A\_";

# Gmail account setting
my $gmail_acc = 'artemis.perl@gmail.com';
my $gmail_pwd = '+Virgo2013';
my $from = "Pearl_d'Artemis";
my $to = $email_recipients;
my $subject = 'HP8591A_Data';

# PGPLOT variables
my %plot_type = (
    'linear', 0,
    'semilogx', 10,
    'semilogy', 20,
    'loglog', 30);

my %axes_type = (
    'arbitrary', 0,
    'equal', 1);

# Initialize Variables
my $bytes_written = 0;
my $bytes_read = 0;
my $vi_return = 0;
my $n_bin = 401;

# c.f. VISA C Reference Help for VISA32 function prototypes
my $VIOpenDefaultRM = Win32::API->new('visa32','viOpenDefaultRM','P','I'); # RM: Resource Manager
my $VIOpen = Win32::API->new('visa32','viOpen','IPIP','I');
my $VIOSetAttribute = Win32::API->new('visa32','viSetAttribute','III','I');
my $VIWrite = Win32::API->new('visa32','viWrite','IPIP','I');
my $VIRead = Win32::API->new('visa32','viRead','IPIP','I');
my $VIBufRead = Win32::API->new('visa32','viBufRead','IPIP','I');
my $VIClose = Win32::API->new('visa32','viClose','I','I');
my $VIReadAsync = Win32::API->new('visa32','viRead','IPIP','I');
my $VIReadSTB = Win32::API->new('visa32','viReadSTB','IP','I');
my $VIClear = Win32::API->new('visa32','viClear','I','I');

# c.f. visa.h for VISA32 constants
my $cVI_NULL = 0; # VI_NULL constant from visa.h
my $cVI_ATTR_TMO_VALUE = 1073676314; # Timeout Attribute Constant from visa.h

# Main
my @x_axis = ();
my @y_axis = ();
my @data_x = ();
my @data_y = ();

my $ans_GPIB = '';
my $buf_bytes = 50;
my $tdf = 'P'; # Trace Data Format

open CFG, ">>$data_file";
print CFG "\%_HP8591A_Spectrum_Analyzer\n";
print CFG "\%_Remark:_", $remark, "\n";
print CFG "\%_Resource_Name:_", $resource_name, "\n";
print CFG "\%_Timeout:_", $timeout, "_ms\n";
print CFG "\%_Number_of_Spans:_", $n_span, "\n";
print CFG "\%_Amplitude_Unit:_", $amp_unit, "\n";
print CFG "\%_Detection_Mode:_", $det_mode, "\n";
print CFG "\%_Input_Impedance:_", $input_z, "\n";
print CFG "\%_Parameters_for_Each_Span:>\n";
print CFG "\%_Reference_Level, Attenuation, Start_Frequency, Stop_Freq, Resolution_Bandwidth, Video_Bandwidth, Video_Averaging\n";
foreach (@scan_param) {
    print CFG "%_";
    foreach (@$_) {
        print CFG $_, ' , ' ;
    }
    print CFG "\n";
}
print CFG "\%_<<\n";
close CFG;

if ($debug_on == 1) {
    open DBG, ">>$debug_file";
}

open DAT, ">>$data_file";

system("cls");
print "\nHP8591A_Spectrum_Analyzer\n\n";
print "Remark:_", $remark, "\n";
print "Resource_Name:_", $resource_name, "\n";
print "Timeout:_", $timeout, "_ms\n";

```

```

print "Number_of_Spans:_", $n_span, "\n";
print "Amplitude_Unit:_", $amp_unit, "\n";
print "Detection_Mode:_", $det_mode, "\n";
print "Input_Impedance:_", $input_z, "\n";
print "\nParameters_for_Each_Span_>_";
print "REF_LVL\t\tATTEN\tFREQA\tFREQB\tRBW\tVBW\tV-AVG\n";
foreach(@scan_param){
    foreach(@$_){
        print $_, "\t";
    }
    print "\n";
}
print "<<\n";

my ($manager_handle, $session_handle) = vi_initialize($resource_name, 0, 0);
# vi_write($session_handle, 'IP;');
vi_write($session_handle, 'DET_' . $det_mode . ');');
vi_write($session_handle, 'INZ_' . $input_z . ');');
vi_write($session_handle, 'AUNITS_' . $amp_unit . ');');
vi_write($session_handle, 'SNGLS;');
vi_write($session_handle, 'TDF_' . $tdf . ');');

my $temp_time = 0;
for (my $i = 0; $i < $n_span; $i++){

    print "Acquiring_Span_#" . ($i+1) , "... \n";

    $temp_time = Time::HiRes::time;
    print DAT sprintf("%_Time_Stamp:_%s,_%16.5f\n", &get_time($temp_time), $temp_time);
    print DAT "%_Span_#" . ($i+1) . "\n";
    print DAT sprintf("%_Bin_No.\tFreq_(Hz)\tAmp_(%s)\tPSD_(%s/rtHz)\n", $amp_unit, $amp_unit);

    vi_write($session_handle, 'RL_' . $scan_param[$i][0] . ');');
    vi_write($session_handle, 'AT_' . $scan_param[$i][1] . ');');
    vi_write($session_handle, 'FA_' . $scan_param[$i][2] . ');');
    vi_write($session_handle, 'FB_' . $scan_param[$i][3] . ');');
    vi_write($session_handle, 'RB_' . $scan_param[$i][4] . ');');
    vi_write($session_handle, 'VB_' . $scan_param[$i][5] . ');');
    vi_write($session_handle, 'VAVG_' . $scan_param[$i][6] . ');');

    vi_write($session_handle, 'CLRAVG;');
    vi_write($session_handle, 'TS;');

    vi_write($session_handle, 'DONE?');
    # $ans_GPIB = vi_read($session_handle, $buf_bytes);

    vi_write($session_handle, 'TRA?');
    # $ans_GPIB = '';
    $ans_GPIB = vi_read($session_handle, 5000);

    if ($debug_on == 1){
        print DBG "%_Span_#" . ($i+1) . "\n";
        print DBG "Raw_answer_from_GPIB_after_the_TRA?_command_>>\n\n";
        print DBG $ans_GPIB;
        print DBG "<<\n\n";
    }

    # $ans_GPIB =~ s/\s\D?\s*//;
    # $ans_GPIB =~ s/\x00\D?\x00*//;
    # $ans_GPIB =~ chomp($ans_GPIB);
    $ans_GPIB =~ s/\r\n.*//;

    if ($debug_on == 1){
        print DBG "After_processing_with_regular_expression_s/\r\n.*\s*//>>' . "\n";
        print DBG $ans_GPIB;
        print DBG "\n<<\n\n";
    }

}

&freq_axis_lin(&freq_str2num($scan_param[$i][2]), &freq_str2num($scan_param[$i][3]), $n_bin, \@x_axis);
&psd_parse($ans_GPIB, \@y_axis);
for (my $j = 0; $j < $n_bin; $j++){
    print DAT $j+1, "\t", $x_axis[$j], "\t", $y_axis[$j], "\t",
        &ewo0("%.4E", ($y_axis[$j]/sqrt(&freq_str2num($scan_param[$i][4])))), "\n";
}
foreach(@x_axis){$_ = log($_)/log(10);}
foreach(@y_axis){$_ = log($_/sqrt(&freq_str2num($scan_param[$i][4])))/log(10);}
if ($i != 0){
    shift @x_axis;
    shift @y_axis;
}
push @data_x, @x_axis;
push @data_y, @y_axis;

print(sprintf("\tDone_in_%.03f_seconds.\n", (Time::HiRes::time-$temp_time)));
print DAT sprintf("%_Span#_#d_acquisition:_%.03f_seconds\n", ($i+1), (Time::HiRes::time-$temp_time));

$temp_time = Time::HiRes::time;
print DAT sprintf("%_Time_Stamp:_%s,_%16.5f\n", &get_time($temp_time), $temp_time);
}
&vi_close($manager_handle, $session_handle);

print DAT "\n";
close DAT;

```

```

print "Data_file_created:_" . $data_file . "\n";

my @rl_f = (); # reference level
my @rl_psd = ();
my @rl_psd_value = ();
my @mf_psd = (); # measurement floor
my @mf_psd_value = ();
foreach(@scan_param){
    my @rl_f_span = ();
    my @rl_psd_span = ();
    my @mf_psd_span = ();
    push @rl_f_span, (log(&freq_str2num($$_[2]))/log(10));
    push @rl_f_span, (log(&freq_str2num($$_[3]))/log(10));
    push @rl_psd_span, (log($$_[0]/sqrt(&freq_str2num($$_[4])))/log(10));
    push @rl_psd_span, (log($$_[0]/sqrt(&freq_str2num($$_[4])))/log(10));
    push @mf_psd_span, (log($$_[0]*1e-4/sqrt(&freq_str2num($$_[4])))/log(10));
    push @mf_psd_span, (log($$_[0]*1e-4/sqrt(&freq_str2num($$_[4])))/log(10));
    push @rl_f, \@rl_f_span;
    push @rl_psd, \@rl_psd_span;
    push @mf_psd, \@mf_psd_span;
    push @rl_psd_value, @rl_psd_span;
    push @mf_psd_value, @mf_psd_span;
}

my ($x_min, $x_max) = (floor(min @data_x), ceil(max @data_x));
my ($y_min, $y_max) = ( floor(min (@data_y, @rl_psd_value, @mf_psd_value)),
    ceil (max (@data_y, @rl_psd_value, @mf_psd_value)) );

&pgopen("$plot_file/ps");
&pgenv($x_min, $x_max, $y_min, $y_max, $axes_type{$axes}, $plot_type{$plot});
&pglabel('Frequency_(Hz)', "PSD_($amp_unit/rtHz)", "[HP8591A:_" . $start_time . ']' . $remark);
&pgline($n_span*(($n_bin-1)+1), \@data_x, \@data_y);
&pgsls(2);
for(my $i=0; $i<$n_span; $i++){
    &pgline(2, \@{$rl_f[$i]}, \@{$rl_psd[$i]});
    &pgline(2, \@{$rl_f[$i]}, \@{$mf_psd[$i]});
}
&pgclos;
print "Plot_file_created:_" . $plot_file . "\n";
print "\n(Close_the_plot_to_return_to_program...) \n\n";

system("$gsview_$plot_file");

# Subroutines / Functions

sub vi_initialize{
    my $resource_name = shift;
    my $manager_handle = shift;
    my $session_handle = shift;

    $manager_handle = pack('i', $manager_handle); # Resource Manager Handle
    $vi_return = $fViOpenDefaultRM->Call($manager_handle);
    die ("Could_not_open_Resource_Manager_Error:_", $vi_return, "\n" ) unless ($vi_return == 0);
    $manager_handle = unpack('i', $manager_handle);

    $session_handle = pack('i', $session_handle); # Instrument Handle
    $vi_return = $fViOpen->Call($manager_handle, $resource_name, $cVI_NULL, $cVI_NULL, $session_handle);
    die ("Could_not_open_Resource_Session_Error:_", $vi_return, "\n" ) unless ($vi_return == 0);
    $session_handle = unpack('i', $session_handle);

    $vi_return = $fViSetAttribute->Call($session_handle, $cVI_ATTR_TMO_VALUE, $timeout);
    die ("Could_not_set_timeout_Attribute_Error:_", $vi_return, "\n" ) unless ($vi_return == 0);

    print "\nConnection_Established_at_" . $resource_name . "\n\n";

    return ($manager_handle, $session_handle);
}

sub vi_write{
    my $session_handle = shift;
    my $bufferToWrite = shift;

    my $bytesToWrite = length($bufferToWrite);
    $bytes_written = pack('i', 0);
    $vi_return = $fViWrite->Call($session_handle, $bufferToWrite, $bytesToWrite, $bytes_written);
    die ("Could_not_write_" . $bufferToWrite . "_to_Device_Error:_", $vi_return, "\n" ) unless ($vi_return == 0);
    $bytes_written = unpack('i', $bytes_written);
}

sub vi_read{
    my $session_handle = shift;
    my $bytesToRead = shift;
    my $response = "\0" x $bytesToRead;
    $bytes_read = pack('i', 0);
    $vi_return = $fViRead->Call($session_handle, $response, $bytesToRead, $bytes_read);
    die ("Could_not_Read_Response_from_Device_Error:_", $vi_return, "\n" ) unless ($vi_return == 0);
    $bytes_read = unpack('i', $bytes_read);
    # $response =~ s/\s+$/;/;
    # $response =~ s/\x00+$/;/;
    return $response;
}

sub vi_close{
    my $manager_handle = shift;
    my $session_handle = shift;
    $vi_return = $fViClose->Call($session_handle);
}

```

```

die ("Could_not_close_Resource_Session_Error:_", $vi_return, "\n" ) unless ($vi_return == 0);
$vi_return = $fViClose->Call($manager_handle);
die ("Could_not_close_Resource_Manager_Error:_", $vi_return, "\n" ) unless ($vi_return == 0);

print "\nConnection_Closed.\n\n";
}

sub freq_axis_lin{
my $f_a = shift;
my $f_b = shift;
my $n_bin = shift;
my $ptr_array = shift;
for (my $i = 0; $i < $n_bin; $i++){
    $ptr_array[$i] = $f_a + ($f_b-$f_a)/($n_bin-1)*$i;
    # $$ptr_array[$i] = log($f_a + ($f_b-$f_a)/($n_bin-1)*$i)/log(10);
}
}

sub psd_parse{
my $data_str = shift;
my $ptr_array = shift;
@$ptr_array = split(/,/ , $data_str);
}

sub get_time{
my $time_hi_res = shift;
my $time = floor($time_hi_res);
my $sec_fraction = floor(($time_hi_res - $time)*1000);
my ($sec,$min,$hour,$mday,$mon,$year,$yday,$yday,$isdst) = localtime($time);
$year -= 100;
$mon += 1;
return (sprintf("%02d%02d%02d%02dh%02dm%02ds%03d", $year, $mon, $mday, $hour, $min, $sec, $sec_fraction));
}

sub GMail_Send(){
my $gmail_acc = shift;
my $gmail_pwd = shift;
my $from = shift;
my $to = shift;
my $subject = shift;
my $body = shift;

my $smtp = Net::SMTP::SSL->new('smtp.gmail.com', Port => 465, Debug => 1)
|| die "Could_not_connect_to_server\n";

$smtp->auth($gmail_acc, $gmail_pwd)
|| die "Authentication_failed!\n";

$smtp->mail($from . "\n");
my @reipients = split(/,/ , $to);
foreach (@reipients){
    $smtp->to($_ . "\n");
}
$smtp->data();
$smtp->datasend("From:_" . $from . "\n");
$smtp->datasend("To:_" . $to . "\n");
$smtp->rawdatasend("Subject:_" . $subject . "\n");
$smtp->datasend("Content-Type:_text/plain;" . "\n");
$smtp->datasend("Content-Transfer-Encoding:_8bit" . "\n");
$smtp->datasend("\n");
$smtp->rawdatasend($body . "\n");
$smtp->datasend("\n");
$smtp->dataend();
$smtp->quit;
}

sub freq_str2num{
my $freq_str = shift;
$freq_str =~ s/kHz$/000/i;
$freq_str =~ s/MHz$/000000/i;
$freq_str =~ s/GHz$/0000000/i;
return $freq_str;
}

sub ewo0{
# (e)xponential form (w)ith(o)ut leading (0)'s in exponent
my $input = sprintf(shift, shift); # (format, input)
my $tail = chop $input;
my $temp = '0';
    $temp = chop $input; if ($temp ne '0'){ $tail = $temp . $tail};
    $temp = chop $input; if ($temp ne '0'){ $tail = $temp . $tail};
return ($input . $tail);
}

```

Appendix H

NI-DAQmx Wrapped with Perl

We also use the Perl programming language to wrap the NI-DAQmx library for ADC data acquisition. LabVIEW was also used for some early graphic implementations with GUI, but in view of the flexibility, the ease of code maintenance and the concept of free software, the migration to Perl took place. The source code is attached despite the lack of proper arrangement and optimization. We note that in this example code the acquisition between multiple input channels is asynchronous so that we can take advantage of the maximum sampling rate of the ADC card for individual input channels, at the cost of finite delay between channels. It should be straightforward though to change the implementation to synchronous acquisition. The ability to read from thermal couple probes is also implemented, as well as features like: threshold alarm with hysteresis and email notifications. In general for long-term monitoring only the statistics of the acquired time series are registered at each acquisition. The acquired time series may however be also registered at a given time interval.

```
#!/usr/bin/perl -w
use strict;
use POSIX qw(floor);
use Win32::API;
use Math::Int64 qw(int64 uint64);
use Time::HiRes qw(usleep);
use Term::ReadKey;
use Net::SMTP::SSL;
use MIME::Base64;
$I = 1;
my $cd_path = 'C:\perldaq';

#####

# ADC settings: 1 = Yes, -1 = No
my $remark = 'Remark';
my $sampling_rate = 20_000;
my $samples_per_ch = 10_000;
my @channels = (
# Physical      Name      Type  Min  Max  Alert  Thres  Hyste  Remark
# 0             1       2    3    4    5      6      7      8
# Type: just an identifier on what to do with this channel in the following code
# Alert: Off(0)/If Larger(1)/Smaller(-1) Than; Thres = Threshold Level; Hyster = Hysteresis Threshold
[ 'dev2/ai0', 'Ch0', 1, -10, 10, 0, 0.00, 0.00, 'Channel_Description'],
[ 'dev2/ai1', 'Ch1', 1, -1, 1, -1, 0.70, 0.71, 'NPRO_Laser'],
[ 'dev2/ai2', 'Ch2', 1, -5, 5, -1, 2.70, 2.74, 'Photodiode'],
[ 'dev2/ai6', 'Ch3', 1, -5, 5, 0, 0.00, 0.00, 'Calorimeter'],
[ 'dev2/ai3', 'Ch4', 1, -5, 5, 0, 0.00, 0.00, 'Quadrant_Photodiode,_Horizontal'],
[ 'dev2/ai4', 'Ch5', 1, -5, 5, 0, 0.00, 0.00, 'Quadrant_Photodiode,_Vertical'],
[ 'dev1/ai0', 'Ch13', 2, 0, 100, +1,26.00,25.00, 'Temperature_Thermal_Couple,_J-Type'],
);
my $data_dir_path = 'D:\pl_data\daq';
my $data_dir_path = 'C:\Documents and Settings\liwei\Bureau\liwei\data\pl_data\daq';
my $read_interval = 10.0; # Read ADC every $read_interval seconds
my $delay_after_acq = 0.00; # Delay after each ADC acquisition
my $save_data = -1; # 1 = Yes, -1 = No
my $data_interval = 1; # Save data (Mean, Std. Dev., RMS) every $data_interval * $read_interval
my $save_raw = 1; # 1 = Yes, -1 = No
```



```

my $raw_interval = 6*15; # Save raw ADC acquisitions every $raw_interval * $data_interval
my $check_alert = 1; # 1 = Yes, -1 = No
my $email_interval = 6*30; # Send Email Alert every $email_interval * $data_interval
my $email_recipients = 'xxxxx@xxx.xxx,yyy@yyy.yyy';
my $fString = q(10.10s);
my $fStringA = q(8.8s);
my $fDisp = q(%11.4e);
my $fDispA = q(%9.2e);
my $fData = $fDisp;
my $fRaw = $fDisp;
my $locked = -1; # Key input locked or not on start, 1 = Yes, -1 = No

#####

my $sync = -1;

my $task_name = 'plMulti';
my $task_handle = 0;
my $n_channels = $#channels + 1;

# c.f. NI-DAQmx C Reference Help for NIDAQmx function prototypes
my $fCreateTask = Win32::API->new('nicaiu', 'DAQmxCreateTask', 'PP', 'i');
my $fCreateAIVoltageChan = Win32::API->new('nicaiu', 'DAQmxCreateAIVoltageChan', 'iPPiDiP', 'i');
my $fCreateAIThrmcp1Chan = Win32::API->new('nicaiu', 'DAQmxCreateAIThrmcp1Chan', 'iPPDDiDiP', 'i');
my $fSetRate = Win32::API->new('nicaiu', 'DAQmxCfgSampClkTiming', 'iPDiiQ', 'i');
my $fStartTask = Win32::API->new('nicaiu', 'DAQmxStartTask', 'i', 'i');
my $fReadAnalogScalarF64 = Win32::API->new('nicaiu', 'DAQmxReadAnalogScalarF64', 'iDPP', 'i');
my $fReadAnalogF64 = Win32::API->new('nicaiu', 'DAQmxReadAnalogF64', 'iiDiPiPP', 'i');
my $fWaitUntilTaskDone = Win32::API->new('nicaiu', 'DAQmxWaitUntilTaskDone', 'iD', 'i');
my $fStopTask = Win32::API->new('nicaiu', 'DAQmxStopTask', 'i', 'i');
my $fClearTask = Win32::API->new('nicaiu', 'DAQmxClearTask', 'i', 'i');

# c.f. NIDAQmx.h for NIDAQmx constants
my $cDAQmx_Val_Cfg_Default = -1;
my $cDAQmx_Val_RSE = 10083;
my $cDAQmx_Val_NRSE = 10078;
my $cDAQmx_Val_Diff = 10106;
my $cDAQmx_Val_PseudoDiff = 12529;
my $cTerminalConfig = $cDAQmx_Val_RSE;
my $cDAQmx_Val_Volts = 10348;
my $cDAQmx_Val_DegC = 10143;
my $cCustomScaleName = ""; #
my $cDAQmx_Val_Rising = 10280;
my $cDAQmx_Val_Falling = 10171;
my $cActiveEdge = $cDAQmx_Val_Rising;
my $cDAQmx_Val_FiniteSamps = 10178;
my $cDAQmx_Val_ContSamps = 10123;
my $cDAQmx_Val_HWTimedSinglePoint = 12522;
my $cSampleMode = $cDAQmx_Val_FiniteSamps;
my $cReserved = 0; # Reserved
my $cInterlace = 0; # 1 // interleaved, 0 // noninterleaved
my $cDAQmx_Val_J_Type_TC = 10072; # 10072 // J-type thermocouple.
my $cDAQmx_Val_BuiltIn = 10200; # source of cold junction compensation: 10200 // Built-In
my $cReadTimeout = 10.0;

# Gmail account setting
my $gmail_acc = 'Gmail_account';
my $gmail_pwd = 'Password';
my $from = "Pearl_d'Artemis";
my $to = $email_recipients;
my $subject = 'Alert_from_Perl-DAQ';

# declare and initialize variables
my $report = 0;
my $scalar_out = 0;
my $waveform_size = $samples_per_ch * $n_channels;
my $waveform_out = "\0" x 8 x $waveform_size;
my @data_array = [(0) x $n_channels], [(0) x $samples_per_ch];
my @mean = ((0) x $n_channels);
my @stddev = ((0) x $n_channels);
my @rms = ((0) x $n_channels);
my $samples_per_ch_read = 0;
my ($i, $j, $k) = 0;
my ($ctr_data, $ctr_raw, $ctr_email) = (0, 0, 0);
my $temp_time = 0;
my $temp_time_prime = 0;
my $config_saved = 0;
my $alert_triggered = -1;
my @alert_status = ((-1) x $n_channels);
my @eyes_no = ('N', 'Y');
my @lg_sm = ('<', '-', '>');
my @alert_disp = ('o', '-', 'x');
my $body = '';

# chdir
chdir($cd_path);

#####

my $start_time = &get_time(Time::HiRes::time);
my $data_file = $data_dir_path . "\data_" . $start_time . ".txt";

$subject = join('_', $subject, $start_time);

my $key_in = "\0"; # whenever undef, make it \0 to avoid using undef values for comparison

```

```

ReadMode 3;          # ReadKey Setting: 4=Turn off controls keys
while ($key_in ne 's' || $locked == 1){
    $temp_time = Time::HiRes::time;

    ## Parse Key Input
    $key_in = ReadKey(-1);
    if (not defined $key_in){ $key_in = "\0"; }
    # whenever undef, make it \0 to avoid using undef values for comparison
    if (defined $key_in){
        if ($key_in eq 'k'){ $locked *= -1; } # k for Locked
        if ($key_in eq 'd'){ if ($locked != 1){ $save_data *= -1; }} # d for Save Data
        if ($key_in eq 'r'){ if ($locked != 1){ $save_raw *= -1; }} # r for Save Raw
        if ($key_in eq 'a'){ if ($locked != 1){ $check_alert *= -1; }} # a for Save Raw
        if ($key_in eq 'h'){ # c for Save Config
            if ($locked != 1){
                open CFG, ">>$data_file";
                print CFG "\%_Remark:_", $remark, "\n";
                print CFG "\%_Sampling_Rate:_", $sampling_rate, "\n";
                print CFG "\%_Samples_per_Channel:_", $samples_per_ch, "\n";
                print CFG "\%_Sync:_", $yes_no[($sync+1)/2], "\n\n";
                for ($i = 0; $i < $n_channels; $i++){
                    print CFG "\%_",
                        $channels[$i][0], "_", $channels[$i][1], "_", $channels[$i][2], "_",
                        $channels[$i][3], "_", $channels[$i][4], "_", $channels[$i][5], "_",
                        $channels[$i][6], "_", $channels[$i][7], "_", $channels[$i][8], "\n";
                }
                print CFG "\%_n%_Perl_Seconds\tTime";
                for ($i = 0; $i < $n_channels; $i++){
                    print CFG sprintf("\tCh%i-Mean\tCh%i-StdDev\tCh%i-RMS", $i);
                }
                print CFG "\n\n";
                close CFG;
                $config_saved++;
            }
        }
        if ($key_in eq 'g'){ # g for Debug
            $save_raw_data(@data_array, $n_channels, $samples_per_ch, $data_dir_path,
                'raw', 'debug', 'txt', $fRaw);
        }
    }

    ## Display Config
    system("cls");
    print "\nPerl-DAQ->>_Time:_", &get_time($temp_time), ";_t0:_", $start_time, "\n";
    print "\nChannels:_", $n_channels, ";_Sampling_Rate:_", $sampling_rate, ";_S/Ch:_",
        $samples_per_ch, ";_Sync:_", $yes_no[($sync+1)/2], "\n";
    print "Lock:_", $yes_no[($locked+1)/2], ";";
    print "Save_Head:_", $yes_no[($config_saved>0+1)/2], "(", $config_saved, ");";
    print "Save_Data:_", $yes_no[($save_data+1)/2], "(", $ctr_data, ");";
    print "Save_Raw:_", $yes_no[($save_raw+1)/2], "(", $ctr_raw, ");";
    print "Alert:_", $yes_no[($check_alert+1)/2], "(", $ctr_email, ")";
    print "\n\n<k>Lock<h>SvHead<d>SvData<r>SvRaw<a>Alert<g>Debug<s>STOP\n\n";
    print "\n....._Mean....._Std._Dev....._RMS....._Alert_IF\n";

    if ($save_data == 1 && $ctr_data == 0){
        ## Print DAT
        open DAT, ">>$data_file";
        print DAT sprintf("%16.5f", $temp_time), "\t", &get_time($temp_time);
    }

    # -- unsync channel scanning >> #
    $body = '';
    for ($i = 0; $i < $n_channels; $i++){
        $task_handle = pack('i', $task_handle);
        $report = $fCreateTask->Call($task_name, $task_handle);
        die ("!-Could_not_Create_Task._Error:_", $report, "\n" ) unless ($report == 0);
        $task_handle = unpack('i', $task_handle);
        if ($channels[$i][2] == 1){
            $report = $fCreateAIVoltageChan->
                Call($task_handle, $channels[$i][0], $channels[$i][1], $cTerminalConfig,
                    $channels[$i][3], $channels[$i][4], $cDAQmx_Val_Volts, $cCustomScaleName);
            die ("!-Could_not_add_Channel._Error:_", $report, "\n" ) unless ($report == 0);
            $report = $fSetRate ->Call($task_handle, "", $sampling_rate, $cActiveEdge,
                $cSampleMode, int64($samples_per_ch));
            die ("!-Could_not_set_ADC_sampling_rate._Error:_", $report, "\n" ) unless ($report == 0);
            $report = $fStartTask->Call($task_handle);
            die ("!-Could_not_start_Task._Error:_", $report, "\n" ) unless ($report == 0);
            $samples_per_ch_read = pack('i', $samples_per_ch_read);
            $report = $fReadAnalogF64->
                Call($task_handle, $samples_per_ch, $cReadTimeout, $cInterlace, $waveform_out,
                    $waveform_size, $samples_per_ch_read, $cReserved);
            $samples_per_ch_read = unpack('i', $samples_per_ch_read);
            @arrange_data_lch($i, $samples_per_ch, $waveform_out, @data_array);
            ($mean[$i], $stddev[$i], $rms[$i]) = &mean_stddev_rms($data_array[$i], $samples_per_ch);
        }
        elsif ($channels[$i][2] == 2){
            $report = $fCreateAIThrmcp1Chan->
                Call($task_handle, $channels[$i][0], $channels[$i][1], $channels[$i][3], $channels[$i][4],
                    $cDAQmx_Val_DegC, $cDAQmx_Val_J_Type_TC, $cDAQmx_Val_BuiltIn, 0.0, '');
            die ("!-Could_not_add_Channel._Error:_", $report, "\n" ) unless ($report == 0);
            $report = $fStartTask->Call($task_handle);
            die ("!-Could_not_start_Task._Error:_", $report, "\n" ) unless ($report == 0);
            $scalar_out = pack('d', $scalar_out);
            $report = $fReadAnalogScalarF64->Call($task_handle, $cReadTimeout, $scalar_out, $cReserved);
        }
    }
}

```

```

        die ("Could_not_read_Value_Error:_", $report, "\n" ) unless ($report == 0);
        $scalar_out = unpack('d', $scalar_out);
        $waveform_out = "\0" x 8 x $waveform_size;
        &arrange_data_1ch($i, $samples_per_ch, $waveform_out, \@data_array);
        ($mean[$i], $stddev[$i], $rms[$i]) = ($scalar_out, 0, 0);
    }

    # Check Alerts; format: [0]Off(0)/If Larger(1)/Smaller(-1) Than, [1]Trigger Threshold, [2]Release Threshold
    if ($check_alert == 1){
        if (($channels[$i][5] != 0)){
            if ($alert_status[$i] == 0){
                if (($channels[$i][5]*$mean[$i]) > ($channels[$i][5]*$channels[$i][6])){
                    $alert_status[$i] = 1; # trigger alert
                } else { $alert_status[$i] = -1; } # release alert
            }
            elsif (($alert_status[$i] != 0)){
                if ($alert_status[$i] == -1){
                    if (($channels[$i][5]*$mean[$i]) > ($channels[$i][5]*$channels[$i][6])){
                        $alert_status[$i] = 1; # trigger alert
                    }
                }
                elsif ($alert_status[$i] == 1){
                    if (($channels[$i][5]*$mean[$i]) < ($channels[$i][5]*$channels[$i][7])){
                        $alert_status[$i] = -1; # release alert
                    }
                }
            }
        }
        elsif (($channels[$i][5] == 0)){
            $alert_status[$i] = 0;
        }
        if ($alert_status[$i] != 1){
            $body = join(' ', $body, sprintf("Ch%2d.%8s_\\%fString;_\\n", $i,
                $channels[$i][8], &ewo0($fDisp, $mean[$i]));
        }
        elsif ($alert_status[$i] == 1){
            $body = join(' ', $body,
                sprintf("Ch%2d.%8s_\\%fString_\\%fStringA_\\%fStringA;_\\n",
                    $i, $channels[$i][8], &ewo0($fDisp, $mean[$i]),
                    $lg_sm[$channels[$i][5]+1], &ewo0($fDispA, $channels[$i][6]),
                    &ewo0($fDispA, $channels[$i][7]));
        }
    }
    elsif ($check_alert == -1){
        $alert_status[$i] = 0;
    }
}

## Display
printf("Ch%2d.%8s_\\%fString_\\%fString_\\%fString_\\%fStringA_\\%fStringA;_\\n",
    $i, $channels[$i][8], &ewo0($fDisp, $mean[$i]), &ewo0($fDisp, $stddev[$i]), &ewo0($fDisp, $rms[$i]),
    $lg_sm[$channels[$i][5]+1], &ewo0($fDispA, $channels[$i][6]),
    &ewo0($fDispA, $channels[$i][7]), $alert_disp[$alert_status[$i]+1]);

## Print DAT
# if ($save_data == 1 && $ctr_data == 0){ print DAT "\t", $mean[$i], "\t", $stddev[$i], "\t", $rms[$i]; }
if ($save_data == 1 && $ctr_data == 0){
    print DAT "\t", &ewo0($fData, $mean[$i]), "\t",
        &ewo0($fData, $stddev[$i]), "\t", &ewo0($fData, $rms[$i]);
}

$report = $WaitUntilTaskDone->Call($task_handle, $cReadTimeout);
die ("!-Could_not_wait_until_Task_done_Error:_", $report, "\n" ) unless ($report == 0);
$report = $fStopTask->Call($task_handle);
die ("!-Could_not_stop_Task_Error:_", $report, "\n" ) unless ($report == 0);
$report = $fClearTask->Call($task_handle);
die ("!-Could_not_clear_Task_Error:_", $report, "\n" ) unless ($report == 0);
usleep($delay_after_acq*1_000_000);
}

# << unsync channel scanning -- #

## Print DAT
if ($save_data == 1 && $ctr_data == 0){ print DAT "\n"; }
if ($save_data == 1 && $ctr_data == 0){ close DAT; }

## Timing Section
if ($save_data == 1 && $ctr_data == 0){
    $ctr_data = $data_interval - 1;
    if ($save_raw == 1 && $ctr_raw == 0){
        &save_raw_data(\@data_array, $n_channels, $samples_per_ch, $data_dir_path,
            $start_time, 'raw_' . &get_time($temp_time) . '.txt', $fRaw);
        $ctr_raw = $raw_interval - 1;
    }
    elsif ($save_raw == 1 && $ctr_raw > 0){ $ctr_raw--; }
    if ($check_alert == 1){
        $alert_triggered = -1;
        foreach(@alert_status){ if ($_ == 1){ $alert_triggered = 1; } }
        if ($alert_triggered == 1 && $ctr_email == 0){
            # print "\n", $body, "\n";
            &GMail_Send($gmail_acc, $gmail_pwd, $from, $to, $subject, $body);
            $ctr_email = $email_interval - 1;
        }
        elsif ($alert_triggered == 1 && $ctr_email > 0){ $ctr_email--; }
        elsif ($alert_triggered == -1){ $ctr_email = 0; }
    }
}
}
}

```

```

elseif ($save_data == 1 && $ctr_data > 0){ $ctr_data--; }
if ($save_data == -1){ $ctr_data = 0; }
if ($save_raw == -1){ $ctr_raw = 0; }
if ($check_alert == -1){ $ctr_email = 0; }

## Display Config
# print "\n\n", $body, "\n\n";

## Dump irrelevant keys (other than 's' when not locked, everything when locked)
while($key_in ne "\0"){
  if ($key_in eq 's'){
    if ($locked == 1){
      $key_in = ReadKey(-1);
      if (not defined $key_in){ $key_in = "\0"; }
    }
    elseif ($locked == -1){
      last;
    }
  }
  elseif($key_in ne 's'){
    $key_in = ReadKey(-1);
    if (not defined $key_in){ $key_in = "\0"; }
  }
}

## Sleep until time interval
$temp_time_prime = Time::HiRes::time;
if ($read_interval > ($temp_time_prime - $temp_time)){
  usleep(($read_interval- ($temp_time_prime - $temp_time))*1_000_000);
}
if ($read_interval < 0){
  system('pause')
};
}
ReadMode 0; # Reset tty mode before exiting

#####

sub arrange_data_lch{
  my $i_channel = shift;
  my $samples_per_ch = shift;
  my $waveform_out = shift;
  my $ptr_array = shift;
  my $j = 0;
  for ($j = 0; $j < $samples_per_ch; $j++){
    $$ptr_array[$i_channel][$j] = unpack('d', substr($waveform_out, $j*8, 8));
  }
}

sub arrange_data_sync{
  my $n_channels = shift;
  my $samples_per_ch = shift;
  my $waveform_out = shift;
  my $ptr_array = shift;
  my $interleaved = shift;
  my ($i, $j) = 0;
  for ($i = 0; $i < $n_channels; $i++){
    for ($j = 0; $j < $samples_per_ch; $j++){
      if ($interleaved == 1){
        $$ptr_array[$i][$j] = unpack('d', substr($waveform_out, (($j)*$n_channels+$i)*8, 8));
      }
      elseif ($interleaved == 0){
        $$ptr_array[$i][$j] = unpack('d', substr($waveform_out, (($i)*$samples_per_ch+$j)*8, 8));
      }
    }
  }
}

sub get_time{
  my $time_hi_res = shift;
  my $time = floor($time_hi_res);
  my $sec_fraction = floor(($time_hi_res - $time)*1000);
  my ($sec,$min,$hour,$mday,$mon,$year,$yday,$isdst) = localtime($time);
  $year -= 100;
  $mon += 1;
  return (sprintf("%02d%02d%02d%02dh%02dm%02ds%03d", $year, $mon, $mday, $hour, $min, $sec, $sec_fraction));
}

sub save_raw_data{
  my $ptr_array = shift;
  my $n_channels = shift;
  my $samples_per_ch = shift;
  my $data_dir_path = shift;
  my $raw_dir = shift;
  my $raw_dir_path = $data_dir_path . "\\\" . $raw_dir;
  my $raw_file = shift;
  my $fRaw = shift;
  my ($i, $j) = 0;
  if ( ! (-e $raw_dir_path) ){
    mkdir($raw_dir_path);
  }
  open RAW, ">$raw_dir_path\\$raw_file";
  print RAW "\%#";
  for ($i = 0; $i < $n_channels; $i++){
    print RAW "\tCh", $i;
  }
}

```

```

}
print RAW "\n";
for ($j = 0; $j < $samples_per_ch; $j++){
    print RAW $j;
    for ($i = 0; $i < $n_channels; $i++){
        print RAW "\t", &ewo0($fRaw, $$ptr_array[$i][$j]);
    }
    print RAW "\n";
}
close RAW;
}

sub mean_stddev_rms{
    my $ptr_array = shift;
    my $size_array = shift;
    my $j = 0;
    my $mean = 0;
    for ($j = 0; $j < $size_array; $j++){
        $mean += $$ptr_array[$j];
    }
    $mean /= $size_array;
    my $stddev = 0;
    my $rms = 0;
    for ($j = 0; $j < $size_array; $j++){
        $stddev += (($ptr_array[$j]-$mean)**2);
        $rms += (($ptr_array[$j])**2);
    }
    $stddev = sqrt($stddev/$size_array);
    $rms = sqrt($rms/$size_array);
    return ($mean, $stddev, $rms);
}

sub GMail_Send(){
    my $gmail_acc = shift;
    my $gmail_pwd = shift;
    my $from = shift;
    my $to = shift;
    my $subject = shift;
    my $body = shift;

    my $smtp = Net::SMTP::SSL->new('smtp.gmail.com', Port => 465, Debug => 1)
        || die "Could_not_connect_to_server\n";

    $smtp->auth($gmail_acc, $gmail_pwd)
        || die "Authentication_failed!\n";

    $smtp->mail($from . "\n");
    my @reipients = split(/,/, $to);
    foreach (@reipients){
        $smtp->to($_ . "\n");
    }
    $smtp->data();
    $smtp->datasend("From:_ " . $from . "\n");
    $smtp->datasend("To:_ " . $to . "\n");
    $smtp->rawdatasend("Subject:_ " . $subject . "\n");
    $smtp->datasend("Content-Type:_text/plain;" . "\n");
    $smtp->datasend("Content-Transfer-Encoding:_8bit" . "\n");
    $smtp->datasend("\n");
    $smtp->rawdatasend($body . "\n");
    $smtp->dataend("\n");
    $smtp->dataend();
    $smtp->quit;
}

sub ewo0{
    # (e)xponential form (w)ith(o)ut leading (0)'s in exponent
    my $input = sprintf(shift, shift); # (format, input)
    my $tail = chop $input;
    my $temp = '0';
    $temp = chop $input; if ($temp ne '0'){ $tail = $temp . $tail; }
    $temp = chop $input; if ($temp ne '0'){ $tail = $temp . $tail; }
    return ($input . $tail);
}

```

Appendix I

Calorimeter: Certificate of Calibration

Certificate #:	199696-120216	Customer Name:	
Model Number:	XLP12-3S-H2-D0	Instrument ID:	V5
Serial Number:	199696	Date of Calibration:	Feb. 16, 2012
Filter Number:		Calibration Due Date:	*
Cal. Procedure:	420- 19325		

Calibration Data

Calibration										
λ	Sensitivity		Into Load	Power Level		Ambient Temp.	Relative humidity	0-95% Risetime	Beam Ø	
				Power	Rep.Rate					
µm	mV/W	%	Ω	Watts	Hz	°C	%	s	mm	
1.064	^P 156.3	± 2.5	100k	0.5	10	23	20	2.5	8.4	

^S Value Corrected According To Spectral Absorption Curve
^P Sensitivity programmed in detector head
Note: V5 and Higher version detectors contain additional data that allow Gentec-EO monitors to apply a Personal wavelength correction TM. Refer to the monitor's manual for more information. For all other cases, adjust the power with :

$$P(\lambda_2) \text{ Watts} = P(\lambda_1) \text{ Watts} \times \frac{S(\lambda_1)}{S(\lambda_2)}$$

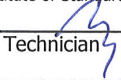
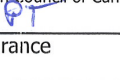
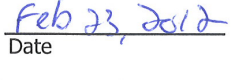
λ1: Wavelength listed above
 λ2: The new wavelength
 P(1): Measured Power
 P(2): Power adjusted for new wavelength
 S(1): Sensitivity listed above
 S(2): Sensitivity at new wavelength. Infer from absorption table and plot.

Test Equipment and Standards Used

ID#	Description	Serial#	Last Cal.	By	Certificate #
EO-1202	ND: YAG 943Q, Laser Application Pulsed , beam profile: Semi-Gaussian	P1106	n/a	n/a	n/a
EO-273	National Instrument, NI 4351 for PCI	D64A36	Nov. 23, 2011	Gentec-EO	D64A36-111123
EO-180	Gentec-EO, PSV-3103, 'Wattmeter	59054	Jun. 10, 2011	NIST	813163-280219-11

Declaration of Conformity

Gentec Electro-Optics certifies that, at the time of calibration, the above listed instrument meets or exceeds all of the specifications defined in the calibration procedure(s) or customer specification(s). The above listed instrument has been calibrated using standards traceable to the National Institute of Standards and Technology (NIST) or the National Research Council of Canada (NRC).

 Technician
 Quality Assurance
 Date

***For Customer Use Only**

The calibration interval of this instrument begins on the date of receipt by the customer. The recommended calibration interval is 12 months. Please fill in appropriate dates as indicated.

Date Instrument Received: _____ Calibration Due Date: _____

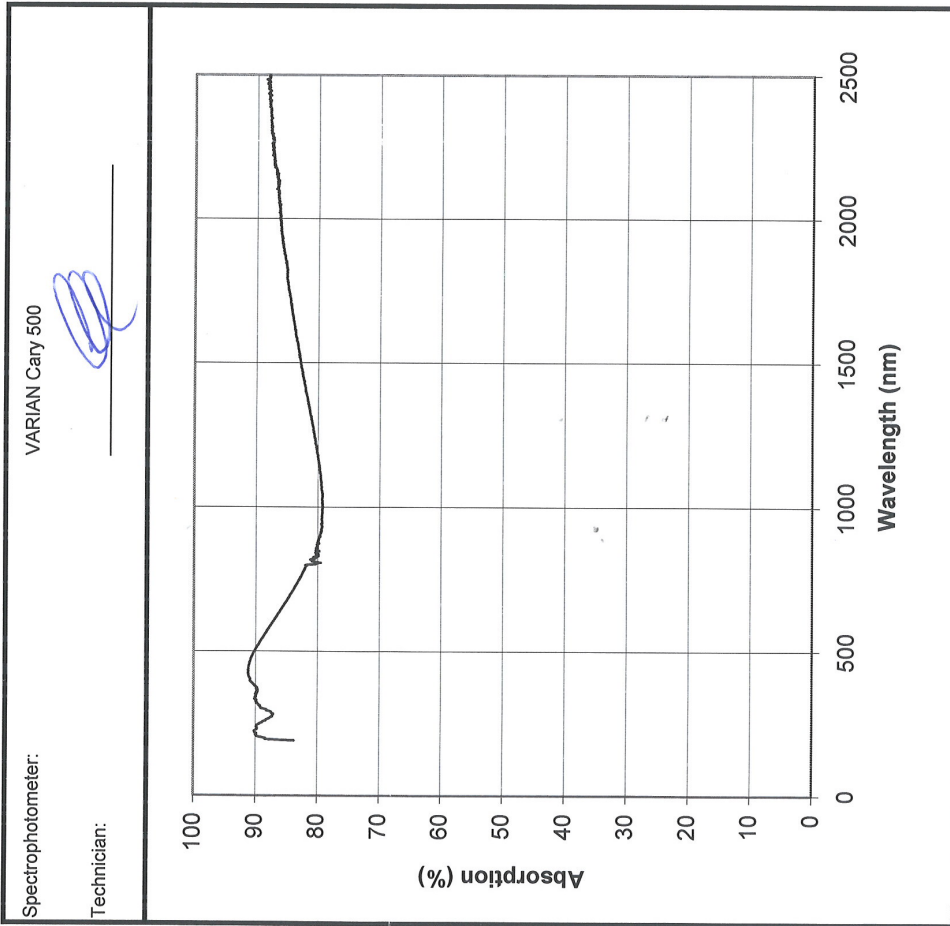
No reproduction of this document is permitted except in full 190059 Rev Y
 ACI-1379

GENTEC ÉLECTRO-OPTIQUE inc. GENTEC ELECTRO-OPTICS, Inc.



Personal wavelength correction™ Certificate

Spectral Absorption Plot measured for: XLP12-3S-H2-D0 Power Detector Serial #199696



Personal Wavelength Correction™	
Wavelength (nm)	Correction multiplier
193	0.916
213	0.883
248	0.889
266	0.904
308	0.890
337	0.882
355	0.885
488	0.878
514	0.884
532	0.889
578	0.903
632	0.920
694	0.940
720	0.948
810	0.988
980	1.001
1064 *	1.000
1550	0.954
2100	0.916
10600**	0.930

* Calibration wavelength
** Typical value

Adjustment multiplier for wavelength under 250 nm are not traceable.
For Gentec-EO monitors, select the proper wavelength in menu
For other monitors, multiply by the correction multiplier
Energy corrected = Energy read x correction multiplier
Example: Energy (488 nm) = 10mJ x 0.878 = 8.78 mJ

Certificate #:	124746-141126	Customer Name:	OPTON LASER INTERNATIONAL
Model:	PS-330WB	V5	
Serial Number:	124746	Instrument ID:	
Filter Number:		Date of Calibration:	Nov. 25, 2014
Cal. Procedure:	420- 19325	Calibration Due Date:	Nov. 25, 2015

Calibration Data

Calibration									
λ	Sensitivity (95% level of confidence)		Into Load	Power Level		Ambient Temp.	Relative Humidity	0-95% Risetime	Beam \varnothing
				Power	Rep. Rate				
μm	mV/W	%	Ω	Watts	Hz	$^{\circ}\text{C}$	%	s	mm
^P 1.064	20.98	\pm 2.5	100k	15.1	cw	24	30	2.6	40

^S Value Corrected According To Spectral Absorption Curve

^P Sensitivity programmed in detector head

Note: V5 and Higher version detectors contain additional data that allow Gentec-EO monitors to apply a *Personal wavelength correction*™. Refer to the monitor's manual for more information. For all other cases, adjust the power with :

$$P(\lambda_2) \text{ Watts} = P(\lambda_1) \text{ Watts} \times \frac{S(\lambda_1)}{S(\lambda_2)}$$

$P(\lambda_1)$: Measured Power

$S(\lambda_1)$: Sensitivity listed above

λ_1 : Wavelength listed above

λ_2 : The new wavelength

$P(\lambda_2)$: Power adjusted for new wavelength

$S(\lambda_2)$: Sensitivity at new wavelength. Infer from absorption table and plot.

Test Equipment and Standards Used

ID#	Description	Serial#	Last Cal.	By	Certificate #
EOC-1201	Quantronix, Model 117, ND:YAG, CW Laser, beam profile: Multimode	1213	n/a	n/a	n/a
EOCE-303	Gentec-EO, UP55N, wattmeter	159411	Sep. 08, 2014	NIST	814641-285133-14
EOCE-701	National Instrument, NI 4351 for PCI	1233DEC	Nov. 10, 2014	Gentec-EO	1233DEC-141110

Declaration of Conformity

Gentec Electro-Optics certifies that, at the time of calibration, the above listed instrument meets or exceeds all of the specifications defined in the calibration procedure(s) or customer specification(s). The above listed instrument has been calibrated using standards traceable to the National Institute of Standards and Technology (NIST) or the National Research Council of Canada (NRC).

Technician

Quality Assurance

Date

Nov. 26, 2014

Variance Report

	Last Calibration	As Received	New Calibration
Date	Oct. 01, 1998	Nov. 19, 2014	Nov. 25, 2014
Sensitivity (mV/W)	21.71	21.07	20.98
Difference (from last calibration)	-----	-0.6	-0.7
Change (%)	-----	-2.9	-3.4

Remark : Detector was repaired.

No reproduction of this document is permitted except in full

190059 Rev AF
ACI-1931

GENTEC ÉLECTRO-OPTIQUE inc. GENTEC ELECTRO-OPTICS, Inc.

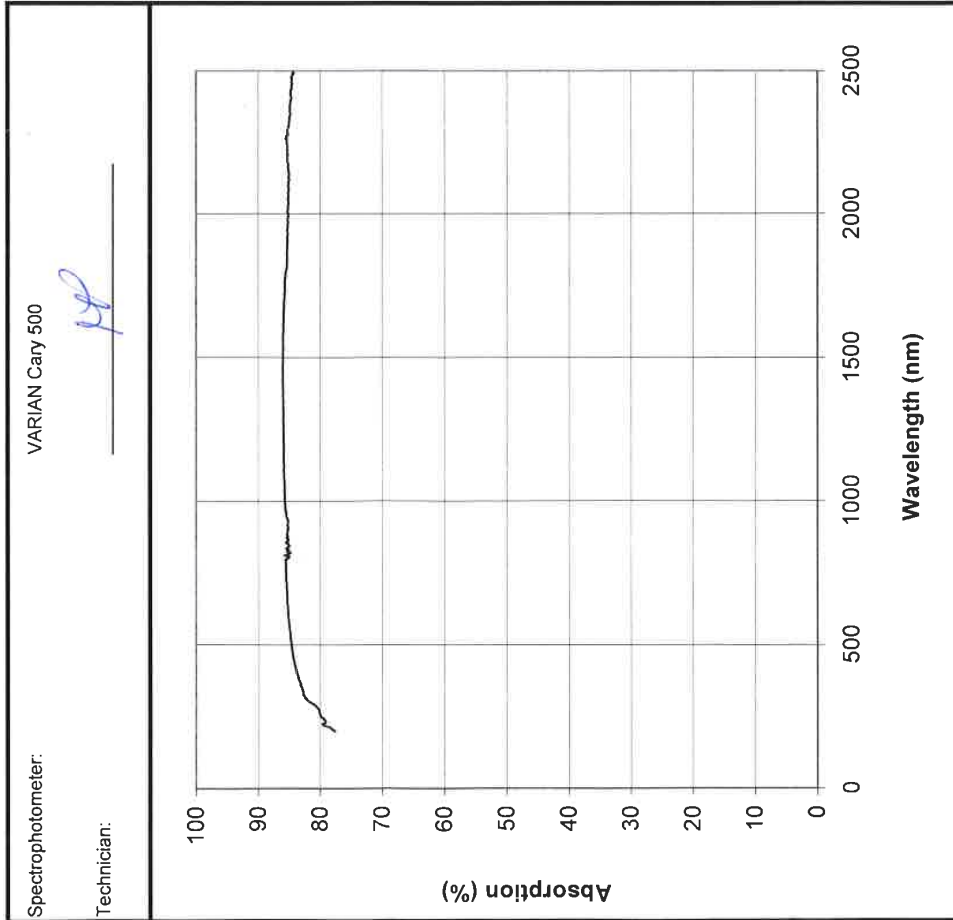
445, St-Jean-Baptiste, Suite 160, Québec, QC, G2E 5N7, Canada T) 418.651.8003 F) 418.651.1174 1.888.5Gentec (543.6832) E) info@gentec-eo.com W) gentec-eo.com



Personal wavelength correction™ Certificate

Serial #124746

Spectral Absorption Plot measured for: PS-330WB Power Detector



Personal Wavelength Correction™	
Wavelength (nm)	Correction multiplier
193	1.137
213	1.093
248	1.075
266	1.070
308	1.044
337	1.036
355	1.032
488	1.014
514	1.012
532	1.011
578	1.009
632	1.006
694	1.004
720	1.003
810	1.004
980	1.001
1064 *	1.000
1550	0.998
2100	1.008

* Calibration wavelength

Adjustment multiplier for wavelength under 250 nm are not traceable.

For Gentec-EO monitors, select the proper wavelength in menu

For other monitors, multiply by the correction multiplier

Power corrected = Power read x correction multiplier

Example: Power (488 nm) = 10mW x 1.014 = 10.14 mW

Certificate #:	175292-141118	Customer Name:	OPTON LASER INTERNATIONAL
Model:	UP55N-300F-H9-D0 V5	Instrument ID:	
Serial Number:	175292	Date of Calibration:	Nov. 18, 2014
Filter Number:		Calibration Due Date:	Nov. 18, 2015
Cal. Procedure:	420- 19325		

Calibration Data

λ	Sensitivity (95% level of confidence)		Into Load	Power Level		Ambient Temp.	Relative Humidity	0-95% Risetime	Beam Ø
				Power	Rep.Rate				
				Ω	Watts				
μm	mV/W	%	Ω	Watts	Hz	°C	%	s	mm
^P 1.064	0.0875	± 2.5	100k	101	cw	23	15	2.0	40

^s Value Corrected According To Spectral Absorption Curve

^P Sensitivity programmed in detector head

Note: V5 and Higher version detectors contain additional data that allow Gentec-EO monitors to apply a *Personal wavelength correction*™. Refer to the monitor's manual for more information. For all other cases, adjust the power with :

$$P(\lambda_2) \text{Watts} = P(\lambda_1) \text{Watts} \times \frac{S(\lambda_1)}{S(\lambda_2)}$$

P(λ₁): Measured Power

S(λ₁): Sensitivity listed above

λ₁: Wavelength listed above

λ₂: The new wavelength

P(λ₂): Power adjusted for new wavelength

S(λ₂): Sensitivity at new wavelength. Infer from absorption table and plot.

Test Equipment and Standards Used

ID#	Description	Serial#	Last Cal.	By	Certificate #
EOC-1201	Quantronix, Model 117, ND:YAG, CW Laser, beam profile: Multimode	1213	n/a	n/a	n/a
EOCE-904	Gentec-EO, UP55G, wattmeter	180178	Sep. 08, 2014	NIST	814892-285133-14
EOCE-701	National Instrument, NI 4351 for PCI	1233DEC	Nov. 10, 2014	Gentec-EO	1233DEC-141110

Declaration of Conformity

Gentec Electro-Optics certifies that, at the time of calibration, the above listed instrument meets or exceeds all of the specifications defined in the calibration procedure(s) or customer specification(s). The above listed instrument has been calibrated using standards traceable to the National Institute of Standards and Technology (NIST) or the National Research Council of Canada (NRC).

Technician

Quality Assurance

Date Nov. 26, 2014

Variance Report

	Last Calibration	As Received	New Calibration
Date	Feb. 27, 2008	Nov. 18, 2014	Nov. 18, 2014
Sensitivity (mV/W)	0.0886	0.0875	0.0875
Difference (from last calibration)	-----	-0.0011	-0.0011
Change (%)	-----	-1.2	-1.2

Remark : When no repair is made to the detector, the "As received" and "New Calibration" values are the same.

No reproduction of this document is permitted except in full

190059 Rev AF
ACI-1931

GENTEC ÉLECTRO-OPTIQUE INC.

GENTEC ELECTRO-OPTICS, INC.

445, St-Jean-Baptiste, Suite 160, Québec, QC, G2E 5N7, Canada T) 418.651.8003 F) 418.651.1174 1.888.5Gentec (543.6832) E) info@gentec-eo.com W) gentec-eo.com



Personal wavelength correction™ Certificate

Serial #175292

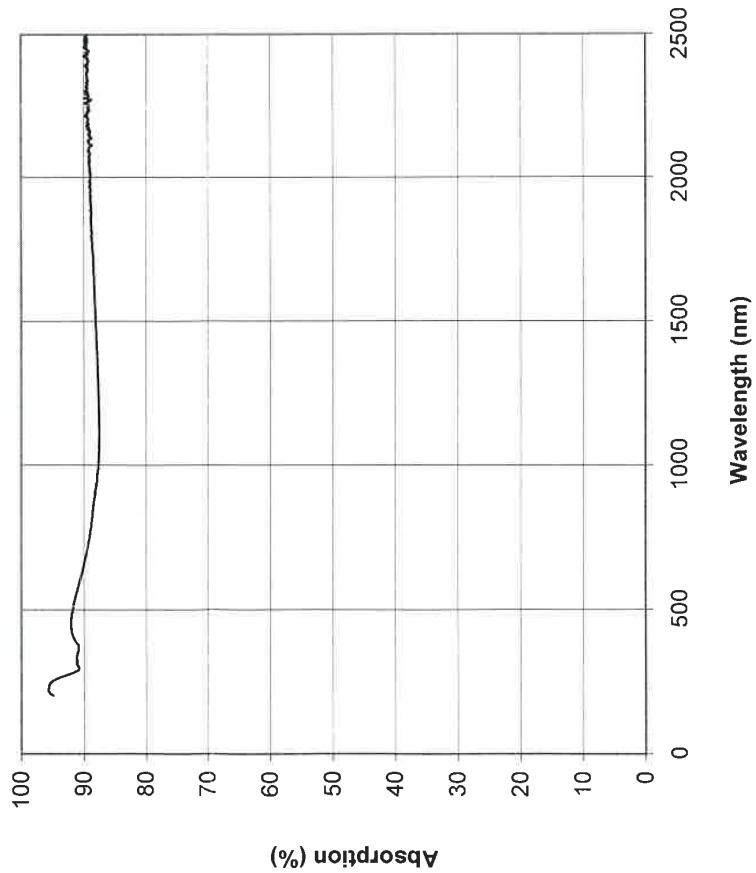
Spectral Absorption Plot measured for: UP55N-300F-H9-D0 Power Detector

Spectrophotometer:

VARIAN Cary 500

Technician:





Personal Wavelength Correction™	
Wavelength (nm)	Correction multiplier
193	0.930
213	0.916
248	0.920
266	0.938
308	0.961
337	0.961
355	0.963
488	0.953
514	0.955
532	0.958
578	0.963
632	0.970
694	0.977
720	0.980
810	0.987
980	0.998
1064*	1.000
1550	0.993
2100	0.982
10600**	0.930

* Calibration wavelength
** Typical value
Adjustment multiplier for wavelength under 250 nm are not traceable.
For Gentec-EO monitors, select the proper wavelength in menu
For other monitors, multiply by the correction multiplier
Power corrected = Power read x correction multiplier
Example: Power (488 nm) = 10mW x 0.953 = 9.53 mW

100046 revision V

ACI-1931

Acknowledgments

My interest in the field of laser interferometric gravitational wave detectors started from a summer internship with Dr. Frédéric Cleva, to whom I would also like to express my gratitude for the proposal of the thesis work, for the tutoring of numerous experimental techniques, and for the discussions across a broad spectrum of topics. I wish to thank him at least as much as what I have learned from him.

Secondly, I would like to thank Dr. Catherine Nary Man for the supervision of the thesis work and the coordination of the support throughout the ARTEMIS¹ laboratory, in particular our colleagues in the Advanced Virgo Pre-Stabilized Laser team: Jean-Pierre Coulon, Dr. Fabien Kéfélian, Mourad Merzougui and Dr. Margherita Turconi. In addition, I wish to thank Dr. Walid Chaibi for the discussions on fiber laser amplifiers.

I am also in debt to Dr. Michel Lintz, the office mate of Frédéric and myself, for his prompt and inspiring replies to many of my pop-up questions.

The three years here at the Observatoire de la Côte Azur had been enjoyable. Many thanks to our colleagues for supporting such a great infrastructure.

The thesis work is under the framework of the Advanced Virgo project and is co-funded by the European Gravitational Observatory and the Région Provence-Alpes-Côte d'Azur of France.



Observatoire
de la CÔTE d'AZUR



EGO EUROPEAN
GRAVITATIONAL
OBSERVATORY



¹UMR 7250 CNRS, Astrophysique Relativiste Théories Expériences Métrologie Instrumentation Signaux, <https://artemis.oca.eu/>

Remerciements

Ma connaissance du domaine des interféromètres de laser comme des détecteurs d'ondes gravitationnelles a commencé comme un stage d'été avec M. Frédéric Cleva, à qui j'aimerais remercier également pour la proposition de ce sujet de thèse, pour l'apprentissage de nombreuses techniques expérimentales, et pour les discussions de sujets variés. Je souhaite de lui remercier au moins autant que ce que j'ai appris de lui.

Deuxièmement, j'aimerais remercier Mme. Catherine Nary Man pour la direction du travail de thèse et la coordination pour un soutien solide du laboratoire ARTEMIS², surtout de notre collègues dans l'équipe du Laser Pré-Stabilisé pour le projet Advanced Virgo: M. Jean-Pierre Coulon, M. Fabien Kéfélian, M. Mourad Merzougui et Mme. Margherita Turconi. En plus, je souhaite remercier M. Walid Chaibi pour les discussions sur les amplificateurs à fibre.

Je souhaite aussi remercier M. Michel Lintz, avec qui Frédéric et moi partagent le bureau, pour ses réponses rapides et inspirantes à mes questions pop-up.

Les trois ans ici à l'Observatoire de la Côte d'Azur ont été très agréables. Merci beaucoup aux collègues qui soutient cette infrastructure géniale.

Ce travail de thèse est dans le cadre du projet Advanced Virgo, et est co-financé par l'European Gravitational Observatory et la Région Provence-Alpes-Côte d'Azur.



²UMR 7250 CNRS, Astrophysique Relativiste Théories Expériences Métrologie Instrumentation Signaux, <https://artemis.oca.eu/>

Curriculum Vitae

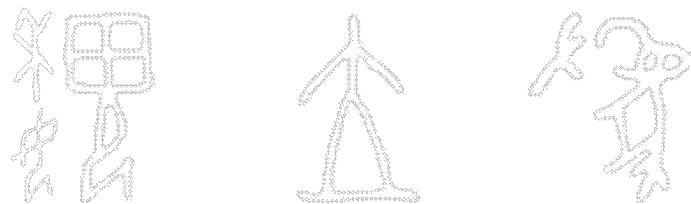
魏立為

Li-Wei WEI

born November 28, 1985

in Fengyuan, Taiwan

- 2001 – 2004 National Taichung First Senior High School, Taiwan
- 2004 – 2008 National Chiao Tung University, Hsinchu, Taiwan
B.Sc. in Photonics
Fabrication and characterization of polarized polymer light-emitting diodes
- 2008 – 2009 Naval Officer, Ensign, Military Service, Kaohsiung, Taiwan
- 2009 – 2011 Erasmus Mundus Scholarship, European Commission
M.Sc. in Optics, Material and Plasmas
Institut d'Optique Graduate School, Palaiseau, France
M.Sc.Eng. in Photonics Engineering
Warsaw University of Technology, Poland
Finite difference methods in frequency domain (FDFD)
Light propagation in photonic liquid crystal fibers
- 2012 Joined ARTEMIS (UMR 7250 CNRS–OCA–UNS)
at the Observatoire de la Côte d'Azur as part of the
Pre-Stabilized Laser group of the Virgo collaboration



“Essentially, all models are wrong, but some are useful.”

— George E. P. Box